

Exploration of Second Sphere Reactivity: Carbon Dioxide Hydrogenation and Applications of Bis(amidinato)-N-Heterocyclic Carbene Iron Complexes

Author: Jessica Lin Drake

Persistent link: <http://hdl.handle.net/2345/bc-ir:104492>

This work is posted on [eScholarship@BC](#),
Boston College University Libraries.

Boston College Electronic Thesis or Dissertation, 2015

Copyright is held by the author, with all rights reserved, unless otherwise noted.

Boston College
The Graduate School of Arts and Sciences
Department of Chemistry

EXPLORATION OF SECOND SPHERE REACTIVITY: CARBON DIOXIDE
HYDROGENATION AND APPLICATIONS OF
BIS(AMIDINATO)-N-HETEROCYCLIC CARBENE IRON COMPLEXES

A dissertation

by

JESSICA LIN DRAKE

submitted in partial fulfillment of the requirements

for the degree of

Master of Science

August 2015

© copyright by JESSICA LIN DRAKE

2015

EXPLORATION OF SECOND SPHERE REACTIVITY: CARBON DIOXIDE
HYDROGENATION AND APPLICATIONS OF
BIS(AMIDINATO)-N-HETEROCYCLIC CARBENE IRON COMPLEXES

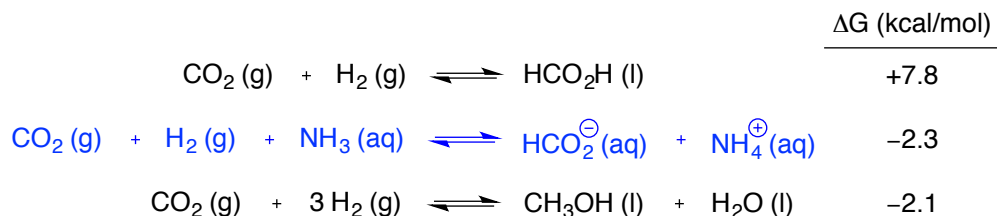
Jessica Lin Drake

Thesis Advisor: Jeffery A. Byers

Abstract

Chapter 1. Overview of Carbon Dioxide Hydrogenation for the Production of Formic Acid

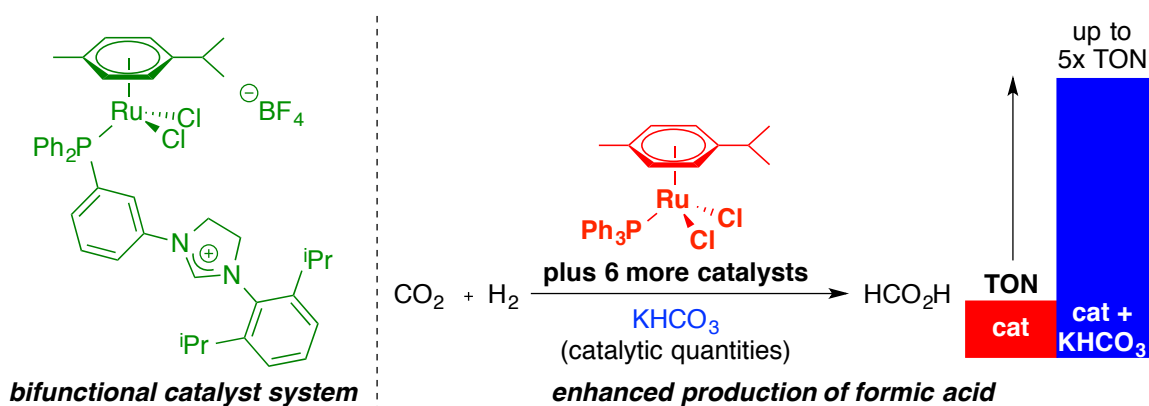
As the world's energy demands increase, our resources dwindle and the need for a sustainable energy source is pertinent. Our current energy infrastructure is dominated by fossil fuel use. Hydrogen, on the other hand, is potentially an ideal energy carrier as it is emissions-free when burned and can be used in fuel cells. Significant advances are still needed to develop more efficient ways to produce and store H₂. The hydrogenation of CO₂ to formic acid and/or methanol provides an encouraging and reversible approach for a hydrogen storage material.



The first example of homogeneously catalyzed hydrogenation of carbon dioxide was in 1976. Over the past 40 years, there has been excellent progress in the development of catalysts for CO₂ hydrogenation. Typically, homogenous catalysts found to be effective are 2nd and 3rd row transition metals of groups 8-10. In recent years, base-metals (common and inexpensive metals) have demonstrated promising results. This chapter is designed to highlight important discoveries throughout the history of carbon dioxide hydrogenation.

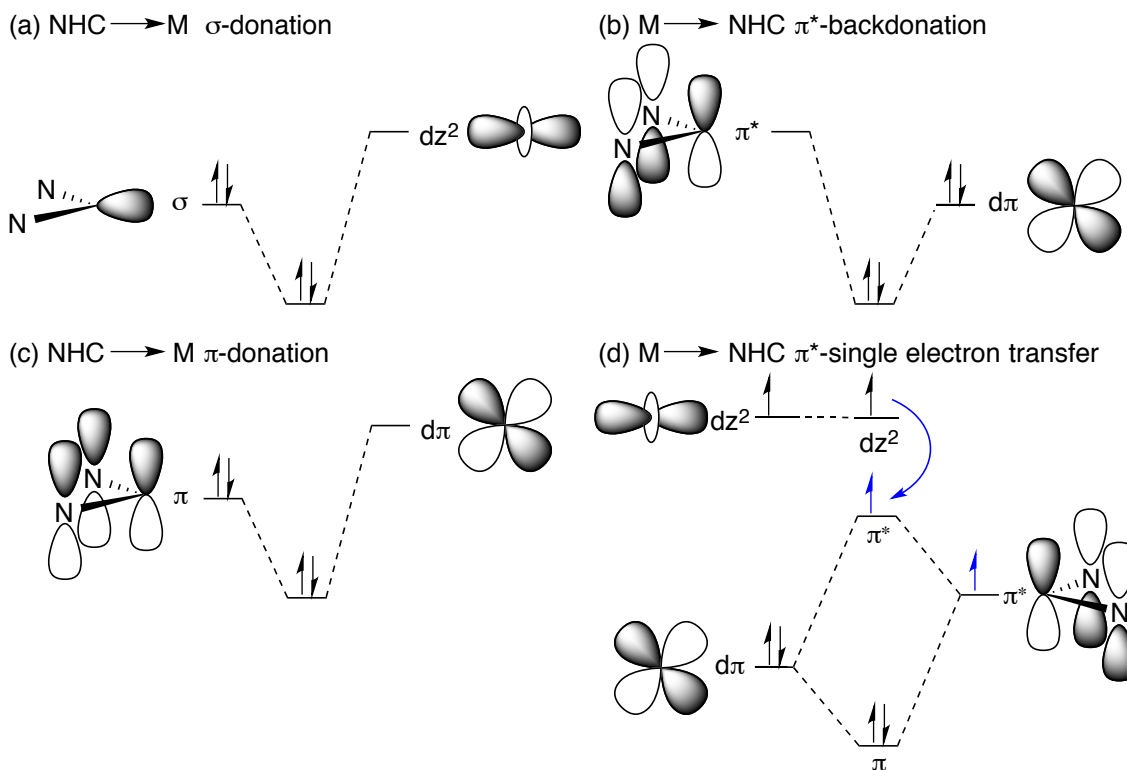
Chapter 2. Development of a Transition Metal / N-Heterocyclic Carbene Cooperative System for the Hydrogenation of Carbon Dioxide to Formic Acid

Over the past few decades, the conversion of small molecules such as H₂, N₂, O₂, CH₄, C₂H₄, CO, and CO₂ have attracted considerable attention. Many of these molecules are thermodynamically or kinetically stable and their usefulness depends on overcoming significant barriers. Frustrated Lewis pairs and N-heterocyclic carbenes have become common strategies to activate unreactive small molecule likes CO₂ and H₂. However, a hybrid approach utilizing both a transition metal and an activator has only recently been investigated for the transformation of small molecules to more useful and complex compounds. A novel method for these transformations is the use of a bifunctional catalyst system that incorporates a Lewis basic N-heterocyclic carbene and a Lewis acidic transition metal. This chapter highlights our serendipitous discovery that small quantities of bicarbonate and other inorganic salts enhanced the productivity of formic acid in CO₂ hydrogenation reactions. The phenomenon was general for many noble-metal catalysts and for one of the most efficient base-metal hydrogenation catalysts. Additionally, the synthesis of a transition metal complex bearing a pendant dihydroimidazolium salt is described. Stoichiometric and catalytic applications of the newly designed complex were explored in investigate our Lewis base / transition metal approach to small molecule activation.



Chapter 3. Chemistry of Iron N-Heterocyclic Carbene Complexes

N-heterocyclic carbenes are one of the most versatile ligands in organometallic chemistry due to their unique properties as ancillary ligands. Although NHCs are typically potent σ -donors (a) with minor contributions from π^* -backdonation (b), they also have the ability to accept electron density from the metal center as two-electron (c) or one-electron (d) interactions.



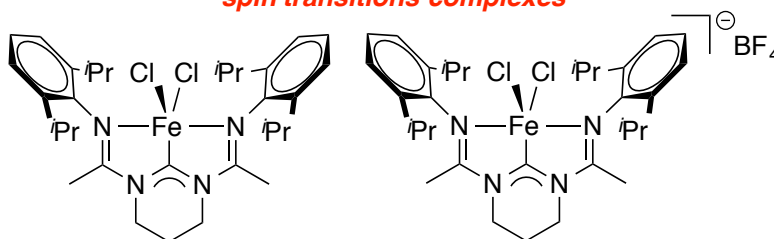
Since the first examples of metal–NHC complexes were reported in the 1960's, numerous studies have been devoted to the synthesis of new NHCs, to their characterization, and to their use as ligands in transition metal complexes. The coordination chemistry of NHCs with late transition metals has been studied extensively. However, the chemistry of iron–NHC complexes has not been developed to the same extent as other late transition metals. This chapter highlights important discoveries throughout the history of iron–NHC complexes, while emphasizing the nature of the metal–carbene bond.

Chapter 4. Reactivity of Bis(amidinato)-N-Heterocyclic Carbene Iron Complexes

Over the past few decades, the development of highly active and selective transition metal catalysts has attracted considerable attention. While the metal employed largely influences the expectations for catalytic activity, the importance of supporting ligands in tuning the reactivity of any given complex is vital. Our group recently synthesized a bis(amidinato)-N-heterocyclic carbene complex of iron as an analogy to the highly active bis(imino)pyridine iron complexes. We hypothesized that having an N-heterocyclic carbene as the central donor instead of pyridine could have significant impacts on the reactivity of such iron complexes. This chapter highlights the synthesis of iron bis(amidinato)-N-heterocyclic carbene complexes spanning multiple oxidation states previously described by our group. Through a combination characterization techniques, the bis(amidinato)-N-heterocyclic carbene was discovered to have unique interactions with the iron center, which change depending on the oxidation state of the metal. Additionally, we undertook investigations into the reactivity of these complexes with azides, hydrides, alkyl reagents, and ethylene. The results of which supported the capability of the bis(amidinato)-N-heterocyclic carbene ligand to act as a redox and chemical non-innocent ligand.

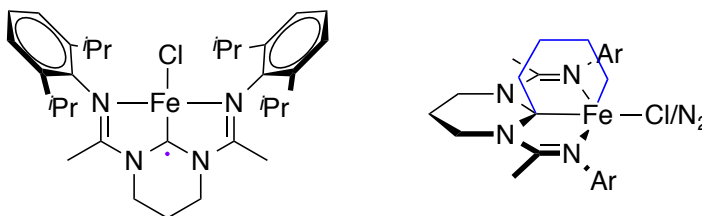
(a) high oxidation states

spin transitions complexes



active for diazene formation

(b) low oxidation states



redox non-innocent ligand

chemical non-innocent ligand

Contents

Chapter 1. Overview of Carbon Dioxide Hydrogenation for the Production of Formic Acid	1
1.1 Introduction	2
1.1.1 Hydrogen Production	2
1.1.2 Hydrogen Storage Systems	3
1.1.3 Hydrogenation of Carbon Dioxide to Formic Acid and/or Methanol.....	5
1.2 Noble-Metal Catalysts	8
1.2.1 Rhodium.....	8
1.2.2 Ruthenium.....	12
1.2.3 Iridium.....	20
1.3 Base-Metal Catalysts	28
1.3.1 Iron	29
1.3.2 Cobalt.....	33
1.4 References	38
Chapter 2. Development of a Transition Metal / N-Heterocyclic Carbene Cooperative System for the Hydrogenation of Carbon Dioxide to Formic Acid	41
2.1 Introduction	42
2.1.1 Reactivity of Frustrated Lewis Pairs with CO ₂	42
2.1.2 Hybrid Transition Metal / Frustrated Lewis Pair Approach for Activation of CO ₂	47
2.1.3 Reactivity of N-Heterocyclic Carbenes with CO ₂	50
2.2 Design of a Transition Metal / N-Heterocyclic Carbene Cooperative System	55
2.2.1 Strategies to Increase Nucleophilicity of Metal-Hydride Bonds	55
2.2.2 Approaches to Increase Electrophilicity of Carbon Dioxide	59
2.3 Addition of Imidazolium, Dihydroimidazolium, Bicarbonate, and Other Salts.....	62
2.3.1 Imidazolium and Dihydroimidazolium Salts	62
2.3.2 Bicarbonate and Other Inorganic Salts	70
2.4 Synthesis, Characterization, and Activity of a Ruthenium Complex Bearing a Pendant Dihydroimidazolium.....	80
2.4.1 Design, Synthesis, and Characterization.....	80
2.4.2 Stoichiometric Reactivity.....	86

2.4.3	Catalytic Activity	93
2.5	Conclusions	98
2.6	Experimental	99
2.6.1	General Considerations	99
2.6.2	Experimental Procedures	101
2.7	References	117
2.8	Spectra	120
Chapter 3.	Chemistry of Iron N-Heterocyclic Carbene Complexes	149
3.1	Introduction	150
3.2	Notable Examples of σ -Donating NHC Ligands.....	151
3.2.1	Ruthenium Catalyzed Olefin Metathesis	151
3.2.2	Palladium Catalyzed C–C Cross Coupling Reactions	154
3.3	Reactivity with σ -Donating Iron–NHC Complexes	158
3.3.1	Polymerization Reactions	159
3.3.1.1	Atom Transfer Radical Polymerization.....	159
3.3.1.2	Ring-Opening Polymerization.....	161
3.3.2	C–C Bond Forming Reactions	165
3.3.2.1	Kumada Cross-Coupling	165
3.3.2.2	Allylic Alkylation.....	170
3.3.3	Reduction Reactions	173
3.3.3.1	Hydrosilylation.....	173
3.3.3.2	Hydrogenation.....	177
3.4	π -Bonding and Single Electron Bonding in Metal–NHC Complexes.....	180
3.5	References	189
Chapter 4.	Reactivity of Bis(amidinato)-N-Heterocyclic Carbene Iron Complexes	192
4.1	Introduction	193
4.1.1	Bis(imino)pyridine Iron Complexes	193
4.1.1.1	Reactivity	194
4.1.1.2	Electronic Structure and its Effects on Reactivity	200
4.1.2	Modifications to the Bis(imino)pyridine Ligand Structure	206

4.2 Synthesis and Characterization of Complexes Bearing Bis(amidinato)-N-heterocyclic Carbene Ligands	213
4.2.1 Introduction.....	213
4.2.1.1 Iron(II) and Iron(III) Complexes.....	213
4.2.1.2 Formally Iron(I) and Dicarbonyl Iron(0) Complexes	217
4.2.2 Synthesis of a Bis(dinitrogen) Formally Iron(0) Complex	222
4.3 Catalytic and Stoichiometric Reactivity of Complexes Bearing Bis(amidinato)-N-heterocyclic Carbene Ligands	225
4.3.1 Aziridination and Diazene Homo-coupling	225
4.3.2 Redox and Chemical Non-Innocence of CDA Ligands.....	229
4.3.2.1 Reactivity with Super Hydride.....	229
4.3.2.2 Reactivity with an Alkyl Lithium Reagent	233
4.3.2.3 Reactivity with Ethylene	235
4.4 Conclusions	239
4.5 Experimental	241
4.5.1 General Considerations.....	241
4.5.2 Experimental Procedures	244
4.6 References	250
4.7 Spectra	253
Appendix. X-ray Crystallographic Data	255
A.1 Data for (κ^2 -carbonate)(<i>p</i> -cymene)(triphenylphosphine)ruthenium (2.40) at 100 K	256
A.2 Data for {N,N-1,3-bis[1-(2,6-diisopropylphenylimino)ethyl]-2-(κ^2 -butane)4,5,6-trihydropyrimidyl}iron chloride or dinitrogen (4.40) at 100 K.....	268

Acknowledgements

I have been extremely fortunate to have had many people in my life that have supported me and shaped me into the person that I am today. I would like to express my sincere gratitude to Boston College and the Boston College Chemistry department. Dale Mahoney and Ian Parr have been constant sources of support and guidance for me. I also would like to thank Professors Lynne O'Connell and Neil Wolfman for helping me reaffirm my passion and love for teaching. They have reminded me that making a positive impact on the future of our world doesn't have to mean being a professor who cares more about cutting-edge research than their students. Instead, my aim as a teacher can be to prepare my students to be good citizens of the world and to be satisfied, well-rounded human beings. They have made me realize that it's not just a job; it's a purpose for living.

I am extremely appreciative of my advisor, Jeffery A. Byers, for allowing me to be one of the first members of his group. It was a unique opportunity to see what it takes to be an assistant professor. I will forever be grateful for his continued interest in my education. Jeff has always challenged and encouraged me to be a better scholar and scientist. Without him, I'd be nowhere near the scientist that I am today. I would also like to thank my former undergraduate research advisor, Professor Timothy W. Funk. He has been helpful in providing me advice many times during my graduate school career. Tim was and remains my best role model for a scientist, mentor, and teacher. Additionally, I would like to thank the members of my thesis committee, Professors Amir H. Hoveyda and T. Ross Kelly for their continued support and guidance.

Furthermore, I would like to thank all the graduate, undergraduate, and post-doctoral students who have made graduate school an unforgettable experience. Every member of the Byers group at one point or another (Ashley Biernesser, David Cote, Julia Curley, Kayla Delle Chiaie, Carolyn Heusser, Hilan Kaplan, Aman Kaur, Jeff Kehl, Zhehui Li, Teresa Mako, Cesar Manna, Ben Reiner, Aris Vasilopoulos, Mikey Wojnar, Charlie Wolstenholme, Lauren Yablon, and

Xiaofei Zhang) has made a great impact on the person that I am today. Specifically, Hilan has been an extremely influential person and mentor for me at Boston College. He has taught me to think critically, over-analyze everything I do, and always do control reactions in a timely manner. Lauren and Julia have truly become two of my best friends. They are both incredibly smart and talented people who I know will be extraordinarily successful in anything and everything they do. My mentees, Charlie, Julia, and Aris, have all be amazingly intelligent and gifted students. I've enjoyed getting to know them and watching them grow as chemists and as people. Lastly, Cesar has given me guidance and unwavering encouragement. He has always been motivating and inspiring. He has taught me patience and compassion and helped me realize that I need to try and enjoy my life because I only get one.

Finally, I would like to thank my parents, Peter and Marcella Drake, for all of the love and support they have given me. Thank you for telling me what I'm capable of. For giving me the support that I needed when I didn't know I needed it. For believing that I have the talent to reach any goal I aspire to. For teaching me I should never settle for less than what I deserve. For showing me how to fight for what I believe in and giving me the strength to stand up for myself. For reminding me that being successful shouldn't come at the price of happiness. And for understanding that my journey, albeit unusual, is whatever I make of it and not what other people think of it. You have shown me true love in its rarest form, what it feels like, and how it can extend beyond life's obstacles and challenges. Without each of you, I'd be nowhere near the person I am today, and the person I'm still working on becoming.

Abbreviations

$ \Delta E $	quadrupole splitting (Mössbauer)
α	alpha
β	beta
δ	chemical shift (NMR); isomer shift (Mössbauer)
μ	micro
X	magnetic susceptibility
Γ	half width at half height (Mössbauer)
Å	angstrom
Ac	acetyl
acac	acetylacetonyl
alkyl-PP ₃	tris(2-(diphenylphosphino)ethyl)phosphine
AIBN	azobisisobutyronitrile
Ar	aryl
aryl-PP ₃	tris(2-(diphenylphosphino)phenyl)phosphine
Bn	benzyl
br	broad
BS	broken symmetry
Bu	butyl
bpy	2,2'-bipyridine
cal	calorie(s)
cald	calculated
CAAC	cyclic(alkyl)(amino)carbene
cat.	catalyst
CDA	carbenodiamidine, bis(amidinato)-N-heterocyclic carbene
cod	cyclooctadiene
conv.	conversion
Cp	cyclopentadienyl
Cy	cyclohexane
d	doublet (NMR)
DABCO	1,4-diazabicyclo[2.2.2]octane

DBU	1,8-diazabicycloundec-7-ene
dcpe	1,2-bis(dicyclohexylphosphino)ethane
dd	doublet of doublets (NMR)
ddd	doublet of doublet of doublets (NMR)
DFT	density functional theory
DMAP	4-(dimethylamino)pyridine
dmdppe	(2-(dimethylphosphino)ethyl)diphenylphosphine
DMF	dimethylformamide
dmpbz	1,2-bis(dimethylphosphino)benzene
dmpb	1,4-bis(dimethylphosphino)butane
dmpe	1,2-bis(dimethylphosphino)ethane
dmpent	1,5-bis(dimethylphosphino)pentane
dmpp	1,3-bis(dimethylphosphino)propane
DMSO	dimethylsulfoxide
DOE	department of energy
dppb	1,4-bis(diphenylphosphino)butane
dppbz	1,2-bis(diphenylphosphino)benzene
dppe	1,2-bis(diphenylphosphino)ethane
dq	doublet of quartets (NMR)
dt	doublet of triplets (NMR)
EPR	electron paramagnetic resonance
equiv.	equivalent(s)
ESI+	electrospray ionization (positive ion mode)
Et	ethyl
Fc	ferrocene
G	giga
g	gram(s)
GC	gas chromatography
h	hour(s)
hept	heptet (NMR)
hfacac	hexafluoroacetylacetone
HMDS	hexamethyldisilazane (bis(trimethylsilyl)amine)

HOMO	highest occupied molecular orbital
HRMS	high resolution mass spectrometry
Hz	hertz
IR	infrared spectroscopy
ⁱ Pr	isopropyl
<i>J</i>	coupling constant in Hz (NMR)
k	kilo
L	liter(s)
LAH	lithium aluminium hydride
LUMO	lowest occupied molecular orbital
M	molarity (mol/L); molecular formula (HRMS)
m	milli; multiplet (NMR)
MALDI	matrix-assisted laser desorption
MAO	methylaluminoxane
Me	methyl
Mes	mesityl, 2,4,6-trimethylphenyl
MHz	megahertz
min.	minute(s)
MMAO	modified methylaluminoxane
mol	mole(s)
nbd	2,5-norbornadiene
ⁿ Bu	n-butyl
Oct	octyl
NHC	N-heterocyclic carbene
NH ₄ O ₂ CNH ₂	ammonium carbonate
NMR	nuclear magnetic resonance
ORTEP	Oak Ridge thermal ellipsoid plot
PDI	pyridyldiimine, bis(imino)pyridine; polydispersity index
pent	pentet (NMR)
<i>p</i>	<i>para</i>
pent	pentet
Ph	phenyl

pin	pinacol
phen	1,10-phenanthroline
PLA	poly(lactic acid)
PNP	2,6-((di-substituted-phosphino)methyl)pyridine
Pr	propyl
pyr	pyridine
q	quartet (NMR)
s	singlet (NMR)
S	spin
scCO ₂	supercritical carbon dioxide
SET	single electron transfer
SQUID	superconducting quantum interference device
t	triplet (NMR)
TAEA	tris(2-aminoethyl)amine
^t Bu	tert-butyl
td	triplet of doublets (NMR)
temp.	temperature
THF	tetrahydrofuran
TLC	thin layer chromatography
TMEDA	N,N,N,N-tetramethylethylenediamine
TMP	2,2,6,6-tetramethylpiperidine
TMS	trimethylsilyl
TON	turnover number
TOF	turnover frequency
triphos-1	1,1,1-tris(diphenylphosphino)methane
triphos-2	1,1,1-tris(diphenylphosphinomethyl)ethane
Ts	tosyl, <i>p</i> -toluenesulfonyl
tt	triplet of triplets (NMR)
Vkd	Verkade's base, 2,8,9-triisopropyl-2,5,8,9-tetraaza-1-phospha-bicyclo[3.3.3]undecane)
v/v	volume/volume
VT	variable temperature

Chapter 1

Overview of Carbon Dioxide Hydrogenation for the Production of Formic Acid

1.1 Introduction

As the world's energy demands increase, our resources dwindle and the need for a sustainable energy source is pertinent. Our current energy infrastructure is dominated by fossil fuel use. Hydrogen, on the other hand, is potentially an ideal energy carrier as it is emissions-free when burned and can be used in fuel cells. A number of key challenges must be overcome for hydrogen to be used broadly to solve global energy problems. Significant advances are needed to develop more energy efficient and cost-effective methods for purification and delivery, to design more effective hydrogen storage systems, and to enable more durable fuel cells for converting hydrogen into electrical energy.

1.1.1 Hydrogen Production

Industry already produces and uses hydrogen on a massive scale. The current platforms for producing hydrogen are largely based on fossil fuels, are unsustainable for energy use, and lead to the emission of significant quantities of CO₂, a greenhouse gas (Table 1.1).^{1,2}

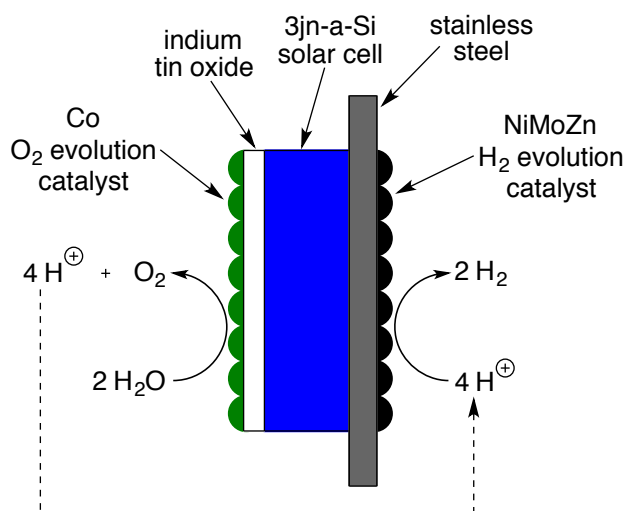
Table 1.1. Current industrial methods of hydrogen production

Process	Reaction	ΔH (kcal/mol)	Advantages	Disadvantages
steam reformation	$\text{CH}_4 + \text{H}_2\text{O} \rightleftharpoons \text{CO} + 3 \text{H}_2$	+49	high H ₂ /CO ₂ ratio	non-abundant feedstock
gasification	$3 \text{C} + \text{O}_2 + \text{H}_2\text{O} \rightleftharpoons 3 \text{CO} + \text{H}_2$	+22	reusable by-products	expensive
water-gas shift	$\text{CO} + \text{H}_2\text{O} \rightleftharpoons \text{CO}_2 + \text{H}_2$	-9.8	cheap	CO ₂ emissions

In order for hydrogen to replace fossil fuels and become a widely used energy source, its production must come from a sustainable feedstock. Recently, scientists have taken a step toward this goal by producing hydrogen from water. Advances in thermochemical water-splitting,³

electrolysis of water,⁴ and photochemical water-splitting⁵ are making it economically feasible to obtain hydrogen from an abundant source. For example, Daniel Nocera's group has developed wireless solar water-splitting cells from earth abundant metals for direct solar-to-fuel conversion (Figure 1.1).⁶ The cell mimics photosynthesis by generating H_2 and O_2 using inorganic materials consisting of catalysts interfaced with light harvesting semiconductors. This significant advancement in direct solar-to-fuel conversion is one of the first steps toward realizing a world fueled by a sustainable energy source.

Figure 1.1. Wireless solar water-splitting cell using silicon-based semiconductors and earth abundant catalysts⁶

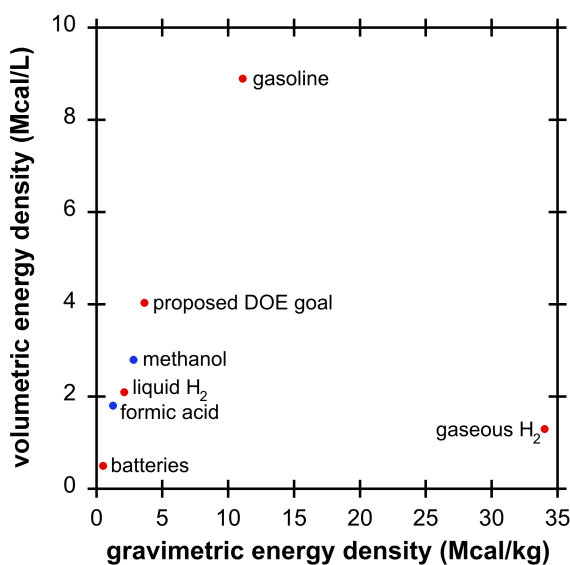


1.1.2 Hydrogen Storage Systems

Despite hydrogen's great potential as an alternate fuel, its use as a general energy carrier is limited.⁷ The public opinion of hydrogen usage as a fuel is skewed by the Hindenburg catastrophe. However, recent investigations into this disaster have shown that the ship caught on fire due to its highly flammable "skin" material, not because of the hydrogen gas it contained.⁸ The process of burning hydrogen can be done in an efficient and controlled way to provide

energy as needed. In addition, hydrogen has a high energy-to-weight ratio, especially compared to gasoline, which makes it an ideal alternative fuel (Figure 1.2). However, due to the low volumetric energy density, on-board storage in the size of current vehicles is almost impossible. Therefore, the development of a hydrogen storage material for stationary, portable, and transportation applications is necessary.

Figure 1.2. Energy densities of current and potential fuel sources



A variety of systems have been investigated for hydrogen storage including metal organic frameworks,⁹ metal hydrides,¹⁰ amine boranes,¹¹ biomass,¹² and hydrogenation of carbon dioxide to methanol (MeOH)¹³ or formic acid¹⁴ (Table 1.2). While each system has its advantages and disadvantages, the hydrogenation of carbon dioxide to formic acid and/or methanol is a promising candidate for the production of easily transportable liquid fuels or hydrogen storage materials. These processes are highly reversible and can be used as direct fuels or in fuel cells as opposed to many of the other systems for H₂ storage.

Table 1.2. Systems for the storage of molecular hydrogen¹⁵

System	H ₂ Capacity (wt%)	Advantages	Disadvantages
Gaseous H ₂	5	easily burned	high pressure equipment
metal organic frameworks	8-12	tunable	low temperature
metal hydrides	10-18	solid-state storage	low reversibility
ammonia borane	20	high wt%	low reversibility
biomass	15	well developed	sustainability issues
methanol	12.6	excellent fuel	poor atom economy
formic acid	4.4	high reversibility	low storage capacity

1.1.3 Hydrogenation of Carbon Dioxide to Formic Acid and/or Methanol

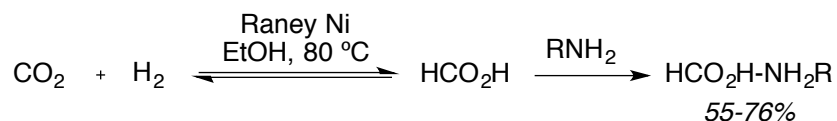
The hydrogenation of carbon dioxide to formic acid and/or methanol provides an encouraging approach to the development of an efficient and reversible hydrogen storage material (Table 1.3). Although the production of formic acid from carbon dioxide and hydrogen is uphill by +7.8 kcal/mol, with the addition of a base the reaction proceeds favorably to the formate salt (entry 2). Despite favorable thermodynamics, transformations of carbon dioxide have high kinetic barriers, which necessitate the need for a catalyst to efficiently produce formic acid from CO₂. This transformation can also undergo further hydrogenation to give methanol. However, this process loses one equivalent of hydrogen as water per molecule of methanol produced (entry 3). Alternatively, formic acid has also recently been utilized in direct formic acid fuel cells.¹⁶ Both of these strategies could provide economically and chemically viable hydrogen storage materials.

Table 1.3. Hydrogenation of carbon dioxide to formic acid and methanol¹⁴

Entry	Reaction	ΔG (kcal/mol)
1	CO ₂ (g) + H ₂ (g) \rightleftharpoons HCO ₂ H (l)	+7.8
2	CO ₂ (g) + H ₂ (g) + NH ₃ (aq) \rightleftharpoons HCO ₂ [⊖] (aq) + NH ₄ [⊕] (aq)	-2.3
3	CO ₂ (g) + 3 H ₂ (g) \rightleftharpoons CH ₃ OH (l) + H ₂ O (l)	-2.1

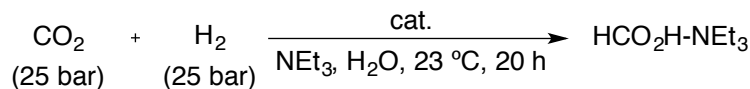
The first example of the synthesis of formic acid by the hydrogenation of CO₂ was reported by Farlow and Adkins in 1935 using Raney nickel as the catalyst (Scheme 1.1).¹⁷ The rate and yield of the reaction (determined based on the amine present) varied with the structure of the amine. However, at 100-200 bar and between 80 °C and 150 °C, all reactions proceeded with at least a 55% yield of the desired formate of the amine.

Scheme 1.1. Homogenously catalyzed hydrogenation of carbon dioxide to formic acid in the presence of amines



In 1976, Inoue *et al.* reported the first homogeneously catalyzed example.¹⁸ (Table 1.4) Reactions proceeded with selective formation of HCO₂H-NEt₃ (triethylamine) as the only organic product. Rhodium and ruthenium complexes bearing triphenylphosphine (PPh₃) ligands demonstrated high TONs (turnover numbers) and TOFs (turnover frequencies) than palladium and nickel complexes containing PPh₃ or 1,2-bis(diphenylphosphino)ethane (dppe) ligands.

Table 1.4. First homogeneously catalyzed hydrogenation of CO₂ to formic acid

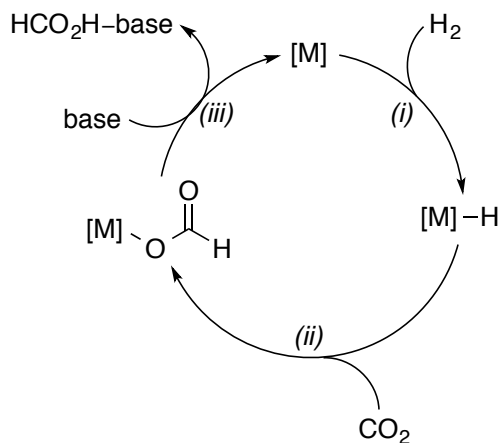


Entry	Cat.	TON ^a	TOF (h ⁻¹) ^b
1	Pd(dppe) ₂	12	0.60
2	Ni(dppe) ₂	7	0.4
3	Pd(PPh ₃) ₄	3	0.2
4	RhCl(PPh ₃) ₃	22	1.1
5	H ₂ Ru(PPh ₃) ₄	87	4.4
6	H ₃ Ir(PPh ₃) ₃	15	0.75

^aTON = (mol HCO₂H-NEt₃)/(mol cat.). ^bTOF = (mol HCO₂H-NEt₃)/(mol cat.)/(20 h).

At this point the mechanism was not fully understood, but the group postulated (i) formation of a metal-hydride followed by (ii) insertion into CO_2 to yield a metal formate. Upon addition of water or base, (iii) the formate salt would be released and H_2 would regenerate the active metal-hydride species.

Scheme 1.2. Proposed mechanism for CO_2 hydrogenation by Inoue *et al.*



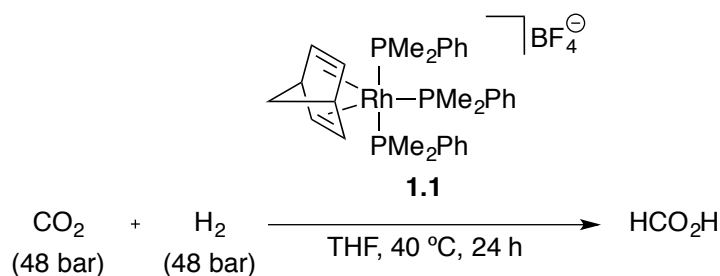
Since these first discoveries, there has been excellent progress in the development of catalysts for the hydrogenation of CO_2 to formic acid. Typically, homogeneous catalysts found to be effective for this reaction are 2nd and 3rd row metals of groups 8-10 with halides or hydrides as anionic ligands. In recent years, base-metals (common and inexpensive metals such as aluminum, iron, cobalt, nickel, copper and zinc) have demonstrated promising results. The following sections are designed to highlight important discoveries throughout the history of carbon dioxide hydrogenation. They are by no means a comprehensive list of all catalysts capable of this reaction.

1.2 Noble-Metal Catalysts

1.2.1 Rhodium

Many of the investigations after the initial discovery by Inoue *et al.* demonstrated the use of rhodium catalysts for the hydrogenation of CO₂ to formic acid. Nicholas and Tasi utilized [Rh(nbd)(PMe₂Ph)₃]BF₄ (**1.1**, nbd = 2,5-norbornadiene) for CO₂ hydrogenation (Table 1.5) based on the complex's previous reactivity to promote hydrogenation of polar functional groups like ketones (Table 1.5).¹⁹ Reactions proceeded on par with TOFs previously reported in 1976.

Table 1.5. [Rh(nbd)(PMe₂Ph)₃]BF₄ (1.1**) catalyzed hydrogenation of CO₂ to formic acid**

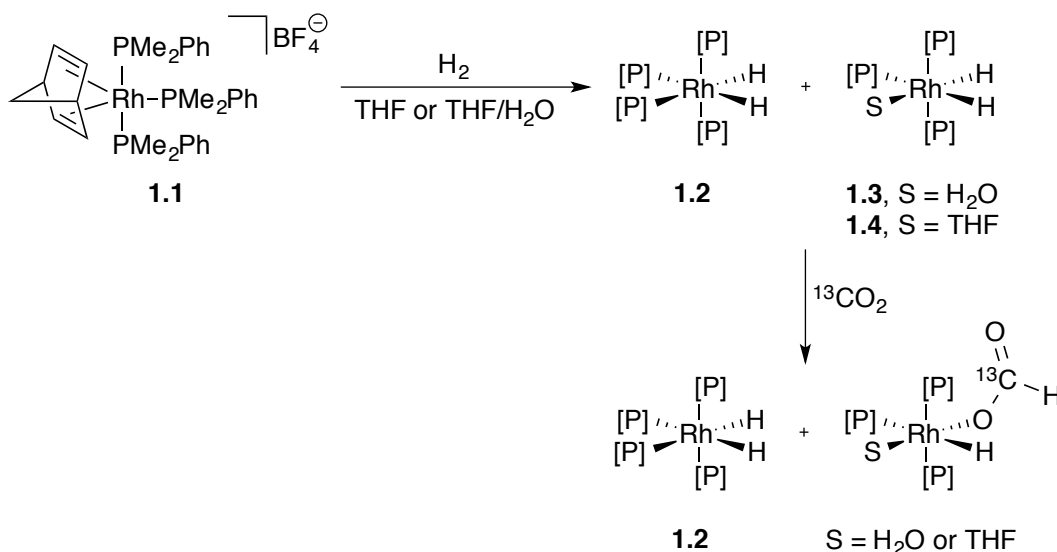


Entry	Conditions	TON ^a	TOF (h ⁻¹) ^b
1	dry THF	34	1.4
2	wet THF (0.4% H ₂ O)	78	3.3
3	pretreat with H ₂ , wet THF	130	5.3

^aTON = (mol HCO₂H)/(mol cat.). ^bTOF = (mol HCO₂H)/(mol cat.)/(24 h).

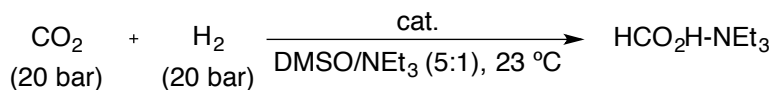
These results indicated that an increase in water content accelerates formic acid production (entries 1 and 2). Upon addition of H₂ to complex **1.1**, rhodium dihydride species (**1.2**-**1.4**) were formed (Scheme 1.3). Submitting these complexes to 10 bar ¹³CO₂ revealed that rhodium-aquo complex **1.3** and rhodium-THF complex **1.4** underwent insertion of CO₂, while complexes **1.1** and **1.2** were unreactive, which supported the importance of H₂O in this system.

Scheme 1.3. Stoichiometric H₂ and ¹³CO₂ reactions with [Rh(nbd)(PMe₂Ph)₃]BF₄ (1.1) ([P] = PMe₂Ph)



In the early 1990's, Walter Leitner and coworkers also investigated the use of rhodium catalysts for hydrogenation of CO₂ to formic acid. Over the span of three years, Leitner *et al.* published on a variety of rhodium complexes that demonstrated higher activity than ever reported before (Table 1.6).²⁰⁻²³

Table 1.6. Rhodium catalyzed hydrogenation of CO₂ by Leitner *et al.*



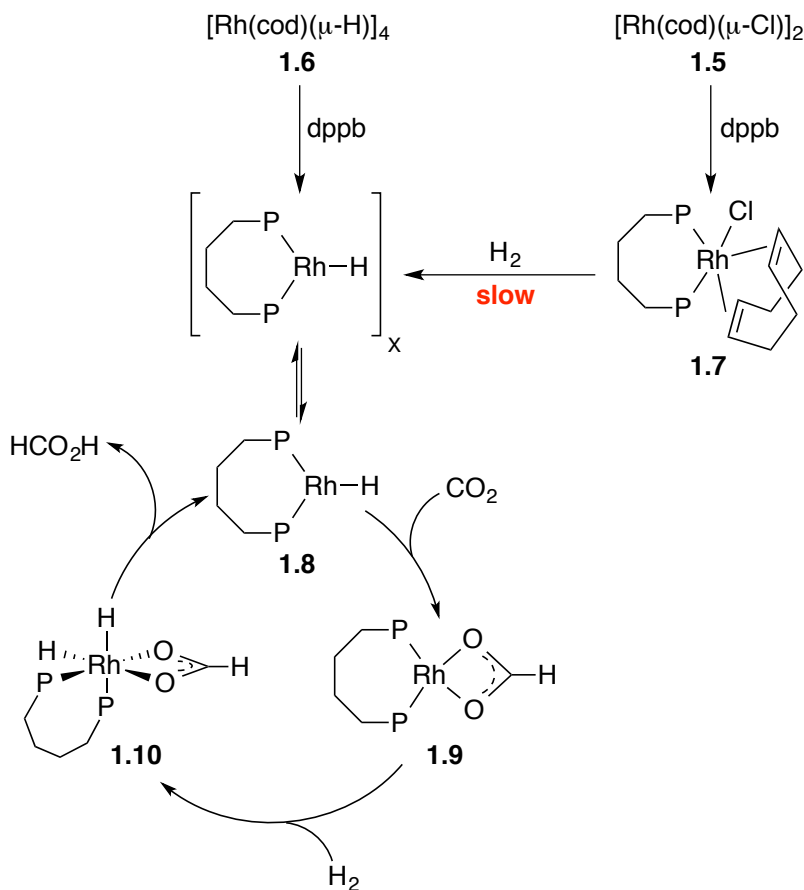
Entry	Cat.	Time (h)	TON ^a	TOF (h ⁻¹) ^b
1	[Rh(cod)(μ-Cl)] ₂ (1.5)	20	12	0.60
2	1.5 + dppb ^c	6	250	42
3	1.5 + PPh ₃ ^d	18	120	6.4
4	[Rh(cod)(μ-H)] ₄ (1.6)	18	21	1.2
5	1.6 + dppb ^c	18	2200	120

^aTON = (mol HCO₂H-NEt₃)/(mol cat.). ^bTOF = (mol HCO₂H-NEt₃)/(mol cat.)/(time). ^c1.2 equiv./cat. ^d2.4 equiv./cat.

The reactivity of $[\text{Rh}(\text{cod})(\mu\text{-Cl})_2]$ (**1.5**, cod = 1,5-cyclooctadiene) used directly or in the presence of either 1,4-bis(diphenylphosphino)butane (dppb) or PPh_3 was investigated. The TONs and TOFs increased significantly with the addition of a phosphine ligand (entries 1–3). Therefore, the presence of a phosphine ligand is necessary for high activity and the stability of the catalyst. In comparison to the results of Nicholas and Tsai, hydride complex $[\text{Rh}(\text{cod})(\mu\text{-H})_4]$ (**1.6**) was synthesized and tested for its catalytic competency with dppb as the ligand. The system showed a high efficiency with up to 2200 TONs achieved in 18 hours (entry 5).

Based on these results, the authors postulated a mechanism accounting for the large increase in formic acid production by rhodium species **1.6** (Scheme 1.4).²³

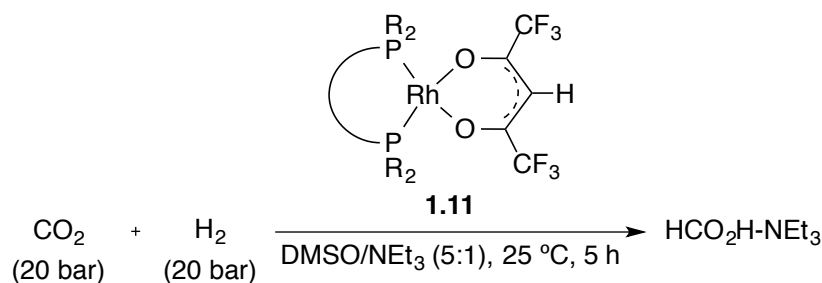
Scheme 1.4. Proposed mechanism for the rhodium catalyzed hydrogenation of CO_2



Previous reports of reactions with complex **1.5**, dppb, and H₂ have described the slow formation of rhodium hydrides similar to complex **1.8**.²⁴ When the hydride-bridged complex **1.6** was used as the catalyst precursor, it was postulated that in the presence of dppb, intermediate **1.8** would form rapidly. Based on the increased activity of this system, species **1.8** was concluded to be the active catalytic intermediate that would then undergo hydride insertion into CO₂ to form intermediate **1.9**. Addition of H₂ to form **1.10** followed by reductive elimination would then regenerate the active species; thus yielding a very active catalytic system.

In the late 1990's, Leitner *et al.* investigated a variety of rhodium phosphine complexes demonstrating the highest TOFs reported to date (Table 1.7).^{25, 26}

Table 1.7. Catalytic activity of [(R₂P)-(X)-(PR₂)]Rh(hfacac) (1.11**) complex derivatives**



Entry	Complex	X	R	P-Rh-P Angle (°)	TON ^a	TOF (h ⁻¹) ^b
1	1.11a	(CH ₂) ₂	Cy	84.97(2)	390	77
2	1.11b	(CH ₂) ₂	ⁱ Pr	86.01(7)	480	95
3	1.11c	(CH ₂) ₃	Ph	90.77(6)	1500	300
4	1.11d	(CH ₂) ₄	Ph	93.08(3)	2800	570
5	1.11e	(CH ₂) ₄	Cy	98.93(6)	6700	1300

^aTON = (mol HCO₂H-NEt₃)/(mol cat.). ^bTOF = (mol HCO₂H-NEt₃)/(mol cat.)/(5 h).

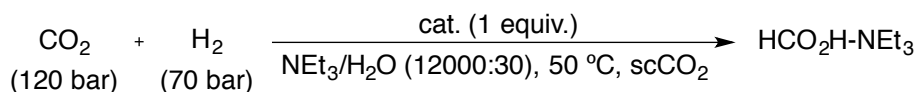
Complexes bearing the general structure [(R₂P)-(X)-(PR₂)]Rh(hfacac) (**1.11**, hfacac = hexafluoroacetate) were synthesized in order to improve the catalytic activity by variation of the ligand structure. All of complexes (**1.11a-1.11e**) were catalytically active and the ligand structure had a significant influence on their activity. For the series of ligands, an increase of the

relative catalytic activity with increasing P–Rh–P angle was observed. This increase is due to a combination of the chain length and the substituents of the bi-dentate phosphine, although electronic effects were not ruled out. Complex **1.11e**, bearing a cyclohexyl-substituted phosphine binding through a five-membered chelate with rhodium, was the most active species for CO₂ hydrogenation at the time.

1.2.2 Ruthenium

Although many investigations at the time were geared toward the use of rhodium catalysts, Noyori, Jessop, and Ikariya reported the first highly active ruthenium species in the early 1990's.²⁷ They discovered that certain ruthenium catalysts were active for the hydrogenation of CO₂ in a supercritical state (scCO₂). When carbon dioxide is heated beyond its critical point, 73 bar and 31 °C, the gas and liquid phases merge into a single supercritical phase. The authors postulated that the use of scCO₂ would be ideal because supercritical fluids combine characteristics associated with gas phase reactions (such as miscibility with other gases and high mixing rates) with properties of liquid solvents (such as their ability to dissolve and transport organic compounds).²⁸ Reactions in scCO₂ were indeed more efficient than analogous reactions in benzene or THF using RuH₂(PMe₃)₄ (**1.12**) as the catalyst (entries 1-3). In addition, reactions demonstrated TOFs on par with the most active rhodium species at this time.

Table 1.8. Hydrogenation of CO₂ to formic acid in scCO₂

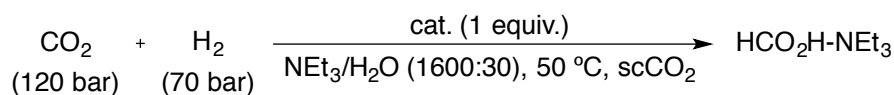


Entry	Cat.	Solvent	TOF (h ⁻¹) ^a
1	RuH ₂ (PMe ₃) ₄ (1.12)	benzene	4
2	1.12	THF	80
3	1.12	scCO ₂	1400
4	RuCl ₂ (PMe ₃) ₄ (1.13)	scCO ₂	1040

^aTOF = (mol HCO₂H-NEt₃)/(mol cat.)(1 h).

The activity of $\text{RuCl}_2(\text{PMe}_3)_4$ (**1.13**) was also investigated in scCO_2 . This species efficiently catalyzed the hydrogenation; however, it showed a distinct induction period during which the yellow species **1.13** changed to colorless. The authors postulated this induction period was due to the base (triethylamine) promoting slow conversion of **1.13** to either the dihydride complex **1.12** or $\text{RuHCl}(\text{PMe}_3)_4$. Further investigations of **1.12** and **1.13** showed the unique difference between these two complexes (Table 1.9).²⁹

Table 1.9. Effect of catalyst precursor on TON and TOF of hydrogenation

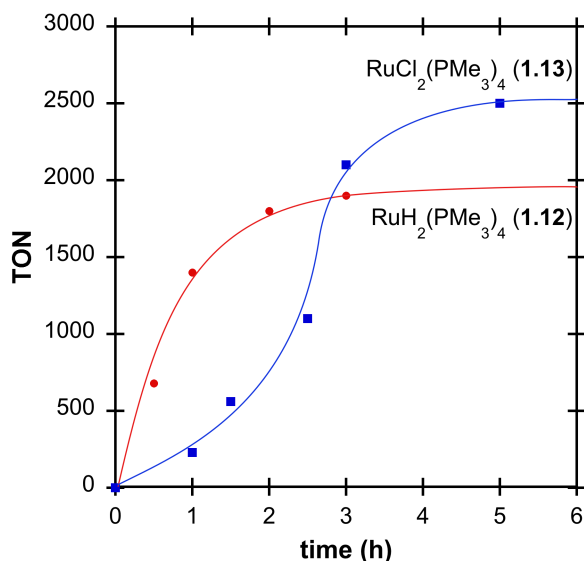


Entry	Cat.	Time (h)	TON ^a	TOF (h ⁻¹) ^b
1	1.12	1	1400	1400
2	1.12	3	1900	630
3	1.13	1	230	230
4	1.13	16	2600	160

^aTON = (mol $\text{HCO}_2\text{H-NEt}_3$)/(mol cat.). ^bTOF = (mol $\text{HCO}_2\text{H-NEt}_3$)/(mol cat.)/(1 h).

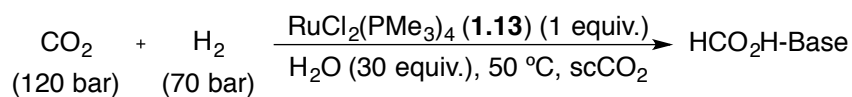
Within the first hour, dihydride complex **1.12** was much faster than dichloride complex **1.13** (Table 1.9, entries 1 and 3). However, an interesting effect occurred over the course of the reaction. The production of formic acid catalyzed by $\text{RuH}_2(\text{PMe}_3)_4$ (**1.12**) decreased as the reaction proceeded until plateauing at 3 hours (Figure 1.3). On the other hand, reactions catalyzed by $\text{RuCl}_2(\text{PMe}_3)_4$ (**1.13**) exhibited an induction period of approximately 1 hour, but continued to produce formic acid. Unfortunately, the authors provided no explanation for these curious results.

Figure 1.3. Dependence of formic acid production on reaction time. Reaction conditions are defined in Table 1.9. Trend lines are shown as a guide for the eye only.



Further efforts by Jessop were geared toward optimizing the reaction and providing a detailed mechanism for the ruthenium catalyzed hydrogenation of CO₂. First, the effect of the base was explored by changing the identity and the quantity (Table 1.10). The authors found that the reaction was profoundly dependent on the identity and quantity of the base.

Table 1.10. Effect of the base on the TON of hydrogenation



Entry	Base	Base Equiv.	Time (h)	TON ^a	TOF (h ⁻¹) ^b	Prod/Base ^c
1	K ₂ CO ₃	280	16	140	8.8	0.48
2	KOH	1900	15	260	17	0.14
3	NH ₄ O ₂ CNH ₂	960	15	39	2.6	0.041
4	NEt ₃	1600	16	2600	160	1.6
5	NEt ₃	3700	24	3400	140	1.2
6	NEt ₃	9400	84	6000	71	0.63
7	NEt ₃	12000	47	7200	150	0.61

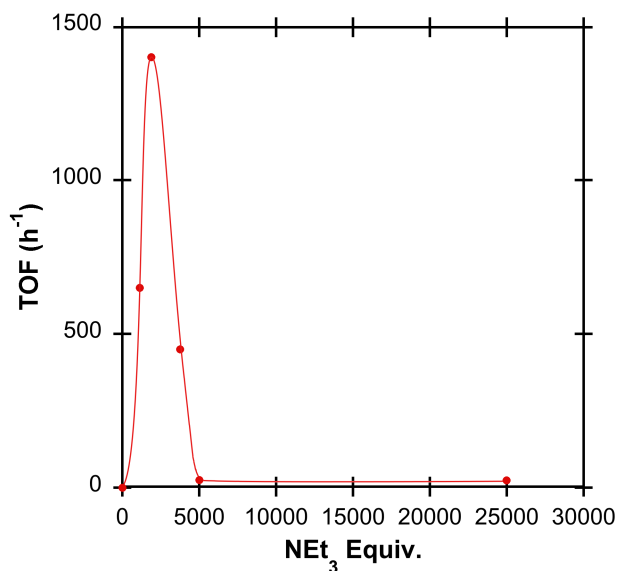
^aTON = (mol HCO₂H-Base)/(mol cat.). ^bTOF = (mol HCO₂H-Base)/(mol cat.)/(time).

^cProd/Base = (mol HCO₂H-Base)/(mol base).

Reactions with solid bases such as potassium carbonate, potassium hydroxide, or ammonium carbamate ($\text{NH}_4\text{O}_2\text{CNH}_2$) facilitated production of formic acid, but with lower TONs (entries 1-3). The amount of NEt_3 had a strong effect on the rate of the reaction (entries 4-7).

The authors determined that the optimal amount of NEt_3 was 1600 equivalence relative to the catalyst. This was supported by reactions under these conditions demonstrating the highest initial TOF (after 1 h) among all those tested (Figure 1.4). Reactions with a large excess of base were thought to have lower TOFs because NEt_3 is not very miscible with supercritical CO_2 causing phase separations. Any attempts to utilize bases insoluble in scCO_2 yielded lower amounts of formic acid, indicating the rate of formic acid production is greater if the system is homogeneous.

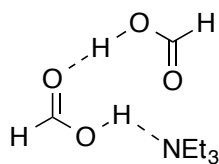
Figure 1.4. Effect of the amount of NEt_3 on the initial rate of formic acid production as measured during the first hour. Reaction conditions are defined in Table 1.9. Trend lines are shown as a guide for the eye only.



The authors also noted the importance on the amount of base relative to the amount of formic acid produced (Table 1.10, Prod/Base). This number is valuable because the presence of

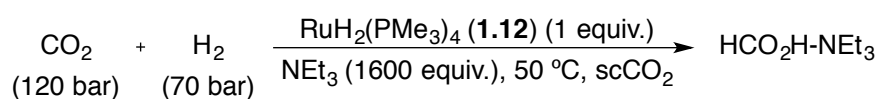
base is crucial for favorable thermodynamics. In this catalytic system, the optimal amount of base occurred at a product to base ratio of 1.6. Leitner *et al.* observed product to base ratios of 1.6-1.8 in DMSO with the most active rhodium catalysts.²³ Ratios of greater than one are common for nonprotic solvents where acid-base adducts can form (Figure 1.5).

Figure 1.5. Acid-base adducts commonly formed in nonprotic solvents



In addition, the rate of hydrogenation was improved in the presence of promoting additives. These additives are commonly water or alcohols (Table 1.11). Both water and methanol increased the rate of the reaction. However, methanol had a much larger effect on the production of formic acid. As with the base, reactions of single-phase tend to be much faster than those with multiple phases.

Table 1.11. Effect of additives on the rate of formic acid production

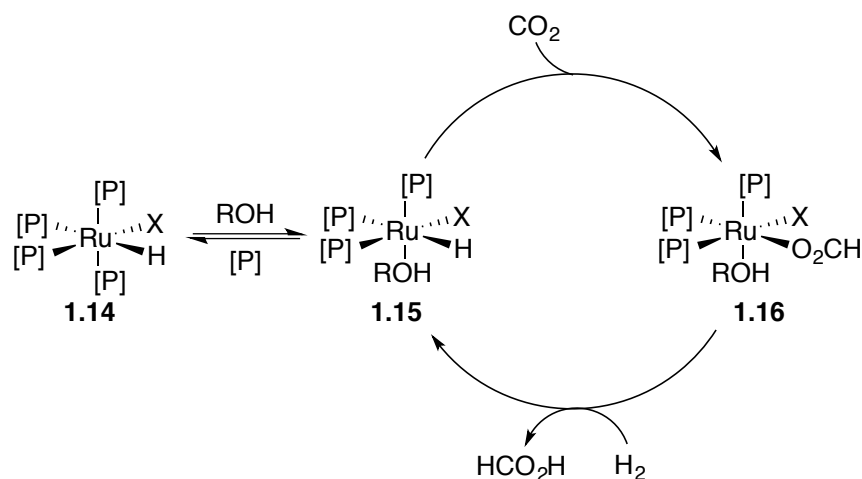


Entry	Additive	Additive Equiv.	Phases	Time (h)	TON ^a	TOF (h ⁻¹) ^b
1	N/A	N/A	1	1	680	680
2	H ₂ O	30	1	1	1400	1400
3	H ₂ O	190000	2	1	34	34
4	MeOH	4300	1	0.5	2000	4000
5	MeOH	83000	2	0.5	750	1500

^aTON = (mol HCO₂H-NEt₃)/(mol cat.). ^bTOF = (mol HCO₂H-NEt₃)/(mol cat.)/(1 h).

Based on these results, the authors proposed a mechanism for the hydrogenation of CO₂ to formic acid (Scheme 1.5). Previous mechanisms proposed by Leitner *et al.* required a metal hydride species. Although catalyst precursor **1.13** does not contain hydride ligands, conversion into a hydride species should be facile in the presence of H₂ and base. In fact, hydrogenation reactions catalyzed by *trans*-RuCl₂(dmpe)₂ (dmpe = 1,2-bis(dimethylphosphino)ethane) demonstrated no activity because the ruthenium species could not be converted to a hydride complex.³⁰ Therefore, a hydride ligand in the catalyst is a prerequisite for catalytic activity. Scheme 1.4 illustrates a possible mechanism under current reaction conditions, where water or alcohol would act as a promoter. In this mechanism, a phosphine ligand on ruthenium hydride **1.14** is replaced by ROH (water or alcohol) to generate species **1.15**. Insertion of CO₂ into the ruthenium–hydride bond would occur to give **1.16**, which upon addition of H₂ would produce HCO₂H and regenerate active species **1.15**.

Scheme 1.5. Proposed mechanism for ruthenium catalyzed CO₂ hydrogenation to formic acid. (X = H or Cl, R = H or Me, [P] = PMe₃)

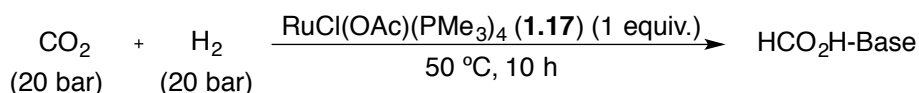


In more recent reports, Jessop and coworkers focused on studying the mechanism further and improving the catalytic activity. In 2002, the activity of RuCl(OAc)(PMe₃)₄ (**1.17**) was

investigated because of its similarities to the active species **1.16** containing formate as a ligand.³¹

Under non-supercritical conditions, complex **1.17** was utilized to test the effect of different bases and additives on the reaction (Table 1.12).

Table 1.12. Optimization of RuCl(OAc)(PMe₃)₄ (1.17**) catalyzed hydrogenation reactions under non-supercritical conditions**



Entry	Base ^a	Additive ^b	TON ^c	TOF (h ⁻¹) ^d
1	KOH	MeOH	2	0.2
2	K ₂ CO ₃	MeOH	7	0.7
3	NEt ₃	N/A	10	1
4	NEt ₃	MeOH	180	18
5	NEt ₃	PhOH	320	32
6	NEt ₃	C ₆ F ₅ OH	510	51
7	NPr ₃	C ₆ F ₅ OH	560	56
8	NOct ₃	C ₆ F ₅ OH	40	4
9	TMEDA	C ₆ F ₅ OH	490	49
10	DBU	C ₆ F ₅ OH	530	53

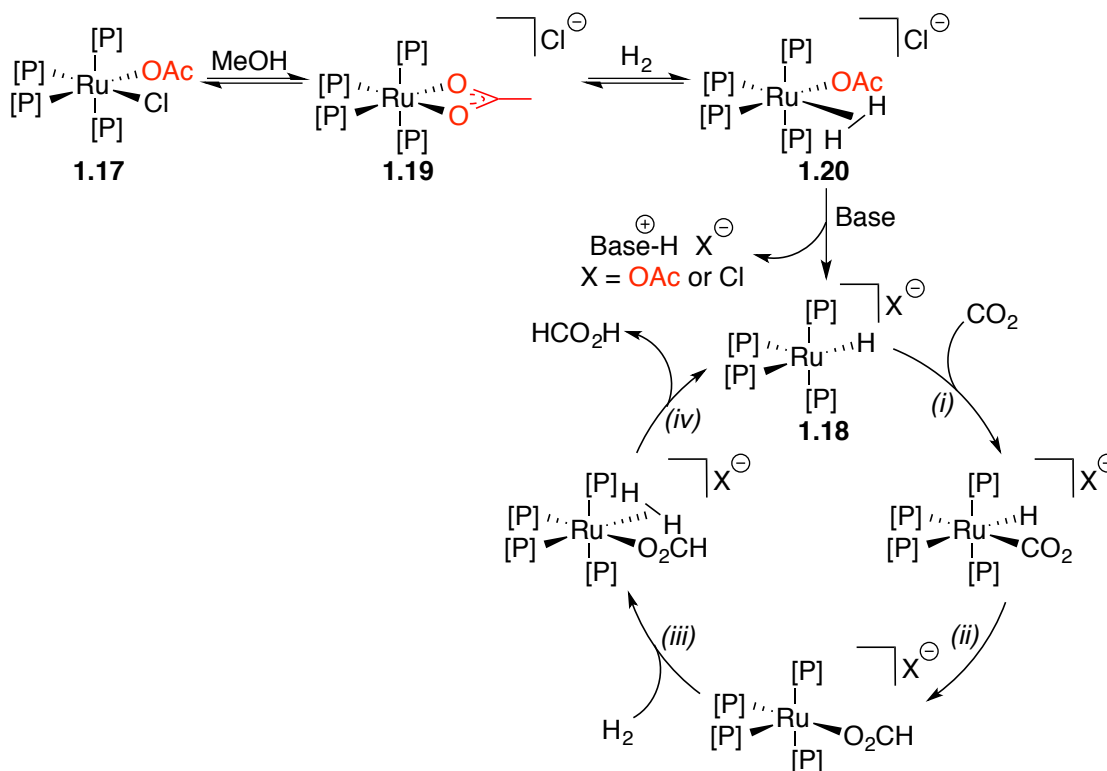
^a1600 equiv. ^b30 equiv. ^cTON = (mol HCO₂H-Base)/(mol cat.). ^dTOF = (mol HCO₂H-Base)/(mol cat.)/(10 h).

A variety of organic [NEt₃, tripropylamine (NPr₃), trioctylamine (NOct₃), 1,8-diazabicycloundec-7-ene (DBU)] and inorganic [KOH, K₂CO₃, tetramethylethylenediamine (TMEDA)] bases were tested for their ability to promote the production of formic acid. For solid bases, MeOH was added as the solvent and for liquid bases, the base itself was the solvent. All inorganic bases were ineffective, while organic bases with intermediate basicity were the most effective. Additionally, a range of alcohols was tested and although water and MeOH were previously used, more acidic alcohols were found to be far more effective.

Based on these results, Jessop and coworkers demonstrated that reactions catalyzed by **1.17** using pentafluorophenol as the alcohol and triethylamine as the base in supercritical CO₂ gave a TOF of 95,000 h⁻¹, more than an order of magnitude greater than previously observed. In

fact, these activities remain among the highest ever reported for this reaction. In 2009, Linehan, Jessop, and coworkers reported a mechanistic investigation using high pressure NMR spectroscopy (Scheme 1.6).³²

Scheme 1.6. Mechanism of CO₂ hydrogenation catalyzed by RuCl(OAc)(PMe₃)₄ (1.17**) ([P] = PMe₃)**



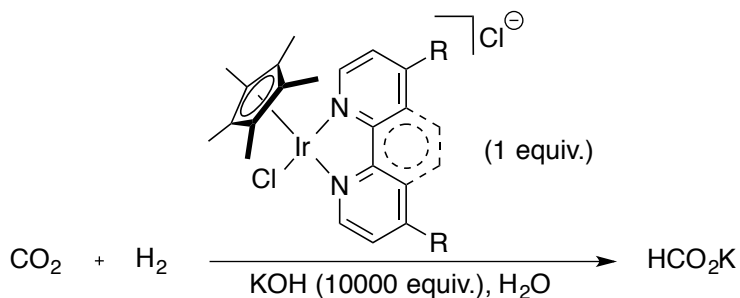
They proposed the active catalytic species is a cationic ruthenium hydride (**1.18**) formed by the addition of H₂, base, and alcohol. Addition of an alcohol to RuCl(OAc)(PMe₃)₄ (**1.17**) would facilitate the isomerization to a κ^2 -acetate species (**1.19**). Independently synthesized species similar to **1.19** performed the hydrogenation reaction well in the presence and absence of alcohol. After addition of H₂, a ruthenium dihydrogen complex (**1.20**) would be formed. At this point, the authors proposed the acetate ligand would act as an internal base to deprotonate the metal-bound hydrogen forming the ruthenium-hydride **1.18**. The addition of an external base would accelerate

this process by forming a strong acid-base adduct with acetic acid or hydrochloric acid. Without the acetate ligand to act as an internal base, the catalytic activity was decreased suggesting that the formation of **1.18** was slower. The reaction would then proceed as previously described with (i) addition of CO₂, (ii) hydride insertion, (iii) addition of H₂, and (iv) release of formic acid.

1.2.3 Iridium

Despite the significant advancements in CO₂ hydrogenation by ruthenium complexes, the desire for more efficient complexes was still strong. Work in the early 2000's began to focus on iridium complexes even though the first example by Inoue *et al.* demonstrated low activity (Table 1.4, entry 6). In 2004, Himeda *et al.* reported the use of half-sandwich iridium complexes for CO₂ hydrogenation based on their previous activity in transfer hydrogenations (Table 1.13).³³

Table 1.13. Iridium bipyridyl or phenanthroline catalyzed hydrogenation of CO₂

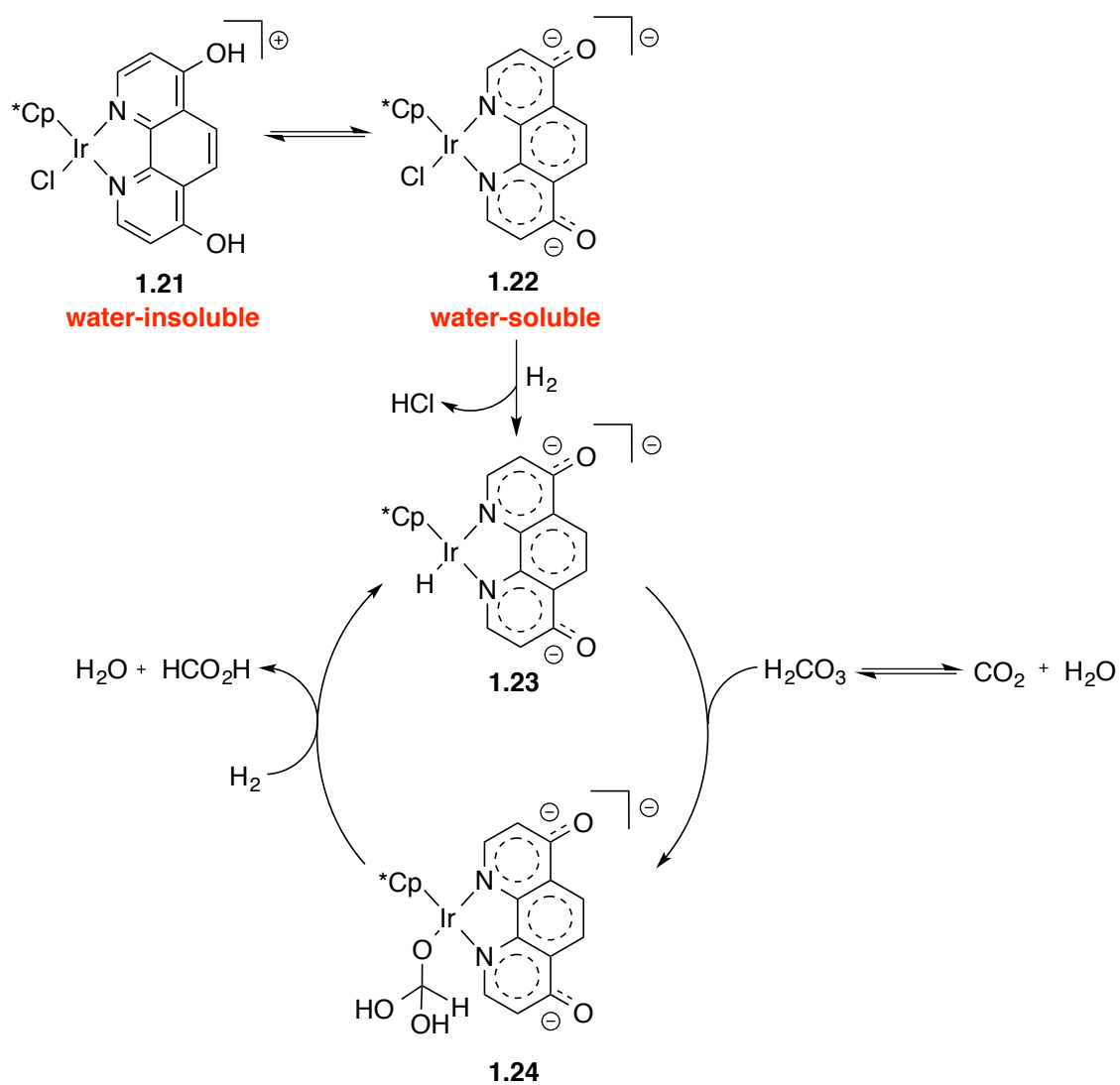


Entry	Ligand	R	Temp. (°C)	Pressure (bar) ^a	TON ^b	TOF (h ⁻¹) ^c
1	bpy	H	80	40	105	6
2	bpy	OH	80	40	6800	4000
3	bpy	OH	120	60	190000	42000
4	phen	H	80	40	59	3
5	phen	OH	80	40	6100	2600
6	phen	OH	120	60	222000	33000

^aTotal pressure. CO₂/H₂ = 1:1. ^bTON = (mol HCO₂K)/(mol cat.). ^cTOF = (mol HCO₂K)/(mol cat.)/(1 h).

Although initial catalytic systems demonstrated low activity (entries 1 and 4), optimization of the ligand and the catalytic conditions provided highly active catalytic systems.^{34,35} The addition of the two hydroxyl substituents on the 2,2'-bipyridine (bpy) or 1,10-phenanthroline (phen) ligand caused a dramatic enhancement of catalytic activity (entries 3 and 6). The authors proposed a mechanism for the hydrogenation of CO₂ in aqueous media (Scheme 1.7).

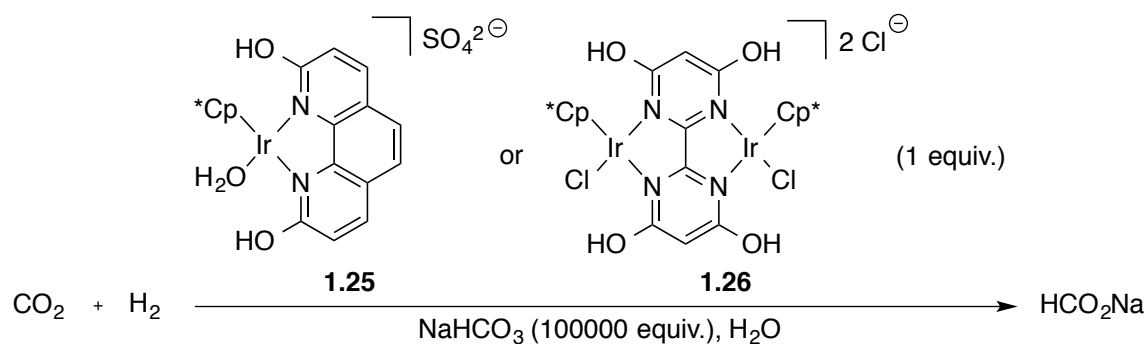
Scheme 1.7. Proposed mechanism for hydrogenation of CO₂ in aqueous media



Typical reaction conditions were initially basic, which would facilitate the deprotonation of pre-catalyst **1.21**. This transformation would convert the water-insoluble species **1.21** into the water-soluble iridium complex **1.22**. The active catalytic species **1.23** would be generated in the presence of H₂. The authors then proposed an outer-sphere metal-hydride insertion into bicarbonate, which would likely form under high pressures of CO₂ in H₂O. The formation of tetrahedral intermediate **1.24**, followed by addition of H₂ would produce H₂O and formate, while regenerating the iridium-hydride species **1.23**. The high catalytic activities with the addition of hydroxyl substituents on the catalyst were attributed to the strong electron donating effects of the oxyanion formed under basic conditions.

In the early 2010's, Fujita, Himeda, and coworkers investigated alterations to iridium complexes like **1.21** to improve the catalytic activity (Table 1.14).^{36–38} Complexes with hydroxyl groups at the *ortho*-position instead of *para* (**1.25** and **1.26**) demonstrated higher TOFs within the first hour of formate production.

Table 1.14. Hydrogenation of CO₂ catalyzed by iridium complexes bearing ligands with *ortho*-substituted hydroxyl groups

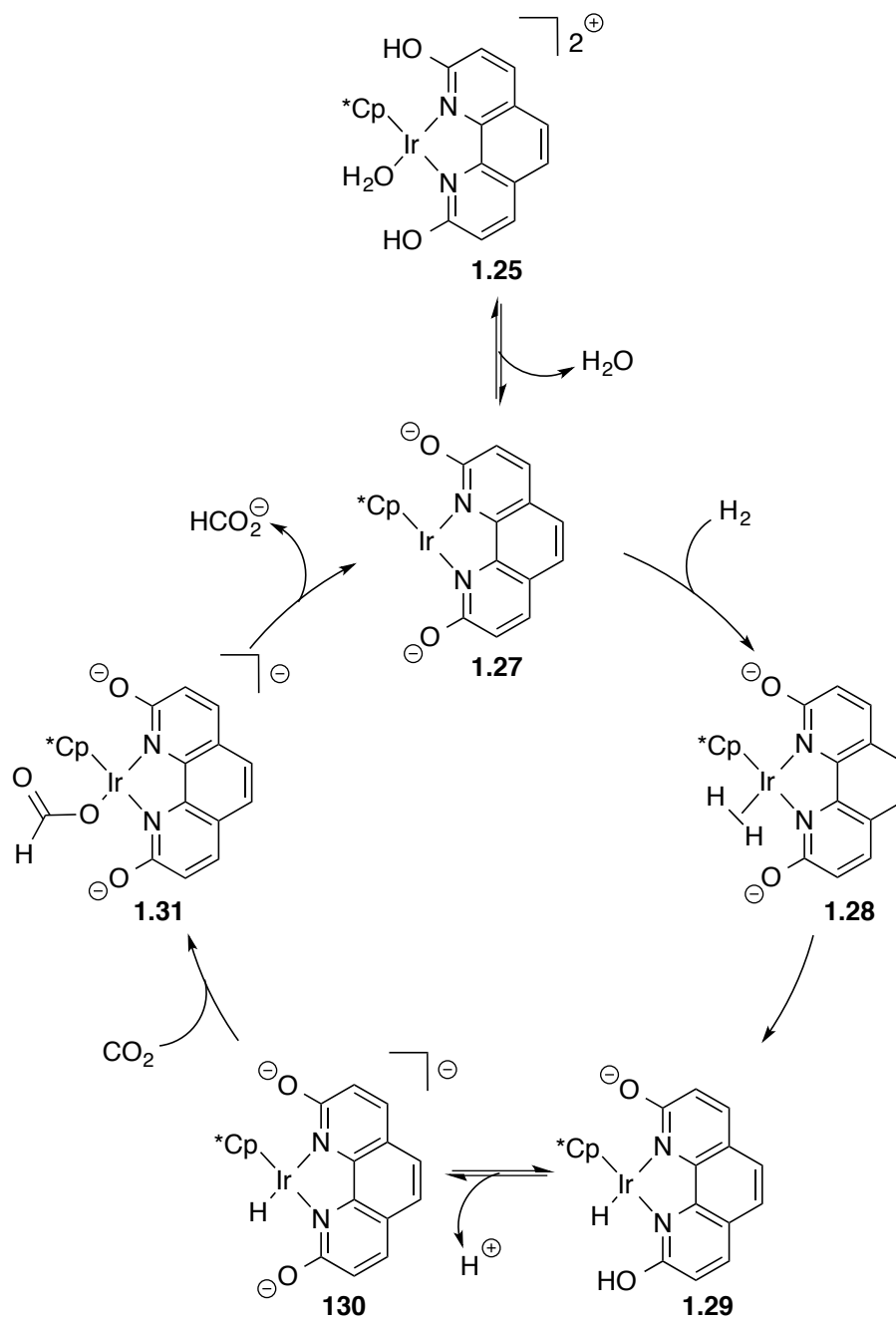


Entry	Cat.	Temp. (°C)	Pressure (bar) ^a	TON ^b	TOF (h ⁻¹) ^c
1	1.25	80	10	9000	8000
2	1.25	120	10	11000	23000
3	1.26	50	40	150000	16000
4	1.26	80	50	80000	54000

^aTotal pressure. CO₂/H₂ = 1:1. ^bTON = (mol HCO₂Na)/(mol cat.). ^cTOF = (mol HCO₂Na)/(mol cat.)/(1 h).

The authors proposed a mechanism based on the increased activity due to the change in hydroxyl position on the ligand (Scheme 1.8).

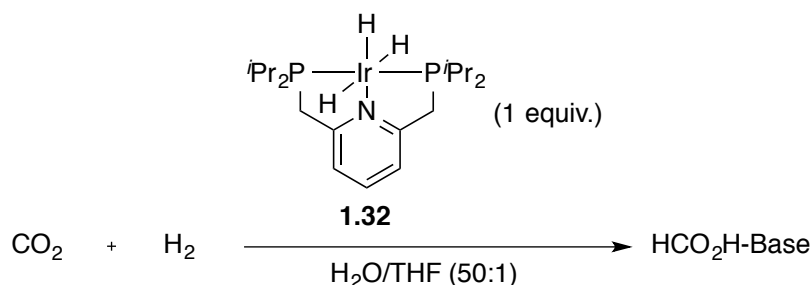
Scheme 1.8. Proposed mechanism for iridium catalysts bearing ligands with *ortho*-substituted hydroxyl groups



Upon loss of water and deprotonation of **1.25**, iridium complex **1.27** would be generated. After addition of H₂ to **1.27**, an iridium dihydrogen complex **1.28** would be formed. The *ortho*-substituted hydroxyl groups would act as pendant bases to deprotonate complex **1.28**. The role of the *ortho*-substituted hydroxyl groups to facilitate formation of the iridium-hydride **1.29** was supported by DFT calculations as the energy barrier of heterolytic H₂ cleavage was stabilized (12 kcal/mol versus 14 kcal/mol for **1.21**).³⁷ Although bases in solution could deprotonate species **1.29**, a proton-relay to give iridium-hydride **1.30** was preferred according to DFT calculations. Hydride insertion into CO₂ would give iridium-formate **1.31** followed by release of formate to regenerate iridium complex **1.27**.

In addition, Nozaki *et al.* reported on the synthesis and catalytic activity of an iridium-PNP-pincer complex (PNP = 2,6-((di-substituted-phosphino)methyl)pyridine) (Table 1.15).³⁹

Table 1.15. Iridium-PNP-pincer **1.32 catalyzed hydrogenation of CO₂**



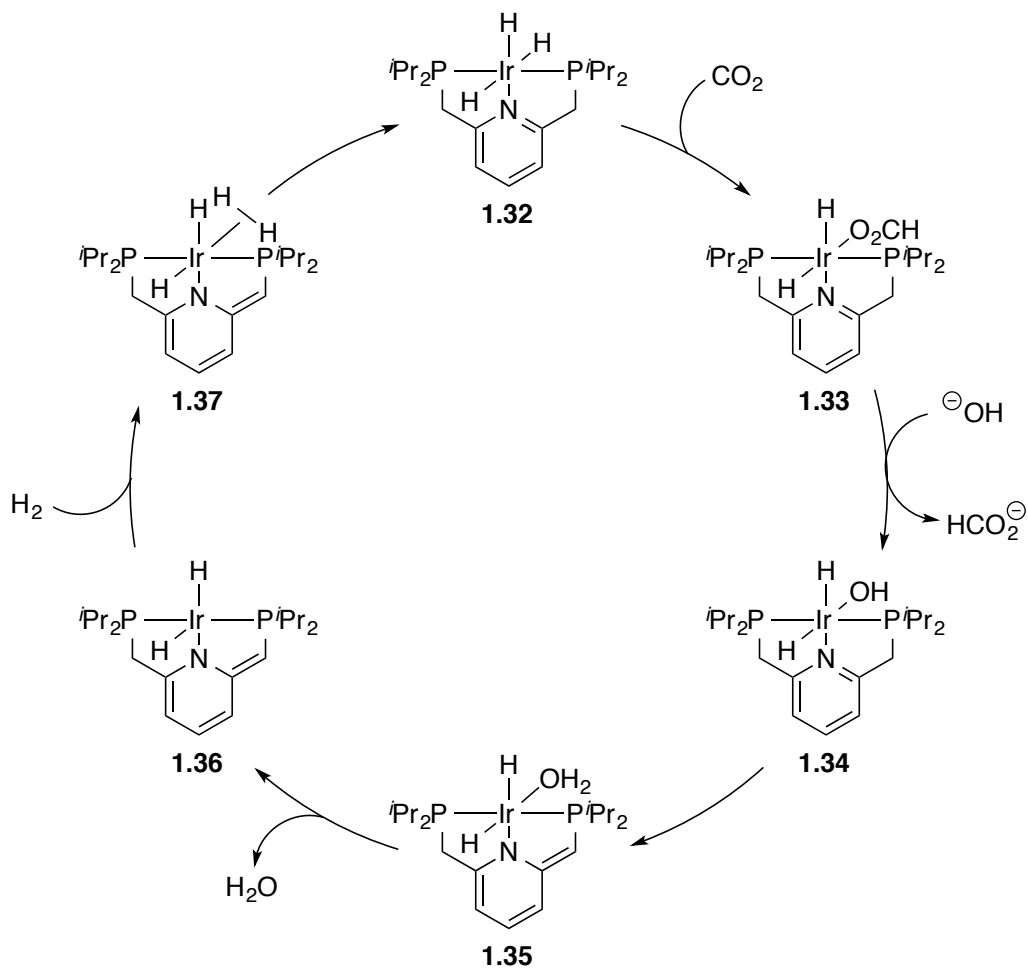
Entry	Base ^a	Temp. (°C)	Pressure (bar) ^b	Time (h)	TON ^c	TOF (h ⁻¹) ^d
1	KOH	25	50	48	0	0
2	KOH	100	1.3	40	43	1
3	KOH	120	60	48	3500000	73000
4	KOH	200	50	2	300000	150000
5	NEt ₃	200	50	2	75	380
6	N(CH ₂ CH ₂ OH) ₃	200	50	2	29000	14000

^a5 x 10⁶ equiv. ^bTotal pressure. CO₂/H₂ = 1:1. ^cTON = (mol HCO₂H-Base)/(mol cat.). ^dTOF = (mol HCO₂H-Base)/(mol cat.)/(1 h).

The iridium complex with isopropyl groups on the phosphorous atoms (**1.32**) showed higher activity than reported for any other catalyst to date. Under aqueous conditions, the temperature, the pressure, and the identity of the base significantly effected the production of formic acid. With KOH as the base at 120 °C and 60 bar, complex **1.32** demonstrated a TON of 3.5 million and a TOF of 73,000 h⁻¹ (entry 3).

In 2011, Nozaki *et al.* investigated the mechanism of iridium-PNP-pincer catalyzed hydrogenation reactions based on experimental and theoretical results (Scheme 1.9).⁴⁰

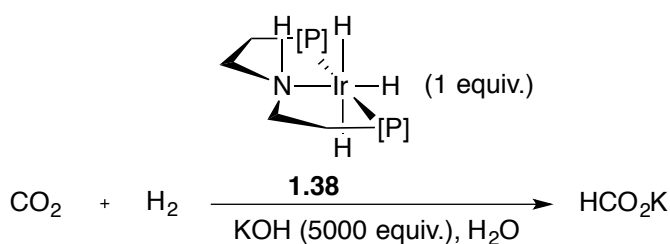
Scheme 1.9. Mechanism of iridium-PNP-pincer catalyzed CO₂ hydrogenation



The authors first proposed the facile insertion of the iridium-hydride into carbon dioxide to form iridium-formate species **1.33**. Ligand substitution facilitated by excess base and release of formate would lead to complex **1.34**. DFT calculations indicated that the formation of **1.34** is thermodynamically favorable, although kinetically inaccessible at room temperature supporting the need for higher temperatures (Table 1.15, entries 1 and 3). Deprotonative dearomatization of complex **1.34** would then give iridium-aquo species **1.35**, which would then release water to form iridium-dihydride **1.36**. The generation of iridium species **1.36** is thermodynamically favorable and the activation barrier for the proton transfer was calculated to be 14.4 kcal/mol. Addition of H₂ to **1.36**, forming iridium-hydrogen species **1.37**, followed by rearomatization of the ligand would regenerate the iridium-trihydride complex **1.32**. The rate-determining step was proposed to be the deprotonative dearomatization of complex **1.34**. This hypothesis was supported by the importance of the identity and amount of the base utilized (entries 4-6, footnote *a*).

In 2011, Hazari *et al.* also investigated iridium-pincer complexes for their reactivity in CO₂ hydrogenation (Table 1.16).⁴¹

Table 1.16. Iridium-pincer ([P] = P^{*i*}Pr₂) catalyzed hydrogenation of CO₂



Entry	Temp. (°C)	Pressure (bar) ^a	TON ^b	TOF (h ⁻¹) ^c
1	125	55	3800	160
2	145	55	49000	2100
3	165	55	120000	4900
4	185	55	350000	15000
5	185	41	39000	1600
6	185	28	28000	1200
7	185	14	3900	160

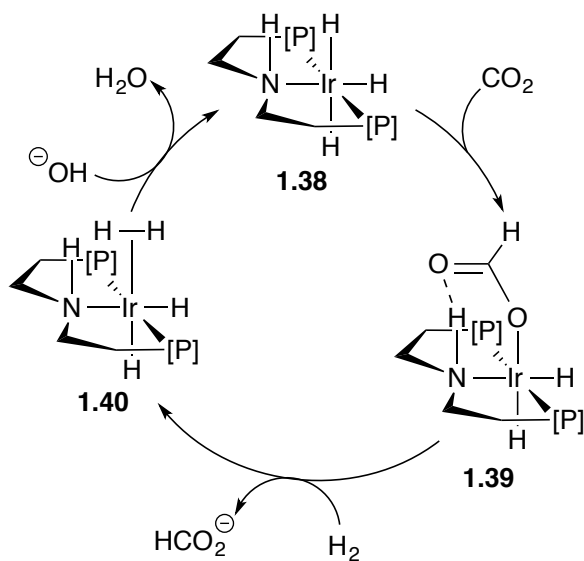
^aTotal pressure. CO₂/H₂ = 1:1. ^bTON = (mol HCO₂K)/(mol cat.).

^cTOF = (mol HCO₂K)/(mol cat.)/(24 h).

They explored *trans*-(HN(CH₂CH₂PⁱPr₂))IrH₃ (**1.38**) for its catalytic activity in the hydrogenation of CO₂ to formic acid. Similar to Nozaki's complex, **1.38** demonstrated higher TONs and TOFs than with previously investigated rhodium and ruthenium complexes. Decreases in temperature and pressure led to lower catalytic activities for iridium-trihydride complex **1.38**.

The authors proposed a simple mechanism for hydrogenation (Scheme 1.10). Insertion of the iridium-hydride bond into CO₂ would generate iridium-formate **1.39**, which would be facilitated by the H-bond donor on the ligand. Then, addition of H₂ would release formate and form iridium **1.40**. Iridium-pincer **1.38** would be regenerated by addition of base to **1.40**.

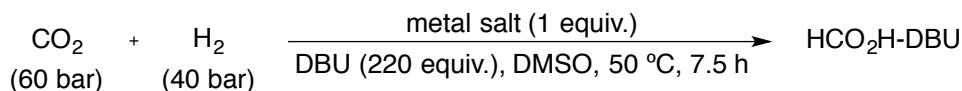
Scheme 1.10. Proposed mechanism of iridium-pincer catalyzed CO₂ hydrogenation



1.3 Base-Metal Catalysts

Most complexes developed for hydrogenation of CO₂ to formic acid involve noble-metals that are expensive and rare. In order for this process to be beneficial for industrial scale and transportation applications, an inexpensive base-metal catalyst that produces formic acid with activities that rival the noble-metal systems is required. The first example following the investigation by Inoue *et al.* in 1976 (Table 1.4, entry 2) was reported by Jessop and coworkers in 2003.⁴² In a series of tests, combinations of base-metal salts and phosphine ligands were explored (Table 1.17). The results showed that 1,2-bis(dicyclohexylphosphino)ethane (dcpe) was the optimal ligand for both metal salts compared to PPh₃ and dppe. A pre-formed batch of NiCl₂(dcpe) was tested and found to be capable of catalyzing the production of formic acid in up to 4400 TONs (entry 7). Although this does not approach that of the very efficient rhodium, ruthenium, or iridium catalyst precursors, the TON exceeded that of the only previously reported base-metal catalyst for this reaction.

Table 1.17. Base-metal screening for CO₂ hydrogenation



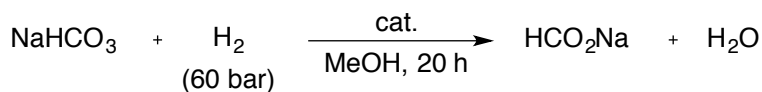
Entry	Metal Salt	Phosphine ^a	TON ^b	TOF (h ⁻¹) ^c
1	FeCl ₃	PPh ₃	20	2.7
2	FeCl ₃	dppe	23	3.1
3	FeCl ₃	dcpe	113	15
4	NiCl ₂	PPh ₃	0	0
5	NiCl ₂	dppe	45	6.0
6	NiCl ₂	dcpe	117	16
7 ^d	NiCl ₂ (dcpe)	N/A	4400	20

^aMono-dentate phosphine = 3 equiv. Bi-dentate phosphine = 1.5 equiv. ^bTON = (mol HCO₂H-DBU)/(mol metal salt). ^cTOF = (mol HCO₂H-DBU)/(mol metal salt)/(7.5 h). ^dConditions: cat. = pre-formed NiCl₂(dcpe), DBU (12000 equiv.), time = 216 h.

1.3.1 Iron

In 2010, Beller and coworkers investigated different iron precursors and various nitrogen and phosphorous containing ligands for hydrogenation of bicarbonate (Table 1.18).⁴³ No catalysis was observed with bi- or tri-dentate phosphines or amines such as dppe, 1,1,1-tris(diphenylphosphino)methane (triphos-1), and tris(2-aminoethyl)amine (TAEA) (entries 1-3). However, the hydrogenation proceeded with a catalyst formed *in situ* from Fe(BF₄)₂ and the tetra-dentate ligand (alkyl-PP₃, tris(2-(diphenylphosphino)ethyl)phosphane) (entry 4). Lower or higher temperatures (entries 5 and 6), as well as noncationic iron salts like Fe(acac)₃ (acac = acetylacetonate) and FeCl₂ (entries 7 and 8) led to a decrease in activity.

Table 1.18. Iron catalyzed hydrogenation of sodium bicarbonate

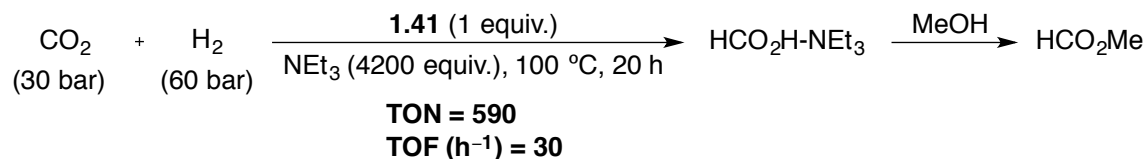


Entry	Cat.	Temp. (°C)	TON ^a	TOF (h ⁻¹) ^b
1	Fe(BF ₄) ₂ /dppe	80	0	0
2	Fe(BF ₄) ₂ /triphos-1	80	0	0
3	Fe(BF ₄) ₂ / TAEA	80	0	0
4	Fe(BF ₄) ₂ /alkyl-PP ₃ ^f (1.41)	80	610	31
5	1.41	60	83	4.2
6	1.41	100	76	3.8
7	Fe(acac) ₃ /alkyl-PP ₃	80	173	8.7
8	FeCl ₂ / alkyl-PP ₃	80	69	3.5

^aTON = (mol HCO₂Na)/(mol cat.). ^bTOF = (mol HCO₂Na)/(mol cat.)/(20 h).

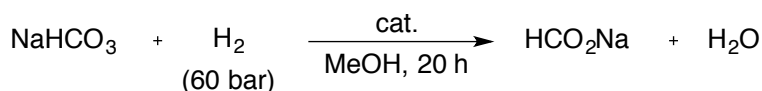
The Fe(BF₄)₂/alkyl-PP₃ (**1.41**) catalyst was then applied to the hydrogenation of CO₂ to produce methyl formate in the presence of methanol (Scheme 1.11). Methyl formate was generated with a TON of 590, which is five times higher than the previous best result with iron catalysts (Table 1.17, entry 3).

Scheme 1.11. Fe(BF₄)₂/PP₃ (tris(2-(diphenylphosphino)ethyl)phosphane) catalyzed hydrogenation of CO₂ to methyl formate



In 2012, Beller *et al.* reported the modified synthesis of a tetra-dentate phosphine ligand (aryl-PP₃, tris-(2-(diphenylphosphino)phenyl)phosphane).^{44, 45} The activity of Fe(BF₄)₂ and the new aryl-PP₃ ligand was explored for hydrogenation of sodium bicarbonate (Table 1.19.). Similar to reactions with the alkyl-PP₃ ligand, higher and lower temperatures led to decreases in reactivity (entries 2 and 4). However, the catalyst was stable at 100 °C, which is an advantage to the previously more sensitive alkyl-PP₃ ligand. Changes to the iron precursor revealed that in addition to Fe(BF₄)₂, Fe(acac)₃, FeCl₂, Fe(acac)₂, and FeF₂ all showed high catalytic activity (entries 5-8).

Table 1.19. Iron aryl-PP₃ catalyzed hydrogenation of sodium bicarbonate

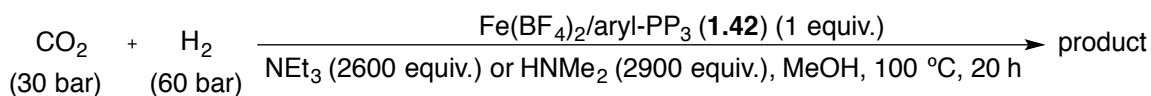


Entry	Cat.	Temp. (°C)	TON ^a	TOF (h ⁻¹) ^b
1	Fe(BF ₄) ₂ /aryl-PP ₃ (1.42)	80	1600	80
2	1.42	60	870	44
3	1.42	100	1500	75
4	1.42	120	280	14
5	Fe(acac) ₃ /aryl-PP ₃	80	1600	80
6	FeCl ₂ /aryl-PP ₃	80	900	45
7	Fe(acac) ₂ /aryl-PP ₃	80	1600	80
8	FeF ₂ /aryl-PP ₃	80	1500	75

^aTON = (mol HCO₂Na)/(mol cat.). ^bTOF = (mol HCO₂Na)/(mol cat.)/(20 h).

The hydrogenation of CO₂ in methanol using **1.42** as the catalyst was also investigated in the presence of an amine base (Table 1.20). The direct hydrogenation of CO₂ in the presence of triethylamine led to a mixture of formic acid and methyl formate. Addition of water suppressed the formation of methyl formate, generating only formic acid (entry 2). When using dialkylamines as the base such as dimethylformamide (DMF), the formation of formamides was observed. The TONs achieved with the aryl-PP₃ ligand are over an order of magnitude higher in comparison with any previously reported iron system.

Table 1.20. Hydrogenation of CO₂ to methyl formate or dimethylformamide



Entry	Products	Additive	TON ^a	TOF (h ⁻¹) ^b
1	HCO ₂ Me/HCO ₂ H (1:1)	N/A	1700	85
2	HCO ₂ H	H ₂ O ^c	1900	95
3	DMF/HCO ₂ H (24:1)	N/A	2300	115
4	DMF/HCO ₂ H (10:1)	HNMe ₂ ^d	5100	260

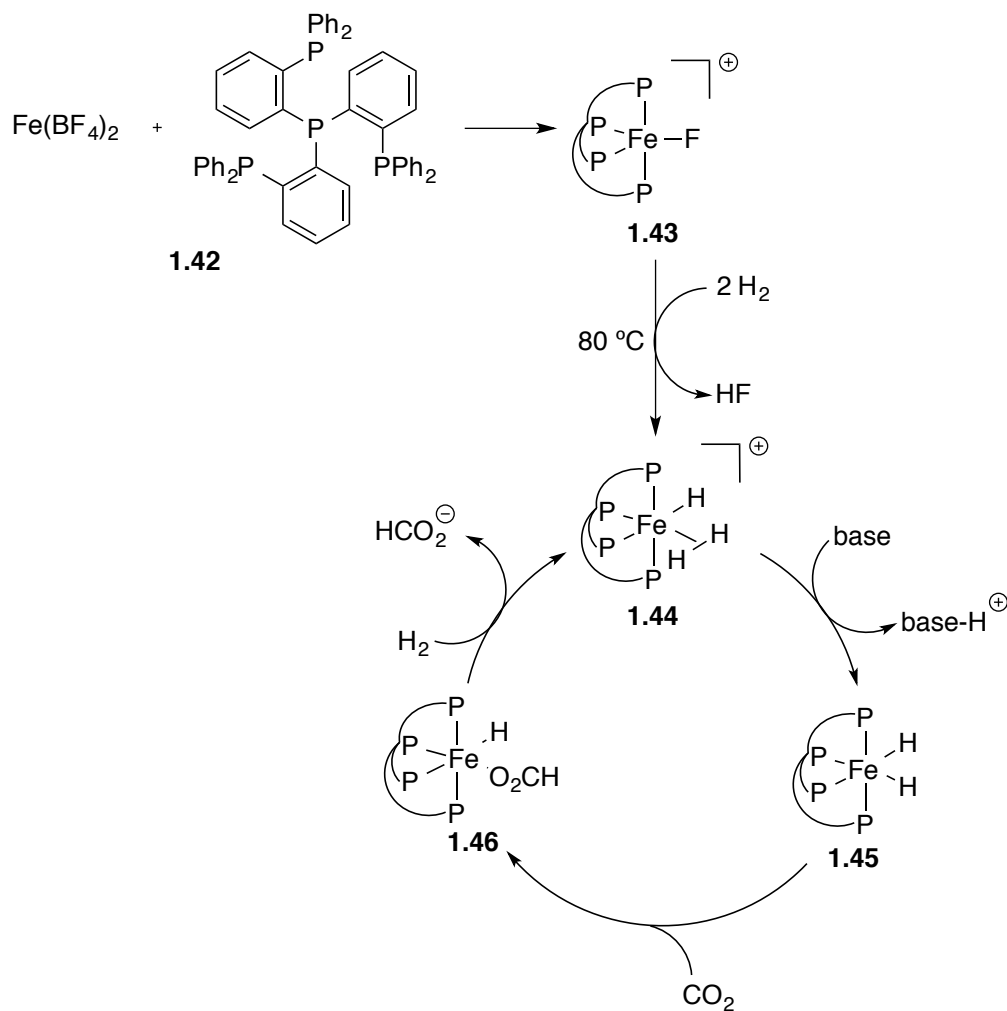
^aTON = (mol product)/(mol cat.). ^bTOF = (mol product)/(mol cat.)/(20 h).

^cH₂O = 12 equiv. ^dHNMe₂ = 5800 equiv.

To understand the mechanism of these Fe-catalyzed hydrogenation reactions, *in situ* NMR measurements were performed (Scheme 1.12). Addition of aryl-PP₃ to Fe(BF₄)₂ in THF generated iron species **1.43** exhibiting one fluorine ligand derived from the original BF₄⁻ anion. The formation of an iron-hydride-hydrogen complex **1.44** at 80 °C with the addition of H₂ was proposed. Addition of CO₂ to complex **1.44** provided no formation of formic acid or formate. Only after the addition of base did the group observe the disappearance of **1.44** and the formation of product. The presence of base is necessary to convert iron-hydride-hydrogen complex **1.44** into a more active reduction catalyst **1.45**. Subsequent insertion of CO₂ into the iron-hydride bond

generated **1.46**, followed by coordination of H_2 produced formate and regenerated the complex **1.44**.

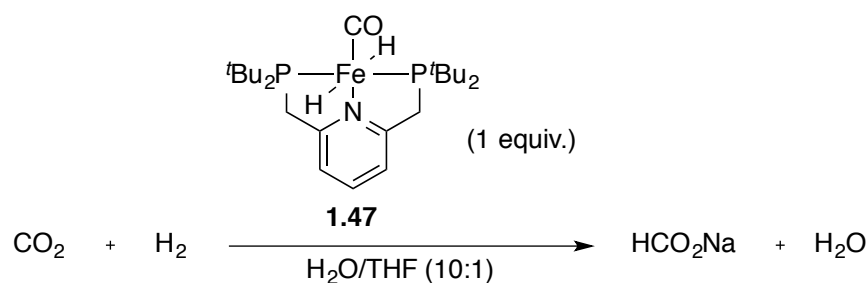
Scheme. 1.12. Postulated mechanism for iron catalyzed hydrogenation of CO_2



Work by Milstein and coworkers also demonstrated significant advancements in iron catalyzed hydrogenation of CO_2 to formic acid. In 2011, the group reported the synthesis and catalytic activity of an iron-PNP-pincer complex similar to the iridium species **1.32** (Table 1.15, Scheme 1.9) developed by Nozaki (Table 1.21).⁴⁶ The iron complex with tert-butyl groups on the phosphorous atoms (**1.47**) demonstrated high activity at low pressures of CO_2 and H_2 under

aqueous conditions. The group found that decreasing the pressure led to lower catalytic activity. In a similar fashion as $\text{RuH}_2(\text{PMe}_3)_4$ (**1.12**), developed by Noyori and coworkers, Milstein *et al.* discovered that the amount of base was important for high TONs and TOFs. Milstein and others⁴⁷ postulated a mechanism that was the same as iridium-PNP-pincer **1.32** involving deprotonative dearomatization of the ligand (Scheme 1.9).

Table 1.21. Iron-PNP-pincer 1.47 catalyzed hydrogenation of CO_2



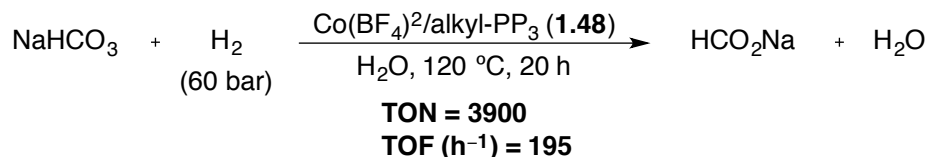
Entry	NaOH Equiv.	Pressure H_2 , CO_2 (bar)	Time (h)	TON ^a	TOF (h^{-1}) ^b
1	1000	4.15, 4.15	14	340	24
2	1000	5.52, 2.76	8	480	60
3	1000	6.66, 3.33	10	530	53
4	500	6.66, 3.33	10	340	34
5	1500	6.66, 3.33	5	570	110
6	2000	6.66, 3.33	5	790	160
7	3000	6.66, 3.33	5	690	120

^aTON = (mol HCO_2Na)/(mol cat.). ^bTOF = (mol HCO_2Na)/(mol cat.)/(time).

1.3.2 Cobalt

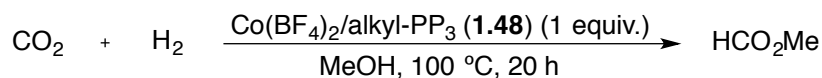
In addition to iron catalysts, recent work has been focused on the use of cobalt catalysts for the hydrogenation of CO_2 to formic acid. In 2012, Beller *et al.* investigated the use of the alkyl- PP_3 ligand with cobalt complexes instead of iron (as in **1.41**). First, they investigated the combination of $\text{Co}(\text{BF}_4)_2$ and alkyl- PP_3 (**1.48**) for use in hydrogenation of bicarbonate (Scheme 1.13).⁴⁸ Similar to that of the analogous iron complex, tests with bi- or tri-dentate ligands showed no activity, which cobalt salts $\text{Co}(\text{acac})_3$, $\text{Co}(\text{acac})_2$, and CoCl_2 showed similar activity.

Scheme 1.13. Cobalt catalyzed hydrogenation of sodium bicarbonate



The complex was then tested for its ability to catalyze CO₂ hydrogenation to produce methyl formate (Table 1.22). Methyl formate was generated with a TON of 430, which is on par with the iron catalyzed variant. Increasing the amount of base resulted in higher catalytic activity as the cobalt catalyzed demonstrated TONs of 660 and TOFs of 33, which are slightly higher than that of iron (entry 4).

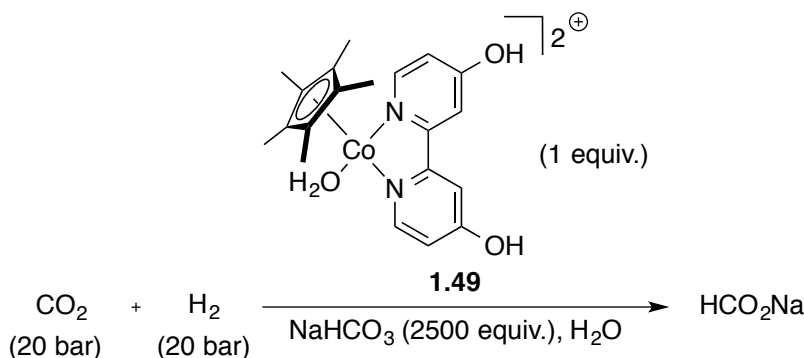
Table 1.22. Co(BF₄)₂/alkyl-PP₃ (1.48) catalyzed hydrogenation of CO₂ to methyl formate



Entry	NEt ₃ Equiv.	Pressure H ₂ , CO ₂ (bar)	TON ^a	TOF (h ⁻¹) ^b
1	500	60, 30	430	22
2	500	10, 10	60	3.0
3	500	5, 5	26	1.3
4	4000	60, 30	660	33

^aTON = (mol HCO₂Me)/(mol cat.). ^bTOF = (mol HCO₂Me)/(mol cat.)/(20 h).

In 2013, Fujita and Himeda synthesized and explored a cobalt complex analogous to the half-sandwich complexes **1.21** and **1.25** for CO₂ hydrogenation (Table 1.23).⁴⁹ Cobalt bipyridyl complex **1.49** demonstrated the hydrogenation of CO₂ to formate. The activity decreased as the temperature was decreased. Although TONs and TOFs were lower than previously synthesized cobalt complexes, this is the first example of a non-phosphine cobalt complex that can mediate CO₂ hydrogenation under aqueous conditions without the addition of organic solvents.

Table 1.23. Cobalt bipyridyl 1.49 catalyzed hydrogenation of CO₂

Entry	Temp. (°C)	Time (h)	TON ^a	TOF (h ⁻¹) ^b
1	100	2	42	21
2	90	2	49	25
3	80	7	59	8.4
4	25	38	7.0	0.18

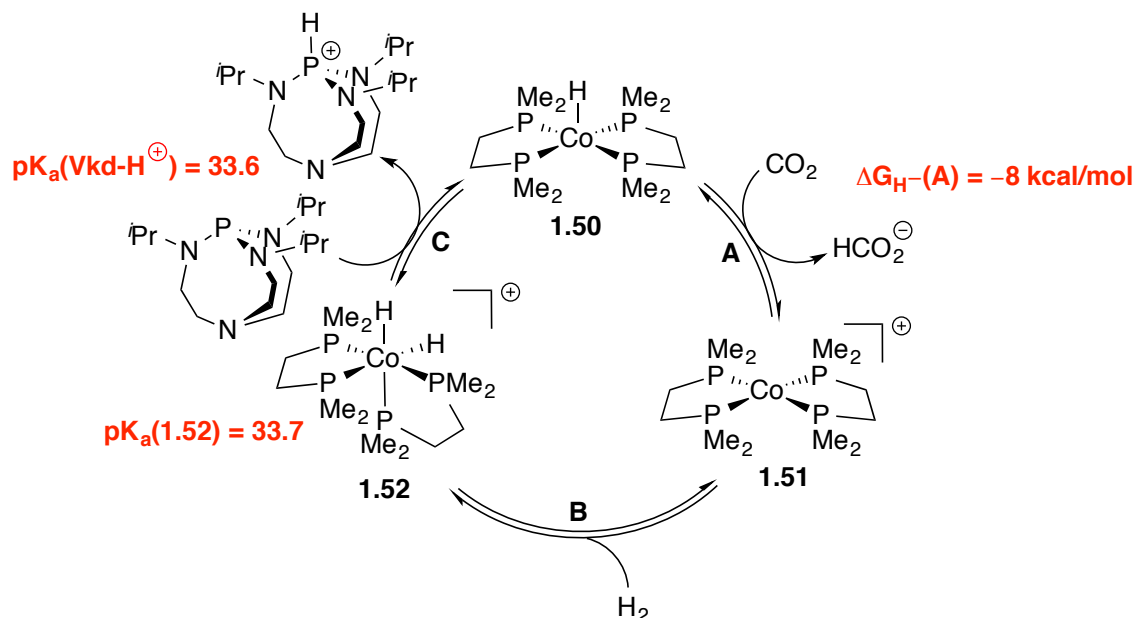
^aTON = (mol HCO₂Na)/(mol cat.). ^bTOF = (mol HCO₂Na)/(mol cat.)/(20 h).

The most recent significant example of a cobalt based catalyst for the hydrogenation of CO₂ was reported by Linehan *et al.* in 2013.^{50–52} Using thermodynamic parameters of hydricity (ΔG_{H^-}) and acidity (pK_{a}) as guides, the group designed a catalytic system based on a simple catalytic cycle (Scheme 1.14). The catalytic cycle contains three essential reactions: (A) a hydride transfer from metal complex **1.50** to CO₂, (B) addition of H₂ to the resulting metal complex **1.51**, and (C) the regeneration of the metal hydride complex **1.50** by deprotonation of **1.52**. In order to obtain catalytic results at room temperature and pressure, the energetics of the reactions in steps A and C needed to be well matched in the catalytic system.

Hydride donor abilities (or the free energy for cleaving H⁻ from a metal hydride) have been characterized for a range of complexes using experimental and computational approaches.^{53–56} Noble-metal based phosphine complexes are better hydride donors than their respective cobalt counterparts. However, improving the hydride donating ability of complexes like **1.50** increases the strength of the base needed to deprotonate dihydride species like **1.52**. If steps A

and C are significantly mismatched in energy, catalysis will be slower. Therefore, Linehan and coworkers designed their catalytic system so that step A would be thermodynamically favorable ($\Delta G_{\text{H}^-}(\text{A}) = -8 \text{ kcal/mol}$)^{57,58} and that complex **1.52** could be deprotonated ($\text{pK}_{\text{a}}(\mathbf{1.52})_{\text{calc}} = 33.7$)⁵⁵. The deprotonation of **1.52** requires a base that has a conjugate acid with a similar or higher pK_{a} value. The group chose Verkade's base (Vkd, 2,8,9-triisopropyl-2,5,8,9-tetraaza-1-phosphabicyclo[3.3.3]undecane) because with a reported pK_{a} of 33.6 for its conjugate acid, it is matched in energy.⁵⁹

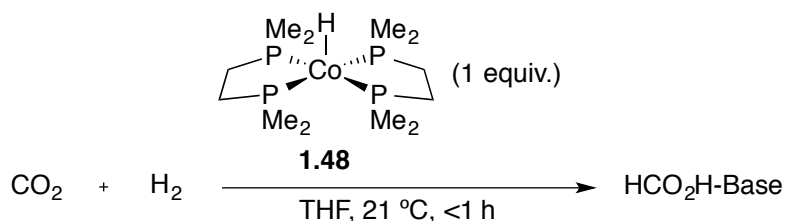
Scheme 1.14. Proposed catalytic cycle for CO₂ hydrogenation using cobalt complex 1.50



Co(dmpe)₂H (**1.50**, dmpe = 1,2-bis(dimethylphosphino)ethane) was investigated for hydrogenation of CO₂ to formate using Verkade's base and other commonly used bases (Table 1.24). Consistent with the thermodynamic data, **1.50** was active for hydrogenation of CO₂ to formate. To confirm that the strength of the base affects the activity, the group tested weaker bases like NEt₃ and DBU for which the corresponding conjugate acids have pK_{a} values of 24.3

and 18.8, respectively.⁶⁰ With the weaker bases, the catalytic activity was much lower as compared to Verkade's base (entries 1-3). Cobalt complex **1.50** demonstrated a TON of 9,400 and TOF of 74,000 h⁻¹ after less than an hour with a low catalyst loading. The complex was also active at pressures as low as 1.0 bar (entry 6).

Table 1.24. Catalytic conversion of CO₂ and H₂ to formate with Co(dmpe)₂H (1.50**)**



Entry	Cat. Loading (mM)	Base	Pressure (bar) ^a	TON ^b	TOF (h ⁻¹) ^c
1	40	NEt ₃	40	2	N/A
2	40	DBU	20	59	140
3	0.40	Vkd	20	2100	54000
4	0.040	Vkd	20	9400	74000
5	0.28	Vkd	1.8	1900	6400
6	0.28	Vkd	1.0	2000	3400
7	2.8	Vkd	1.8	210	850

^aTotal pressure. CO₂/H₂ = 1:1. ^bTON = (mol HCO₂H-Base)/(mol cat.). ^cTOF = (mol HCO₂H-Base)/(mol cat.)/(< 1 h).

The rationally designed cobalt complex **1.50** demonstrates activities comparable to the best noble-metal complexes developed to date. The present system, although remarkably active, is still limited as Verkade's base is expensive and obscure, which may prevent scale-up or development into a commercially viable process. However, this work done by Linehan and coworkers demonstrates the utility of using fundamental thermodynamic parameters to help design effective catalytic systems. Future work in the field of CO₂ hydrogenation is focused on the development of new catalytic systems that are cheap and efficient.

1.4 References

1. Joó, F. *ChemSusChem* **2008**, *1*, 805.
2. Xu, J.; Froment, G. F. *AIChE J.* **1989**, *35*, 88.
3. Onuki, K.; Kubo, S.; Terada, A.; Sakaba, N.; Hino, R. *Energy Environ. Sci.* **2009**, *2*, 491.
4. Rausch, B.; Symes, M. D.; Chisholm, G.; Cronin, L. *Science* **2014**, *345*, 1326.
5. Walter, M. G.; Warren, E. L.; McKone, J. R.; Boettcher, S. W.; Mi, Q.; Santori, E. A.; Lewis, N. S. *Chem. Rev.* **2010**, *110*, 6446.
6. Reece, S. Y.; Hamel, J. A.; Sung, K.; Jarvi, T. D.; Esswein, A. J.; Pijpers, J. J. H.; Novera, D. G. *Science* **2011**, *334*, 645.
7. Schlapbach, L.; Züttel, A. *Nature* **2001**, *414*, 353.
8. Bain, A.; Van Vorst, W. D. *Int. J. Hydrogen Energy* **1999**, *24*, 399.
9. Suh, M. P.; Park, H. J.; Prasad, T. K.; Lim, D. W. *Chem. Rev.* **2011**, *112*, 782.
10. Sakintuna, B.; Lamari-Darkrim, F.; Hirscher, M. *Int. J. Hydrogen Energy* **2007**, *32*, 1121.
11. Staubitz, A.; Robertson, A. P. M.; I., M. *Chem. Rev.* **2010**, *110*, 4079.
12. Navarro, R. M.; Peña, M. A.; Fierro, J. L. G. *Chem. Rev.* **2007**, *107*, 3952.
13. Jadhav, S. G.; Vaidya, P. D.; Bhanage, B. M.; Joshi, J. B. *Chem. Eng. Res. Des.* **2014**, *92*, 2557.
14. Jessop, P. G.; Ikariya, T.; Noyori, R. *Chem. Rev.* **1995**, *95*, 259.
15. Enthaler, S. *ChemSusChem* **2008**, *1*, 801.
16. Yu, X.; Pickup, P. G. *J. Power Sources* **2008**, *182*, 124.
17. Farlow, M. W.; Adkins, H. *J. Am. Chem. Soc.* **1935**, *57*, 2222.
18. Inuoe, Y.; Izumida, H.; Sasaki, Y.; Hashimoto, H. *Chem. Lett.* **1976**, 863.
19. Tsai, J. C.; Nicholas, K. M. *J. Am. Chem. Soc.* **1992**, *114*, 5117.
20. Graf, E.; Leitner, W. *J. Chem. Soc., Chem. Commun.* **1992**, 623.
21. Burgemeister, T.; Kastner, F.; Leitner, W. *Angew. Chem. Int. Ed. Engl.* **1993**, *32*, 739.
22. Gassner, F.; Leitner, W. *J. Chem. Soc., Chem. Commun.* **1993**, 1465.
23. Leitner, W.; Dinjus, E.; GaBner, F. *J. Organomet. Chem.* **1994**, *475*, 257.
24. Bényei, A.; Joó, F. *J. Mol. Catal.* **1990**, *58*, 151.
25. Fornika, R.; Göris, H.; Seemann, B.; Leitner, W. *J. Chem. Soc., Chem. Commun.* **1995**, 1479.
26. Angermund, K.; Baumann, W.; Dinjus, E.; Fornika, R.; Gorls, H.; Kessler, M.; Kruger, C.; Leitner, W.; Lutz, F. *Chem. Eur. J.* **1997**, *3*, 755.
27. Jessop, P. G.; Ikariya, T.; Noyori, R. *Nature* **1994**, *368*, 231.
28. Shaw, R. W.; Brill, T. B.; Clifford, A. A.; Eckert, C. A.; U., F. E. *Chem. Engng. News* **1991**, *69*, 26.
29. Jessop, P. G.; Hsiao, Y.; Ikariya, T.; Noyori, R. *J. Am. Chem. Soc.* **1996**, *118*, 344.
30. Bautista, M. T.; Cappellani, E. P.; Drouin, S. D.; Morris, R. H.; Schweitzer, C. T.; Stella, A.; Zubkowski, J. *J. Am. Chem. Soc.* **1991**, *113*, 4876.

31. Munshi, P.; Main, A. D.; Linehan, J. C.; Tai, C. C.; Jessop, P. G. *J. Am. Chem. Soc.* **2002**, *124*, 7963.
32. Getty, A. D.; Tai, C. C.; Linehan, J. C.; Jessop, P. G.; Olmstead, M. M.; Rheingold, A. L. *Organometallics* **2009**, *28*, 5466.
33. Himeda, Y.; Onozawa-Komatsuzaki, N.; Sugihara, H.; Arakawa, H.; Kasuga, K. *Organometallics* **2004**, *23*, 1480.
34. Himeda, Y.; Onozawa-Komatsuzaki, N.; Sugihara, H.; Kasuga, K. *J. Am. Chem. Soc.* **2005**, *127*, 13118.
35. Himeda, Y.; Onozawa-Komatsuzaki, S. H.; Kasuga, K. *Organometallics* **2007**, *26*, 702.
36. Hull, J. F.; Himeda, Y.; Wang, W. H.; Hashiguchi, B.; Periana, R.; Szalda, D. J.; Muckerman, J. T.; Fujita, E. *Nature Chem.* **2012**, *4*, 383.
37. Wang, W. H.; Hull, J. F.; Muckerman, J. T.; Fujita, E.; Himeda, Y. *Energy Environ. Sci.* **2012**, *5*, 7923.
38. Wang, W. H.; Muckerman, J. T.; Fujita, E.; Himeda, Y. *ACS Catal.* **2013**, *3*, 856.
39. Tanaka, R.; Yamashita, M.; Nozaki, K. *J. Am. Chem. Soc.* **2009**, *131*, 14168.
40. Tanaka, R.; Yamashita, M.; Chung, L. W.; Morokuma, K.; Nozaki, K. *Organometallics* **2011**, *30*, 6742.
41. Schmeier, T. J.; Dobereiner, G. E.; Crabtree, R. H.; Hazari, N. *J. Am. Chem. Soc.* **2011**, *133*, 9274.
42. Tai, C. C.; Chang, T.; Roller, B.; Jessop, P. G. *Inorg. Chem.* **2003**, *42*, 7340.
43. Federsel, C.; Boddien, A.; Jackstell, R.; Jennerjahn, R.; Dyson, P. J.; Scopelliti, R.; Laurenczy, G.; Beller, M. *Angew. Chem. Int. Ed.* **2010**, *49*, 9777.
44. Ziebart, C.; Federsel, C.; Anbarasan, P.; Jackstell, R.; Baumann, W.; Spannenberg, A.; Beller, M. *J. Am. Chem. Soc.* **2012**, *134*, 20701.
45. Hartley, J. G.; Venanzi, L. M.; Goodall, D. C. *J. Chem. Soc.* **1963**, 3930.
46. Langer, R.; Diskin-Posner, Y.; Leitius, G.; Shimon, L. J. W.; Ben-David, Y.; Milstein, D. *Angew. Chem. Int. Ed.* **2011**, *50*, 9948.
47. Yang, X. *Inorg. Chem.* **2011**, *50*, 12836.
48. Federsel, C.; Ziebart, C.; Jackstell, R.; Baumann, W.; Beller, M. *Chem. Eur. J.* **2012**, *18*, 72.
49. Badiei, Y. M.; Wang, W. H.; Hull, J. F.; Szalda, D. J.; Muckerman, J. T.; Himeda, Y.; Fujita, E. *Inorg. Chem.* **2013**, *52*, 12576.
50. Jeletic, M. S.; Mock, M. T.; Appel, A. M.; Linehan, J. C. *J. Am. Chem. Soc.* **2013**, *135*, 11533.
51. Kumar, N.; Camaioni, D. M.; Dupuis, M.; Raugei, S.; Appel, A. M. *Dalton Trans.* **2014**, *43*, 11803.
52. Jeletic, M. S.; Helm, M. L.; Hulley, E. B.; Mock, M. T.; Appel, A. M.; Linehan, J. C. *ACS Catal.* **2014**, *4*, 3755.
53. DuBois, D. L.; Berning, D. E. *Appl. Organomet. Chem.* **2000**, *14*, 860.

54. Curtis, C. J.; Miedaner, A.; Ellis, W. W.; DuBois, D. L. *J. Am. Chem. Soc.* **2002**, *124*, 1918.
55. Qi, X. J.; Liu, L.; Fu, Y.; Guo, Q. X. *Organometallics* **2006**, *25*, 5879.
56. Qi, X. J.; Fu, Y.; Liu, L.; Guo, Q. X. *Organometallics* **2007**, *26*, 4197.
57. DuBois, D. L.; Blake, D. M.; Miedaner, A.; Curtis, C. J.; DuBois, M. R.; Franz, J. A.; Linehan, J. C. *Organometallics* **2006**, *25*, 4414.
58. Mock, M. T.; Potter, R. G.; O'Hagan, M. J.; Camaioni, D. M.; Dougherty, W. G.; Kassel, W. S.; DuBois, D. L. *Inorg. Chem.* **2011**, *50*, 11914.
59. Kisanga, P. B.; Verkade, J. G.; Schwesinger, R. *J. Org. Chem.* **2000**, *65*, 5431.
60. Kaljurand, I.; Kutt, A.; Soovali, L.; Rodima, T.; Maemets, V.; Leito, I.; Koppel, I. A. *J. Org. Chem.* **2005**, *70*, 1019.
61. Crabtree, R. H. *The Organometallic Chemistry of the Transition Metal*, 5th ed.; Wiley, 2009.

Chapter 2

Development of a Transition Metal / N-Heterocyclic Carbene Cooperative System for the Hydrogenation of Carbon Dioxide to Formic Acid

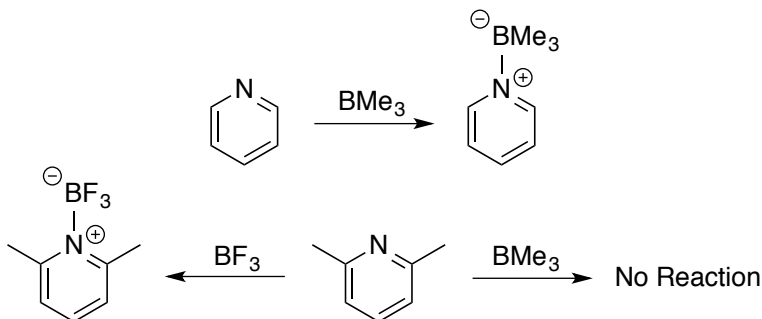
2.1 Introduction

Over the past few decades, the conversion of small molecules such as H_2 , N_2 , O_2 , CH_4 , C_2H_4 , CO , and CO_2 have attracted considerable attention.^{1,2} Many of these small molecules are thermodynamically or kinetically stable and their usefulness depends on overcoming significant barriers. However, because their usefulness could be beneficial for the survival of the world, fundamental research is of great importance. Although small molecule activation has historically been exclusively associated with transition metals,¹ the use of compounds with main group elements has become more ubiquitous in recent research.³⁻⁵

2.1.1 Reactions of Frustrated Lewis Pairs with CO_2

In 1923, Gilbert N. Lewis classified molecules that behave as electron-pair donors as bases and conversely electron-pair acceptors as acids.⁶ The combination of a simple Lewis acid and Lewis base results in neutralization similar to the corresponding combination of Brønsted acids and bases.⁷ However, in the case of Lewis acids and bases, instead of forming water, the combination results in a Lewis acid-base adduct. In 1942, Brown and coworkers noted that although most combinations of Lewis acids and bases formed classical Lewis adducts, steric demands can intervene in the formation of donor-acceptor adducts of pyridines with trimethylborane (BMe_3) (Scheme 2.1).⁸

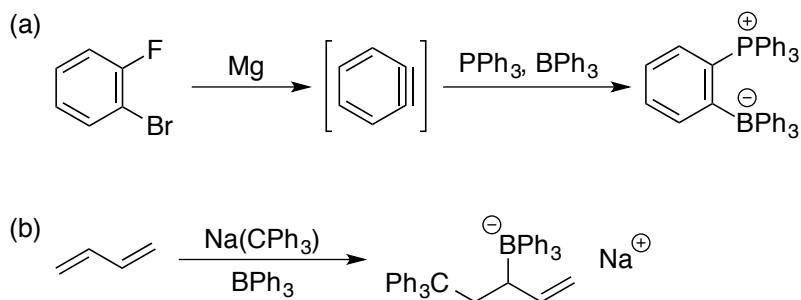
Scheme 2.1. Reactivity of pyridines with BMe_3 and BF_3



Adduct formation was observed for pyridine, but lutidine failed to form an adduct. Additionally, lutidine formed a stable adduct with BF_3 but did not react with BMe_3 . Molecular models provided a rationale for this observation based on steric interactions of the *ortho*-methyl groups of lutidine with the methyl groups of the borane.

In 1950, Wittig and Benz described the reaction of 1,2-didehydrobenzene (generated *in situ* from *o*-fluorobromobenzene) reacted with a mixture of the Lewis base triphenylphosphine and the Lewis acid triphenylborane (BPh_3) to give an *o*-phenylene-bridge phosphonium-borate (Scheme 2.2a).⁹ Years later, Tochtermann, a former member of the Wittig group, observed the formation of a non-classical Lewis acid-base adduct from trityl anion and BPh_3 (Scheme 2.2b).¹⁰ At the time, both groups had not realized the special nature of the bulky Lewis pairs that did not yield the classical Lewis acid-base adducts.

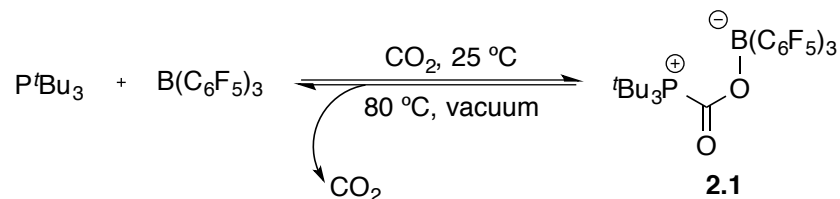
Scheme 2.2. Early FLP reagents



In a collaborative report, Stephan *et al.* and Erker *et al.* found that CO_2 reacted with frustrated Lewis pairs in a straightforward fashion.¹¹ A solution of $\text{B}(\text{C}_6\text{F}_5)_3$ and tri-*tert*-butylphosphine (P^tBu_3) was covered with an atmosphere of CO_2 , resulting in the immediate precipitation of a white solid (Scheme 2.3). The structural data for this compound confirmed the formula was ${}^t\text{Bu}_3\text{P}(\text{CO}_2)\text{B}(\text{C}_6\text{F}_5)_3$ (**2.1**) in which CO_2 reacted with phosphine and borane to form P–C and O–B bonds. X-ray crystallography revealed that the geometry about the carbon atom

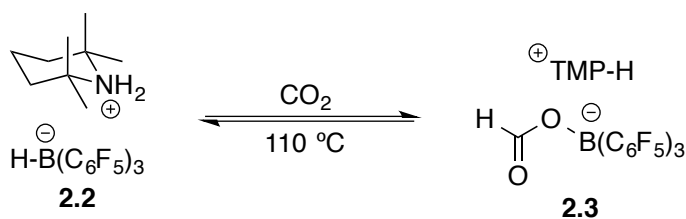
from the CO₂ molecule was approximately trigonal-planar. The thermal stability of **2.1** was examined and liberation of CO₂ occurred upon heating to 80 °C under vacuum, indicating that the CO₂ addition is reversible.

Scheme 2.3. Reversible CO₂ uptake and release by frustrated phosphine-borane Lewis pairs



After this initial discovery, many groups focused their research on the transformation of CO₂ to other useful chemicals. In 2009, Ashley, O'Hare, and coworkers demonstrated the first homogeneous process for the conversion of CO₂ into methanol utilizing FLPs.¹² The reaction of H₂ with an equimolar mixture of TMP (Me₄C₅NH, 2,2,6,6-tetramethylpiperidine) and B(C₆F₅)₃ gave the salt [TMPH]⁺–[HB(C₆F₅)₃][–] (**2.2**).¹³ Ashley *et al.* found that the addition of CO₂ to **2.2** produced [TMPH]⁺–[HCO₂B(C₆F₅)₃][–] (**2.3**), a formatoborate complex (Scheme 2.4).

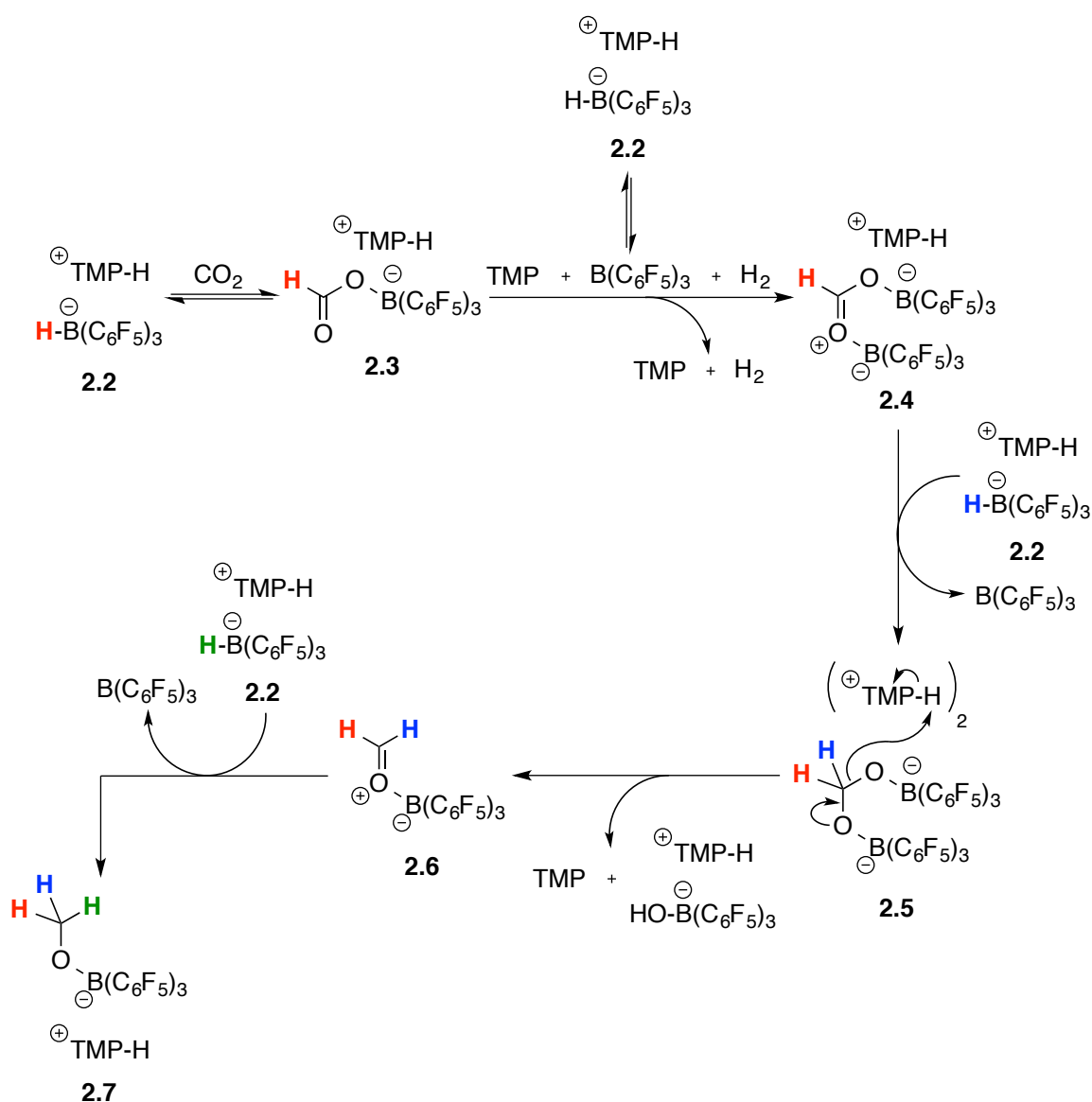
Scheme 2.4. Reversible reduction of CO₂ to formate **2.3 with H₂ activation by FLP **2.2****



When complex **2.3** was heated above 110 °C for long periods of time, the production of multiple new species was evident. Field-ionization mass spectrometry of reactions with ¹³CO₂ showed the mixture comprised B(C₆F₅)₃, TMP, and ¹³CH₃OB(C₆F₅)₃. Based on these results, a

mechanism was proposed to support the formation of these species (Scheme 2.5). The reversible decomposition of the borohydride salt **2.2** generates free H₂, TMP, and B(C₆F₅)₃. The attack of B(C₆F₅)₃ on the acyl oxygen atom of formatoborate **2.3** would produce intermediate **2.4**. Hydride reduction of the activated formate **2.4** by an equivalent of salt [TMPH]⁺·[HB(C₆F₅)₃][−] (**2.2**) then would lead to the formaldehyde acetal intermediate **2.5** and B(C₆F₅)₃.

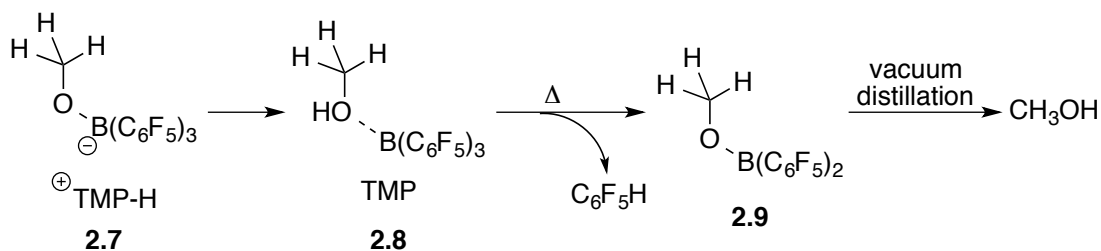
Scheme 2.5. Proposed mechanism for the reduction of CO₂ by [TMPH]⁺·[HB(C₆F₅)₃][−] (2.2**)**



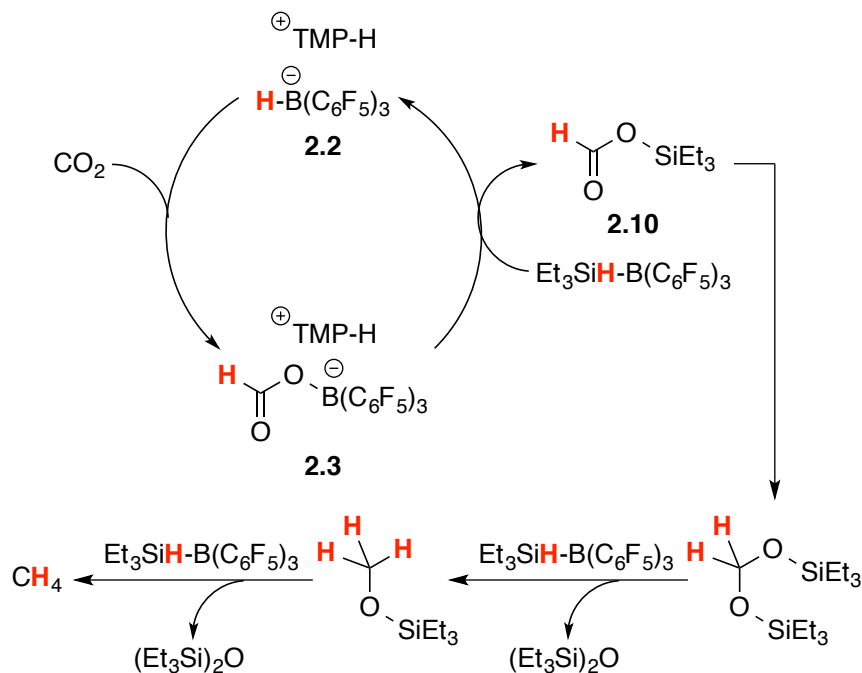
Hydride reduction of the activated formate **2.4** by an equivalent of salt [TMPH]-[HB(C₆F₅)₃] (**2.2**) then would lead to the formaldehyde acetal intermediate **2.5** and B(C₆F₅)₃. The [TMPH]⁺ counterions may serve as H⁺ donors in the cleavage of **2.5** to give H₂CO-B(C₆F₅)₃ (**2.6**) and [TMPH]-[HOB(C₆F₅)₃]. Intermediate **2.5** is expected to be a potent electrophile and would undergo a final hydride reduction in the presence of **2.2** to form [TMPH]-[CH₃OB(C₆F₅)₃] **2.7**.

The group postulated thermolysis of species **2.7** would lead to the formation of methanol (Scheme 2.6). Since the only labile source of protons is the [TMPH]⁺ cation, the [TMP][CH₃OH·B(C₆F₅)₃] adduct **2.8** would form. Previous studies have shown that such adducts can dissociate to give free CH₃OH and B(C₆F₅)₃. At the high temperatures required for this reaction, protonation of the C₆F₅ rings (to yield CH₃O-B(C₆F₅)₂ (**2.9**) and C₆F₅H) appeared to be faster, which precluded any catalytic turnover.

Scheme 2.6. Thermolysis of [TMPH]-[CH₃OB(C₆F₅)₃] (2.7**) to produce methanol**



In 2010, Piers *et al.* reported the tandem frustrated Lewis pair/borane catalyzed deoxygenative hydrosilylation of carbon dioxide to methane.¹⁴ In the presence of triethylsilane, the same FLP-derived species [TMPH]-[HCO₂B(C₆F₅)₃] (**2.3**) was converted to a formatosilane (**2.10**), which could then be hydrosilylated to methane (Scheme 2.7).

Scheme 2.7. Proposed mechanism of deoxygenative hydrosilylation of CO₂ to CH₄

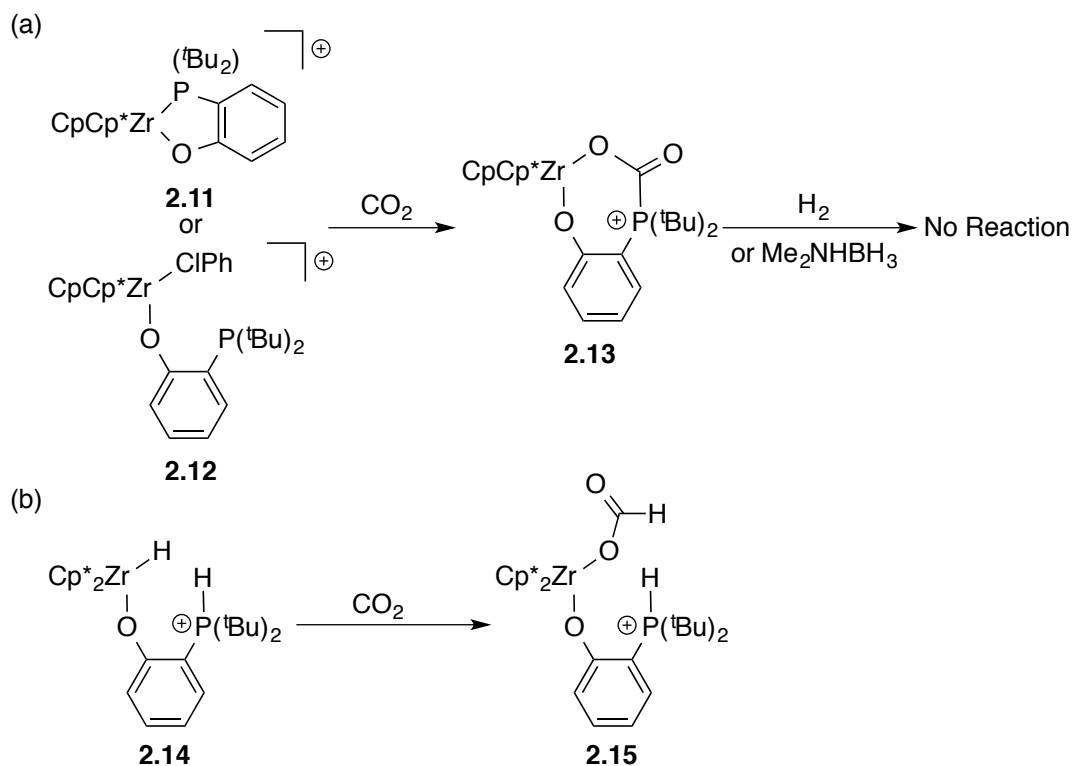
2.1.2 Hybrid Transition Metal / Frustrated Lewis Pair Approach for Activation of CO₂

In recent years, Stephan¹⁵ and Wass¹⁶ have targeted a hybrid approach to carbon dioxide activation by exploiting both transition metal systems and the concept of FLPs. While the previous main group FLPs offered novel ways to activate unreactive substrates, some of these systems suffer from a common limitation in that, apart from stoichiometric chemistry the products are often inert toward further reactivity. While advances have been made recently, the current systems are unrealistic in terms of technological applications because reactive co-reagents are necessary.

In 2011, Wass *et al.* reported analogues of main group FLPs where the Lewis acidic borane component is replaced with an electrophilic transition metal center.¹⁶ By combining the ability of transition metal complexes in catalysis with the capability of FLPs to activate substrate molecules new pathways and reactivity patterns could be exploited. The group synthesized a

variety of zirconium complexes containing phosphinoaryloxy ligands that could be used to activate carbon dioxide (Scheme 2.8). Exposure of chlorobenzene solutions of zirconium complexes **2.11** and **2.12** to 1 bar CO₂ resulted in an immediate reaction to complex **2.13**, which is similar to reactivity with main group FLPs (Scheme 2.8a). However, unlike main group systems, these transition metal analogues do not liberate CO₂ upon thermolysis, instead they slowly decompose. Attempts to reduce **2.13** with H₂ or amine boranes (like Me₂NHBH₂) were unsuccessful.

Scheme 2.8. Reactivity of cationic zirconocene-phosphinoaryloxy complexes

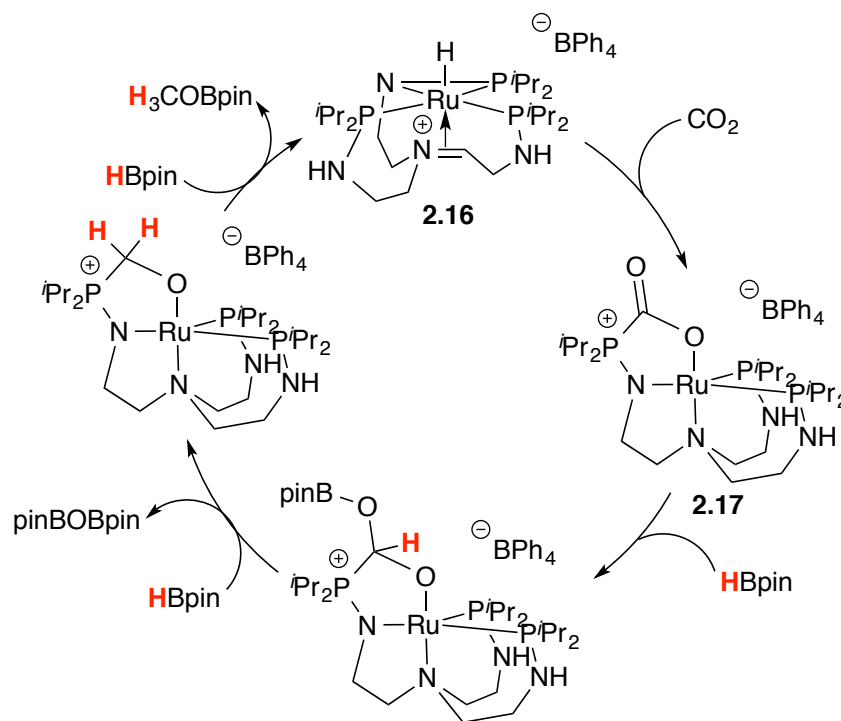


The group previously reported the synthesis of the zirconocene-hydride complex **2.14** from heterolytic cleavage of H₂ with complex **2.12**. Exposure of **2.14** with 1 bar of CO₂ yielded the formate complex **2.15** (Scheme 2.8b). Further reactivity of formate species **2.15** was not

attempted, however, this intermediate for stepwise CO₂ reduction suggests promise for these systems in the future.

In 2012, Sgro and Stephan published the frustrated Lewis pair inspired CO₂ reduction by a ruthenium tris(aminophosphine) complex (**2.16**).¹⁵ The system demonstrated capture and activation of CO₂ for catalytic reductions of boranes, yielding methoxyboranes and O(BR₂)₂ as products (Scheme 2.9). Exposure of ruthenium **2.16** to CO₂ resulted in immediate precipitation of **2.17**, which upon addition of excess HBpin generated MeOBpin and O(Bpin)₂. The mechanism is thought to involve successive hydroborations of the CO₂ fragment of **2.17**. The binding of CO₂ in **2.17** exploits the cooperative action of the pendant Lewis basic phosphine and Lewis acidic ruthenium center. These observations demonstrate that transition metal catalysts can be designed based on an activation strategy that is analogous to main group frustrated Lewis pairs.

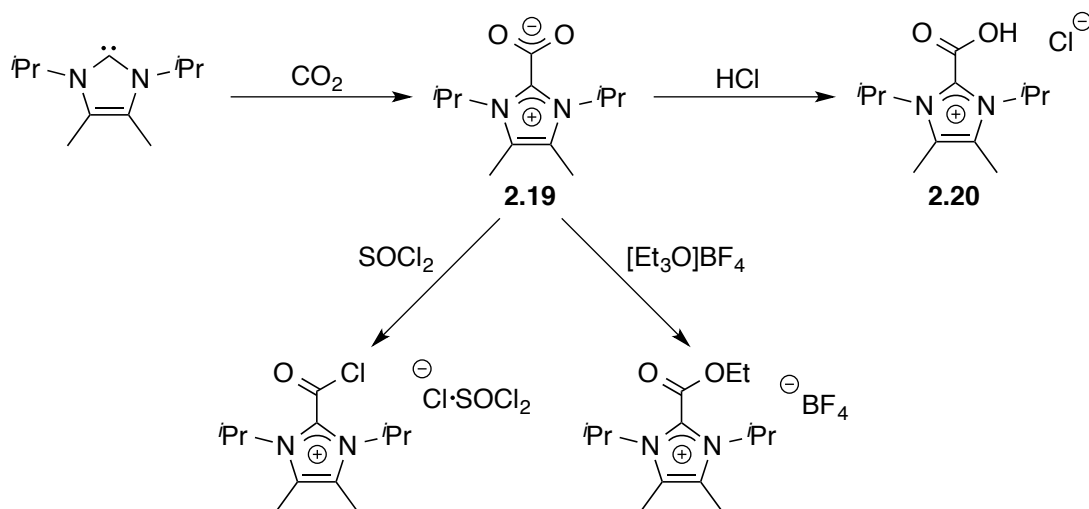
Scheme 2.9. Proposed catalytic cycle for the reduction of CO₂ by ruthenium complex 2.16



2.1.3 Reactions of N-Heterocyclic Carbenes with CO₂

In addition to frustrated Lewis pairs, the activation of carbon dioxide by N-heterocyclic carbenes (NHCs) has attracted significant interest recently. Although known for ligands on transition metals¹⁷ or nucleophilic catalysts,¹⁸ NHCs have become widely investigated for small molecule activation.^{19,20} In 1999, Kuhn and coworkers first discovered the reactivity of NHCs with CO₂ to form imidazolium carboxylates like **2.19** (Scheme 2.10).²¹ Subsequent reactions with **2.19** generated isolable imidazolium species with carboxylic acids (**2.20**), esters, or acid chlorides, which were mostly unreactive in further investigations.

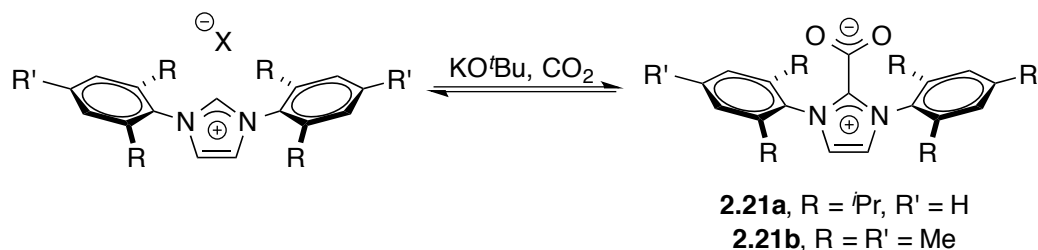
Scheme 2.10. Reactivity of N-Heterocyclic Carbenes with CO₂



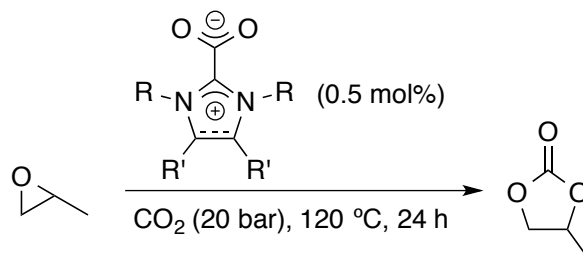
Since the reactivity of NHCs with CO₂ was discovered, Louie and coworkers have been interested in utilizing the resulting zwitterionic intermediates for the transformation and functionalization of carbon dioxide. In 2003, they reported the reversible carboxylation of NHCs using 1,3-bis(mesityl)imidazolium chloride or 1,3-bis(2,6-diisopropylphenyl)imidazolium tetrafluoroborate and potassium *tert*-butoxide under an atmosphere of CO₂ (Scheme 2.11).²² Using ¹³C NMR analysis, the addition of ¹³CO₂ to a solution of imidazolium carboxylate **2.21a**

led to an enhancement in the carbonyl peak of **2.21a** and suggested that the bound CO₂ was equilibrating with free ¹³CO₂. Thermogravimetric analysis (TGA) provided further evidence for reversible carboxylation. Clean loss of 10.6% of the weight of **2.21a** (corresponding to the mass of CO₂) was observed between 136 and 164 °C. The same behavior was observed with imidazolium carboxylate **2.21b**. The Louie group synthesized a series of imidazolium carboxylates and investigated each for their ability to release CO₂.²³ Based on TGA analysis, as the steric bulk on the N-substituents increased, the ability of the NHC-CO₂ to decarboxylate increased.

Scheme 2.11. Reversible carboxylation of imidazolium salts (X = Cl or BF₄)

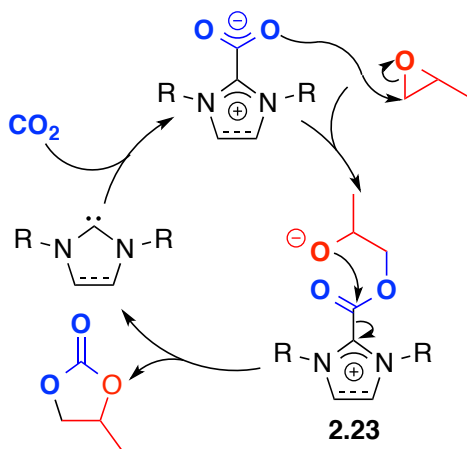


The application of imidazolium carboxylates has typically been limited to the preparation of metal-NHC complexes^{24–26} and ionic liquids.^{27,28} In 2008, Lu *et al.* published on the catalytic activity of an imidazolium carboxylate species toward the coupling of CO₂ with epoxides.²⁹ The group tested a variety of complexes for the catalytic coupling of CO₂ with propylene oxide to afford propylene carbonate (Table 2.1). The structure of the catalyst greatly dictated the yield. Bulky unsaturated imidazolium carboxylates **2.21a** and **2.21b** gave higher yields compared to their saturated counterparts **2.22a** and **2.22b**. Sterically accessible imidazolium salts like 1,3-dimethylimidazolium carboxylate (**2.21c**) only demonstrated 19% yield. Based on thermolysis experiments, unsaturated salts have lower thermal stabilities than their saturated counterparts, indicating that catalysts with higher thermal stability show lower activity.

Table 2.1. Reactions of CO₂ and propylene oxide catalyzed by imidazolium carboxylates

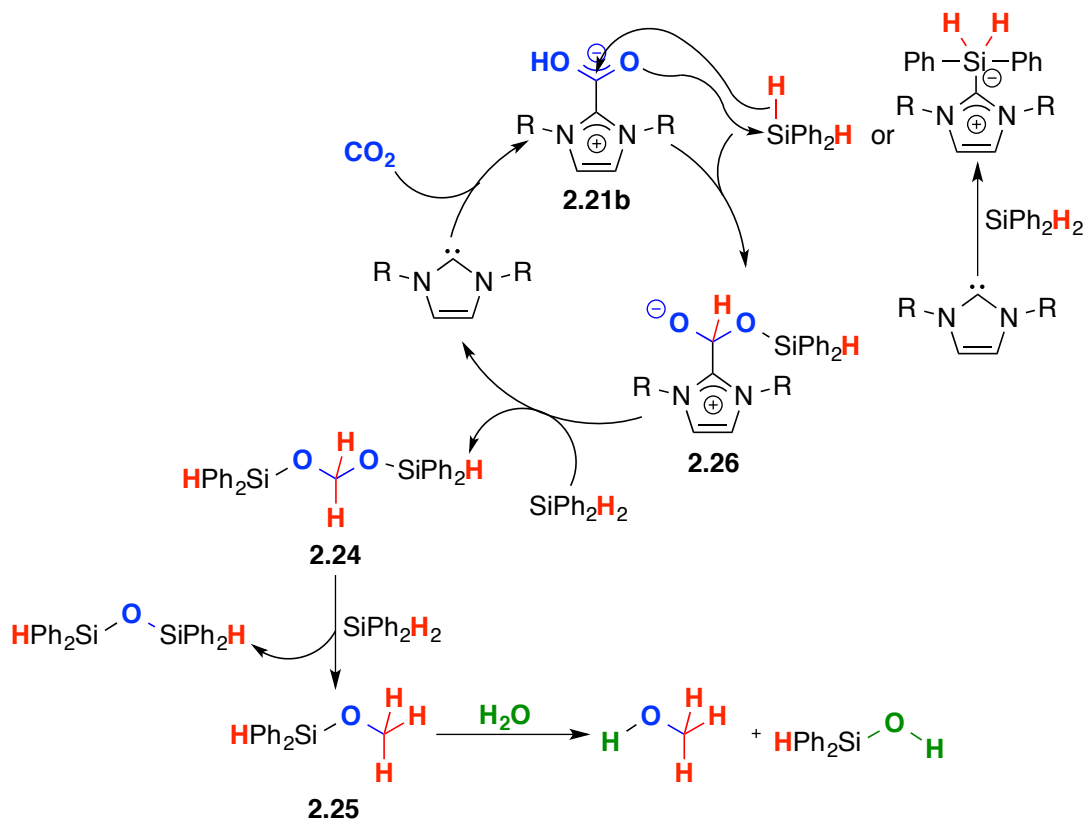
Entry	Cat.	R	R'	Yield (%)
1	2.21a	2,6- <i>i</i> Pr ₂ Ph	H	100
2	2.21b	2,4,6-Me ₃ Ph	H	45
3	2.21c	Me	H	19
4	2.22a	2,6- <i>i</i> Pr ₂ Ph	H ₂	87
5	2.22b	2,4,6-Me ₃ Ph	H ₂	25

The group proposed a possible mechanism based on these findings (Scheme 2.12). The zwitterionic carboxylate would add to the epoxide via nucleophilic attack and generate a new zwitterion **2.23**. The alkoxy anion would attack the carbon atom of the CO₂ group to produce the cyclic carbonate and the free N-heterocyclic carbene, which would quickly react with CO₂ to regenerate the zwitterionic carboxylate catalyst.

Scheme 2.12. Possible mechanism for the reaction of CO₂ with epoxides catalyzed by imidazolium carboxylates

In 2009, Zhang, Ying, and coworkers demonstrated the conversion of CO₂ into methanol with silanes.³⁰ After mixing imidazolium carboxylate **2.21b** and diphenylsilane under 1 bar of CO₂, diphenylsilane was fully consumed. The group performed the reaction with ¹³CO₂ and within 90 minutes, the formation of silylacetal (HPh₂SiOCH₂OSiPh₂H, **2.24**) and methoxide (HPh₂SiOCH₃, **2.25**) intermediates was observed. These NMR studies supported the hypothesis that CO₂ was reduced to methoxide products with hydrosilane as the hydrogen source. After 24 hours, the conversion of diphenylsilane was 90% indicating that imidazolium carboxylates are more efficient than transition metal catalysts, which required weeks to provide such reduction products.³¹ The group proposed a possible reaction pathway based on their spectroscopically observed intermediates (Scheme 2.13).

Scheme 2.13. Proposed catalytic cycle and reaction pathway for conversion of CO₂ to methanol (R = 2,4,6-Me₃Ph)



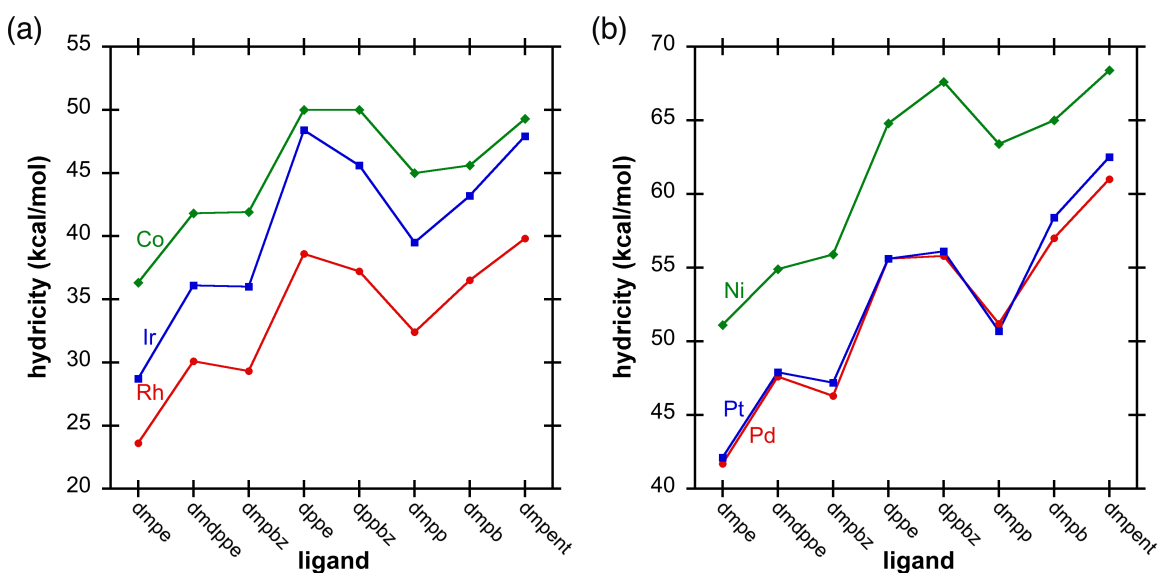
The carboxyl moiety of the zwitterionic imidazolium carboxylate **2.21b** would attack the electropositive hydrosilane center and promote hydride transfer to form intermediate **2.26**. Alternatively, the nucleophilic N-heterocyclic carbene could activate the Si-H bond to facilitate attack by the imidazolium carboxylate. Intermediate **2.26** would react with other free hydrosilanes to provide silylacetal intermediate **2.24** and methoxide **2.25**. To convert the methoxide intermediate **2.25**, the reaction was subjected to hydrolysis conditions and methanol was typically produced in over 90% yield based on the hydrosilane. The TON and TOF for the zwitterionic imidazolium carboxylate catalyst under ambient conditions reached 1840 and 26 h⁻¹, respectively. In contrast, a zirconium catalyst³¹ was reported to have TON and TOF values of only 92 and 0.54 h⁻¹, respectively, and ruthenium catalysts^{32,33} typically achieve values of 78-400 and 2.8-17 h⁻¹, respectively.

2.2 Design of a Transition Metal / N-Heterocyclic Carbene Cooperative System

2.2.1 Strategies to Increase Reactivity of Metal–Hydride Bonds

In order for the process of CO₂ hydrogenation to become beneficial for large scale, an inexpensive and efficient catalytic system that produces formic acid under mild conditions is necessary. Recent work on the development of base-metal catalysts has provided a glimpse into the possibility of constructing a reasonable approach to this reaction. However, most complexes using abundant metals still demonstrate activities that are lower than the best noble-metal catalysts (See Chapter 1). Exceptions to this trend are iron (**1.47**)³⁴ and cobalt (**1.50**)³⁵ systems taking advantage of fundamental organometallic chemistry to rationally design transition metal complexes that are more active. The success of such catalysts is thought to be due to the hydricity of the metal–hydride bond. Hydride donor abilities (or the free energy for cleaving H⁻ from a metal hydride, ΔG_{H^-}) have been characterized for a range of complexes (Figure 2.1).^{36–39}

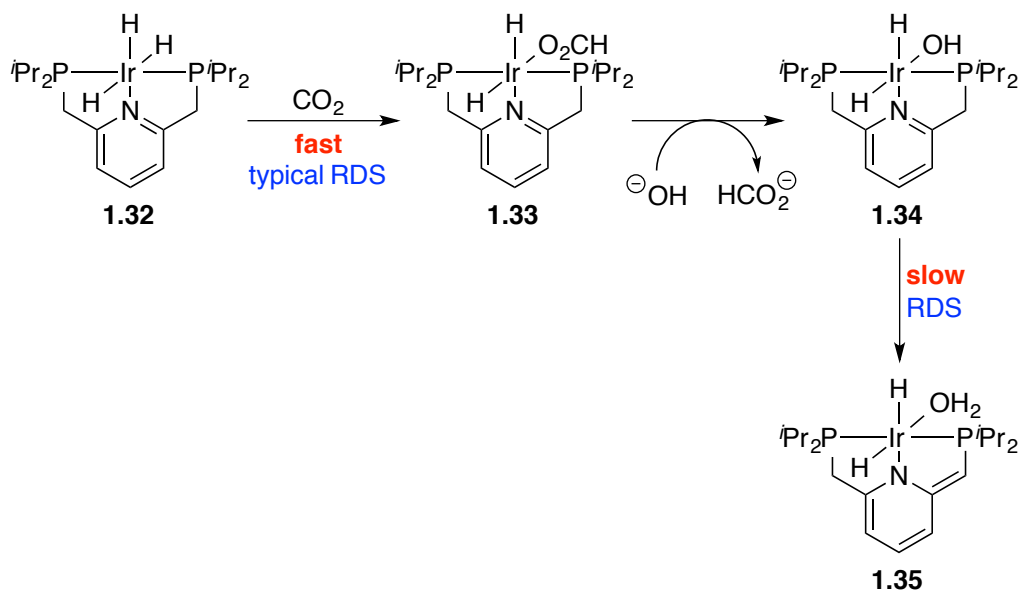
Figure 2.1. Experimentally and computationally measured hydride donor abilities of transition metal complexes of the general structure H–M(ligand)₂³⁹



Second and third row transition metal complexes are better hydride donors than their respective first row transition metal counterparts. Although the ligands bound to the metal dictate the absolute hydricity (ΔG_{H^-}) for all metal-hydride complexes experimentally or computationally explored, the trend remains the same. Most research into the hydrogenation of CO_2 has described the rate-determining step of the catalytic cycle as a metal-hydride insertion into the carbon of CO_2 . These investigations on hydricity support experimental results that indicate base-metal catalysts are less reactive toward carbon dioxide.

In 2009, Nozaki *et al.* reported on the highly active iridium-PNP-pincer complex **1.32**.⁴⁰ Under aqueous conditions, the group proposed the iridium-hydride bond was so hydridic that the rate-determining step was no longer hydride insertion into CO_2 . Instead, the rate-determining step was proposed to be the deprotonative dearomatization of the iridium-hydroxide intermediate **1.34** (Scheme 2.14).

Scheme 2.14. Iridium-PNP-pincer 1.32 catalyzed hydrogenation of CO_2



Hazari and coworkers also highlighted the importance of the nucleophilicity of the metal-hydride by comparing the computational energies for a series of Ir-H insertions into CO₂.⁴¹ They hypothesized that more nucleophilic hydrides would make metal-hydride insertions into CO₂ more favorable. As hydrides are one of the strongest *trans*-effecting ligands,⁴² a variety of *trans*-hydride complexes were compared for their ability to insert into carbon dioxide (Table 2.2).

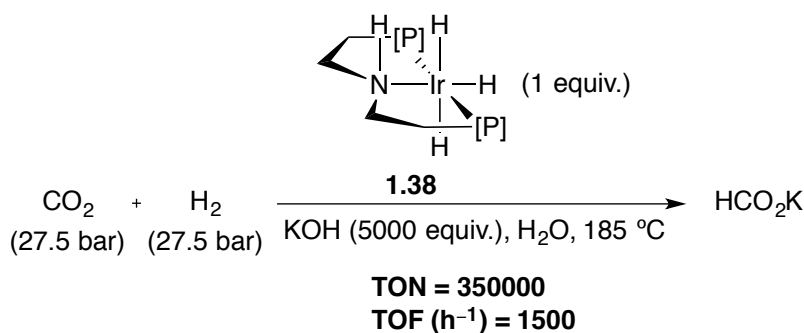
Table 2.2. Comparative computational ΔG_{H^-} for a series of Ir-H insertions into CO₂^a

Entry	Compound	Ir-H Bond Length (Å)	ΔG° (kcal/mol) ^b
1	<i>trans</i> -(PMe ₃) ₃ IrH ₃	1.681 (1.613)	3.75 (15.0)
2	<i>trans</i> -(NHC) ₃ IrH ₃ ^c	1.662 (1.640)	-4.59 (8.68)
3	<i>trans</i> -(PMe ₃) ₂ (NHC)IrH ₃ ^c	1.673 (1.640)	1.01 (7.74)
4	<i>trans</i> -(HN(CH ₂ CH ₂ P ⁱ Pr ₂))IrH ₃ (1.38)	1.678 (1.584)	-4.88 (18.4)

^aNumbers in parentheses refer to values for the hydride *trans* to the L type ligand. ^b ΔG° = Gibbs free energy, 298 K, 1 bar, with solvent corrections for THF. ^cNHC = 1,3-dimethyl-4,5-dihydroimidazol-2-ylidene.

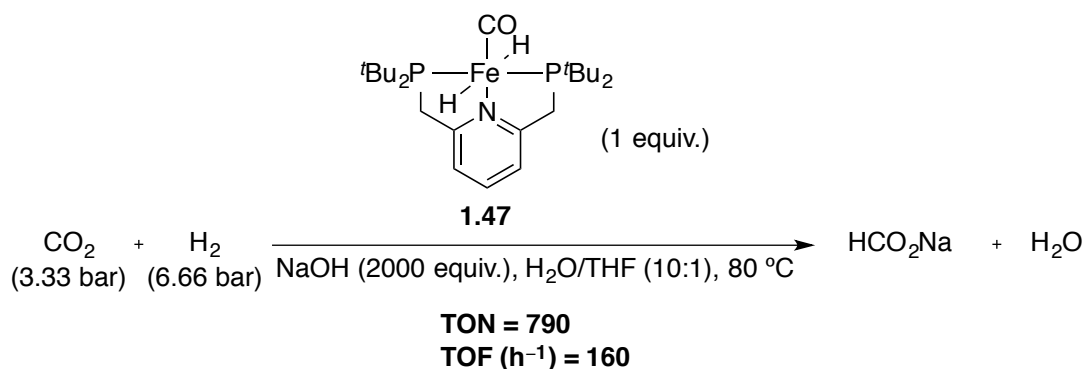
Metal-hydride insertions into CO₂ were favored with iridium-pincer complex *trans*-(HN(CH₂CH₂PⁱPr₂))IrH₃ (**1.38**). To support this phenomenon being kinetic and not thermodynamic, the bond lengths of the metal-hydride bonds were determined to be similar in length with no trend based on the Gibbs free energy (ΔG_{H^-}). Similar to Nozaki's iridium species, *trans*-(HN(CH₂CH₂PⁱPr₂))IrH₃ (**1.38**) demonstrated high TONs and TOFs (Scheme 2.15).

Scheme 2.15. Iridium-pincer **1.38 catalyzed hydrogenation of CO₂**



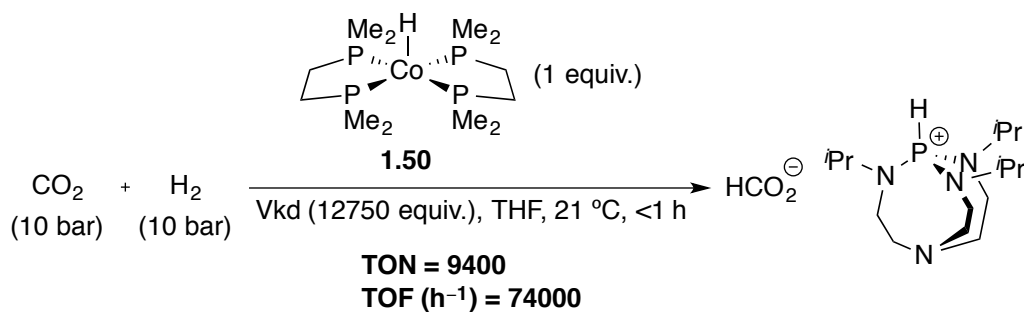
In 2011, Milstein and coworkers attempted to use these investigations to explore iron catalyzed hydrogenation reactions (Scheme 2.16).³⁴ It is hypothesized that the success of Milstein's iron-PNP pincer **1.47** is due to the *trans*-effect of the hydrides making the metal-hydride more nucleophilic compared to typical base-metal catalysts.

Scheme 2.16. Iron-PNP-pincer **1.47 catalyzed hydrogenation of CO₂**



In 2013, Linehan *et al.* reported on the hydrogenation of CO₂ catalyzed by cobalt-hydride species **1.50** (Scheme 2.17).^{35,43,44} Using thermodynamic parameters of hydricity (ΔG_{H^-}) and acidity (pK_a) as guides, the group designed a catalytic system that was extremely active for formic acid production.

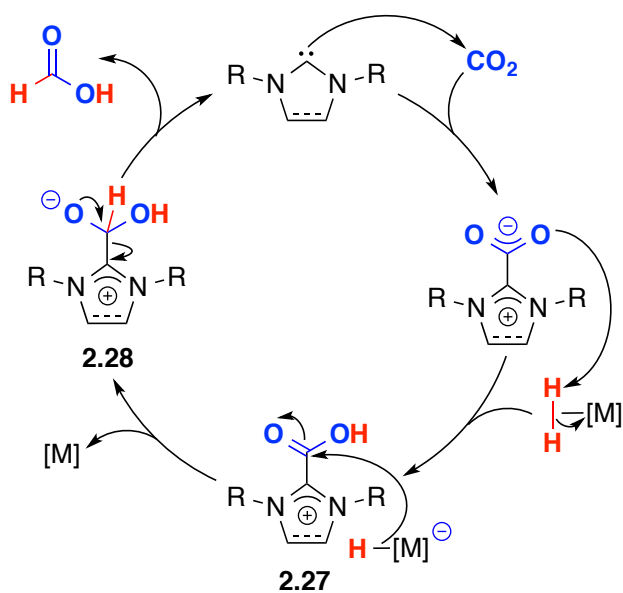
Scheme 2.17. Co(dmpe)₂H (1.50**) catalyzed hydrogenation of CO₂**



2.2.2 Approaches to Increase Reactivity of Carbon Dioxide

A complimentary approach is to activate carbon dioxide to make it more electrophilic, and therefore more prone to nucleophilic attack by a metal–hydride bond. Based on previous success with transition metals and FLPs, we hypothesized that a bifunctional catalyst system that incorporates a Lewis base and a transition metal would be well suited for the conversion of CO₂ to formic acid. Addition of an N-heterocyclic carbene and a transition metal under pressures of CO₂ and H₂ could facilitate the reduction of CO₂ to formic acid (Scheme 2.18).

Scheme 2.18. Proposed CO₂ hydrogenation catalyzed by a Lewis basic NHC and Lewis acidic transition metal

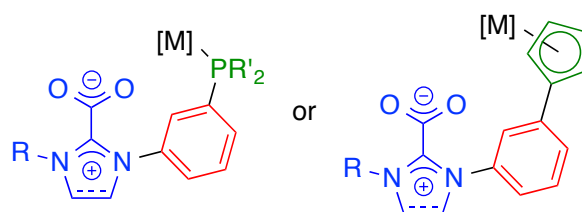


Based on the known reactivity of NHCs with CO₂, formation of a zwitterionic imidazolium or dihydroimidazolium carboxylate should be facile. Protonation of this species by addition of H₂ and a transition metal would form a carboxylic acid intermediate **2.27** that would be prone to nucleophilic attack. The formation of such a species is not unprecedented as Kuhn and coworkers demonstrated the synthesis of imidazolium carboxylic acid moiety **2.20** upon

addition of HCl to imidazolium carboxylate **2.19**.²¹ Delivery of a metal-hydride would form the tetrahedral intermediate **2.28**, which would then eliminate formic acid and regenerate the N-heterocyclic carbene. Again, formation of an intermediate such as **2.28** is not unprecedented as Zhang, Ying, and coworkers proposed the formation of tetrahedral intermediate **2.26**.³⁰ The formation of the carboxylic acid intermediate **2.27** should activate CO₂ and facilitate hydride insertion. Consequently, higher catalytic activity should be observed compared to reactions with free carbon dioxide.

A major challenge with this strategy is the strong tendency for N-heterocyclic carbenes to bind with transition metals. To overcome this hurdle, we have targeted bulky NHCs that will be less likely to interact with the sterically encumbered transition metal. Furthermore, the judicious design of a ligand containing a pendant N-heterocyclic carbene could prevent binding to the metal center (Figure 2.2). In addition to steric bulk around the periphery of the NHC, employing a rigid aryl spacer (with *ortho*-, *meta*-, or *para*-substitution) between the NHC and an ancillary group could provide precise control over the distance between the metal center and the NHC. The steric encumbrance and constrained geometry should discourage binding to the metal center while still allowing for activation of the relatively small carbon dioxide molecule.

Figure 2.2. Ligand design for the development of a bifunctional catalyst (blue = NHC for CO₂ activation with steric bulk, red = geometrically rigid spacer, green = ancillary group)



It is our view that combining the ability of transition metal complexes with the reactivity of N-heterocyclic carbenes offers exciting possibilities for exploration into new activation

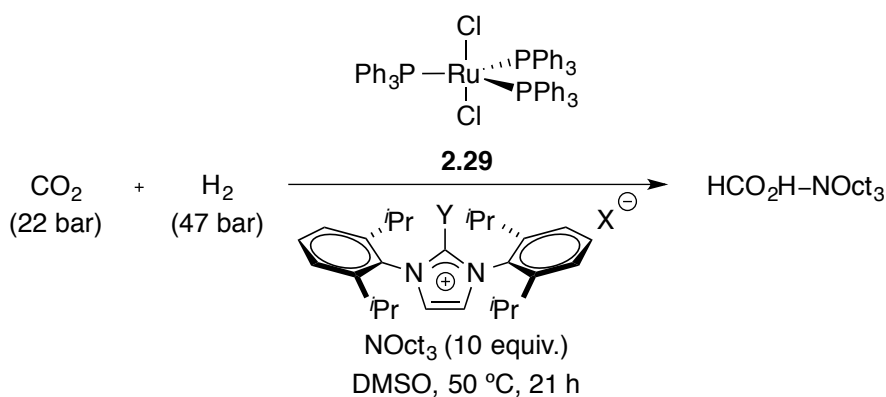
pathways. Although NHCs have been demonstrated to have moderate nucleophilicity but high Lewis and Brønsted basicity, their use as Brønsted bases remains limited. Several transesterification reactions using NHCs have been reported,⁴⁵⁻⁴⁷ in which the carbene species were believed to exhibit Brønsted base characteristics. Additionally, use of NHCs as Brønsted base catalysts for Michael addition reactions⁴⁸ or transformations of rearrangements of cyclopropyl enol esters have been explored recently.⁴⁹ We hypothesize that the addition of an NHC as a pendant Brønsted base on a transition metal catalyst could also provide enhanced production of formic acid. The generation of a bifunctional complex not only has the potential to be used in hydrogenation of CO₂, but also a variety of useful chemical transformations. The general concept of a Lewis acidic transition metal in close proximity with a Lewis base can be advantageous for the activation of other ubiquitous functional groups such as carbon monoxide, methane, alkenes, alkynes, aldehydes, and boranes.

2.3 Addition of Imidazolium, Dihydroimidazolium, Bicarbonate and Other Salts

2.3.1 Imidazolium and Dihydroimidazolium Salts

Initial investigations were focused on the addition of imidazolium salts to a transition metal system. Since base-metal catalysts often have low activity, we chose to investigate ruthenium catalysts that have demonstrated moderate activity in the past. First, we explored the effect of imidazolium salts on reactions catalyzed by $\text{RuCl}_2(\text{PPh}_3)_3$ (**2.29**) (Table 2.3).

Table 2.3. Addition of imidazolium salts to $\text{RuCl}_2(\text{PPh}_3)_3$ (2.29**)**



Entry	X	Y	TON ^a	Acid/Base ^b	Increase (%) ^c
1 ^d	N/A	N/A	55 (19)	5.5	N/A
2 ^{e,f}	Cl	H	65 (17)	6.5	18
3 ^{e,g}	HCO_3^-	H	110 (30)	11	100
4 ^e	N/A	CO_2	111 (26)	11	101

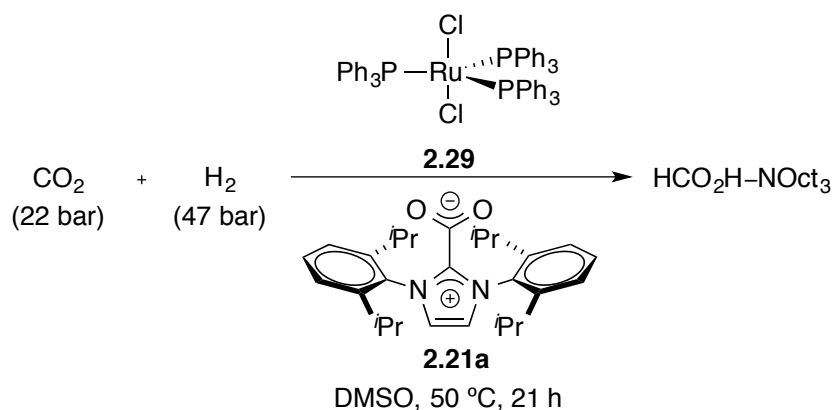
^aTON = (mol $\text{HCO}_2\text{H-NOct}_3$)/(mol cat.), represented as an average of at least three experiments with average errors in parentheses. ^bAcid/Base = (mol $\text{HCO}_2\text{H-NOct}_3$)/(mol NOct_3). ^cIncrease = $\{[\text{TON} - \text{TON}(\text{entry } 1)]/\text{TON}(\text{entry } 1)\} \times 100$. ^dNo additive. ^eAdditive:cat. = 5. ^f1,3-bis(2,6-diisopropylphenyl)imidazolium chloride (**2.30**). ^g1,3-bis(2,6-diisopropylphenyl)imidazolium bicarbonate (**2.31**).

Formic acid production was increased by 100% upon the addition of small quantities of 1,3-bis(2,6-diisopropylphenyl)imidazolium bicarbonate or carboxylate salts. No increase in activity

was observed with imidazolium chloride salts, indicating the presence of the bicarbonate or carboxylate is important.

Based on work done by Jessop and Noyori when studying $\text{RuH}_2(\text{PMe}_3)_4$ (**1.12**) catalyzed reactions,⁵⁰ the amount of base relative to the amount of formic acid produced is extremely important. This number is valuable because the presence of base is crucial for favorable thermodynamics. Jessop, Noyori, and coworkers determined that reactions with product/base ratios of around 1 were ideal. Under our conditions, product to base ratios were between 5 and 11 (Table 2.3, FA/Base). We then investigated the effect of the amount of base on the reaction (Table 2.4). Upon increasing the amount of base, larger amounts of formic acid were produced. Additionally, reactions with added 1,3-bis(2,6-diisopropylphenyl)imidazolium carboxylate salt **2.21a** demonstrated a 199% increase in formic acid production (entries 3 and 4).

Table 2.4. Effect of the amount of base on reactions catalyzed by $\text{RuCl}_2(\text{PPh}_3)_3$ (2.29**)**

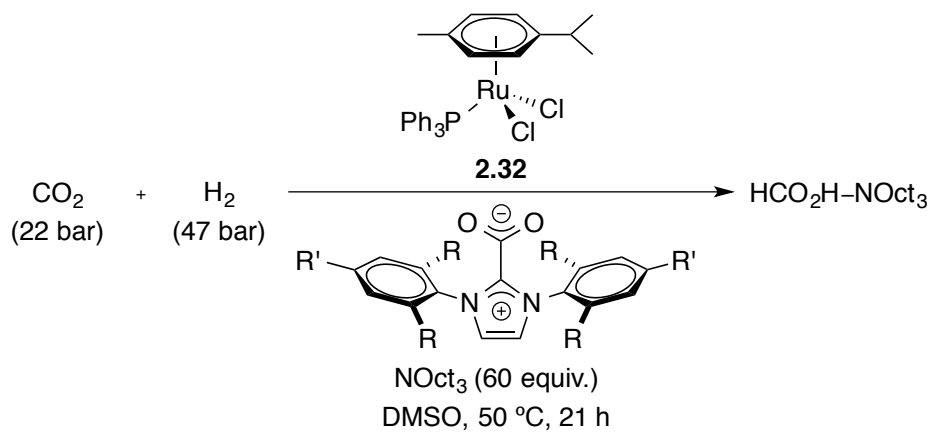


Entry	NOct ₃ Equiv.	TON ^a	TON (2.21a) ^b	Acid/Base ^c	Increase (%) ^d
1	60	69 (3)	123 (4)	2.1	78
2	200	73 (6)	218 (5)	1.1	199

^aTON = (mol HCO₂H-NOct₃)/(mol cat.), represented as an average of at least three experiments with average errors in parentheses. ^bTON with **2.21a**, **2.21a**:cat. = 5. ^cAcid/Base = (mol HCO₂H-NOct₃)/(mol NOct₃) in reactions with **2.21a**. ^dIncrease = {[TON(**2.21a**) - TON]/TON} x 100.

To investigate the generality of these results, CO₂ hydrogenation reactions were carried out using RuCl₂(*p*-cymene)(PPh₃) (**2.32**) in the presence and absence of imidazolium carboxylate salts (Table 2.5). Similar to results with RuCl₂(PPh₃)₃ (**2.29**), the addition of imidazolium carboxylate salts gave higher TONs as compared to reactions without any additives.

Table 2.5. Addition of imidazolium salts to RuCl₂(*p*-cymene)(PPh₃) (2.32**)**



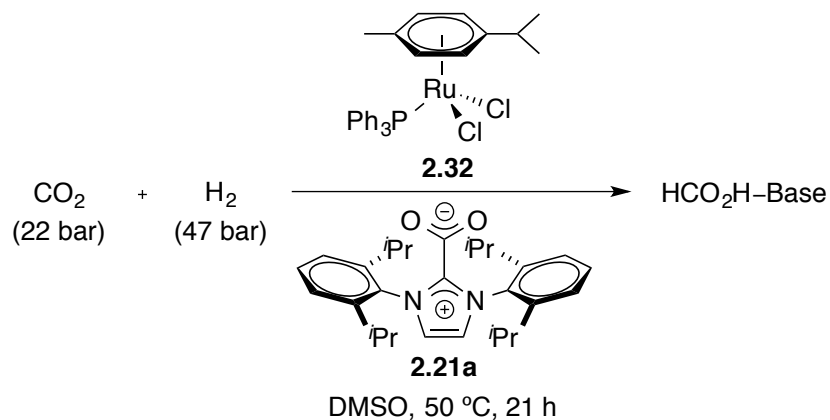
Entry	R	R'	TON ^a	Acid/Base ^b	Increase (%) ^c
1	N/A	N/A	26 (8)	0.4	N/A
2 ^d	ⁱ Pr	H	47 (12)	0.8	81
3 ^d	Me	Me	33 (3)	0.5	27

^aTON = (mol HCO₂H–NOct₃)/(mol cat.), represented as an average of at least three experiments with average errors in parentheses. ^bAcid/Base = (mol HCO₂H–NOct₃)/(mol NOct₃). ^cIncrease = {[TON – TON(entry 1)]/TON(entry 1)} x 100. ^dAdditive:cat. = 5.

Previous investigations into ruthenium-catalyzed hydrogenation of CO₂ discovered that the identity of the base was also extremely important. A base screen was done with 1,4-diazabicyclo[2.2.2]octane (DABCO), 4-(dimethylamino)pyridine (DMAP), TMEDA, tributylamine (NBu₃), and KOH (Table 2.6). The identity of the base affected the production of formic acid, however, neither the aqueous pK_a of the conjugate acid or the state (solid or liquid) of the base dictated whether the activity was high or low. All bases, except for KOH, demonstrated enhanced production of formic acid with the addition of imidazolium carboxylate

2.21a. Reactions utilizing NBu_3 as the base showed the highest TON and increase in TON from reactions without the presence of imidazolium carboxylate **2.21a**.

Table 2.6. Effect of base identity on the activity of $\text{RuCl}_2(p\text{-cymene})(\text{PPh}_3)$ (2.32**)**

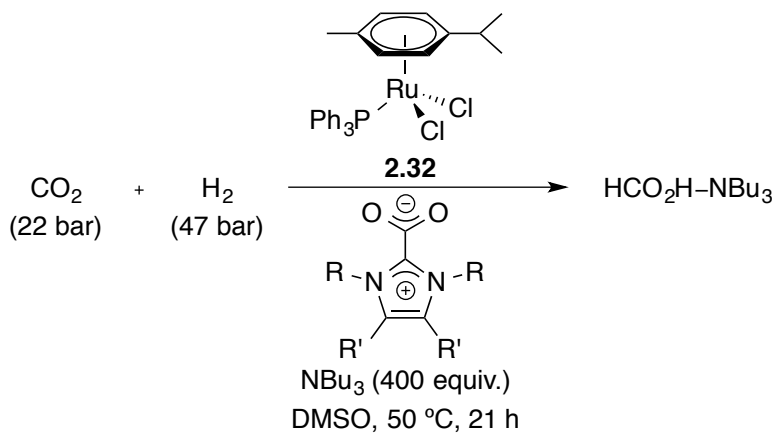


Entry	Base ^a	pK _a ^b	TON ^c	TON (2.21a) ^d	Increase (%) ^e
1	DABCO	3.0, 8.8	173 (18)	231 (7)	34
2	DMAP	9.2	0 (0)	10 (2)	N/A
3	TMEDA	7.4, 10.2	107 (14)	161 (11)	50
4	NBu_3	10.9	307 (45)	547 (60)	78
5	KOH	15.7	369 (33)	333 (100)	-9.8

^a400 equiv. ^bpK_a of the conjugate acid in H_2O . ^cTON = (mol $\text{HCO}_2\text{H-Base}$)/(mol cat.), represented as an average of at least three experiments with average errors in parentheses. ^dTON with **2.21a**, **2.21a**:cat. = 5. ^e{[TON(**2.21a**) – TON]/TON} x 100.

While initial results were obtained with 2,6-diisopropylphenyl or mesityl imidazolium salts, we wanted to investigate the structural dependence of the additive on the reactivity (Table 2.7). Although not all salts demonstrated the same increase, all did show some enhancement in the production of formic acid. Both sterically accessible (**2.21c**) and sterically hindered [1,3-bis(*tert*-butyl)imidazolium (**2.21d**)] salts demonstrated an increase in activity with no trend based on sterics. The mesityl-substituted salt **2.21a** was more active as compared to its dihydroimidazolium counterpart **2.22b**. This observation was not explored further, but the results do not seem to be based on electronics, as there was no trend based on the pK_a of the salt.

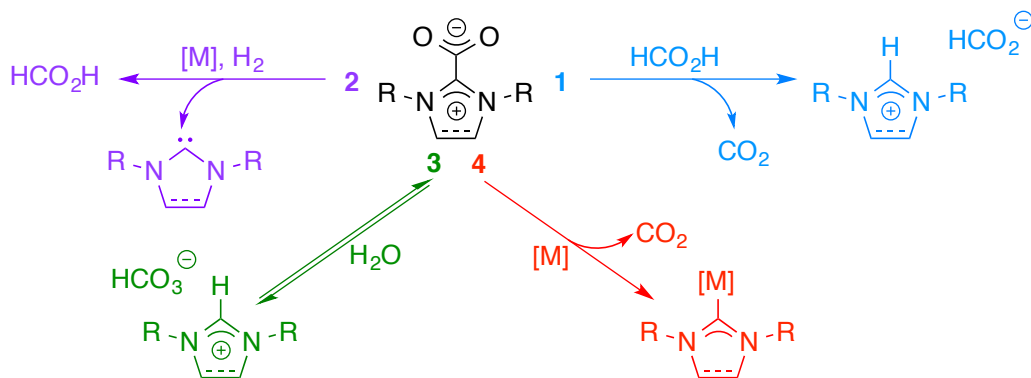
Table 2.7. Effect of the carboxylate structure on the reactivity of catalyst 2.32



Entry	R	R'	pK _a ^a	TON ^b	Increase (%) ^c
1	N/A	H	N/A	307 (45)	N/A
2 ^d	2,4,6-Me ₃ Ph	H	20.8	567 (108)	84
3 ^d	2,4,6-Me ₃ Ph	H ₂	21.3	349 (139)	14
4 ^d	Me	H	23.0	477 (60)	55
5 ^d	^t Bu	H	25.2	362 (44)	18

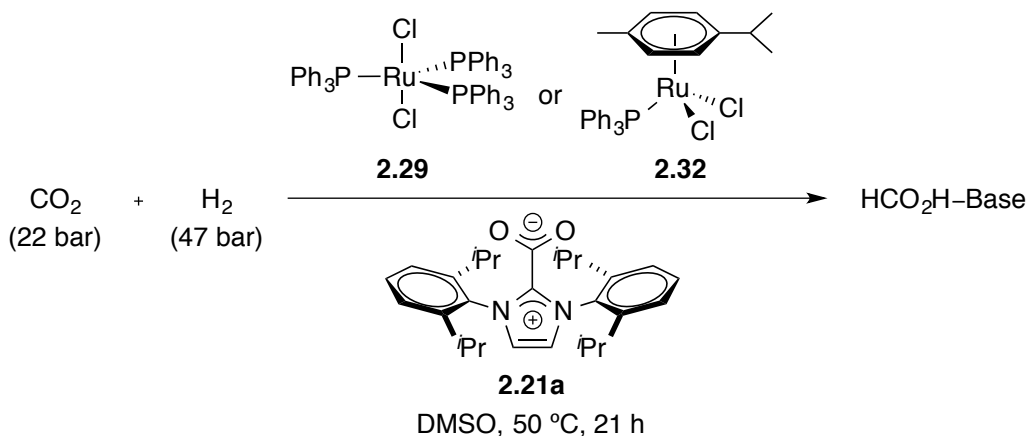
^apK_a of the conjugate acid in H₂O. ^bTON = (mol HCO₂H-NBU₃)/(mol cat.), represented as an average of at least three experiments with average errors in parentheses. ^c{[TON – TON(entry 1)]/TON(entry 1)} × 100. ^dAdditive:cat. = 5.

We hypothesized that the benefit of carboxylate salts could be due to at least four possible roles: (1) a Brønsted base by stabilizing formic acid; (2) a ligand for the transition metal; (3) a source of bicarbonate; (4) an activator to stabilize carbon dioxide.

Scheme 2.19. Possible roles of imidazolium carboxylates on the hydrogenation of CO₂

First, we investigated the ability for the imidazolium carboxylate to act as a Brønsted base. With $\text{RuCl}_2(\text{PPh}_3)_3$ (**2.29**) and $\text{RuCl}_2(p\text{-cymene})(\text{PPh}_3)$ (**2.32**), we compared the activity of reactions with exogenous base only, exogenous base and **2.21a**, and **2.21a** only (Table 2.8).

Table 2.8. Use of imidazolium carboxylate as a Brønsted base



Entry	Cat.	NOct ₃ Equiv.	2.21a Equiv.	TON ^a	Increase (%) ^b
1		60	0	69 (3)	N/A
2	2.29	60	5	123 (4)	78
3		0	65	227 (4)	229
4		60	0	26 (8)	N/A
5	2.32	60	5	47 (12)	81
6		0	65	114 (8)	338

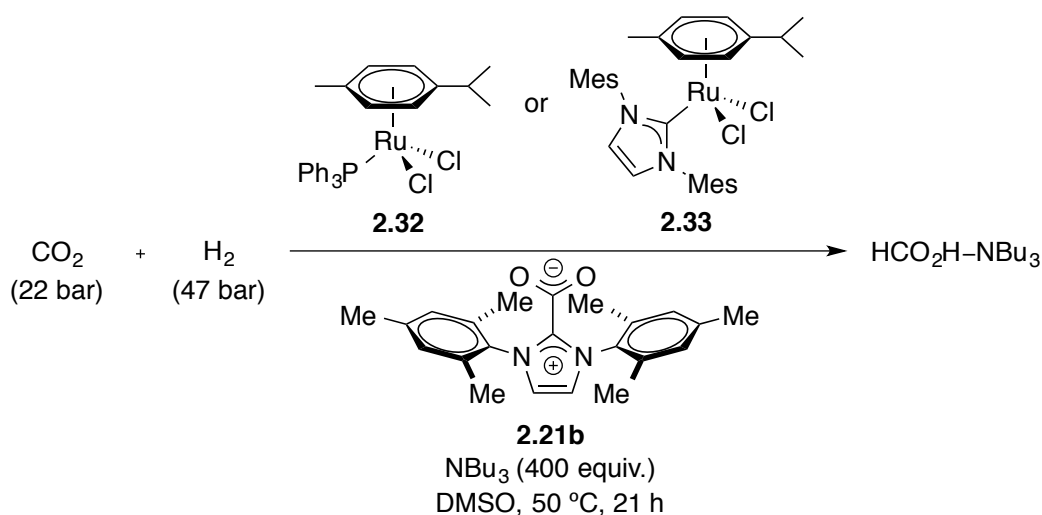
^aTON = (mol HCO₂H-NOct₃)/(mol cat.), represented as an average of at least three experiments with average errors in parentheses. ^bIncrease = {[TON – TON(no additive)]/TON(no additive)} x 100.

If imidazolium carboxylates cannot act as Brønsted bases, then reactions without exogenous base should give no activity. We would anticipate that if the carboxylate were acting solely as a Brønsted base, then reactions with 60 equiv. of NOct₃ / 5 equiv. of **2.21a** and reactions with only 65 equiv. of **2.21a** would give the same TON. The fact that reactions without any NOct₃ (entries 3 and 6) showed activity demonstrates that **2.21a** can act as a Brønsted base. However, since reactions with 60 equiv. of NOct₃ and 5 equiv. of **2.21a** and reactions with 65

equiv. of **2.21a** only gave different results, the imidazolium carboxylate is not acting solely as a Brønsted base.

Second, we explored the possibility that the addition of the imidazolium carboxylate could be facilitating the formation of a metal-NHC complex by synthesizing an N-heterocyclic carbene variant of RuCl₂(*p*-cymene)(PPh₃) (**2.32**), RuCl₂(*p*-cymene)(NHC) (**2.33**) (Table 2.9).⁵¹

Table 2.9. Use of imidazolium carboxylate as an ancillary ligand on ruthenium



Entry	Cat.	TON ^a	TON (2.21b) ^b	Increase (%) ^c
1	2.32	307 (45)	567 (108)	84
2	2.33	294 (67)	508 (1)	-4.2, ^d 65

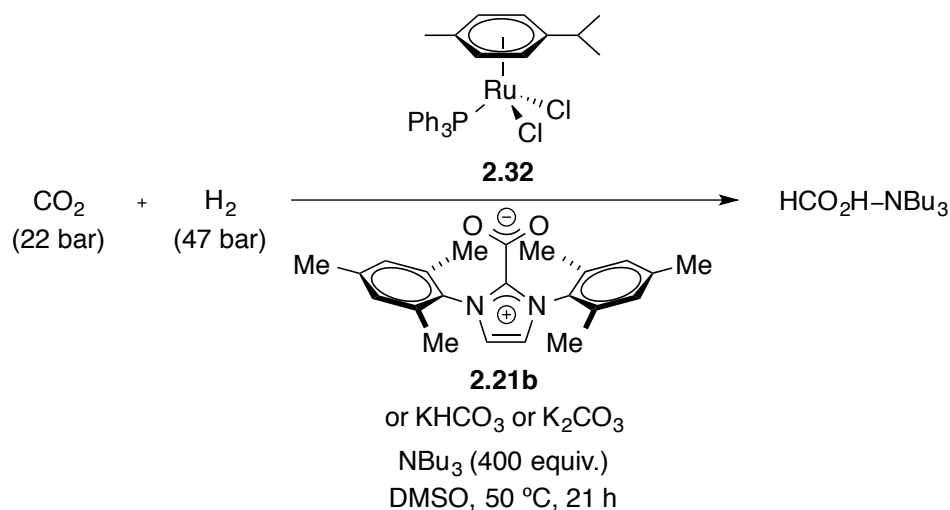
^aTON = (mol HCO₂H-NBu₃)/(mol cat.), represented as an average of at least three experiments with average errors in parentheses. ^bTON with **2.21b**, **2.21b**:cat. = 5. ^cIncrease = {[TON(**2.21b**) - TON]/TON} x 100. ^d{[TON(**2.32**) - TON(**2.33**)]/TON(**2.33**)} x 100.

If a ruthenium-NHC complex provided a similar increase in activity as adding the imidazolium carboxylate, then forming such a complex could possibly be providing the enhancement in reactivity. However, if the ruthenium-NHC complex demonstrates a different TON, then it is unlikely that such a complex is forming. The ruthenium-NHC **2.33** provides a similar activity to that of the complex **2.32** (entries 1 and 3). These results indicate that the addition of **2.21b** is not solely facilitating the formation of a metal-NHC complex. Further

support is the rate enhancement demonstrated with the addition of **2.21b** to RuCl₂(*p*-cymene)(NHC) (**2.33**). However, this does not rule out the possibility that the imidazolium carboxylate is facilitating the formation of a ruthenium-NHC and a supplementary role.

Third, we investigated the capability of the imidazolium carboxylate to act as a source of bicarbonate. It is known that, with the addition of water, imidazolium carboxylates are in equilibrium with their corresponding bicarbonates.⁵² If the addition of a different source of bicarbonate provides similar results, the imidazolium carboxylates could be acting as a source of bicarbonate (Table 2.10). The addition of potassium bicarbonate (KHCO₃) or potassium carbonate (K₂CO₃) provides a similar increase in TON. This indicates that the equilibrium between the imidazolium carboxylate and bicarbonate can provide a source of bicarbonate.

Table 2.10. Use of imidazolium carboxylate as a source of bicarbonate



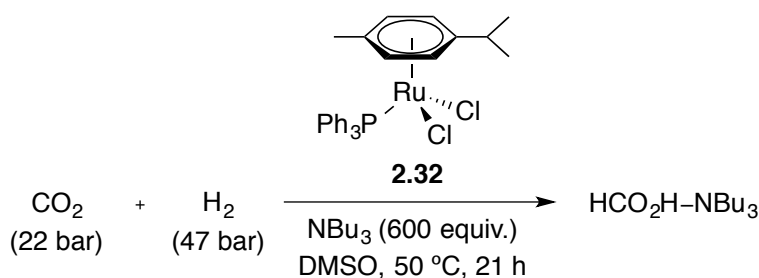
Entry	Additive	TON ^a	Increase (%) ^b
1	N/A	307 (45)	N/A
2 ^c	2.21b	567 (108)	84
3 ^c	KHCO ₃	577 (32)	87
4 ^c	K ₂ CO ₃	562 (53)	83

^aTON = (mol HCO₂H-NBu₃)/(mol cat.), represented as an average of at least three experiments with average errors in parentheses. ^bIncrease = {[TON – TON(entry 1)]/TON(entry 1)} x 100. ^cAdditive:cat. = 5.

2.3.2 Bicarbonate and Other Inorganic Salts

We discovered that formic acid production increased by 84% upon the addition of small quantities of KHCO_3 to reactions catalyzed by $\text{RuCl}_2(p\text{-cymene})(\text{PPh}_3)$ (**2.32**) (Table 2.11) with 600 equivalence of exogenous base.⁵³ Productivity could be further increased by up to 140% with the addition of more KHCO_3 (entries 3 and 4).

Table 2.11. $\text{RuCl}_2(p\text{-cymene})(\text{PPh}_3)$ (**2.32**) catalyzed hydrogenation promoted by KHCO_3

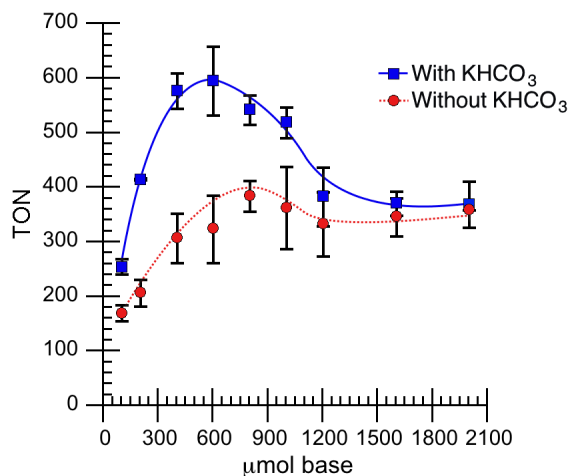


Entry	Additive	KHCO_3 :cat ratio	TON ^a	Increase (%) ^b
1	N/A	N/A	324 (48)	N/A
2	KHCO_3	5	595 (63)	84
3	KHCO_3	50	674 (24)	108
4	KHCO_3	100	779 (52)	140

^aTON = (mol $\text{HCO}_2\text{H-NBu}_3$)/(mol cat.), represented as an average of at least three experiments with average errors in parentheses. ^b{[TON – TON(entry 1)]/TON(entry 1)} x 100.

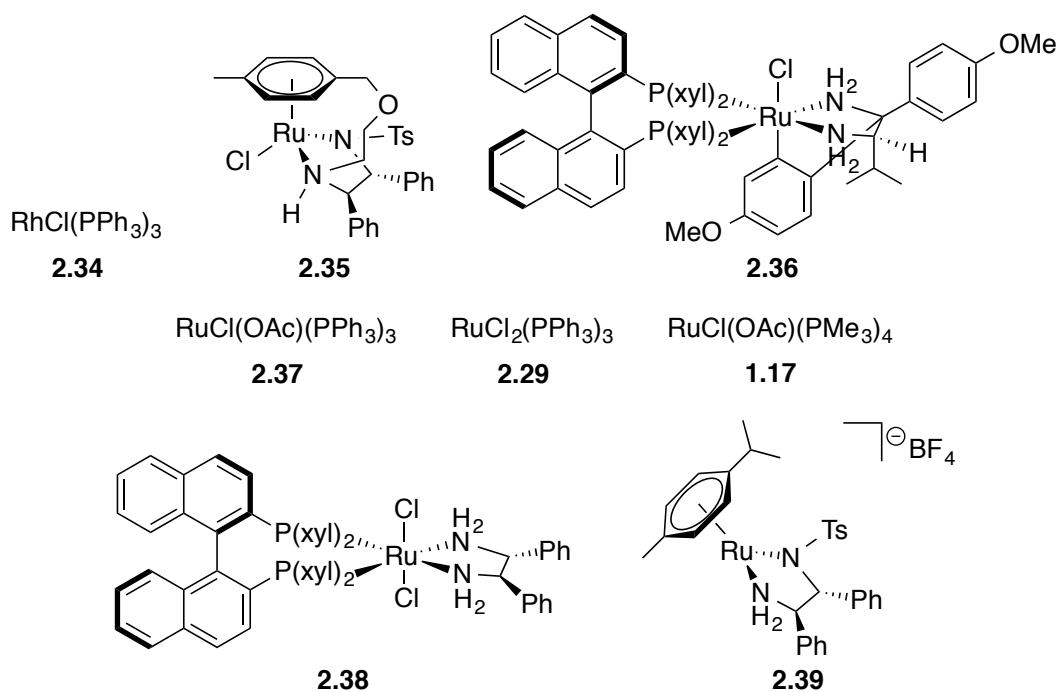
Cognizant of the known sensitivity for CO_2 hydrogenation to base concentration,⁵⁰ we carried out reactions at various tributylamine concentrations in the presence and absence of the KHCO_3 additive. As expected, the activity of the catalytic system was optimal at intermediate base concentrations for reactions run in the presence and absence of KHCO_3 (Figure 2.3). Interestingly, the effect of the added KHCO_3 was more pronounced at an optimal tributylamine concentration.

Figure 2.3. Sensitivity of CO₂ hydrogenations to NBu₃ concentration. Reaction conditions are defined in Table 2.11 where KHCO₃:cat. ratio = 5. Error bars represent average errors. Trend lines shown are a guide for the eye only.



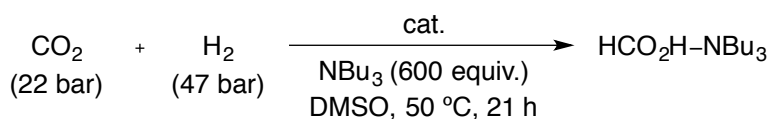
To investigate the generality of the phenomenon, reactions were carried out using a variety of known catalysts in the presence and absence of KHCO₃ (Figure 2.4, Table 2.12).

Figure 2.4. Noble-metal catalysts used for hydrogenation of CO₂



Under our initial conditions, six of nine noble-metal complexes demonstrated at least a 31% and up to a 510% increase in productivity with the addition of KHCO_3 . Two catalysts showed no beneficial effect (entries 6 and 7), and only one showed a substantial decrease in activity (entry 8). Although $\text{RuCl}(\text{OAc})(\text{PMe}_3)_4$ (**1.17**) demonstrated no increase in productivity, the remarkable activity of this catalyst may have masked the beneficial effect of the additive due to the predominance of formic acid decomposition that occurs when formic acid is produced in excess of added base ($\text{HCO}_2\text{H}/\text{NBu}_3 = 2.4$).⁵⁴ The productivity is lower in comparison to the reported value due to differences in solvent and pressure. This explanation does not account for **2.38** and **2.39**, which show no beneficial effect or decrease in activity upon addition of KHCO_3 . We currently have no explanation for these outliers, but it is not associated with the fact that these catalysts proceed by an “outer sphere” rather than an “inner sphere” hydrogenation mechanism; otherwise, catalysts **2.35** and **2.36** would not show enhanced productivity upon addition of KHCO_3 (entries 2 and 3).

Table 2.12. Noble-metal catalyzed hydrogenation of CO_2 in the presence and absence of KHCO_3

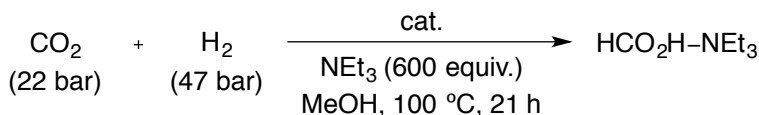


Entry	Cat.	TON ^a	TON (KHCO_3) ^b	Increase (%) ^c
1	2.34	9 (1)	55 (7)	510
2	2.35	130 (13)	260 (30)	100
3	2.36	286 (23)	475 (65)	66
4	2.37	561 (32)	804 (75)	43
5	2.29	386 (8)	505 (22)	31
6	1.17	1332 (88)	1430 (206)	7
7	2.38	692 (53)	634 (78)	-8
8	2.39	419 (19)	165 (16)	-61

^aTON = (mol $\text{HCO}_2\text{H-NBu}_3$)/(mol cat.), represented as an average of at least three experiments with average errors in parentheses. ^bTON with KHCO_3 , KHCO_3 :cat ratio = 5. ^cIncrease = $\{[\text{TON}(\text{KHCO}_3) - \text{TON}]/\text{TON}\} \times 100$.

We next explored an iron CO₂ hydrogenation catalyst reported by Beller and coworkers, Fe(BF₄)₂·6H₂O/alkyl-PP₃ (**1.40**)⁵⁵ (Table 2.13). Utilizing conditions similar to those described in the original report, reactions with **1.40** demonstrated a minimal increase in activity with the addition of KHCO₃ (entry 1). No reaction was observed under the conditions in Table 2.12. However, reactions catalyzed by FeCl₂/alkyl-PP₃ showed an 80% increase in formic acid production with the addition of KHCO₃ (entry 2). The productivity is lower than reported due to the increased concentration of NEt₃ required to achieve reproducible results.

Table 2.13. Iron catalyzed hydrogenation of CO₂ in the presence and absence of KHCO₃

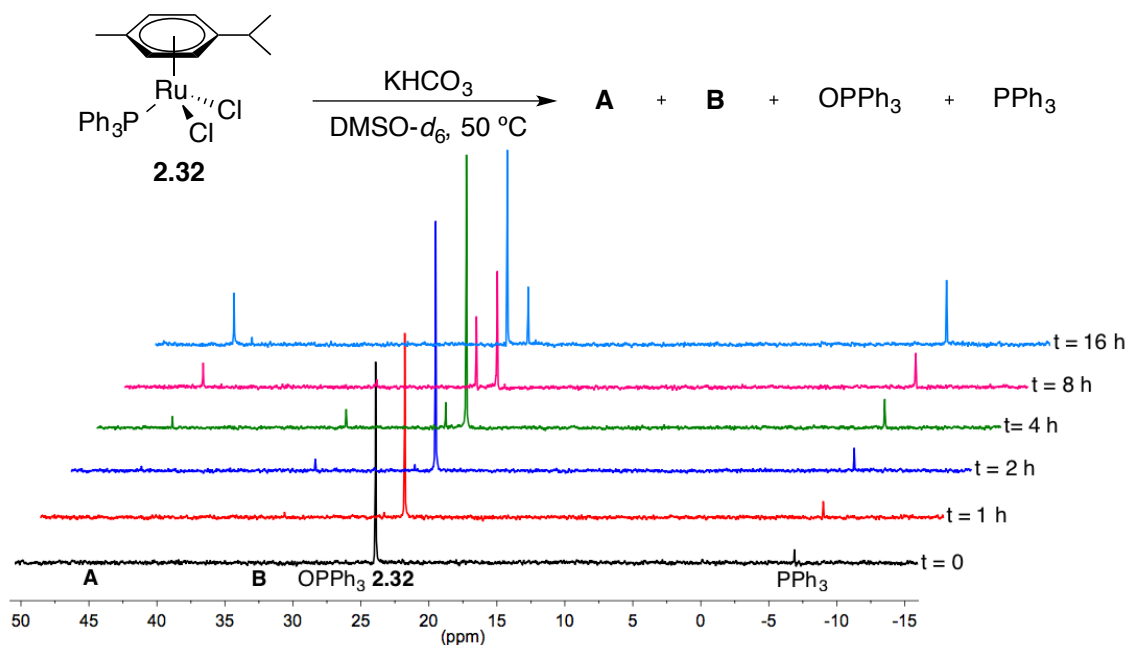


Entry	Cat.	TON ^a	TON (KHCO ₃) ^b	Increase (%) ^c
1	Fe(BF ₄) ₂ /alkyl-PP ₃ (1.40)	124 (5)	187 (58)	51
2	FeCl ₂ /alkyl-PP ₃	142 (8)	256 (60)	80

^aTON = (mol HCO₂H-NEt₃)/(mol cat.), represented as an average of at least three experiments with average errors in parentheses. ^bTON with KHCO₃, KHCO₃:cat ratio = 5. ^cIncrease = {[TON(KHCO₃) – TON]/TON} x 100.

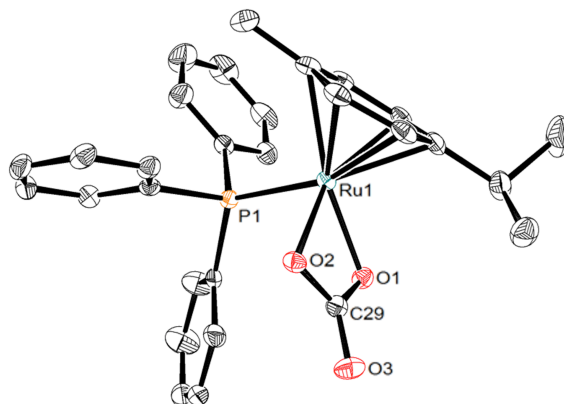
In order to gain some mechanistic understanding, stoichiometric reactions were conducted between RuCl₂(*p*-cymene)(PPh₃) (**2.32**) and KHCO₃ under 1 bar of CO₂ in DMSO-*d*₆ at 50 °C. The progress of these reactions was monitored by ¹H and ³¹P NMR spectroscopy. Analysis of the ³¹P NMR spectrum of the mixture after 16 h indicated the presence of PPh₃, OPPh₃, and two new species with resonances at +33 ppm and +45 ppm (Figure 2.5). In the ¹H NMR spectrum, free *p*-cymene and a new ruthenium species containing bound *p*-cymene were observed.

Figure 2.5. Time course of the stoichiometric ^{31}P experiment of $\text{RuCl}_2(p\text{-cymene})(\text{PPh}_3)$ (**2.32**) and KHCO_3 in $\text{DMSO-}d_6$ at $50\text{ }^\circ\text{C}$ under 1 bar CO_2



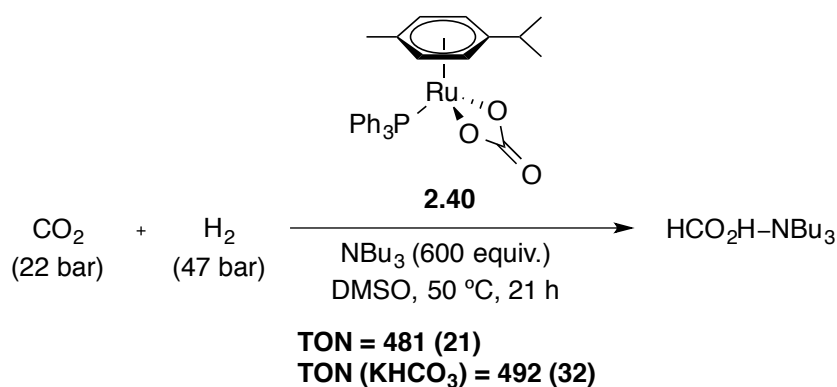
We speculated that the new complexes being formed were ruthenium complexes containing bicarbonate or carbonate as ligands. To verify this hypothesis $\text{Ru}(\kappa^2\text{-O}_2\text{CO})(\text{PPh}_3)(p\text{-cymene})$ (**2.40**) was independently synthesized⁵⁶ and crystals suitable for X-ray crystallography were obtained (Figure 2.6).

Figure 2.6. Crystal structure of $\text{Ru}(\kappa^2\text{-O}_2\text{CO})(\text{PPh}_3)(p\text{-cymene})$ (**2.40**) with thermal ellipsoids represented at the 50% probability level



The ^{31}P NMR spectrum of **2.40** shows a peak at +33 ppm, which is the same shift as one of the two species formed during the reaction between **2.32** and KHCO_3 . To test its catalytic competency, **2.40** was subjected to our standard hydrogenation conditions (Scheme 2.20). Compared to ruthenium-dichloride complex **2.32** (Table 2.11, entries 1 and 2), **2.40** demonstrated a similar activity to what was observed upon the addition of KHCO_3 to **2.32**.

Scheme 2.20. Activity of $\text{Ru}(\kappa^2\text{-O}_2\text{CO})(\text{PPh}_3)(p\text{-cymene})$ (2.40**) for CO_2 hydrogenation**



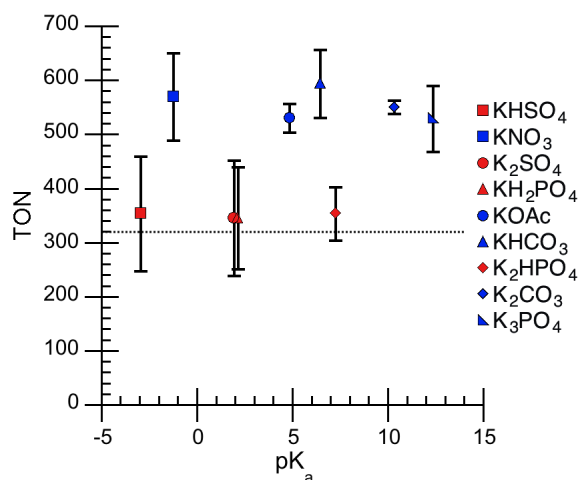
Importantly, no further increase in activity was observed upon addition of additional KHCO_3 . These results suggest that a critical role of the bicarbonate additive is to form complexes similar to **2.40**, which are superior catalysts compared to the dichloride complexes commonly used as CO_2 hydrogenation catalysts.

While several researchers have speculated about the importance of ruthenium bicarbonate or carbonate species for CO_2 hydrogenation,^{57, 58} discrete carbonate complexes had never before been examined as catalysts for CO_2 hydrogenation. However, Noyori, Jessop, and coworkers disclosed that replacing a chloride with an acetate led to increased activity for $\text{RuCl}(\text{OAc})(\text{PMe}_3)_4$ (**1.17**) compared to $\text{RuCl}_2(\text{PMe}_3)_4$ (**1.13**).⁵⁰ In a subsequent report, Jessop concluded that the increased activity observed for **1.17** was due to the complex's ability to more readily form $[\text{RuH}(\text{PMe}_3)_4]^+$ (**1.18**) via the intramolecular deprotonation of $[\text{Ru}(\eta^2\text{-H}_2)(\text{OAc})(\text{PMe}_3)_4]^+$ (**1.20**)

by acetate (Chapter 1, Scheme 1.5).⁵⁹ We hypothesized that the bicarbonate additives disclosed herein serve a similar role as does acetate in **1.17**.

To test this hypothesis, we carried out hydrogenation reactions catalyzed by **2.32** in the presence of various inorganic salts capable of binding in the κ^2 -coordination mode and whose conjugate acids span a wide pK_a range (Figure 2.7).

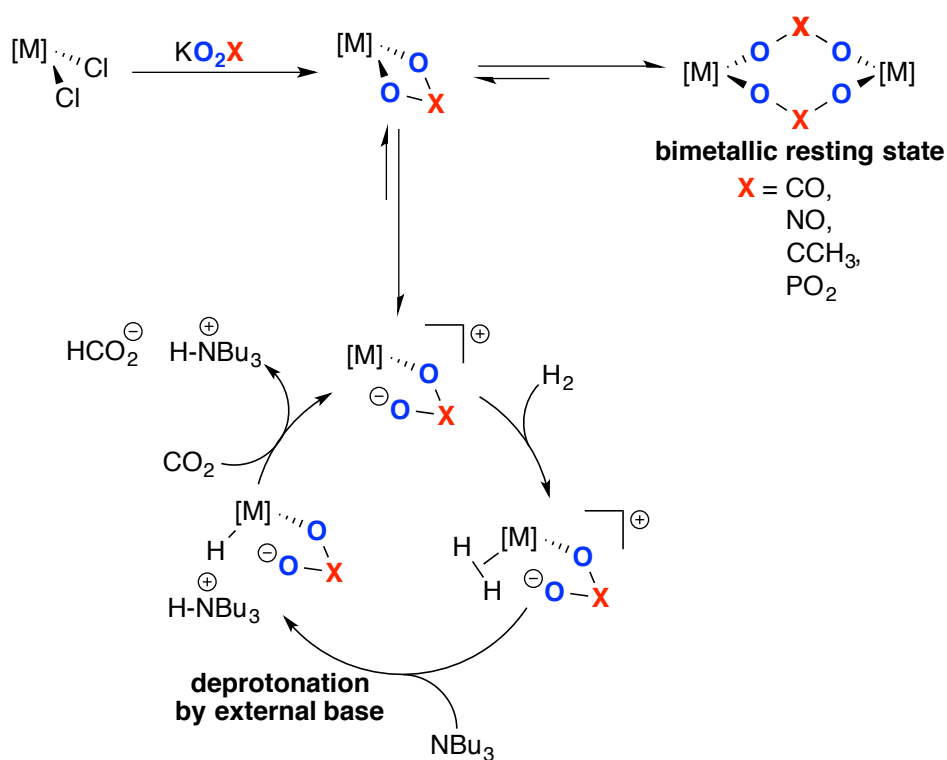
Figure 2.7. Hydrogenation of CO₂ with addition of various inorganic salts. Reaction conditions defined in Table 2.11 where additive:cat. ratio = 5. Error bars represent average errors. (Dotted line = TON without additive)



If the additive serves as an internal base, we reasoned that the productivity of the reaction would depend on the pK_a of the additive. These experiments revealed no trend between productivity and the aqueous pK_a of the additive. For example, KNO₃ was one of the most effective additives for the reaction despite nitrate being significantly less basic than bicarbonate. While many additives resulted in increased activity, some such as sulfates and phosphates demonstrated no improvement. Interestingly, when the additive demonstrated a beneficial effect, the increased productivity occurred at about the same level. This observation further demonstrates that the role of the additive is unrelated to its electronic properties.

Based on these observations, we hypothesize that the role of the additive is related to its structure. One possibility is that the additive prevents decomposition by bridging two metal atoms thereby forming a bimetallic resting state (Scheme 2.21). Jessop and coworkers observed similar dimeric species to be stable and catalytically competent during their mechanistic investigations into the hydrogenation of CO₂ catalyzed by RuCl(OAc)(PMe₃)₄ (**1.17**).⁵⁹

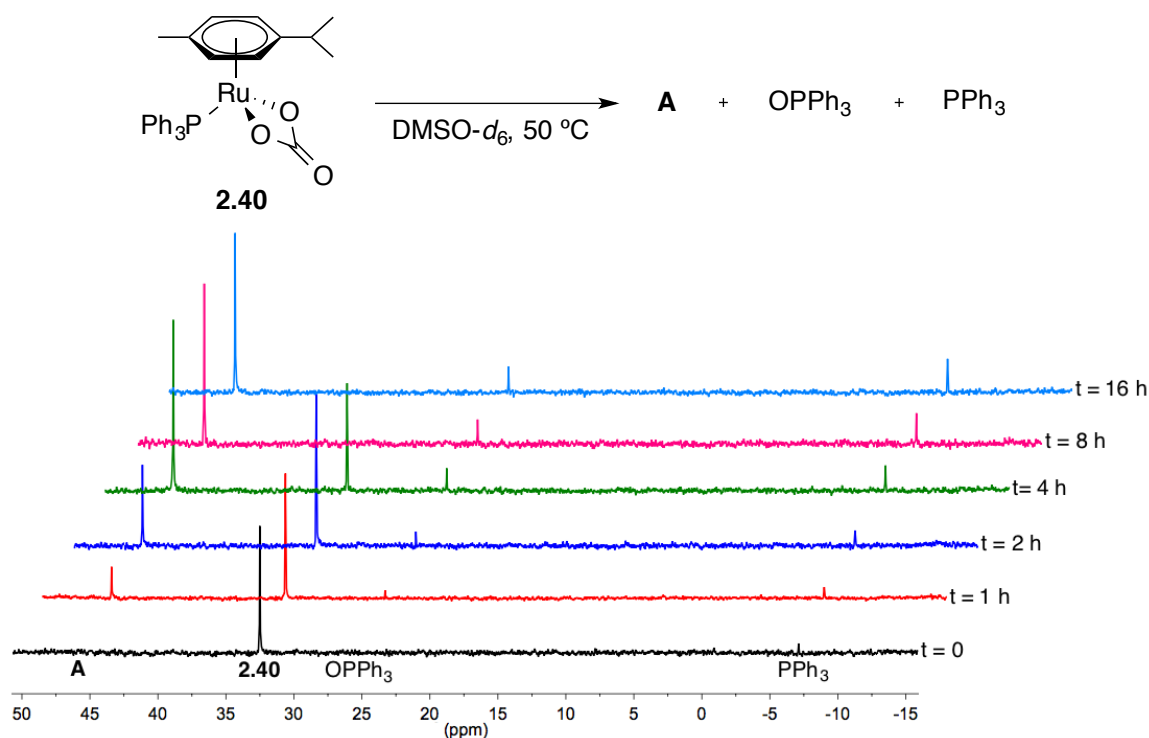
Scheme 2.21. Mechanistic proposal for the role of additives in the hydrogenation of CO₂



Consistent with this possibility was the species observed during the stoichiometric reactions between **2.32** and KHCO₃ with a resonance at +45 ppm in the ³¹P NMR spectrum. This species was also observed as the exclusive product when **2.40** was exposed to DMSO-*d*₆ at 50 °C under one bar of CO₂, and was accompanied by free *p*-cymene observed in the ¹H NMR spectrum (Figure 2.8). These data suggest that the species is a DMSO adduct containing PPh₃ and

carbonate ligands, which was not observed in the absence of KHCO_3 . Although attempts to definitively identify this species have been unsuccessful, one possibility is that it is a bimetallic complex containing bridging carbonate ligands.

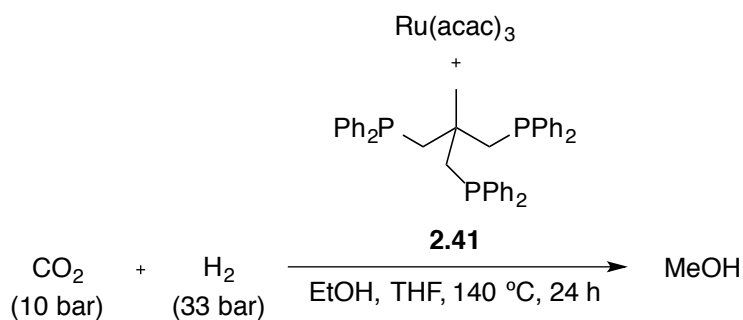
Figure 2.8. Time course of the ^{31}P NMR of $\text{Ru}(\kappa^2\text{-O}_2\text{CO})(\text{PPh}_3)(p\text{-cymene})$ (**2.40**) in $\text{DMSO-}d_6$ at 50°C under 1 bar CO_2



To investigate the importance of our findings, we explored a ruthenium CO_2 hydrogenation catalyst reported by Leitner and coworkers, $\text{Ru}(\text{acac})_3/\text{triphos-2}$ (**2.41**; triphos-2 = 1,1,1-tris(diphenylphosphinomethyl)ethane) (Table 2.14), which is one of the most active homogenous catalyst for methanol production.⁶⁰ Utilizing conditions similar to those described in the original report, reactions with **2.41** demonstrated a decrease in activity with addition of KHCO_3 (entries 2 and 3). However, without the presence of acid (determined by the addition of MeSO_3K instead of MeSO_3H), the activity of **2.41** is much lower (entries 1, 2 and 5). Without acid, the addition of

KHCO_3 increased the activity of **2.41** by 110% (entries 1 and 4), which is consistent with the increased activity demonstrated for catalytic systems producing formic acid.

Table 2.14. Ruthenium catalyzed hydrogenation of CO_2 to methanol



Entry	Additive(s)	TON ^a	Increase (%) ^b
1	N/A	10	N/A
2 ^c	MeSO_3H	50	400
3 ^{c,d}	$\text{MeSO}_3\text{H} / \text{KHCO}_3$	29	190
4 ^d	KHCO_3	21	110
5 ^c	MeSO_3K	6	-40

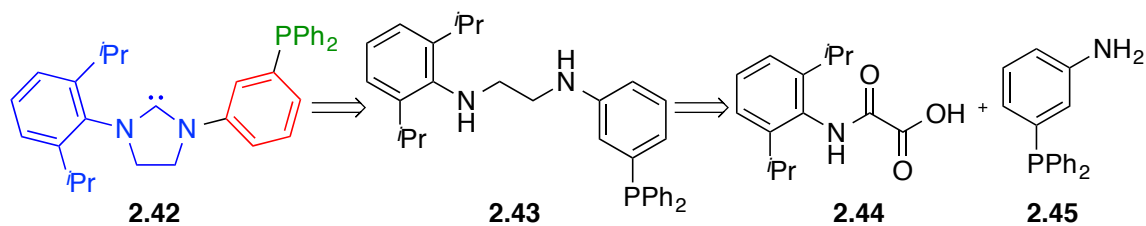
^aTON = (mol MeOH)/(mol cat.). ^bIncrease = $\{[\text{TON} - \text{TON}(\text{entry 1})]/\text{TON}(\text{entry 1})\} \times 100$. ^c $\text{MeSO}_3\text{H}(\text{K})$:cat. = 1.5. ^d KHCO_3 :cat. = 5.

2.4 Synthesis and Activity of a Ruthenium Complex Bearing a Pendant Dihydroimidazolium Salt

2.4.1 Design, Synthesis, and Characterization

We hypothesized that the development of a judiciously designed transition metal complex containing a pendant N-heterocyclic carbene could facilitate the reduction of CO₂ to formic acid. A major challenge with this strategy is the strong tendency for N-heterocyclic carbenes to bind with transition metals. To overcome this hurdle, we have targeted a bulky NHC and rigid aryl spacer with tunable substitution between the NHC and the ancillary phosphine group. The steric encumbrance and constrained geometry should discourage binding to the metal center while still allowing for activation of the relatively small carbon dioxide molecule. A concise and generalized route to the desired N-heterocyclic carbene ligand **2.42** is outlined in Scheme 2.22. Based on the findings of Grubb and coworkers,⁶¹ we envisioned access to the N-heterocyclic carbene ligand **2.42** by cyclization of the dissymmetrically substituted ethylene diamine **2.43**. We plan to form diamine **2.43** through the combination of oxo-acetic acid **2.44** and 3-(diphenylphosphino)aniline (**2.45**).

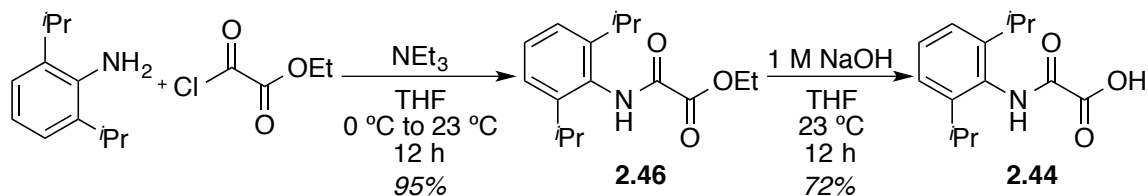
Scheme 2.22. Proposed retrosynthesis for the N-heterocyclic carbene ligand 2.42



The forward synthesis commenced with production of the oxo-acetic acid substrate **2.44** from commercially available starting materials (Scheme 2.23). Addition of chlorooxoacetate to a

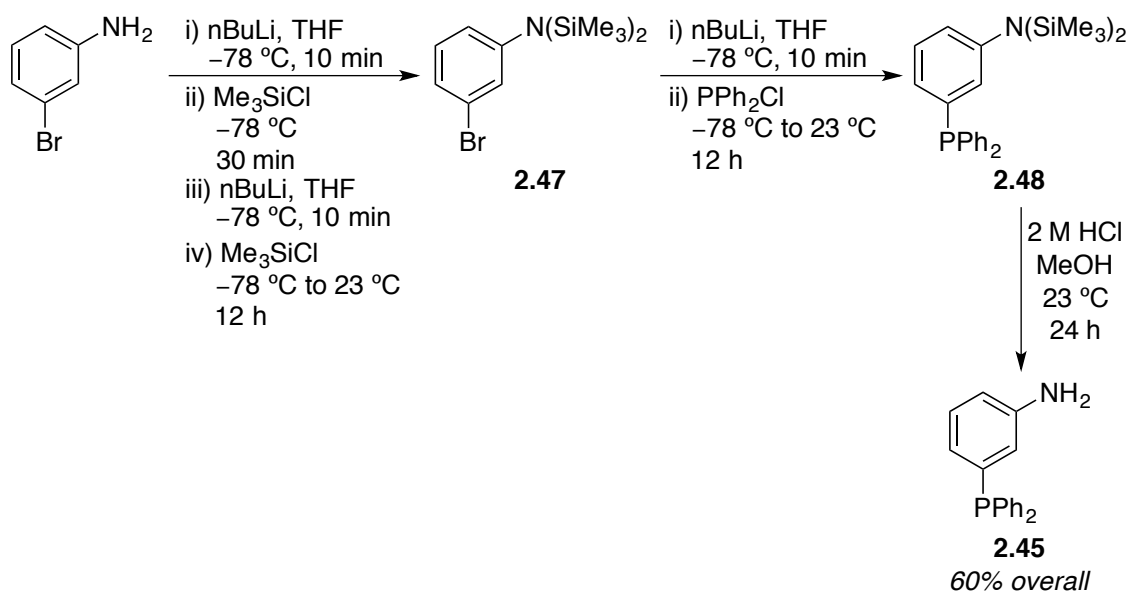
solution of 2,6-diisopropylaniline and NEt_3 gave the oxo-acetate **2.46** in a 95% yield, which was used without further purification. The oxo-acetic acid substrate **2.44** was isolated after the addition of 1 M sodium hydroxide to oxo-acetate **2.46** in a 72% yield.

Scheme 2.23. Synthesis of oxo-acetic acid substrate 2.44



The synthesis of 3-(diphenylphosphino)aniline **2.45** was achieved after slight modifications to a known literature procedure (Scheme 2.24).⁶² Addition of one equivalent of *n*-butyl lithium (*n*BuLi) followed by one equivalent of chlorotrimethylsilane to 3-bromoaniline at $-78\text{ }^\circ\text{C}$ gave the mono-trimethylsilyl (TMS) protected aniline.

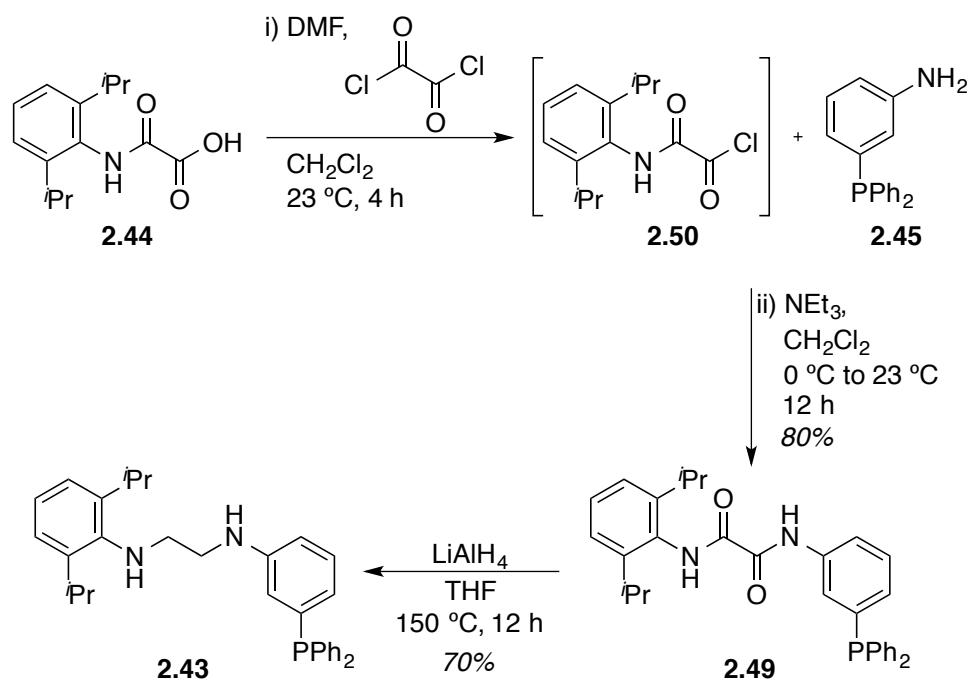
Scheme 2.24. Synthesis of 3-(diphenylphosphino)aniline 2.45



After addition of a second equivalent of each, TMS protected aniline **2.47** was isolated and used without further purification. The use of subsequent one equivalent additions was necessary to avoid lithium-halogen exchange of the aryl-bromine bond. Also important for the same reason were the short reaction times in steps (i) and (iii). At $-78\text{ }^{\circ}\text{C}$, TMS protected aniline **2.47** was treated with *n*BuLi followed by chlorodiphenylphosphine to generate diphenylphosphino TMS protected aniline **2.48**. The desired 3-(diphenylphosphino)aniline **2.45** was isolated by treatment of **2.48** with 2 M hydrochloric acid in 60% 3-step yield after flash chromatography in 10% ethyl acetate in hexanes.

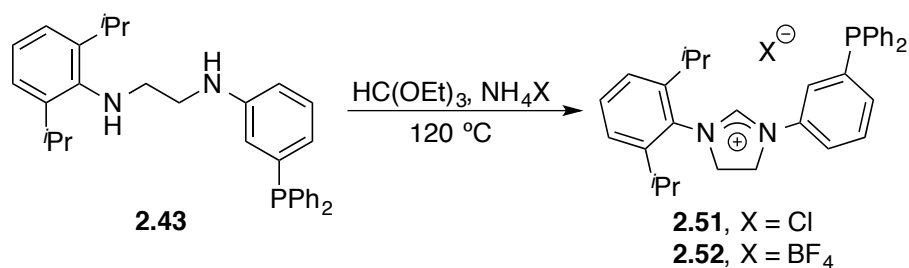
The synthesis of the diamine **2.43** was achieved over two steps (Scheme 2.25). First, intermediate **2.49** was generated by *in situ* formation of acid chloride **2.50** by addition of oxalyl chloride and dimethylformamide (DMF) to oxo-acetic acid **2.44**. Addition of 3-(diphenylphosphino)aniline **2.45** in CH_2Cl_2 followed by NEt_3 gave oxalamide **2.49**. It was necessary to add triethylamine after the addition of **2.45** to achieve reproducible results.

Scheme 2.25. Synthesis of the dissymmetrically substituted ethylene diamine **2.43**



Diamine **2.43** was synthesized upon treating a solution of oxalamide **2.49** in THF with lithium aluminum hydride at 150 °C in a pressure vessel. Reactions at lower temperatures demonstrated reduction of only one of the two amides to the corresponding amine. Cyclization of the dissymmetrically substituted ethylene diamine **2.43** with triethylorthoformate and an ammonium salt generated a dihydroimidazolium salt (Table 2.15). Reactions after 1 hour, utilizing ammonium tetrafluoroborate salts, provided pure material in high yields. Dihydroimidazolium salts **2.51** and **2.52** are sensitive to acid under ambient conditions as they often generate phosphine oxide products; therefore, all reactions under acidic conditions require usage of air and moisture free techniques.

Table 2.15. Synthesis of dissymmetrically substituted dihydroimidazolium salts 2.51 and 2.52

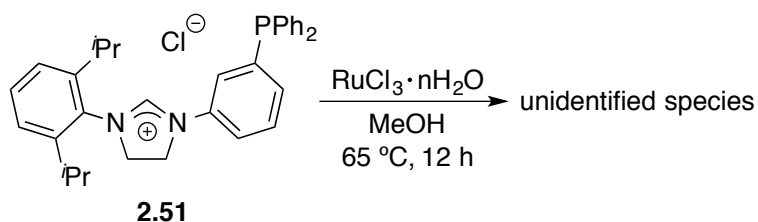


Entry	X	Time (h)	Yield
1	Cl	12	33
2	Cl	1	54
3	BF ₄	1	69

The first attempt to synthesize transition metal complexes bearing a pendant dihydroimidazolium salt ligand **2.51** utilized $\text{RuCl}_3 \cdot n\text{H}_2\text{O}$ in an analogous fashion to the synthesis of $\text{RuCl}_2(\text{PPh}_3)_3$ (**2.29**) (Scheme 2.26). Based on analysis of the ^1H NMR spectrum of the reaction mixture, the diagnostic dihydroimidazolium peak at 11.6 ppm disappeared and a new dihydroimidazolium peak at 11.1 ppm appeared. The ^{31}P NMR spectrum showed a change in the chemical shift from -5.2 ppm to $+28.5$ ppm, which is common for metal bound phosphines.

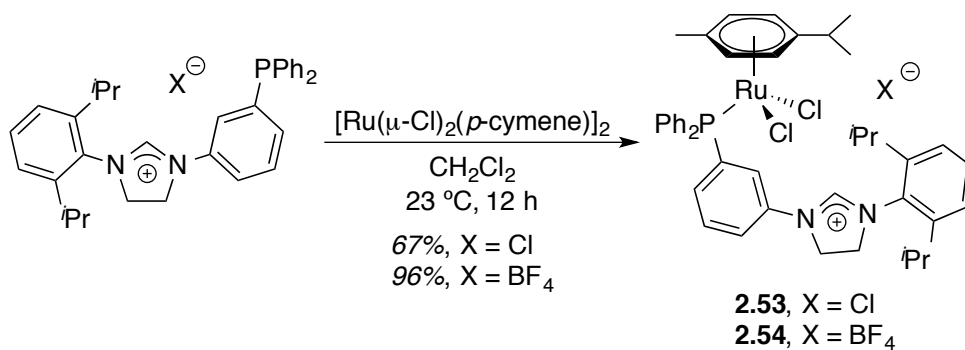
Although it seemed like a new ruthenium complex was formed, further characterization proved difficult because the complex was extremely insoluble in most solvents.

Scheme 2.26. Synthesis of a ruthenium complex bearing a pendant dihydroimidazolium ligand from $\text{RuCl}_3 \cdot n\text{H}_2\text{O}$



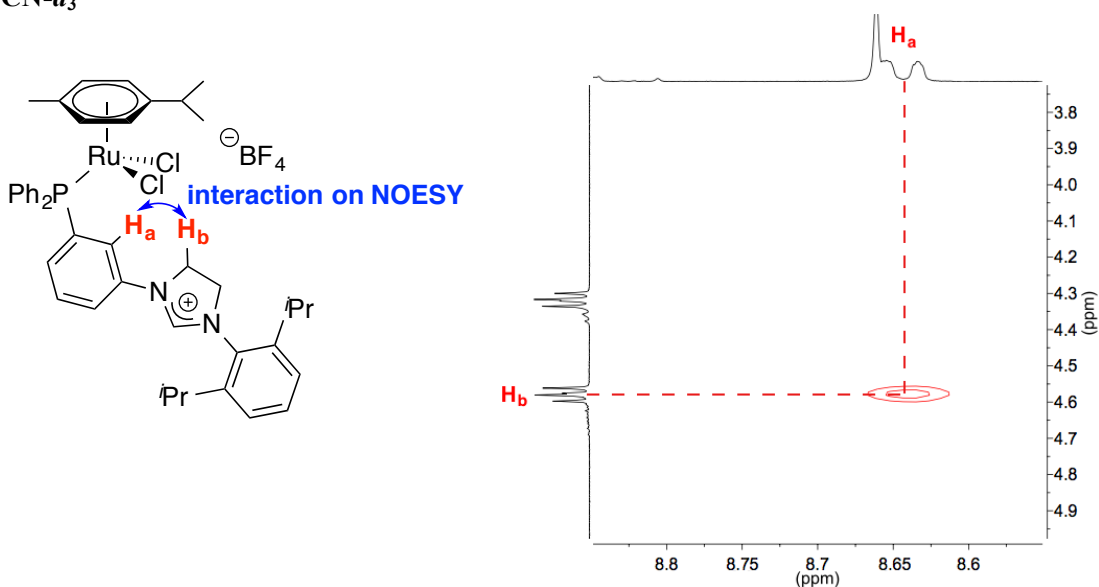
In an effort to synthesize and characterize a ruthenium complex bearing a pendant dihydroimidazolium salt ligand, **2.51** or **2.52** was added to dichloro(*p*-cymene)ruthenium(II) dimer in an analogous fashion to the synthesis of $\text{RuCl}_2(\textit{p}\text{-cymene})(\text{PPh}_3)$ (**2.32**) (Scheme 2.27). Analysis of the ^{31}P NMR spectrum of the isolated red solid indicated the formation of a ruthenium-phosphine bond with a resonance at +25.2 as opposed to -5.2 ppm in the starting material. In the ^1H NMR spectrum, no major changes were observed with the exception of new peaks due to the *p*-cymene group.

Scheme 2.27. Synthesis of a ruthenium complex bearing a pendant dihydroimidazolium ligand from $[\text{Ru}(\mu\text{-Cl})_2(\textit{p}\text{-cymene})]_2$



Although X-ray quality crystals of either **2.53** or **2.54** were not obtained, rigorous ^1H , ^{31}P , ^{13}C , COSY, NOESY, and HSQC NMR analysis were able to elucidate the structure. Specifically, the dihydroimidazolium ring is directed away from the ruthenium center. This determination was made based on a through-space interaction between protons on the backbone of the dihydroimidazolium moiety and a proton on the aryl spacer (Figure 2.9).

Figure 2.9. Solution phase structural determination based on NMR studies of 2.54 in MeCN- d_3



In order to understand the behavior of ruthenium complexes like **2.53** and **2.54** in future stoichiometric and catalytic reactions, ^1H and ^{31}P NMR studies were conducted with complex **2.54**. At room temperature, the complex is stable for up to two days in $\text{MeOD-}d_4$ and $\text{MeCN-}d_3$. However, in $\text{DMSO-}d_6$, the ^{31}P NMR spectrum exhibits two resonances at +25 and +26 ppm in a ratio of 1:3, respectively. Similarly to $\text{RuCl}_2(p\text{-cymene})(\text{PPh}_3)$ (**2.32**), the appearance of a new species is thought to be due to the formation of a ruthenium-DMSO adduct. The complex was then heated to 50 $^\circ\text{C}$ under 1 bar of N_2 in a variety of solvents. In $\text{MeOD-}d_4$ and $\text{MeCN-}d_3$, with the exception of H/D exchange of the dihydroimidazolium proton, no change was observed over

the course of 16 hours. In DMSO-*d*₆, ruthenium complex **2.54** exhibited the same two resonances as at room temperature in addition to free ligand.

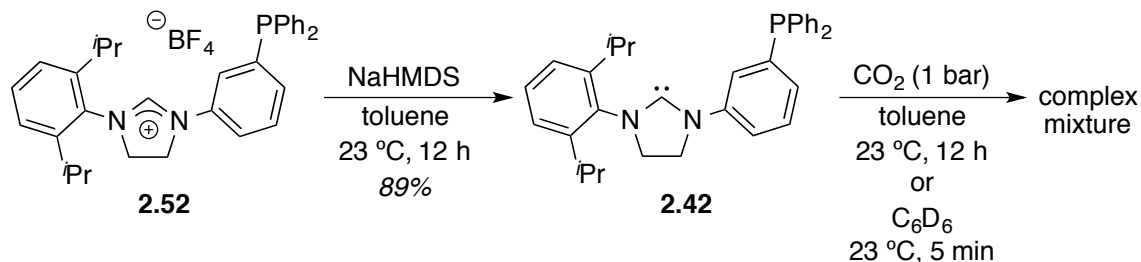
2.4.2 Stoichiometric Reactivity

Based on the fact that, with the addition of water, dihydroimidazolium carboxylates are in equilibrium with their corresponding dihydroimidazolium bicarbonate,⁵² we postulated that the activation of carbon dioxide could be achieved through the synthesis of a dihydroimidazolium bicarbonate species. The reactivity of ruthenium complex **2.54** with KHCO₃ at 50 °C under 1 bar of CO₂ was examined in a variety of solvents. In MeOD-*d*₄, MeCN-*d*₃, and DMSO-*d*₆, the complex decomposed over the course of 16 hours. With the addition of excess base (NBU₃), in DMSO-*d*₆, complex **2.54** was converted into an unknown species. Resonances assigned to the protons of the backbone of the dihydroimidazolium moiety (4.58 (t) and 4.32 (t) ppm) and the protons of the *p*-cymene ring (5.24 (m) ppm) had converted to new peaks ranging from 5.6 to 8.4 ppm. Analysis of the ³¹P NMR spectrum revealed both bound and free phosphine ligand.

Since RuCl₂(*p*-cymene)(PPh₃) (**2.32**) converted to Ru(O₂CO)(*p*-cymene)(PPh₃) (**2.40**), triphenylphosphine, and triphenylphosphine oxide under similar conditions,⁵³ the behavior of the dihydroimidazolium tetrafluoroborate ligand was examined. In DMSO-*d*₆, the addition of KHCO₃ to dihydroimidazolium tetrafluoroborate **2.52** converted the compound to an unknown species with similar ¹H resonances as with ruthenium species **2.54**. With the addition of NBU₃, in DMSO-*d*₆, compound **2.52** was converted into the same unknown species. In addition, oxidation of the phosphine was observed with a shift in the ³¹P NMR resonance from -5.2 ppm to +24 ppm. In MeOD-*d*₄, with the exception of H/D exchange of the dihydroimidazolium proton, no change was observed over the course of 16 hours. Although these properties are unique to **2.52**, reactions were not clean enough to investigate further.

Addition of base to dihydroimidazolium tetrafluoroborate **2.52** afforded free carbene **2.42** (Scheme 2.28). The reactivity of free carbene **2.42** with carbon dioxide was then investigated. In toluene, the free carbene was treated with one atmosphere of CO₂ at room temperature.

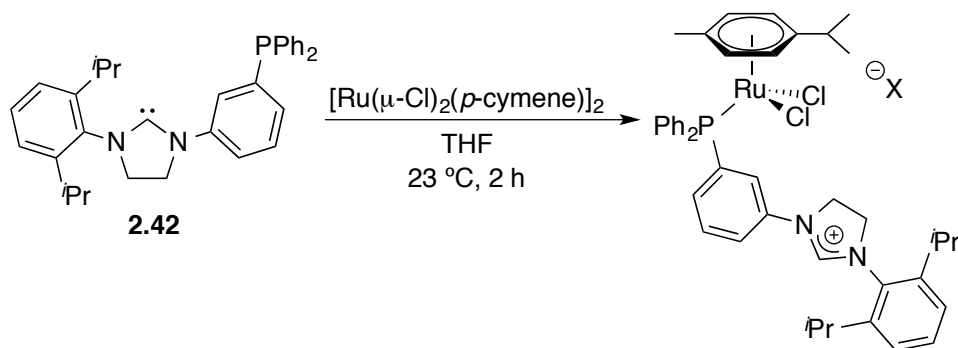
Scheme 2.28. Synthesis and reactivity of free N-heterocyclic carbene 2.42 with CO₂



Using symmetrical NHCs explored in the past, the desired carboxylate salt precipitates out of solution and is isolated by filtration. With free carbene **2.42**, no precipitation occurred and the resulting solid isolated was a complex mixture. Analysis of the ¹H and ³¹P NMR spectra indicated the formation of multiple species and three new phosphorous containing compounds immediately upon addition of CO₂. Unfortunately, this reaction was not clean enough to investigate further.

In order to investigate the ruthenium-phosphine complex **2.54** further, we set out to synthesize the analogous ruthenium-NHC complex (Scheme 2.29).

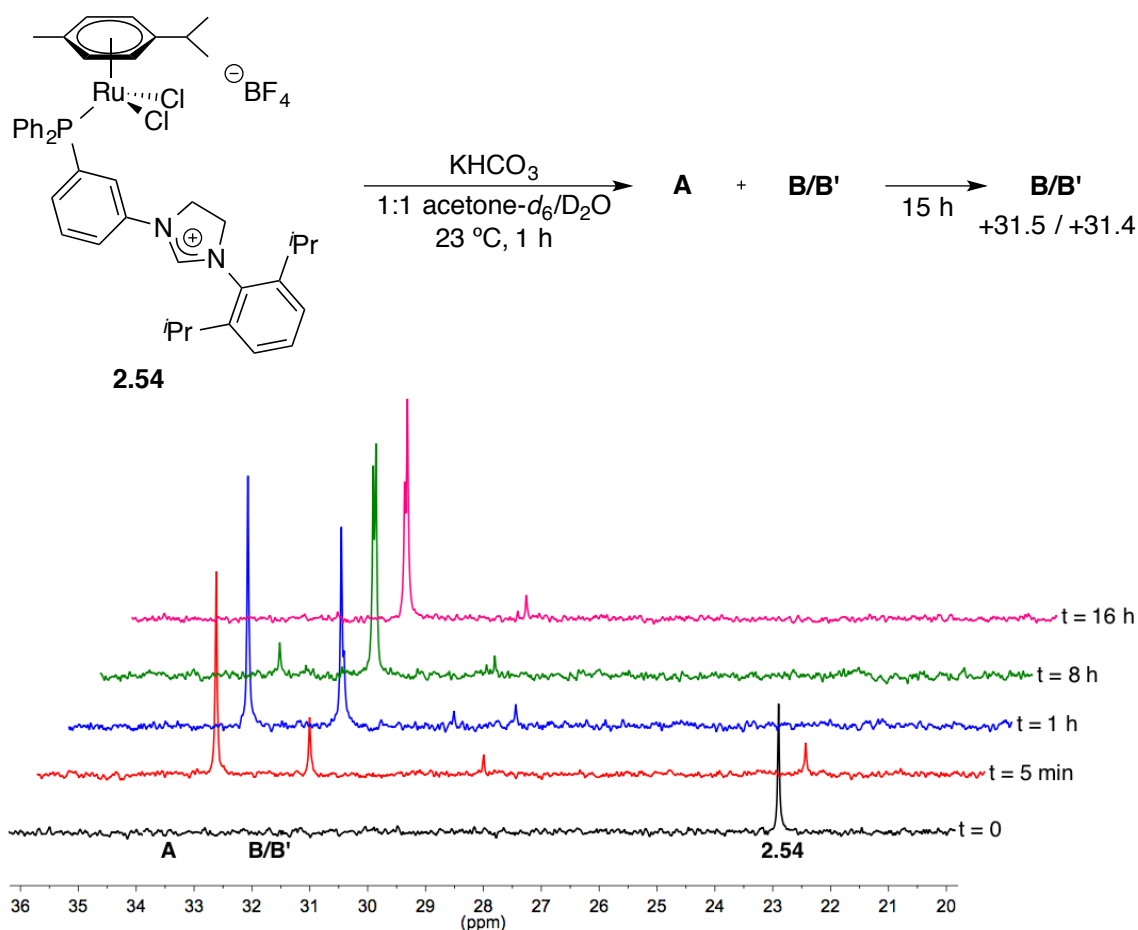
Scheme 2.29. Reactivity of free N-heterocyclic carbene 2.42 with [Ru(μ-Cl)₂(*p*-cymene)]₂



Upon addition of the free N-heterocyclic carbene **2.42** to $[\text{Ru}(\mu\text{-Cl})_2(p\text{-cymene})]_2$, a species similar to the ruthenium-phosphine bound complex **2.54** was isolated. ^1H and ^{31}P NMR spectra match those of complex **2.54** synthesized from the dihydroimidazolium tetrafluoroborate. Interestingly, ruthenium bound N-heterocyclic carbene and free phosphine was not observed.

Although the majority of the NMR studies conducted indicated the instability of ruthenium complex **2.54**, the synthesis of $\text{Ru}(\kappa^2\text{-O}_2\text{CO})(\text{PPh}_3)(p\text{-cymene})$ (**2.40**) was completed in a 1:1 mixture of acetone and water. Therefore, the reactivity of ruthenium complex **2.54** with KHCO_3 was investigated in 1:1 acetone- d_6 / D_2O and the progress of the reaction was monitored by ^1H and ^{31}P NMR spectroscopy (Figure 2.10).

Figure 2.10. ^{31}P NMR spectra of stoichiometric reactions of complex **2.54** with KHCO_3



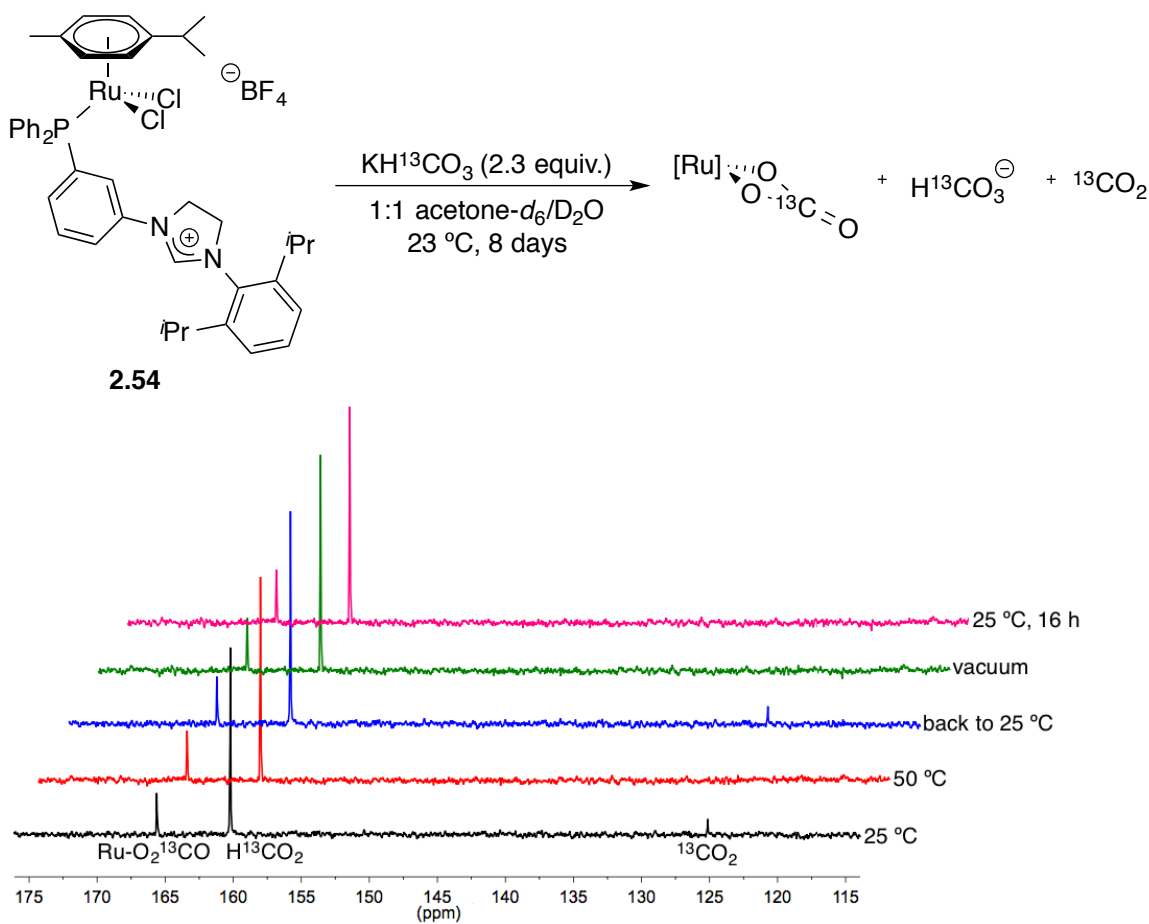
Based on the ^{31}P NMR spectrum, after five minutes the starting material and three new species with resonances at +33.1 (**A**), +31.5 (**B/B'**), and +28.5 ppm were apparent. At one hour, the starting material had been completely consumed and the major phosphorus containing compounds were at +33.1 (**A**), +31.5 (**B**), and +31.4 (**B'**) ppm. After a total of sixteen hours, the ^{31}P NMR spectrum showed two major resonances at +31.5 and +31.4 ppm in a ratio of 1:1.2, respectively. Based on the ^1H NMR spectrum, after 5 minutes resonances for new bound *p*-cymene at 5.94 (d) and 5.63 (d) ppm, new aromatic protons at 7.13 (m) and 6.99 (m) ppm, and new dihydroimidazolium backbone protons at 3.96 (m), 3.43 (t), and 3.38 (t) ppm were observed. After 16 hours, the starting material had been completely consumed and the new resonances observed were the major peaks.

We speculated that the new species **A** being formed was a ruthenium complex containing bicarbonate or carbonate, similar to that observed with $\text{Ru}(\kappa^2\text{-O}_2\text{CO})(\text{PPh}_3)(p\text{-cymene})$ (**2.40**). Based on the knowledge that the dihydroimidazolium bicarbonate and carboxylate are in equilibrium,⁵² we postulated that these could be compounds **B** and **B'**. In order to investigate this equilibrium, ^1H and ^{31}P NMR spectra were collected at 50 °C and then again after cooling to 25 °C. At 50 °C, there was one broad phosphorus resonance at +31.4 ppm in the ^{31}P NMR spectrum. The ^1H NMR signals became broad and the resonances for the dihydroimidazolium backbone at 4.26 (br m), 3.71 (br m), and 3.41 (br m) ppm began to coalesce. Upon cooling back to 25 °C, both the ^1H and ^{31}P NMR spectra were the same as before heating to 50 °C. This supports an equilibrium mixture, not a conversion or decomposition to a new species upon heating. The dihydroimidazolium tetrafluoroborate ligand **2.52** was then treated with KHCO_3 in the same in 1:1 acetone- d_6 / D_2O mixture. The ^1H NMR spectrum showed starting material along with two new species with similar ^1H NMR resonances as those seen with ruthenium complex **2.54**. The ^{31}P NMR spectrum displayed three resonances at -5.58, -5.69, and -5.17 ppm in a 1:1.4:1.4 ratio, respectively. Although the conversion is much lower (due to the fact that dihydroimidazolium

tetrafluoroborate **2.52** is not soluble in 1:1 acetone and water), the ligand and the ruthenium complex act similarly when KHCO_3 is added.

To further explore these new complexes, the reactivity of ruthenium complex **2.54** with $\text{KH}^{13}\text{CO}_3$ was monitored by ^{13}C NMR in 1:1 acetone- d_6 / D_2O (Figure 2.11). Based on ^1H and ^{31}P NMR spectroscopy, complex **2.54** had completely converted to the two new species previously observed after a total of eight days. The ^{13}C NMR spectrum showed three ^{13}C labeled moieties: one at 165 ppm, corresponding to a ruthenium carbonate (similar to that observed for $\text{Ru}(\kappa^2\text{-O}_2\text{CO})(\text{PPh}_3)(p\text{-cymene})$ (**2.40**)); one at 160 ppm, corresponding to bicarbonate, and one at 125 ppm, corresponding to free carbon dioxide.

Figure 2.11. ^{13}C NMR spectra of stoichiometric reactions of complex **2.54** with $\text{KH}^{13}\text{CO}_3$



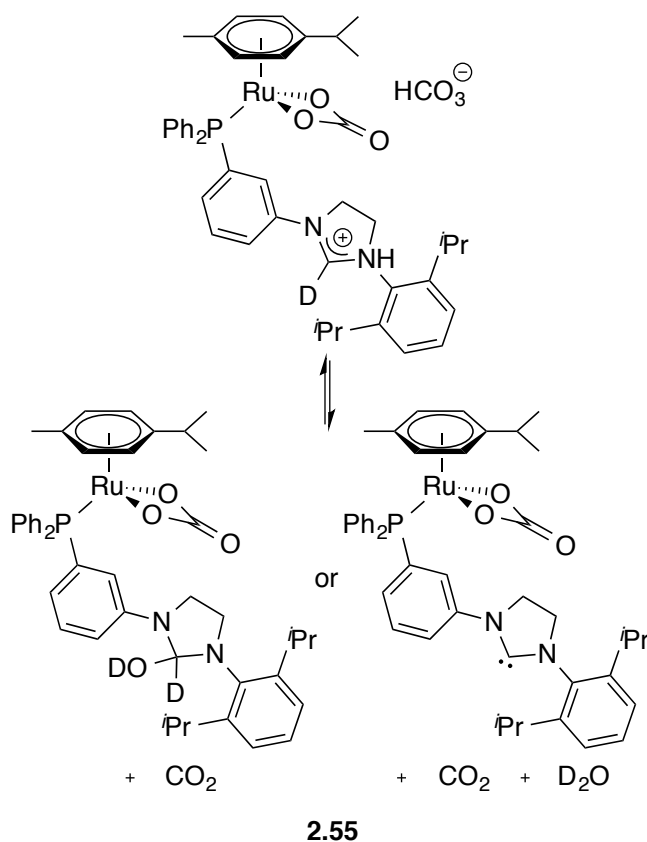
The appearance of a peak corresponding to a carboxylate at 155 ppm was not observed. Assuming the two species formed were in equilibrium, ^{13}C NMR spectra were collected at 50 °C and then again after cooling to 25 °C. At 50 °C, the signal corresponding to free carbon dioxide disappeared, while the other two peaks at 165 and 160 ppm remained unchanged. Upon cooling to 25 °C, both the ^1H and ^{31}P NMR spectra were the same as before heating to 50 °C. We hypothesized that the free CO_2 could be removed and then the equilibrium between **2.54**/ KHCO_3 and the products would produce more CO_2 . Therefore, ^{13}C NMR spectra were collected after exposing the mixture to vacuum and then after 16 hours at 25 °C. After exposure to vacuum, the signal corresponding to free carbon dioxide disappeared. Unfortunately, after allowing the sample to sit for 16 hours at 25 °C, the observation of more CO_2 was not seen. We currently have no explanation for this result, but our other NMR data suggest the structure is an equilibrium mixture.

To make sure that this was not common behavior for dihydroimidazolium compounds, the reactivity of $\text{KH}^{13}\text{CO}_3$ with 1,3-(2,6-diisopropylphenyl)dihydroimidazolium bromide was monitored by ^1H and ^{13}C NMR in 1:1 acetone- d_6 / D_2O . Unlike with ruthenium complex **2.54**, the dihydroimidazolium bicarbonate is not in equilibrium with a second species at 25 °C in 1:1 acetone and water. In addition, based on the ^{13}C NMR spectrum, the only ^{13}C labeled species is bicarbonate. With the 1,3-(2,6-diisopropylphenyl)dihydroimidazolium bromide starting material there is no formation of $^{13}\text{CO}_2$. This does not disprove the existence of the free carbene for this species, but indicates that if in equilibrium with a free carbene, the equilibrium constant is faster than the NMR timescale.

Based on these results, we hypothesized that the result of the reaction between **2.54** and KHCO_3 is an equilibrium between ruthenium carbonate complexes containing a dihydroimidazolium bicarbonate and a free carbene (or quenched in the presence of D_2O) (Figure 2.12). The mass spectrometry data also supports this hypothesis as it suggests a ruthenium (*p*-

cymene) species containing a dihydroimidazolium ligand quenched in the presence of H₂O.

Figure 2.12. Proposed structure of newly formed ruthenium species 2.55

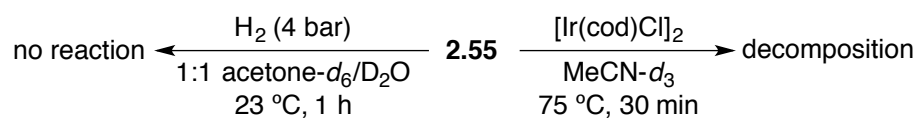


In order to better understand the behavior of this newly formed ruthenium carbonate mixture in future stoichiometric and catalytic reactions, ¹H and ³¹P NMR studies were conducted. At room temperature, the mixture is stable for short periods of time in MeOD-*d*₄ and DMSO-*d*₆. The mixture was then heated to 50 °C under 1 bar of N₂ for sixteen hours. In MeOD-*d*₆, the ratio of the two ³¹P NMR signals changed and a new species at +52.5 ppm was observed. The identity of this new species was never determined. In DMSO-*d*₆, five new ³¹P NMR signals were observed at +45.5, +45.4, +26.1, +26.0, and -5.7 ppm. Similar to the reactivity with Ru(κ²-O₂CO)(PPh₃)(*p*-cymene) (**2.40**) in DMSO-*d*₆, these peaks were attributed to ruthenium-DMSO adducts (+45.5,

+45.4), oxidized phosphine dihydroimidazolium ligand salts (+26.1, +26.0), and free dihydroimidazolium ligand (-5.7), respectively. In 1:1 acetone- d_6 /D₂O, the mixture was stable at room temperature for days and at 50 °C for at least sixteen hours.

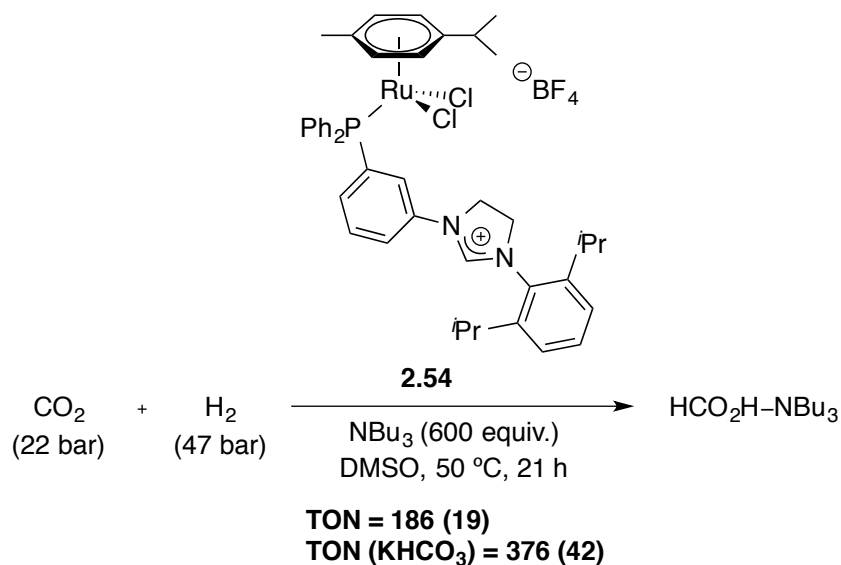
Preliminary stoichiometric reactions with ruthenium carbonate mixture **2.55** were investigated. First, hydrogen was added to the species in 1:1 acetone- d_6 /D₂O at 4 bar (Scheme 2.30). Based on ¹H and ³¹P NMR spectra, after one hour at room temperature no reaction had occurred. The reaction was never heated or allowed to continue further than one hour. Second, iridium-cyclooctadiene dimer was added to the species in MeCN- d_3 . The reaction was heated to 75 °C for thirty minutes, after which time the dark green reaction turned red. Although there was no change in the ¹H NMR signals for [Ir(cod)Cl]₂, there was free *p*-cymene and three resonances in the ³¹P NMR spectrum at +26.5, +22.4, and +22.2 ppm. The identity of these newly formed species were never determined. Although, the behavior of ruthenium carbonate mixture **2.55** in MeCN- d_3 at 75 °C was not investigated, based on the data obtained from other solvents at 50 °C, it is believed that species **2.55** decomposed under the reaction conditions.

Scheme 2.30. Stoichiometric reactions with ruthenium carbonate mixture **2.55**

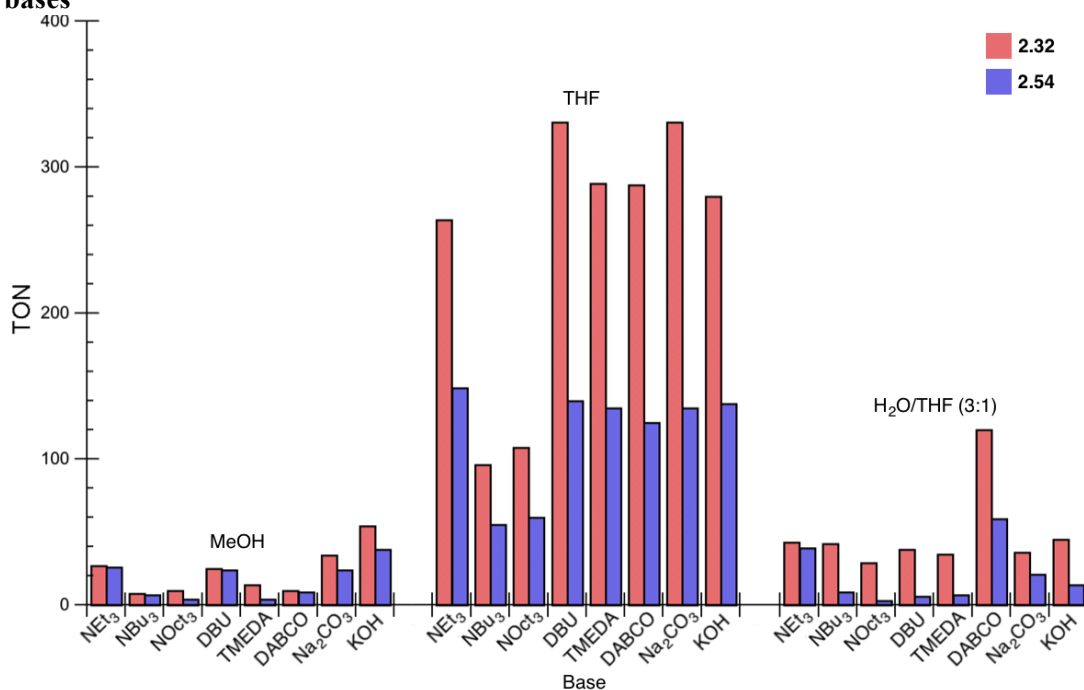


2.4.3 Catalytic Activity

CO₂ hydrogenation reactions were carried out using ruthenium complex **2.54** in the presence and absence of KHCO₃ using our standard reaction conditions (Scheme 2.31). Reactions catalyzed by **2.54** demonstrated a 100% increase in formic acid production with the addition of KHCO₃, which is similar to reactions with RuCl₂(PPh₃)(*p*-cymene) (**2.32**). However, the absolute TONs of complex **2.54** were lower than ruthenium **2.32**.

Scheme 2.31. Hydrogenation of CO₂ catalyzed by ruthenium complex **2.54** in DMSO

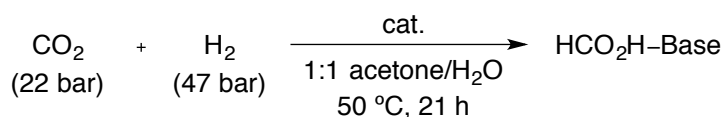
Based on our ¹H and ³¹P NMR studies, complex **2.54** decomposed in DMSO-*d*₆ at 50 °C. Therefore, we sought to explore the activity of **2.54** with various solvents and bases (Figure 2.13).

Figure 2.13. Ruthenium **2.49** catalyzed hydrogenation of CO₂ with alternative solvents and bases

In comparison to $\text{RuCl}_2(\text{PPh}_3)(p\text{-cymene})$ (**2.32**), complex **2.54** demonstrated similar or lower activity in MeOH, THF, and $\text{H}_2\text{O}/\text{THF}$ (3:1). These results are not extremely surprising, as we have previously observed no increase in formic acid productivity with dihydroimidazolium salts that do not have bicarbonate or carboxylate anions.

Therefore, we investigated the catalytic activity of ruthenium carbonate mixture **2.55** in the hydrogenation of CO_2 formic acid. Based on our ^1H and ^{31}P NMR studies of **2.55**, we chose to explore reactions in 1:1 acetone/ H_2O (Table 2.16). Reactions in 1:1 acetone/ H_2O demonstrated overall much lower activity as compared to those previously seen in DMSO. With KOH as the base, reactions catalyzed by $\text{Ru}(\kappa^2\text{-O}_2\text{CO})(\text{PPh}_3)(p\text{-cymene})$ (**2.40**) and ruthenium complex **2.54** showed an increase in activity, while ruthenium mixture **2.55** showed a decrease in activity as compared to complex **2.32**. Since the difference in reactivity is minimal and the average error was not determined, the differences could be insignificant. With NBu_3 as the base, all catalysts produced more formic acid than **2.32**. While the percent increase was significant, the absolute difference in TONs is so minor that it could again be negligible as the average error was not determined.

Table 2.16. Hydrogenation of CO_2 in 1:1 acetone/ H_2O



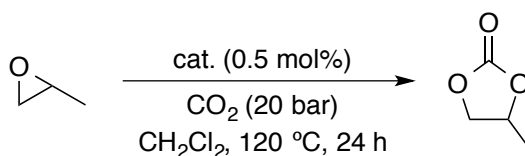
Entry	Base ^a	Cat.	TON ^b	Increase (%) ^c
1		2.32	18	N/A
2	KOH	2.40	20	11
3		2.54	21	17
4		2.55	9	-50
5		2.32	4	N/A
6	NBu_3	2.40	14	250
7		2.54	22	450
8		2.55	10	150

^a600 equiv. ^bTON = (mol $\text{HCO}_2\text{H-NBu}_3$)/(mol cat.).

^cIncrease = $\{[\text{TON} - \text{TON}(\mathbf{2.32})]/\text{TON}(\mathbf{2.32})\} \times 100$.

In addition to the hydrogenation of carbon dioxide to formic acid, we explored the coupling of carbon dioxide and epoxides to give cyclic carbonates. As previously mentioned, multiple research groups have demonstrated this process via NHC catalysis (Table 2.1, Scheme 2.12). Therefore, we believed our metal-imidazolium system could enhance the reactivity of CO₂ toward coupling with epoxides. First, we explored conditions developed by Lu and coworkers for the imidazolium and dihydroimidazolium carboxylate catalyzed coupling of CO₂ and propylene oxide (Table 2.17).²⁴⁻²⁶ At 120 °C, reactions with the previously reported 1,3-(2,6-diisopropylphenyl)imidazolium carboxylate (**2.21a**) gave a 91% yield of the desired cyclic carbonate (entry 1). In an attempt to generate the imidazolium carboxylate in situ, a base known to deprotonate imidazolium salts, 1,8-diazabicycloundec-7-ene (DBU), was added to 1,3-(2,6-diisopropylphenyl)imidazolium chloride (**2.30**) (entry 2). Reactions with this mixture gave the desired product in a 98% yield. Reactions catalyzed by DBU alone generated the product in a 100% yield. This is not surprising considering the DBU catalyzed (or co-catalyzed) coupling of CO₂ and epoxides has previously been demonstrated.^{63, 64}

Table 2.17. Coupling of CO₂ and propylene oxide at 120 °C



Entry	Cat.	Yield ^a
1	2.21a	91
2	2.30 /DBU	98
3	DBU	100
4	2.55	6

^aDetermined by ¹H NMR using DMF as an internal standard.

Reactions with ruthenium mixture **2.55** generated the cyclic carbonate product in only a 6% yield. This result is in agreement with prior ^1H and ^{31}P NMR experiments in $\text{MeOD-}d_4$ and $\text{DMSO-}d_6$ suggesting the decomposition of species **2.55** at elevated temperatures. Therefore, the coupling of carbon dioxide and epoxides to give cyclic carbonates was explored at 50 °C in CH_2Cl_2 , MeOH, DMSO, MeCN, THF, and 1:1 acetone/ H_2O . Under all conditions explored, the ruthenium mixture **2.55** gave no desired product. In addition, reactions with IPr- CO_2 , IPr-HCl / DBu, and DBU gave less than 2% yields in 1:1 acetone/ H_2O . The poor catalytic performance of ruthenium mixture **2.55** suggests that stoichiometric reactions with epoxides (and other electrophiles) are warranted before further catalytic reactions can be explored.

2.5 Conclusions

In conclusion, we have demonstrated that the addition of imidazolium and dihydroimidazolium bicarbonate or carboxylate salts increased activity for the hydrogenation of CO₂ to formic acid. Investigations into the role of such imidazolium and dihydroimidazolium salts led to the discovery that KHCO₃ and other similar additives also increased activity for a variety of transition metal complexes. The increased activity is likely related to the ability of the additive to act as a ligand for the transition metal to form species such as the ruthenium carbonate **2.40**. The effect was general for many noble-metal catalysts and for one of the most efficient base-metal hydrogenation catalysts. Preliminary mechanistic investigations revealed that the additive does not act as an internal base to facilitate catalyst turnover but the activity is instead related to its structural characteristics. Regardless of its specific function, increased formic acid production resulting from the addition of small quantities of inexpensive additives provides a practical and economic way to increase catalytic productivity.

The synthesis of a novel ruthenium complex bearing a pendant dihydroimidazolium salt was carried out. Based on the reactivity of ruthenium complex **2.54** with KH¹³CO₃, the equilibrium mixture between a dihydroimidazolium bicarbonate ligand and either a free carbene or an hydroxyl-masked carbene is promising for small molecule activation. Although initial stoichiometric and catalytic and stoichiometric reactions geared toward utilizing this unique characteristic of ruthenium mixture **2.55** were unsuccessful, further reactions are warranted. Stoichiometric reactions with electrophiles such as CS₂, epoxides, aldehydes, and enones could implicate the importance of such an interesting complex.

2.6 Experimental

2.6.1 General Considerations

Unless otherwise stated, all reactions were carried out in oven-dried glassware in a nitrogen atmosphere glove box or using standard Schlenk line techniques.⁶⁵ Solvents were used after passage through a solvent purification system similar to the one reported by Grubbs⁶⁶ under a blanket of argon. Particularly air-sensitive manipulations were performed using solvent that was then degassed by briefly exposing the solvent to vacuum. Unless otherwise stated, all work-up and purification procedures were carried out with reagent grade solvents (purchased from Fisher Scientific, Inc.) in air. Flash chromatography was performed according to the procedure of Still *et al.*⁶⁷ with ZEOCHEM® SEPIX 560 40-63 mm silica gel. Thin-layer chromatography was performed using Analtech TLC Uniplates™, Silica matrix purchased from Sigma-Aldrich. TLC plates were visualized by exposure to ultraviolet light. Organic reagents were purchased from Sigma-Aldrich, TCI America, or Fisher Scientific. RuCl(OAc)(PMe₃)₄ (**1.17**), RuCl(OAc)(PPh₃)₃ (**2.37**), and Fe(BF₄)₂·6H₂O were purchased from Sigma-Aldrich. Tris(2-(diphenylphosphino)ethyl)phosphine (alkyl-PP₃) was purchased from Acros Organics. RuCl[(R,R)-Ts-DENEB] (**2.35**), RuCl[(R)-xylylbinap][(R)-diapena] (**2.36**), RuCl₂[(R)-xylylbinap][(R,R)-dpen] (**2.38**), RuBF₄(*p*-cymene)[(R,R)-Ts-dpen] (**2.39**), Ru(acac)₃, FeCl₂ and 1,1,1-tris(diphenylphosphinomethyl)ethane (triphos-2) were purchased from Strem Chemicals.

Compounds 1,3-bis(2,6-diisopropylphenyl)imidazolium carboxylate (**2.21a**),⁶⁸ 1,3-bis(2,4,6-trimethylphenyl)imidazolium carboxylate (**2.21b**),⁶⁸ 1,3-dimethylimidazolium carboxylate (**2.21c**),⁶⁹ 1,3-di-*tert*-butylimidazolium carboxylate (**2.21d**),⁷⁰ 1,3-bis(2,6-diisopropylphenyl)dihydroimidazolium carboxylate (**2.22a**),²⁶ 1,3-bis(2,4,6-trimethylphenyl)dihydroimidazolium carboxylate (**2.22b**)²⁶ 1,3-bis(2,6-diisopropylphenyl)imidazolium chloride (**2.30**),⁷¹ and 1,3-bis(2,6-diisopropylphenyl)imidazolium bicarbonate (**2.31**)⁶⁹ were prepared according to the known literature procedures.

^1H NMR spectra were recorded on a Varian VNMRS (500 MHz) or INOVA (500 MHz) spectrometer. Data are reported as follows: chemical shift, multiplicity (s = singlet, br s = broad singlet, d = doublet, dd = doublet of doublets, ddd = doublet of doublet of doublets, dt = doublet of triplets, dq = doublet of quartets, t = triplet, td = triplet of doublets, tt = triplet of triplets, q = quartet, pent = pentet, hept = heptet, m = multiplet), coupling constants (Hz), and integration. ^{13}C NMR spectra were recorded on a Varian VNMRS (125 MHz) or INOVA (125 MHz) spectrometer with complete proton decoupling. All chemical shifts are reported in ppm from tetramethylsilane with the solvent as the internal reference (^1H NMR: Acetone- d_6 = 2.05 ppm, MeCN- d_3 = 1.94 ppm, C_6D_6 = 7.16 ppm, CDCl_3 = 7.26 ppm, D_2O = 4.79 ppm, CD_2Cl_2 = 5.32 ppm, DMSO- d_6 = 2.50 ppm, MeOD- d_4 = 3.31 ppm; ^{13}C NMR: Acetone- d_6 = 29.84, 206.26 ppm, MeCN- d_3 = 1.32, 118.26 ppm, C_6D_6 = 128.06 ppm, CDCl_3 = 77.16 ppm, CD_2Cl_2 = 53.84 ppm, DMSO- d_6 = 39.52 ppm, MeOD- d_4 = 49.00 ppm). ^{31}P NMR spectra were recorded on a Varian VNMRS (202 MHz) or INOVA (202 MHz) spectrometer reported relative to a phosphoric acid external standard (0.00 ppm). Infrared spectra were recorded on a Bruker Alpha-p spectrometer. High-resolution mass spectra were obtained at the Boston College Mass Spectrometry Facility using ESI+ or MALDI ionization mode.

Reactions at elevated pressures were run in 1.5 x 13.5 cm ampules equipped with magnetic stir bars in a 450 mL high-pressure vessel from Parr Instrument. Yields from hydrogenation reactions were determined by ^1H NMR spectroscopy in D_2O using an INOVA 400 NMR spectrometer with a Varian SMS-50 auto-sampler. Quantitative information was obtained by first calibrating the T_1 of the formate proton ($T_1 = 7.246$) and the dimethylformamide standard protons ($T_1 = 6.342$), then by adjusting the delay time (d1) such that it was $5 * T_1$ (d1=40, nt=16).

Selected single crystals suitable for X-ray crystallographic analysis were used for structural determination. The X-ray intensity data were measured at 100(2) K (Oxford Cryostream 700) on a Bruker Kappa APEX Duo diffractometer system equipped with a sealed

Mo-target X-ray tube ($\lambda = 0.71073 \text{ \AA}$) and a high brightness I μ S copper source ($\lambda = 1.54178 \text{ \AA}$). The crystals were mounted on a goniometer head with paratone oil. The detector was placed at a distance of 5.000 cm from the crystal. For each experiment, data collection strategy was determined by APEX software package and all frames were collected with a scan width of 0.5° in ω and ϕ with an exposure time of 10 or 20 s/frame.

The frames were integrated with the Bruker SAINT Software package using a narrow-frame integration algorithm to a maximum 2θ angle of 56.54° (0.75 \AA resolution) for Mo data and 136.50° (0.83 \AA resolution) for Cu data. The final cell constants are based upon the refinement of the XYZ-centroids of several thousand reflections above $20 \sigma(I)$. Analysis of the data showed negligible decay during data collection. Data were corrected for absorption effects using the empirical method (SADABS). The structures were solved and refined by full-matrix least squares procedures on $|F^2|$ using the Bruker SHELXTL (version 6.12) software package. All hydrogen atoms were included in idealized positions for structure factor calculations except those forming hydrogen bonds or on a chiral center. Anisotropic displacement parameters were assigned to all non-hydrogen atoms, except those disordered.

2.6.2 Experimental Procedures

General procedure for hydrogenation of CO₂ in dimethylsulfoxide (DMSO). The desired additive (5 μmol) was added to the ampule if necessary. To each ampule, a 0.001 M solution of the catalyst in DMSO (1 mL, 1 μmol) was added followed by base. The ampules were placed in the pressure vessel and purged with CO₂ for 5 minutes. The vessel was pressurized with CO₂ (22 bar) and allowed to equilibrate for 5 minutes at 23 $^\circ\text{C}$, then heated to 50 $^\circ\text{C}$ for 20 minutes. After 20 minutes at 50 $^\circ\text{C}$, the pressure was approximately 26 bar. The vessel was then pressurized with hydrogen (47 bar, total pressure = 69 bar) and allowed to equilibrate for 5 minutes at 50 $^\circ\text{C}$. The reactions were stirred at 50 $^\circ\text{C}$ for 21 hours. The vessel was then cooled to

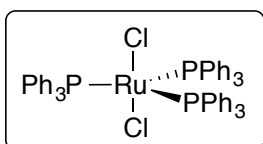
0 °C in an ice bath, and the pressure was slowly released. The ampules were removed from the vessel and allowed to warm to 23 °C. Dimethylformamide (100 µL, 1.29 mmol) was added to each ampule as an internal standard, and an aliquot (200 µL) was removed and mixed with D₂O (700 µL). The mixture was filtered through Celite and analyzed by ¹H NMR spectroscopy.

General procedure for hydrogenation of CO₂ in methanol (MeOH). The metal catalyst (0.030 mmol), P(CH₂CH₂PPh₂)₃ (0.030 mmol), and methanol (120 mL) were added sequentially to the vessel. Upon addition of the P(CH₂CH₂PPh₂)₃, the mixture turned purple (lavender with Fe(BF₄)₂ and bright purple with FeCl₂). When appropriate, potassium bicarbonate (0.15 mmol) was added to the vessel and the mixture was stirred for 1 hour, upon which time the mixture turned pale yellow. Triethylamine (2.5 mL, 18 mmol) was added to the vessel, and the vessel was purged with CO₂ for 5 minutes. The vessel was pressurized with CO₂ (30 bar), and allowed to equilibrate for 5 minutes. The vessel was then pressurized with H₂ (60 bar, total pressure = 90 bar) and allowed to equilibrate for 5 minutes. The vessel was heated to 100 °C at which point the pressure was approximately 129 bar. The reaction was stirred at 100 °C for 21 hours. The vessel was then allowed to cool to 50 °C, then to 0 °C in an ice bath. The pressure was then released and the reaction was allowed to warm to 23 °C. Tetrahydrofuran (2.0 mL, 25 mmol) was added to the solution, and an aliquot (200 µL) was removed and mixed with D₂O (700 µL). The mixture was filtered through Celite and analyzed by ¹H NMR spectroscopy.

General procedure for epoxide and CO₂ coupling. Catalyst (0.025 mmol) was added to the appropriate ampule as necessary. To each ampule, propylene oxide (350 µL, 5.00 mmol) was added followed by solvent (1 mL). The ampules were placed in the pressure vessel and purged with CO₂ for 5 minutes. The vessel was pressurized with CO₂ (20 bar) and allowed to equilibrate for 5 minutes at 23 °C, then heated to the desired temperature for 20 minutes. The reactions were

stirred at for 24 hours. The vessel was then cooled to 0 °C in an ice bath, and the pressure was slowly released. The ampules were removed from the vessel and allowed to warm to 23 °C. Dimethylformamide (100 μL, 1.29 mmol) was added to each ampule as an internal standard, and an aliquot (200 μL) was removed and mixed with D₂O (700 μL). The mixture was filtered through Celite and analyzed by ¹H NMR spectroscopy.

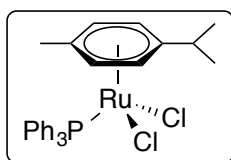
Dichlorotrīs(triphenylphosphine)ruthenium [RuCl₂(PPh₃)₃] (2.29). A mixture of



ruthenium trichloride hydrate (0.290, 1.40 mmol, 1.00 equiv.), triphenylphosphine (2.24 g, 8.53 mmol, 6.10 equiv.), and MeOH (18 mL) was refluxed for 4 hours. The resulting purple/brown mixture was

cooled to 23 °C and filtered, washing with Et₂O. The product was isolated as a red/brown solid (1.29 g, 96%). Spectroscopic data were in agreement with the reported literature values.⁷²

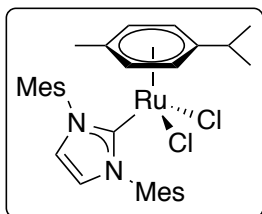
Dichloro(*p*-cymene)(triphenylphosphine)ruthenium [RuCl₂(*p*-cymene)(PPh₃)] (2.32).



A mixture of dichloro(*p*-cymene)ruthenium(II) dimer (0.0979 g, 0.159 mmol, 1.00 equiv.), triphenylphosphine (0.0891 g, 0.339 mmol, 2.10 equiv.), and CH₂Cl₂ (4 mL) was stirred at 23 °C for 24 hours. The dark

orange/red solution was concentrated *in vacuo*. The product was obtained after precipitation of a dark orange solid with hexanes (0.1339 g, 74%). Spectroscopic data were in agreement with the reported literature values.⁷³ [Dichloro(*p*-cymene)ruthenium(II) dimer was synthesized from a mixture of ruthenium trichloride hydrate (0.712 g, 3.43 mmol, 1.00 equiv.), *a*-phellandrene (3.2 mL, 20.0 mmol, 5.80 equiv.), and EtOH (49 mL) was refluxed for 12 hours. The resulting red/orange solution was cooled to 23 °C and concentrated *in vacuo*. The product was obtained after precipitation of an orange solid with hexanes (0.7066 g, 67%). Spectroscopic data were in agreement with the reported literature values.⁷⁴]

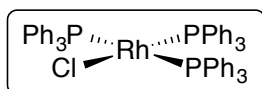
Dichloro(*p*-cymene)(1,3-bis(mesityl)imidazol-2-ylidene)ruthenium [RuCl₂(*p*-cymene)



(NHC)] (2.33). (Performed by Cesar M. Manna.) In an inert atmosphere glove box, a mixture of 1,3-bis(mesityl)imidazolium chloride (1.21 g, 3.56 mmol, 2.00 equiv.), *tert*-butoxide (0.44 g, 4.04 mmol, 2.30 equiv.), and THF (25 mL) were stirred at room temperature for 40 minutes. The

resulting orange solution was concentrated and added to a solution of dichloro(*p*-cymene)ruthenium(II) dimer (1.06 g, 1.78 mmol, 1.00 equiv.) in toluene (25 mL). The reaction mixture was stirred at 23 °C for 2 hours. The resulting brown slurry was concentrated *in vacuo* and the remaining solid was washed with Et₂O and pentane sequentially. The product was obtained in quantitative yield. Spectroscopic data were in agreement with the reported literature values.⁵¹

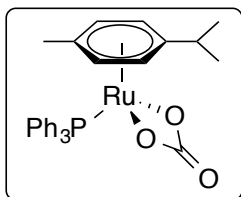
Chlorotris(triphenylphosphine)rhodium [RhCl(PPh₃)₃] (2.34). (Performed by Cesar



M. Manna.) A mixture of rhodium trichloride hydrate (0.40 g, 1.9 mmol, 1.0 equiv.), triphenylphosphine (2.4 g, 9.2 mmol, 4.8 equiv.), and

ethanol (19 mL) was refluxed for 30 minutes. The resulting red slurry was filtered (hot). The red product was obtained in quantitative yield. Spectroscopic data were in agreement with the reported literature values.⁷⁵

(κ²-carbonate)(*p*-cymene)(triphenylphosphine)ruthenium [Ru(κ²-O₂CO)(*p*-cymene)

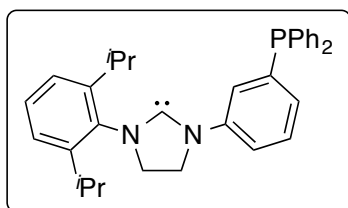


(PPh₃)] (2.40). (Performed by Cesar M. Manna.) A mixture of dichloro(*p*-cymene)(triphenylphosphine)ruthenium (RuCl₂(*p*-cymene)(PPh₃)) (2.32; 0.20 g, 0.35 mmol, 1.0 equiv.), potassium bicarbonate (0.080 g, 0.81 mmol, 2.3 equiv.), acetone (4 mL), and water (0.4 mL) was stirred for 3

hours. The resulting yellow slurry was concentrated to dryness and the remaining solid was

extracted with dichloromethane and filtered through Celite and dried under vacuum. The product was obtained in quantitative yield. ^1H NMR (CD_2Cl_2 , 500 MHz): $\delta = 7.35\text{-}7.53$ (m, 15H, Ph), 5.20 (d, $J = 6.1$ Hz, 2H, C_6H_4), 5.11 (d, $J = 6.4$ Hz, 2H, C_6H_4), 2.49 (pent, $J = 6.9$ Hz, 1H, CHMe_2), 2.00 (s, 3H, MeC_6H_4), 1.19 (d, $^3J_{\text{H,H}} = 6.8$ Hz, 6H, CHMe_2). ^{13}C NMR (CD_2Cl_2 , 125 MHz): $\delta = 165.4$ (s, CO_3), 134.5 (d, $J_{\text{C,P}} = 9.7$ Hz, Ph, *meta*), 131.5 (d, $J_{\text{C,P}} = 44.8$ Hz, Ph, *ipso*), 131.0 (s, Ph, *para*), 128.5 (d, $J_{\text{C,P}} = 9.7$ Hz, Ph, *ortho*), 106.9 (s, *CiPr*, *p*-cymene), 96.5 (s, *CMe*, *p*-cymene), 87.8 (d, $J_{\text{C,P}} = 4.2$ Hz, C_6H_4 , 2CH), 87.3 (d, $J_{\text{C,P}} = 5.4$ Hz, C_6H_4 , 2CH), 31.8 (s, CHMe_2), 22.9 (s, CHMe_2), 18.8 (s, MeC_6H_4). ^{31}P NMR (CD_2Cl_2 , 202 MHz): $\delta = +33.1$. Spectroscopic data were in agreement with the reported literature values. ^{76}IR (neat): 3052, 1649, 1611, 1477, 1433, 1231, 1031, 996, 757, 700.27, 524, 495 cm^{-1} . HRMS (ESI+): Calcd. for $\text{C}_{28}\text{H}_{29}\text{PRu}$ $[\text{M} + \text{H}]^+$ 497.1063, Found 497.1051.

1-(2,6-diisopropylphenyl)-3-(3-(diphenylphosphino)phenyl)dihydroimidazol-2-



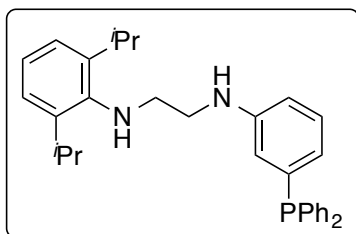
ylidene (2.42). In an inert atmosphere glove box, a mixture of 1-

(2,6-diisopropylphenyl)-3-(3-(diphenylphosphino)phenyl)

dihydroimidazolium tetrafluoroborate (**2.52**; 0.0528 g, 0.0910 mmol, 1.00 equiv.) and sodium bis(trimethylsilylamide) (0.0168

g, 0.0910 mmol, 1.00 equiv.) in toluene (4 mL) was stirred at 23 °C for 12 hours. The yellow mixture was filtered through Celite, washing with toluene. The solvent was removed *in vacuo* to afford the title compound **2.42** as a yellow solid (0.0382 g, 85%). ^1H NMR (C_6D_6 , 500 MHz): δ 8.18 (d, $J = 10$ Hz, 1H), 7.52-7.48 (m, 4H), 7.23 (t, $J = 10$ Hz, 1H), 7.16-7.12 (m, 4H), 7.10-7.01 (m, 7H), 3.22 (t, $J = 10$ Hz, 2H), 3.10 (t, $J = 10$ Hz, 2H), 3.02 (hept, $J = 10$ Hz, 2H), 1.22 (d, $J = 5$ Hz, 6H), 1.17 (d, $J = 5$ Hz, 6H). ^{13}C NMR: Decomposition before obtaining spectrum. ^{31}P NMR (C_6D_6 , 202 MHz): $\delta -4.29$. IR (neat): 2956, 1585, 1431, 1380, 1262, 1189, 739, 691, 490 cm^{-1} . HRMS (ESI+): Calcd. for $\text{C}_{33}\text{H}_{36}\text{N}_2\text{P}$ $[\text{M} + \text{H}]^+$ 491.26161, Found 491.26165.

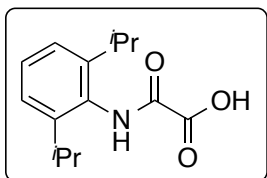
N¹-(2,6-diisopropylphenyl)-N²-(3-(diphenylphosphino)phenyl)ethane-1,2-diamine



(2.43). In an inert atmosphere glove box, lithium aluminum hydride (0.4831 g, 12.7 mmol, 4.00 equiv.) was weighed out in to a pressure vessel (450 mL Parr Instrument) equipped with a magnetic stir bar. THF (24 mL) was added and the mixture was

cooled to 0 °C. A solution of oxalamide **2.49** (1.617 g, 3.18 mmol, 1.00 equiv.) in THF (8 mL) was added drop-wise, during which time the reaction bubbled. The vessel was sealed and the reaction was heated to 150 °C for 12 h. The reaction was monitored by thin layer chromatography with 20% ethyl acetate in hexanes ($R_f = 0.76$). The bright yellow mixture was cooled to 0 °C. Water (20 mL) was carefully added to quench any remaining lithium aluminum hydride, and the mixture was filtered through a pad of Celite. The filtrate was transferred into a separatory funnel containing water (20 mL), and the product was extracted with CH₂Cl₂ (3 x 20 mL). The combined organics were dried over magnesium sulfate, filtered, and concentrated. The crude residue was filtered through a pad of silica gel with 10% ethyl acetate in hexanes as eluent ($R_f = 0.30$) to deliver the title compound **2.43** as a yellow oil (1.1976 g, 78%). ¹H NMR (CDCl₃, 500 MHz): δ 7.38-7.33 (m, 10H), 7.20 (td, $J = 1.5, 7.5$ Hz, 1H), 7.12-7.08 (m, 3H), 6.72-6.64 (m, 3H), 3.34 (t, $J = 5.5$ Hz, 2H), 3.24 (hept, $J = 7$ Hz, 2H), 3.09 (t, $J = 5.5$ Hz, 2H), 1.21 (d, $J = 7$ Hz, 12H). ¹³C NMR (CDCl₃, 125 MHz): δ 148.06 (d, $J_{C,P} = 8.4$ Hz), 142.66, 137.36 (d, $J_{C,P} = 11$ Hz), 133.72 (d, $J_{C,P} = 20$ Hz), 132.08 (d, $J_{C,P} = 11$ Hz), 129.27, 128.57, 128.37 (d, $J_{C,P} = 7.1$ Hz), 124.10, 123.54, 123.08 (d, $J_{C,P} = 18$ Hz), 118.42 (d, $J_{C,P} = 23$ Hz), 117.74, 113.22 (d, $J_{C,P} = 13$ Hz), 50.37, 44.25, 27.61, 24.19. ³¹P NMR (CDCl₃, 202 MHz): δ -3.85. IR (neat): 2959, 1736, 1590, 1433, 1240, 1044, 743, 693 cm⁻¹. HRMS (ESI+): Calcd. for C₃₂H₃₈N₂P₁ [M + H]⁺ 481.27726, Found 481.27723.

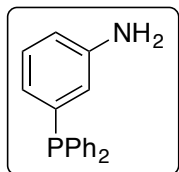
2-((2,6-diisopropylphenyl)amino)-2-oxo-acetic acid (2.44). To a solution of oxoacetate



2.46 (3.610 g, 13.0 mmol, 1.00 equiv.) in THF (87 mL) was added 1 M sodium hydroxide (65 mL, 65 mmol, 5.0 equiv.). The biphasic mixture was stirred at 23 °C for 12 h. The reaction was monitored by thin layer

chromatography with 20% ethyl acetate in hexanes ($R_f = 0$). The mixture was poured into diethyl ether (100 mL). The combined organics were washed with 1 M sodium hydroxide (50 mL). The combined aqueous layers were acidified with 2 M hydrochloric acid (75 mL), and extracted with ethyl acetate (3 x 50 mL). The combined organics were washed with brine (50 mL), dried over magnesium sulfate, and filtered. The solvent was removed *in vacuo* to afford the title compound **2.44** as a colorless solid, which was used without further purification (2.7732 g, 85%). ^1H NMR (CDCl_3 , 500 MHz): δ 8.54 (br s, 1H), 7.37 (t, $J = 7.5$ Hz, 1H), 7.22 (d, $J = 7.5$ Hz, 2H), 2.94 (hept, $J = 7$ Hz, 2H), 1.20 (d, $J = 7$ Hz, 12H). ^{13}C NMR (CDCl_3 , 125 MHz): δ 160.03, 157.24, 145.85, 129.73, 128.71, 124.15, 29.20, 23.80. Spectroscopic data were in agreement with the reported literature values.⁷⁷ IR (neat): 3260, 2960, 1761, 1685, 1528, 1458, 1338, 1229, 1181, 1162, 948, 780, 757, 723, 490 cm^{-1} . HRMS (ESI+): Calcd. for $\text{C}_{14}\text{H}_{20}\text{N}_1\text{O}_3$ $[\text{M} + \text{H}]^+$ 250.14432, Found 250.14508.

3-(diphenylphosphino)aniline (2.45). To a solution of protected aniline phosphine **2.48**

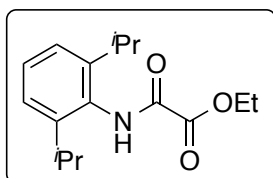


(13.3804 g, 31.7 mmol, 1.00 equiv.) in MeOH (320 mL) was added 2 M hydrochloric acid (79 mL, 160 mmol, 5.0 equiv.) and the reaction was stirred at 23 °C for 2 h. The reaction was monitored by Gas Chromatography (RT: 12.8

min; Column Flow: 1 mL/min H_2 ; Column Temp.: 80 °C - 250 °C; Run Time: 15.5 min.) The mixture was neutralized with 2 M sodium hydroxide (80 mL), and the product was extracted with ethyl acetate (3 x 100 mL). The combined organics were washed with brine (100 mL), dried over magnesium sulfate, filtered, and concentrated. The crude residue was purified by flash column

chromatography with 10% ethyl acetate in hexanes as eluent ($R_f = 0.41$) to deliver the title compound **2.45** as a colorless solid (6.087 g, 69%). ^1H NMR (CDCl_3 , 500 MHz): δ 7.34-7.32 (m, 10H), 7.13 (td, $J = 1.5, 7.5$ Hz, 1H), 6.71 (tt, $J = 1.5, 8.5$ Hz, 1H), 6.66 (dd, $J = 2, 7.5$ Hz, 1H), 6.61 (dt, $J = 1.5, 8.5$ Hz, 1H), 3.63 (br s, 2H). ^{13}C NMR (CDCl_3 , 125 MHz): δ 133.98 (d, $J_{\text{C,P}} = 24$ Hz), 132.30 (d, $J_{\text{C,P}} = 12$ Hz), 132.08 (d, $J_{\text{C,P}} = 12$ Hz), 129.60 (d, $J_{\text{C,P}} = 12$ Hz), 129.57 (d, $J_{\text{C,P}} = 12$ Hz), 128.86, 128.64 (d, $J_{\text{C,P}} = 13$ Hz), 125.11 (d, $J_{\text{C,P}} = 24$ Hz), 121.00 (d, $J_{\text{C,P}} = 26$ Hz), 116.58. ^{31}P NMR (CDCl_3 , 202 MHz): δ -4.86. Spectroscopic data were in agreement with the reported literature values. IR (neat): 3358, 1616, 1587, 1475, 1431, 1299, 1265, 1090, 1025, 991, 782, 743, 690 cm^{-1} . HRMS (ESI+): Calcd. for $\text{C}_{18}\text{H}_{17}\text{N}_1\text{P}_1$ $[\text{M} + \text{H}]^+$ 278.10986, Found 278.10967.⁷⁸

Ethyl 2-((2,6-diisopropylphenyl)amino)-2-oxoacetate (2.46). To a solution of 2,6-

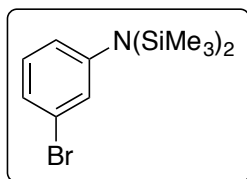


diisopropylaniline (4.0 mL, 21 mmol, 1.1 equiv.) in THF (64 mL) was added triethylamine (3.0 mL, 22 mmol, 1.1 equiv.), and the solution was cooled to 0 °C. Chlorooxoacetate (2.2 mL, 19 mmol, 1.0 equiv.)

was added drop-wise, during which time a colorless solid precipitated out. The mixture then gradually warmed to 23 °C and was stirred for 12 h. The reaction was monitored by thin layer chromatography with 20% ethyl acetate in hexanes ($R_f = 0.46$). The mixture was filtered through a pad of Celite. The filtrate was washed with 2 M hydrochloric acid (50 mL), and extracted with ethyl acetate (3 x 50 mL). The combined organics were washed with brine (50 mL), dried over magnesium sulfate, and filtered. The solvent was removed *in vacuo* to afford the title compound **2.46** as a colorless solid, which was used without further purification (5.3037 g, 99%). ^1H NMR (CDCl_3 , 500 MHz): δ 8.36 (br s, 1H), 7.34 (t, $J = 7.5$ Hz, 1H), 7.20 (d, $J = 8$ Hz, 2H), 4.45 (q, $J = 7$ Hz, 2H), 3.01 (hept, $J = 7$ Hz, 2H), 1.46 (t, $J = 7$ Hz, 3H), 1.21 (d, $J = 7$ Hz, 12H). ^{13}C NMR (CDCl_3 , 125 MHz): δ 161.27, 156.06, 146.04, 129.54, 129.19, 123.94, 63.90, 29.12, 23.86, 14.24.

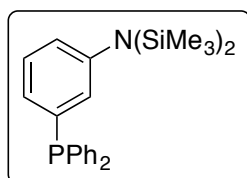
Spectroscopic data were in agreement with the reported literature values.⁷⁷ IR (neat): 2961, 1737, 1685, 1504, 1464, 1368, 1301, 1280, 1205, 1176, 1159, 1019, 797, 732 cm^{-1} . HRMS (ESI+): Calcd. for $\text{C}_{16}\text{H}_{24}\text{N}_1\text{O}_3$ $[\text{M} + \text{H}]^+$ 278.17562, Found 278.17514.

N-(3-bromophenyl)-1,1,1-trimethyl-N-(trimethylsilyl)silanamine (2.47). A solution of



3-bromoaniline (4.0 mL, 37 mmol, 1.0 equiv.) in THF (41 mL) was cooled to $-78\text{ }^\circ\text{C}$ and 2.74 M *n*-butyl lithium in hexanes (14.7 mL, 40.3 mmol, 1.10 equiv.) was added. The reaction was stirred at $-78\text{ }^\circ\text{C}$ for 10 min. Chlorotrimethylsilane (5.1 mL, 40 mmol, 1.1 equiv.) was added and the solution was stirred at $-78\text{ }^\circ\text{C}$ for 30 min. At $-78\text{ }^\circ\text{C}$, 2.74 M *n*-butyl lithium in hexanes (14.7 mL, 40.3 mmol, 1.10 equiv.) was added and the reaction was stirred at $-78\text{ }^\circ\text{C}$ for 10 min. Chlorotrimethylsilane (5.1 mL, 40 mmol, 1.1 equiv.) was added. The solution was then gradually warmed to $23\text{ }^\circ\text{C}$ and stirred for 12 h. The reaction was monitored by gas chromatography (RT: 7.8 min; Column Flow: 1 mL/min H_2 ; Column Temp.: $80\text{ }^\circ\text{C}$ - $250\text{ }^\circ\text{C}$; Run Time: 15.5 min.) The mixture was filtered through a pad of Celite. The filtrate was concentrated to afford the title compound **2.47** as a pale orange oil, which was used without further purification (10.5248 g, 91%). Spectroscopic data were in agreement with the reported literature values.⁷⁸

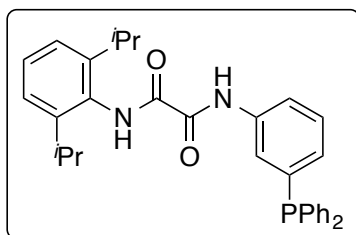
N-(3-(diphenylphosphino)phenyl)-1,1,1-trimethyl-N-(trimethylsilyl)silanamine



(2.48). A solution of protected aniline **2.47** (10.5048 g, 33.2 mmol, 1.00 equiv.) in THF (33 mL) was cooled to $-78\text{ }^\circ\text{C}$ and 2.74 M *n*-butyl lithium in hexanes (13.4 mL, 36.7 mmol, 1.10 equiv.) was added. The reaction was stirred at $-78\text{ }^\circ\text{C}$ for 10 min. Chlorodiphenylphosphine (6.8 mL, 37 mmol, 1.1 equiv.) was added. The solution was then gradually warmed to $23\text{ }^\circ\text{C}$ and stirred for 12 h. The reaction was monitored by gas chromatography (RT: 13.3 min; Column Flow: 1 mL/min H_2 ; Column Temp.:

80 °C - 250 °C; Run Time: 15.5 min.) The mixture was filtered through a pad of Celite. The filtrate was concentrated to afford the title compound **2.48** as a pale yellow oil, which was used without further purification (13.4347 g, 96%). Spectroscopic data were in agreement with the reported literature values.⁷⁸

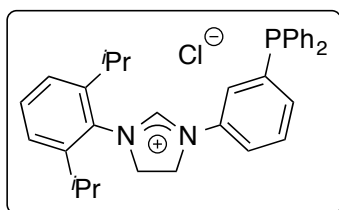
N¹-(2,6-diisopropylphenyl)-N²-(3-(diphenylphosphino)phenyl)oxalamide (2.49). To a



solution of oxo-acetic acid **2.44** (1.0267 g, 4.12 mmol, 1.00 equiv.) in CH₂Cl₂ (20 mL) was added oxalyl chloride (385 μL, 4.55 mmol, 1.10 equiv.). Dimethylformamide (10 μL, 0.13 mmol, 0.030 equiv.) was added, immediately causing the colorless solution to bubble. The reaction was stirred at 23 °C for 4 h, during which time the solution turned bright yellow. The solvent was removed *in vacuo*. The yellow residue was dissolved in CH₂Cl₂ (10 mL) and the solution was cooled to 0 °C. A solution of 3-(diphenylphosphino)aniline (**2.45**; 1.265 g, 4.56 mmol, 1.10 equiv.) in CH₂Cl₂ (10 mL) was added. Triethylamine (805 μL, 5.78 mmol, 1.40 equiv.) was then added drop-wise, during which time the reaction turned cloudy. The mixture then gradually warmed to 23 °C and was stirred for 12 h. The reaction was monitored by thin layer chromatography with 20% ethyl acetate in hexanes (*R_f* = 0.84). The solvent was removed *in vacuo*, and the crude residue was dissolved in CH₂Cl₂ (20 mL). The mixture was poured into saturated aqueous ammonium chloride (20 mL), and extracted with ethyl acetate (3 x 20 mL). The combined organics were washed with 2 M sodium hydroxide (20 mL), brine (20 mL), dried over magnesium sulfate, and filtered. The crude residue was purified by flash column chromatography with 10% ethyl acetate in hexanes as eluent (*R_f* = 0.35) to deliver the title compound **2.49** as an off-white solid (1.726 g, 85%). ¹H NMR (CDCl₃, 500 MHz): δ 9.27 (br s, 1H), 8.84 (br s, 1H), 7.87 (ddd, *J* = 1, 2.5, 8 Hz, 1H), 7.43 (dt, *J* = 1.5, 8 Hz, 1H), 7.39-7.31 (m, 12H), 7.22 (d, *J* = 8 Hz, 2H), 7.17 (tt, *J* = 1, 7.5 Hz, 1H), 3.00

(hept, $J = 7$ Hz, 2H), 1.20 (d, $J = 7$ Hz, 12H). ^{13}C NMR (CDCl_3 , 125 MHz): δ 159.45, 157.60, 145.97, 139.32 (d, $J_{\text{C,P}} = 13$ Hz), 136.69 (d, $J_{\text{C,P}} = 10$ Hz), 133.93 (d, $J_{\text{C,P}} = 19$ Hz), 130.86 (d, $J_{\text{C,P}} = 20$ Hz), 129.53 (d, $J_{\text{C,P}} = 7.7$ Hz), 129.13, 128.78 (d, $J_{\text{C,P}} = 6.8$ Hz), 124.55 (d, $J_{\text{C,P}} = 19$ Hz), 123.87, 120.19, 119.88, 118.43, 115.68, 29.05, 23.78. ^{31}P NMR (CDCl_3 , 202 MHz): δ -4.43. IR (neat): 2961, 1664, 1583, 1498, 1476, 1397, 1383, 1237, 793, 737, 692 cm^{-1} . HRMS (ESI+): Calcd. for $\text{C}_{32}\text{H}_{34}\text{N}_2\text{O}_2\text{P}_1$ $[\text{M} + \text{H}]^+$ 509.23579, Found 509.23328.

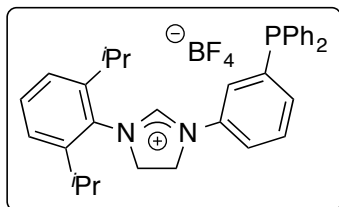
1-(2,6-diisopropylphenyl)-3-(3-(diphenylphosphino)phenyl)imidazolium chloride (2.51)



chloride (2.51). To a mixture of diamine **2.43** (1.177 g, 2.45 mmol, 1.00 equiv.) and ammonium chloride (0.1389 g, 2.59 mmol, 1.03 equiv.) was added triethylorthoformate (12.2 mL, 73.3 mmol, 30.0 equiv.). The reaction was heated to 120 °C for 1

hour. The solvent was removed *in vacuo*. In an inert atmosphere glove box, the crude residue was washed with diethyl ether (10 mL) to afford the title compound **2.51** as an off-white solid (0.7002 g, 54%). ^1H NMR (CD_2Cl_2 , 500 MHz): δ 11.60 (s, 1H), 8.44 (ddd, $J = 0.5, 2.5, 8$ Hz, 1H), 7.55-7.50 (m, 3H), 7.40-7.31 (m, 11H), 7.24 (td, $J = 1, 7$ Hz, 1H), 7.12 (dq, $J = 1, 8$ Hz, 1H), 4.52 (t, $J = 11$ Hz, 2H), 4.26 (t, $J = 11$ Hz, 2H), 2.90 (hept, $J = 7$ Hz, 2H), 1.33 (d, $J = 7$ Hz, 6H), 1.29 (d, $J = 7$ Hz, 6H). ^{13}C NMR (CD_2Cl_2 , 125 MHz): δ 158.38, 148.26, 146.67, 136.76 (d, $J = 11$ Hz), 134.43 (d, $J = 20$ Hz), 132.92, 131.90, 131.08, 129.49 (d, $J = 30$ Hz), 129.34 (d, $J = 12$ Hz), 128.97, 125.52, 125.06, 120.88, 49.42, 29.67, 25.38, 24.48, 24.01. ^{31}P NMR (CD_2Cl_2 , 202 MHz): δ -4.49. IR (neat): 2962, 1617, 1583, 1465, 1407, 1303, 1282, 1179, 743, 693, 557 cm^{-1} . HRMS (ESI+): Calcd. for $\text{C}_{33}\text{H}_{36}\text{N}_2\text{P}_1$ $[\text{M} + \text{H}]^+$ 491.26229, Found 491.26161.

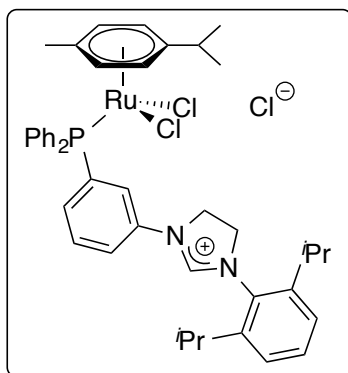
1-(2,6-diisopropylphenyl)-3-(3-(diphenylphosphino)phenyl)dihydroimidazolium



tetrafluoroborate (2.52). To a mixture of diamine **2.43** (0.6171 g, 1.29 mmol, 1.00 equiv.) and ammonium tetrafluoroborate (0.1621 g, 1.55 mmol, 1.20 equiv.) was added triethylorthoformate (6 mL, 40 mmol, 30 equiv.). The reaction

was heated to 120 °C for 1 hour. The solvent was removed *in vacuo*. In an inert atmosphere glove box, the crude residue was washed with diethyl ether (10 mL) to afford the title compound **2.52** as an off-white solid (0.5252 g, 71%). ¹H NMR (DMSO-*d*₆, 500 MHz): δ 9.84 (s, 1H), 7.6-7.53 (m, 4H), 7.44-7.39 (m, 8H), 7.32-7.28 (m, 4H), 7.16 (t, *J* = 5 Hz, 1H), 4.62 (t, *J* = 10 Hz, 2H), 4.29 (t, *J* = 10 Hz, 2H), 3.06 (hept, *J* = 5 Hz, 2H), 1.24 (d, *J* = 5 Hz, 6H), 1.19 (d, *J* = 5 Hz, 6H). ¹³C NMR (DMSO-*d*₆, 125 MHz): δ 156.24, 147.48, 146.66, 145.02, 139.62, 136.21 (d, *J* = 10 Hz), 133.78 (d, *J* = 20 Hz), 131.43, 130.76, 129.76, 129.74, 129.33 (d, *J* = 6.6 Hz), 128.29, 125.22, 119.11, 53.94, 28.07, 25.08, 24.41, 23.71. ³¹P NMR (DMSO-*d*₆, 202 MHz): δ -5.20. IR (neat): 2963, 1617, 1583, 1437, 1312, 1291, 1260, 1128, 1071, 724, 685, 587, 542, 524 cm⁻¹. HRMS (ESI⁺): Calcd. for C₃₃H₃₆N₂P₁ [M + H]⁺ 491.26229, Found 491.26161.

Dichloro(*p*-cymene)(diphenyl-3-(3-(2,6-diisopropylphenyl)dihydroimidazolium chloride)phenyl)ruthenium (**2.53**).

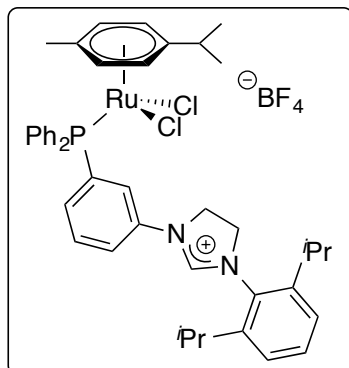


chloride)phenyl)ruthenium (2.53). In an inert atmosphere glove box, a solution of ruthenium dichloro *p*-cymene dimer (0.0159 g, 0.0260 mmol, 1.00 equiv.) and 1-(2,6-diisopropylphenyl)-3-(3-(diphenylphosphino)phenyl)dihydroimidazolium chloride (**2.51**; 0.0285 g, 0.0540 mmol, 2.10 equiv.) in CH₂Cl₂ (1 mL) was stirred at 23 °C for 12 hours.

Hexanes was added to the dark red solution to induce precipitation of the title compound **2.53** as an orange solid (0.0291 g, 67%). ¹H NMR (MeCN-*d*₃, 500 MHz): δ 9.13 (s, 1H), 8.58 (d, *J* = 12

Hz, 1H), 7.84-7.81 (m, 4H), 7.56-7.48 (m, 7H), 7.38-7.35 (m, 4H), 7.12 (t, $J = 8.0$ Hz, 1H), 5.24 (d, $J = 6.3$ Hz, 2H), 5.21 (d, $J = 6.2$ Hz, 2H), 4.55 (t, $J = 11$ Hz, 2H), 4.28 (t, $J = 11$ Hz, 2H), 3.03 (hept, $J = 7.3$ Hz, 2H), 2.52 (hept, $J = 6.7$ Hz, 1H), 1.85 (s, 3H), 1.25 (d, $J = 6.8$ Hz, 2H), 1.22 (d, $J = 6.8$ Hz, 2H), 0.99 (d, $J = 6.6$ Hz, 2H); (MeOD- d_4 , 500 MHz): δ 9.33 (s, 1H), 8.60 (d, $J = 12$ Hz, 1H), 7.88-7.85 (m, 4H), 7.59-7.52 (m, 7H), 7.42-7.36 (m, 4H), 7.59 (t, $J = 8.8$ Hz, 1H), 5.35 (d, $J = 6.4$ Hz, 2H), 5.24 (d, $J = 6.0$ Hz, 2H), 4.65 (t, $J = 10$ Hz, 2H), 4.37 (t, $J = 11$ Hz, 2H), 3.03 (hept, $J = 6.4$ Hz, 2H), 2.64 (hept, 7.1 Hz, 1H), 1.88 (s, 3H), 1.31 (d, $J = 6.8$ Hz, 6H), 1.27 (d, $J = 6.8$ Hz, 6H), 1.07 (d, $J = 6.9$ Hz, 6H); (DMSO- d_6 , 500 MHz): δ 9.68 (m, 1H), 8.26 (d, $J = 12$ Hz, 1H), 7.83-7.79 (m, 4H), 7.55-7.51 (m, 8H), 7.43-7.39 (m, 4H), 5.35 (d, $J = 6.1$ Hz, 2H), 5.31 (d, $J = 6.2$ Hz, 2H), 4.52 (t, $J = 11$ Hz, 2H), 4.31 (t, $J = 10$ Hz, 2H), 3.09-3.04 (m, 3H), 1.78 (s, 3H), 1.22 (d, $J = 6.7$ Hz, 6H), 1.18 (d, $J = 6.5$ Hz, 6H), 0.95 (d, $J = 6.9$ Hz, 6H). ^{13}C (MeCN- d_3 , 125 MHz): δ 154.43, 146.65, 135.17 (d, $J = 44$ Hz), 134.14, 133.84 (d, $J = 10$ Hz), 131.56, 131.47, 130.97 (d, $J = 2.4$ Hz), 129.92, 128.98 (d, $J = 8.4$ Hz), 128.45 (d, $J = 9.9$ Hz), 127.07 (d, $J = 17.5$ Hz), 125.03, 118.81, 109.45, 96.53, 90.00 (d, $J = 4.0$ Hz), 86.96 (d, $J = 5.6$ Hz), 53.86, 49.22, 30.17, 28.17, 24.20, 23.22, 20.94, 16.92. ^{31}P NMR (MeCN- d_3 , 202 MHz): δ +26.61; (MeOD- d_4 , 202 MHz): δ +27.20; (DMSO- d_6 , 202 MHz): δ +26.31. IR (neat): 2962, 1624, 1582, 1465, 1434, 1301, 1260, 1052, 1027, 749, 691, 526, 505 cm^{-1} . HRMS (ESI+): Calcd. for $\text{C}_{43}\text{H}_{50}\text{Cl}_2\text{N}_2\text{PRu} [\text{M} + \text{H}]^+$ 797.2390, Found 797.23501.

Dichloro(*p*-cymene)(diphenyl-(3-(3-(2,6-diisopropylphenyl)dihydroimidazolium tetrafluoroborate)phenyl))ruthenium (2.54).



tetrafluoroborate)phenyl))ruthenium (2.54). In an inert atmosphere glove box, a solution of ruthenium dichloro *p*-cymene dimer (0.0452 g, 0.0740 mmol, 1.00 equiv.) and 1-(2,6-diisopropylphenyl)-3-(3-(diphenylphosphino)phenyl)dihydroimidazolium tetrafluoroborate (**2.52**; 0.1027 g, 0.180 mmol, 2.10 equiv.) in CH₂Cl₂ (3 mL) was stirred at 23 °C for 12 hours.

Hexanes was added to the dark red solution to induce precipitation of the title compound **2.54** as an orange solid (0.1571 g, 92%). ¹H NMR (MeCN-*d*₃, 500 MHz): δ 8.64 (s, 1H), 8.62 (d, *J* = 10 Hz, 1H), 7.84-7.80 (m, 4H), 7.56-7.49 (m, 8H), 7.39-7.36 (m, 3H), 7.32-7.30 (m, 1H), 5.23-5.20 (m, 4H), 4.56 (t, *J* = 5 Hz, 2H), 4.29 (t, *J* = 5 Hz, 2H), 3.06 (hept, *J* = 5 Hz, 2H), 2.51 (hept, *J* = 5 Hz, 1H), 1.85 (s, 3H), 1.26 (d, *J* = 5 Hz, 6H), 1.21 (d, *J* = 5 Hz, 6H), 0.99 (d, *J* = 5 Hz, 6H). ¹³C (MeCN-*d*₃, 125 MHz): δ 155.40, 147.62, 136.14 (d, *J* = 44 Hz), 135.21, 135.10, 134.80 (d, *J* = 9.6 Hz), 132.48 (d, *J* = 13 Hz), 131.93, 130.89, 129.95 (d, *J* = 8.2 Hz), 129.42 (d, *J* = 9.8 Hz), 128.03 (d, *J* = 17 Hz), 126.00, 119.77, 110.42, 97.50, 90.96 (d, *J* = 4.9 Hz), 87.92 (d, *J* = 4.9 Hz), 54.83, 50.19, 31.14, 29.14, 25.17, 24.19, 21.91, 17.89. ³¹P NMR (MeCN-*d*₃, 202 MHz): δ +25.22. IR (neat): 2959, 1624, 1582, 1465, 1433, 1300, 1048, 1030, 749, 692, 526, 505 cm⁻¹. HRMS (ESI+): Calcd. for C₄₃H₅₀Cl₂N₂PRu [M + H]⁺ 797.2132, Found 797.21411.

135.10, 134.06 (d, $J = 10$ Hz), 134.02 (d, $J = 11$ Hz), 132.19 (d, $J = 9.3$ Hz), 131.64 (d, $J = 10$ Hz), 130.56 (d, $J = 2.3$ Hz), 130.49 (d, $J = 2.4$ Hz), 130.20, 129.90, 129.52, 129.20, 129.12, 128.84, 128.45, 128.37, 128.14 (d, $J = 10$ Hz), 128.06 (d, $J = 10$ Hz), 125.74, 124.33, 124.04, 122.07 (d, $J = 9.8$ Hz), 121.93 (d, $J = 11$ Hz), 117.59 (d, $J = 12$ Hz), 117.18 (d, $J = 12$ Hz), 114.55, 114.33, 106.82, 106.70, 96.18, 86.85, 86.60, 50.14, 41.32, 40.65, 31.19, 31.16, 28.33, 28.12, 24.12, 24.00, 22.81, 22.60, 21.42, 17.13. ^{31}P NMR (MeOD- d_4 , 202 MHz): δ +33.39, +33.32 (1.4:1); (1:1 acetone- d_6 /D $_2$ O): δ 31.50, 31.43 (1:1.6). IR (neat): 2961, 1664, 1617, 1590, 1434, 1252, 1054, 743, 693, 509 cm^{-1} . HRMS (ESI+): Calcd. for $\text{C}_{43}\text{H}_{51}\text{N}_2\text{OPRu}$ $[\text{M} + \text{H}]^+$ 743.2795, Found 743.2729.

2.7 References

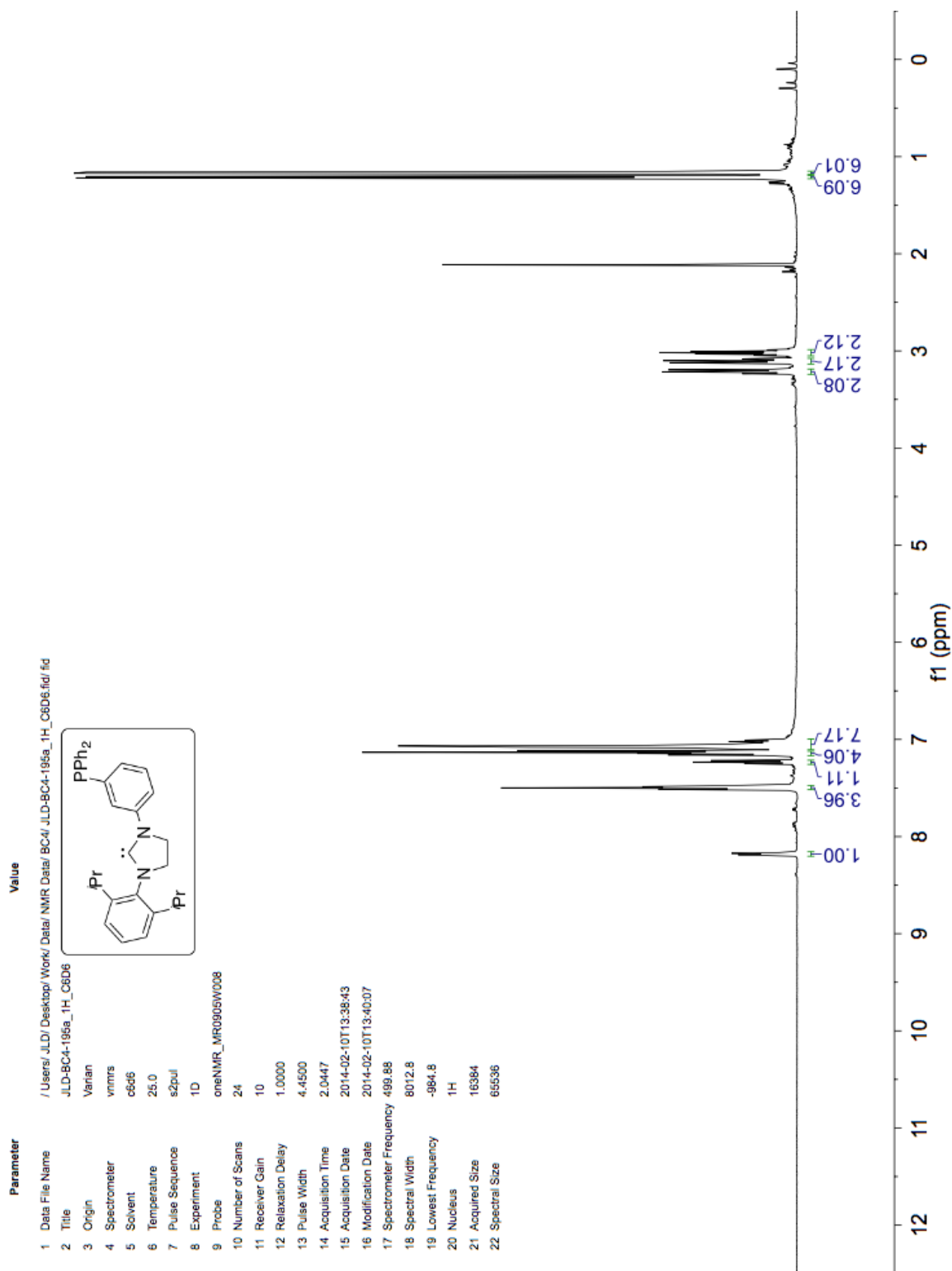
1. Tolman, W. B. *Activation of Small Molecules: Organometallic and Bioinorganic Perspectives*; WILEY-VCH Verlag GmbH & Co. KGaA: Weinheim Germany, 2006.
2. Macyk, W.; Franke, A.; Stochel, G. *Coord. Chem. Rev.* **2005**, *249*, 2437.
3. Stephan, D. W.; Erker, G. *Angew. Chem. Int. Ed.* **2010**, *49*, 46.
4. Power, P. P. *Nature* **2010**, *463*, 171.
5. Dell'Amico, D. B.; Calderazzo, F.; Labella, L.; Marchetti, F.; Pampaloni, G. *Chem. Rev.* **2003**, *103*, 3857.
6. Lewis, G. N. *Valence and the Structure of Atoms and Molecules*; Chemical Catalogue Company: New York, N. Y., 1923.
7. Brønsted, J. N. *Recl. Trav. Chim. Pays-Bas* **1923**, *42*, 718.
8. Brown, H. C.; Schlesinger, H. I.; Cardon, S. Z. *J. Am. Chem. Soc.* **1942**, *64*, 325.
9. Wittig, G.; Benz, E. *Chem. Ber.* **1959**, *92*, 1999.
10. Tochtermann, W. *Angew. Chem. Int. Ed.* **1966**, *5*, 351.
11. Mömming, C. M.; Otten, E.; Kehr, G.; Fröhlich, R.; Grimme, S.; Stephan, D. W.; Erker, G. *Angew. Chem. Int. Ed.* **2009**, *48*, 6643.
12. Ashley, A. E.; Thompson, A. L.; O'Hare, D. *Angew. Chem. Int. Ed.* **2009**, *48*, 9839.
13. Sumerin, V.; Schulz, F.; Nieger, M.; Leskela, M.; Repo, T.; Rieger, B. *Angew. Chem. Int. Ed.* **2008**, *47*, 6001.
14. Berkefeld, A.; Piers, W. E.; Parvez, M. *J. Am. Chem. Soc.* **2010**, *132*, 10660.
15. Sgro, M. J.; Stephan, D. W. *Angew. Chem. Int. Ed.* **2012**, *51*, 11343.
16. Chapman, A. M.; Haddow, M. F.; Wass, D. F. *J. Am. Chem. Soc.* **2011**, *133*, 18463.
17. Glorius, F. *Topics in Organometallic Chemistry: N-Heterocyclic Carbenes in Transition Metal Catalysis*; Springer-Verlag : New York, N. Y., 2007.
18. Marion, N.; Diez-González, S.; Nolan, S. P. *Angew. Chem. Int. Ed.* **2007**, *46*, 2988.
19. Siemeling, U.; Färber, C.; Bruhn, C.; Leibold, M.; Selent, D.; Baumann, W.; von Hopffgarten, M.; Goedecke, C.; Frenking, G. *Chem. Sci.* **2010**, *1*, 697.
20. Siemeling, U. *Aust. J. Chem.* **2011**, *64*, 1109.
21. Kuhn, N.; Steimann, M.; Weyers, G. *Naturforsch, Teil B.* **1999**, *54*, 427.
22. Duong, H. A.; Tekavec, T. N.; Arif, A. M.; Louie, J. *Chem. Commun.* **2004**, 112.
23. Van Ausdall, B. R.; Glass, J. L.; Wiggins, K. M.; Arif, A. M.; Louie, J. *J. Org. Chem.* **2009**, *74*, 7935.
24. Voutchkova, A. M.; Appelhans, L. N.; Chianese, A. R.; Crabtree, R. H. *J. Am. Chem. Soc.* **2005**, *127*, 17624.
25. Voutchkova, A. M.; Feliz, M.; Clot, E.; Eisenstein, O.; Crabtree, R. H. *J. Am. Chem. Soc.* **2007**, *129*, 12834.
26. Tudose, A.; Demonceau, A.; Delaude, L. *J. Organomet. Chem.* **2006**, *691*, 5356.
27. Holbrey, J. D.; Reichert, W. M.; Tkatchenko, I.; Bouajila, E.; Walter, O.; Tommasi, I.; Rogers, R. D. *Chem. Commun.* **2003**, 28.
28. Wang, C.; Luo, H.; Luo, X.; Li, H.; Dai, S. *Green Chem.* **2010**, *12*, 2019.
29. Zhou, H.; Zhang, W.; Liu, C.; Qu, J.; Lu, X. *J. Org. Chem.* **2008**, *73*, 8039.

30. Riduan, S. N.; Zhang, Y.; Ying, J. Y. *Angew. Chem. Int. Ed.* **2009**, *48*, 3322.
31. Matsuo, T.; Kawaguchi, H. *J. Am. Chem. Soc.* **2006**, *128*, 12362.
32. Jansen, A.; Görls, H.; Pitter, S. *Organometallics* **2000**, *19*, 135.
33. Deglmann, P.; Ember, E.; Hofman, P.; Pitter, S.; Walter, O. *Chem. Eur. J.* **2007**, *13*, 2864.
34. Langer, R.; Diskin-Posner, Y.; Leitus, G.; Shimon, L. J. W.; Ben-David, Y.; Milstein, D. *Angew. Chem. Int. Ed.* **2011**, *50*, 9948.
35. Jeletic, M. S.; Mock, M. T.; Appel, A. M.; Linehan, J. C. *J. Am. Chem. Soc.* **2013**, *135*, 11533.
36. DuBois, D. L.; Berning, D. E. *Appl. Organomet. Chem.* **2000**, *14*, 860.
37. Curtis, C. J.; Miedaner, A.; Ellis, W. W.; DuBois, D. L. *J. Am. Chem. Soc.* **2002**, *124*, 1918.
38. Qi, X. J.; Liu, L.; Fu, Y.; Guo, Q. X. *Organometallics* **2006**, *25*, 5879.
39. Qi, X. J.; Fu, Y.; Liu, L.; Guo, Q. X. *Organometallics* **2007**, *26*, 4197.
40. Tanaka, R.; Yamashita, M.; Nozaki, K. *J. Am. Chem. Soc.* **2009**, *131*, 14168.
41. Schmeier, T. J.; Dobereiner, G. E.; Crabtree, R. H.; Hazari, N. *J. Am. Chem. Soc.* **2011**, *133*, 9274.
42. Crabtree, R. H. *The Organometallic Chemistry of the Transition Metal*, 5th ed.; Wiley, 2009.
43. Kumar, N.; Camaioni, D. M.; Dupuis, M.; Raugei, S.; Appel, A. M. *Dalton Trans.* **2014**, *43*, 11803.
44. Jeletic, M. S.; Helm, M. L.; Hulley, E. B.; Mock, M. T.; Appel, A. M.; Linehan, J. C. *ACS Catal.* **2014**, *4*, 3755.
45. Connor, E. F.; Nyce, G. W.; Myers, M.; Möck, A.; Hedrick, J. L. *J. Am. Chem. Soc.* **2002**, *124*, 914.
46. Nyce, G. W.; Lamboy, J. A.; Connor, E. F.; Waymouth, R. M.; L., H. J. *Org. Lett.* **2002**, *4*, 3587.
47. Grasa, G. A.; Kissling, R. M.; Nolan, S. P. *Org. Lett.* **2002**, *4*, 3583.
48. Chen, J.; Huang, Y. *Nat. Commun.* **2014**, *5*, 3437.
49. Candish, L.; Lupton, D. W. *Chem. Sci.* **2012**, *3*, 380.
50. Jessop, P. G.; Hsiao, Y.; Ikariya, T.; Noyori, R. *J. Am. Chem. Soc.* **1996**, *118*, 344.
51. Lo, C.; Cariou, R.; Fischmeister, C.; Dixneuf, P. H. *Adv. Synth. Catal.* **2007**, *349*, 546.
52. Fèvre, M.; Pinaud, J.; Leteneur, A.; Gnanou, Y.; Vignolle, J.; Taton, D.; Miqueu, K.; Sotiropoulos, J. M. *J. Am. Chem. Soc.* **2012**, *134*, 6776.
53. Drake, J. B.; Manna, C. M.; Byers, J. A. *Organometallics* **2013**, *32*, 6891.
54. Munshi, P.; Main, A. D.; Linehan, J. C.; Tai, C. C.; Jessop, P. G. *J. Am. Chem. Soc.* **2002**, *124*, 7963.
55. Ziebart, C.; Federsel, C.; Anbarasan, P.; Jackstell, R.; Baumann, W.; Spannenberg, A.; Beller, M. *J. Am. Chem. Soc.* **2012**, *134*, 20701.
56. Demerseman, B.; Mbaye, M. D.; Sémeril, D.; Toupet, L.; Bruneau, C.; Dixneuf, P. J. *Eur. J. Inorg. Chem.* **2006**, 1174.
57. Gowrisankar, S.; Federsel, C.; Neumann, H.; Ziebart, C.; Jackstell, R.; Spannenberg, A.; Beller, M. *ChemSusChem* **2013**, *6*, 85.
58. Elek, J.; Nádasdi, L.; Papp, G.; Laurenczy, G.; Joó, F. *Appl. Catal., A* **2003**, *255*, 59.
59. Getty, A. D.; Tai, C. C.; Linehan, J. C.; Jessop, P. G.; Olmstead, M. M.; Rheingold, A. L. *Organometallics* **2009**, *28*, 5466.

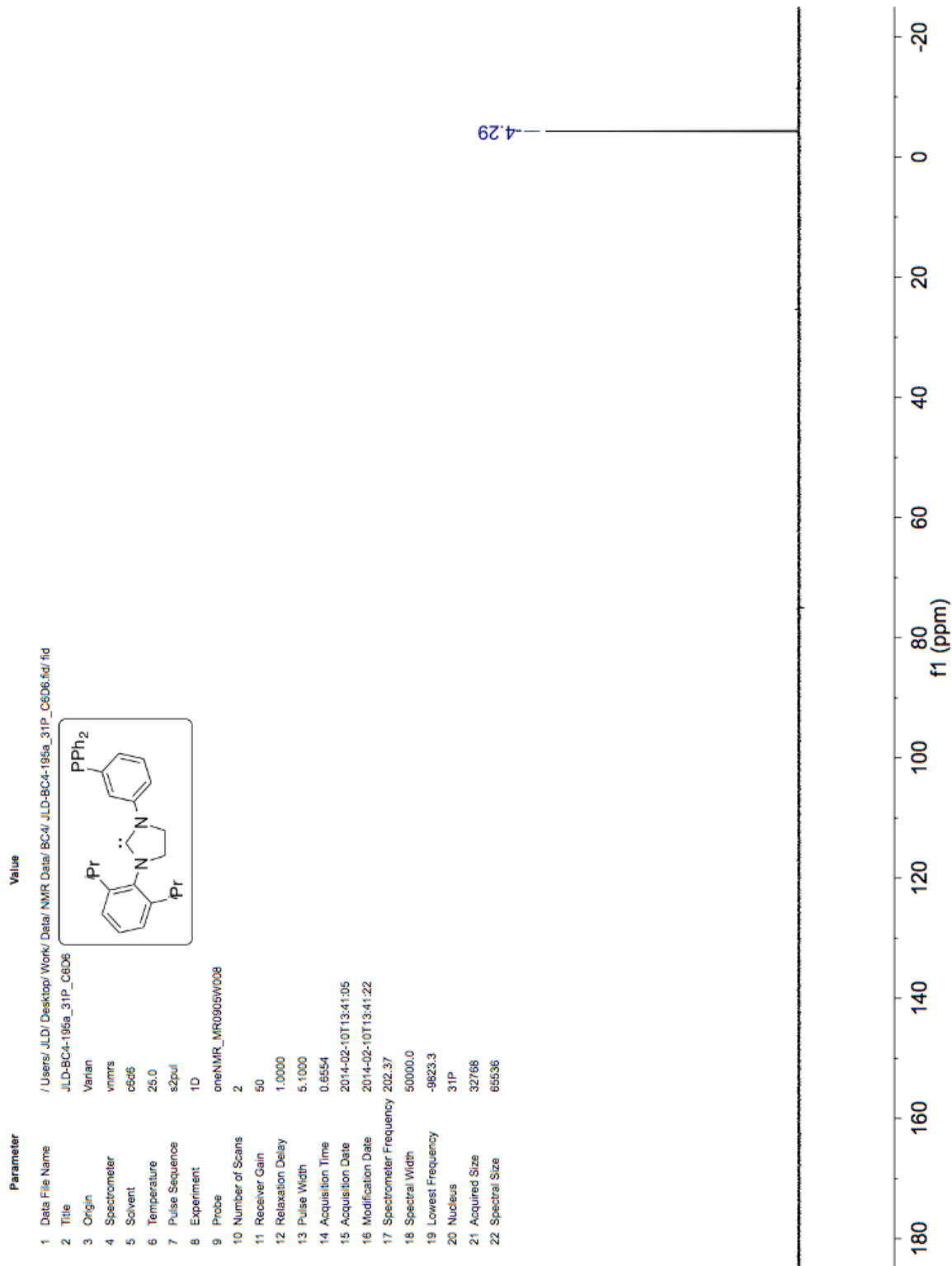
60. Wesselbaum, S.; vom Stein, T.; Klankermayer, J.; Leitner, W. *Angew. Chem. Int. Ed.* **2012**, *51*, 7499.
61. Waltman, A. W.; Grubbs, R. H. *Organometallics* **2004**, *23*, 3105.
62. Laungani, A. C.; Keller, M.; Slattery, J. M.; Krossing, I.; Breit, B. *Chem. Eur. J.* **2009**, *15*, 10405.
63. Gong, Q.; Luo, H.; Cao, D.; Zhang, H.; Wang, W.; Zhou, X. *Bull. Korean Chem. Soc.* **2012**, *33*, 1945.
64. Liu, H.; Zeng, R.; Hua, R. *Int. J. Mol. Sci.* **2014**, *15*, 9945.
65. Burger, J. B.; Bercaw, J. E. *New Developments in the Synthesis, Manipulation, and Characterization of Organometallic Compounds*; American Chemical Society: Washington, D.C., 1987.
66. Pangborn, A. B.; Giardello, M. A.; Grubbs, R. H.; Rose, R. K.; Timmers, F. J. *Organometallics* **1996**, *15*, 1518.
67. Still, W. C.; Kahn, M.; Mitra, A. *J. Org. Chem.* **1978**, *43*, 2923.
68. Duong, H. A.; Tekavec, T. N.; Arif, A. M.; Louie, J. *Chem. Commun.* **2004**, 112.
69. Fèvre, M.; Pinaud, J.; Leteneur, A.; Gnanou, Y.; Vignolle, J.; Taton, D. *J. Am. Chem. Soc.* **2012**, *134*, 6776.
70. Van Ausdall, B. R.; Glass, J. L.; Wiggins, K. M.; Aarif, A. M.; Louie, J. *J. Org. Chem.* **2009**, *74*, 7935.
71. Tang, P.; Wang, W.; Ritter, T. *J. Am. Chem. Soc.* **2011**, *133*, 11482.
72. Mura, P.; Olby, B. G.; Robinson, S. D. *J. Chem. Soc., Dalton Trans* **1985**, 2101.
73. Joslin, E. E.; McMullin, C. L.; Gunnoe, T. B.; Cundrai, T. R.; Sabat, M.; Myers, W. H. *Inorg. Chem.* **2012**, *51*, 4791.
74. Hodson, E.; Simpson, S. J. *Polyhedron* **2004**, *23*, 2695.
75. Diao, Y.; Li, J.; Wang, L.; Yang, P.; Yan, R.; Jiang, L.; Zhang, H.; Zhang, S. *Catal. Today* **2013**, *200*, 54.
76. Demerseman, B.; Mbaye, M. D.; Sémeril, D.; Toupet, L.; Bruneau, C.; Dixneuf, P. H. *Eur. J. Inorg. Chem.* **2006**, 1174.
77. Waltman, A. W.; Grubbs, R. H. *Organometallics* **2004**, *23*, 3105.
78. Laungani, A. C.; Keller, M.; Slattery, J. M.; Krossing, I.; Breit, B. *Chem. Eur. J.* **2009**, *15*, 10405.

2.8 Spectra

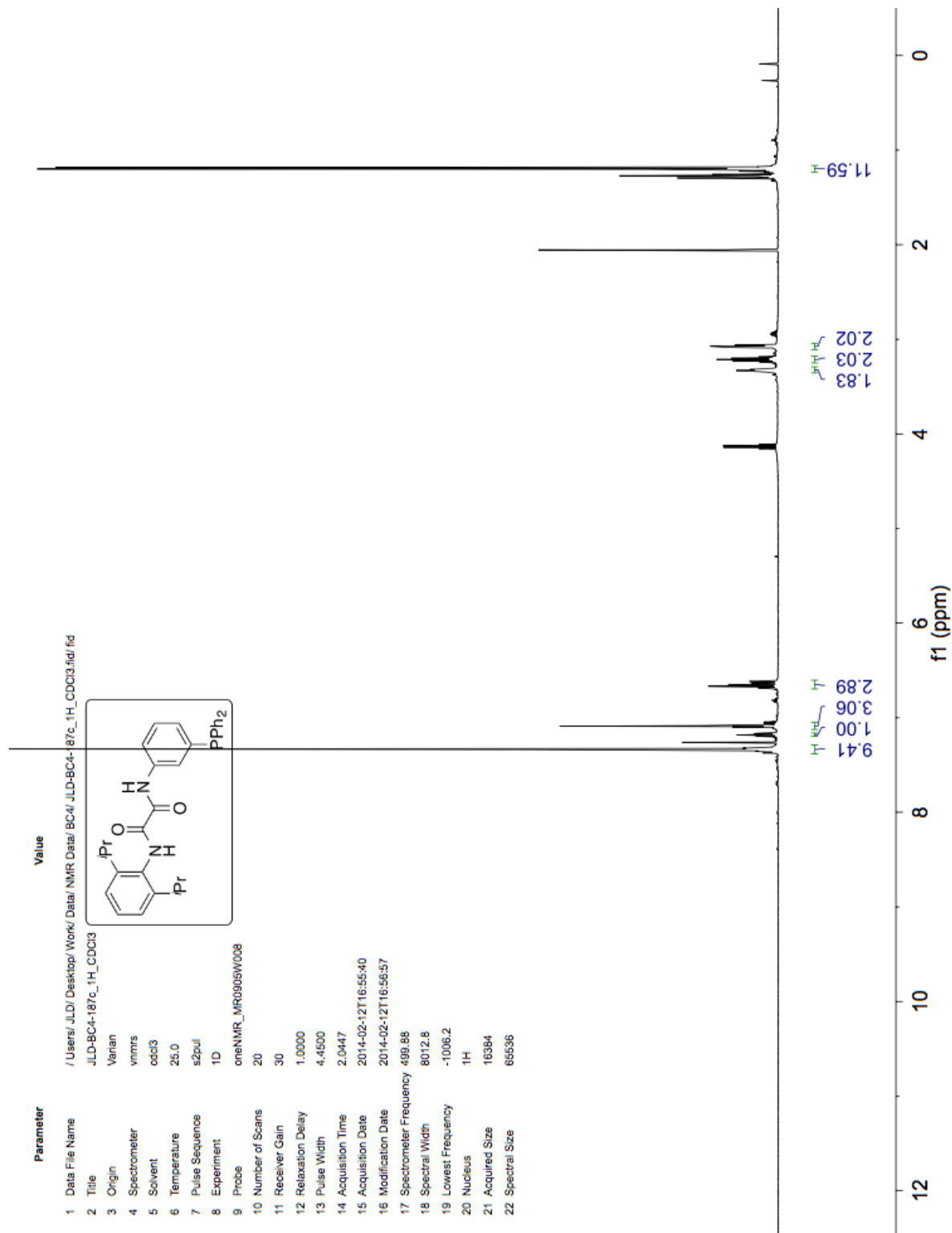
¹H NMR Spectrum of 1-(2,6-diisopropylphenyl)-3-(3-(diphenylphosphino)phenyl)dihydroimidazol-2-ylidene (2.42) in C₆D₆.



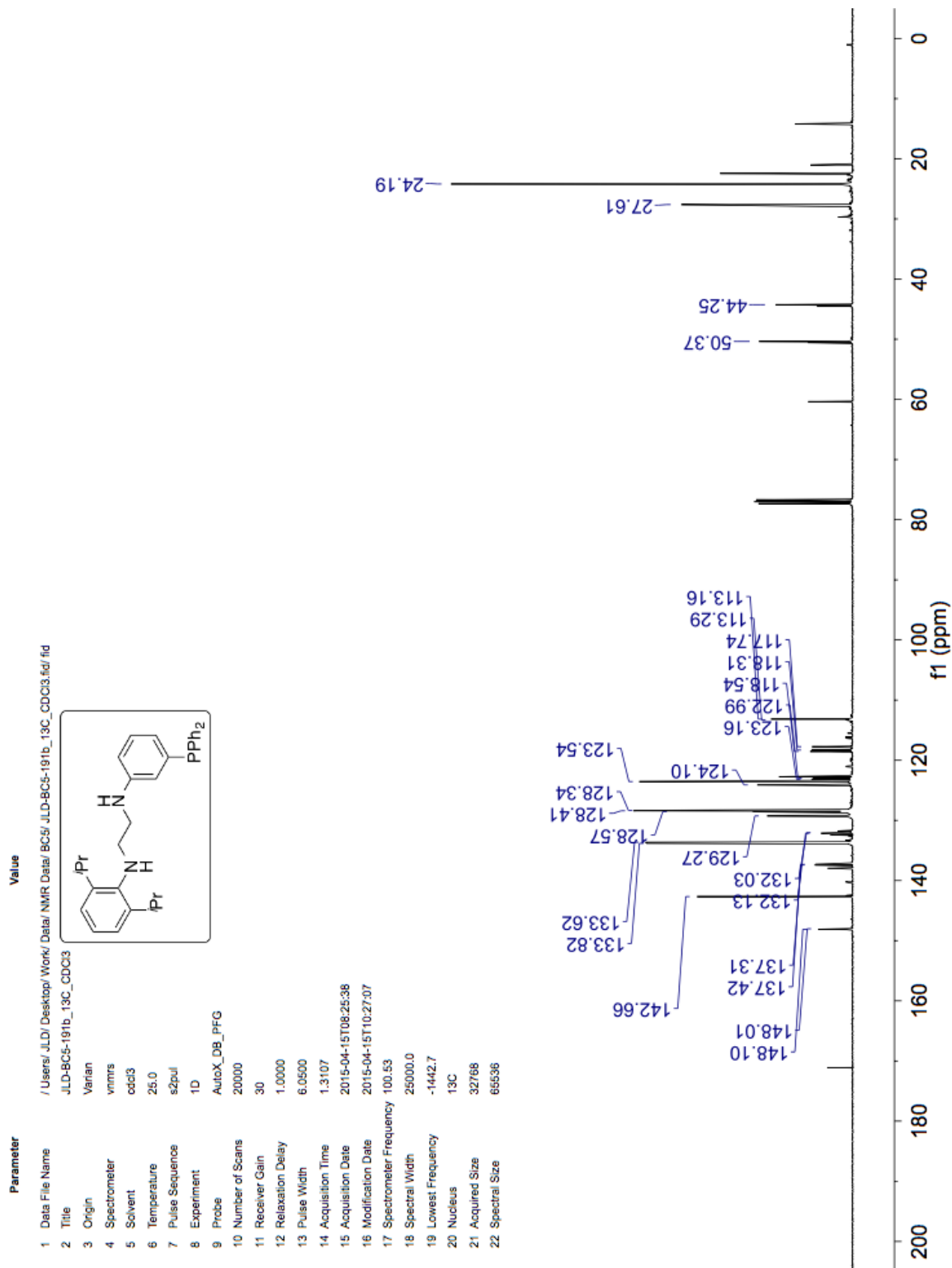
³¹P NMR Spectrum of 1-(2,6-diisopropylphenyl)-3-(3-(diphenylphosphino)phenyl)dihydroimidazol-2-ylidene (2.42) in C₆D₆.



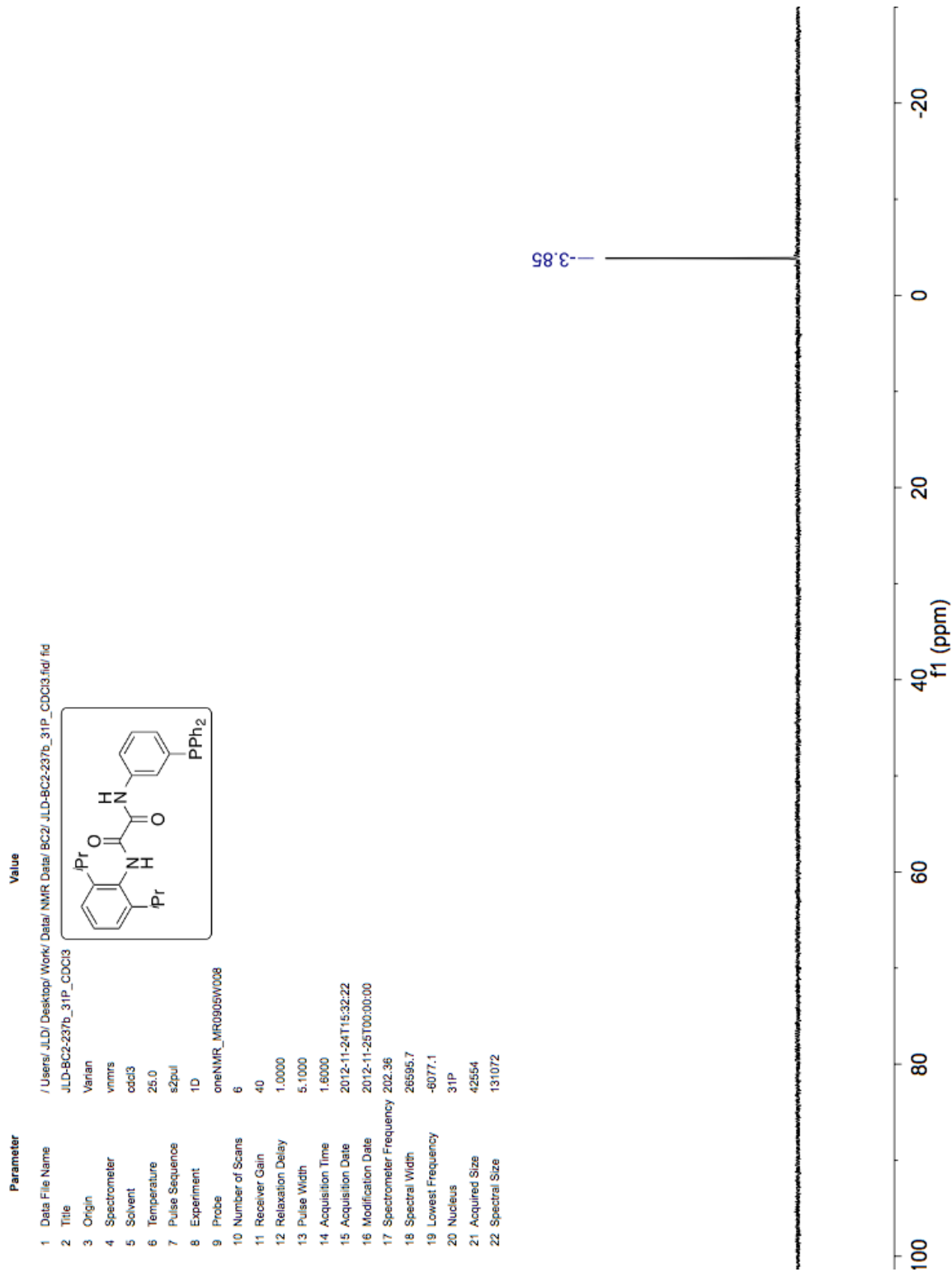
^1H NMR Spectrum of N^1 -(2,6-diisopropylphenyl)- N^2 -(3-(diphenylphosphino)phenyl)ethane-1,2-diamine (2.43) in CDCl_3 .



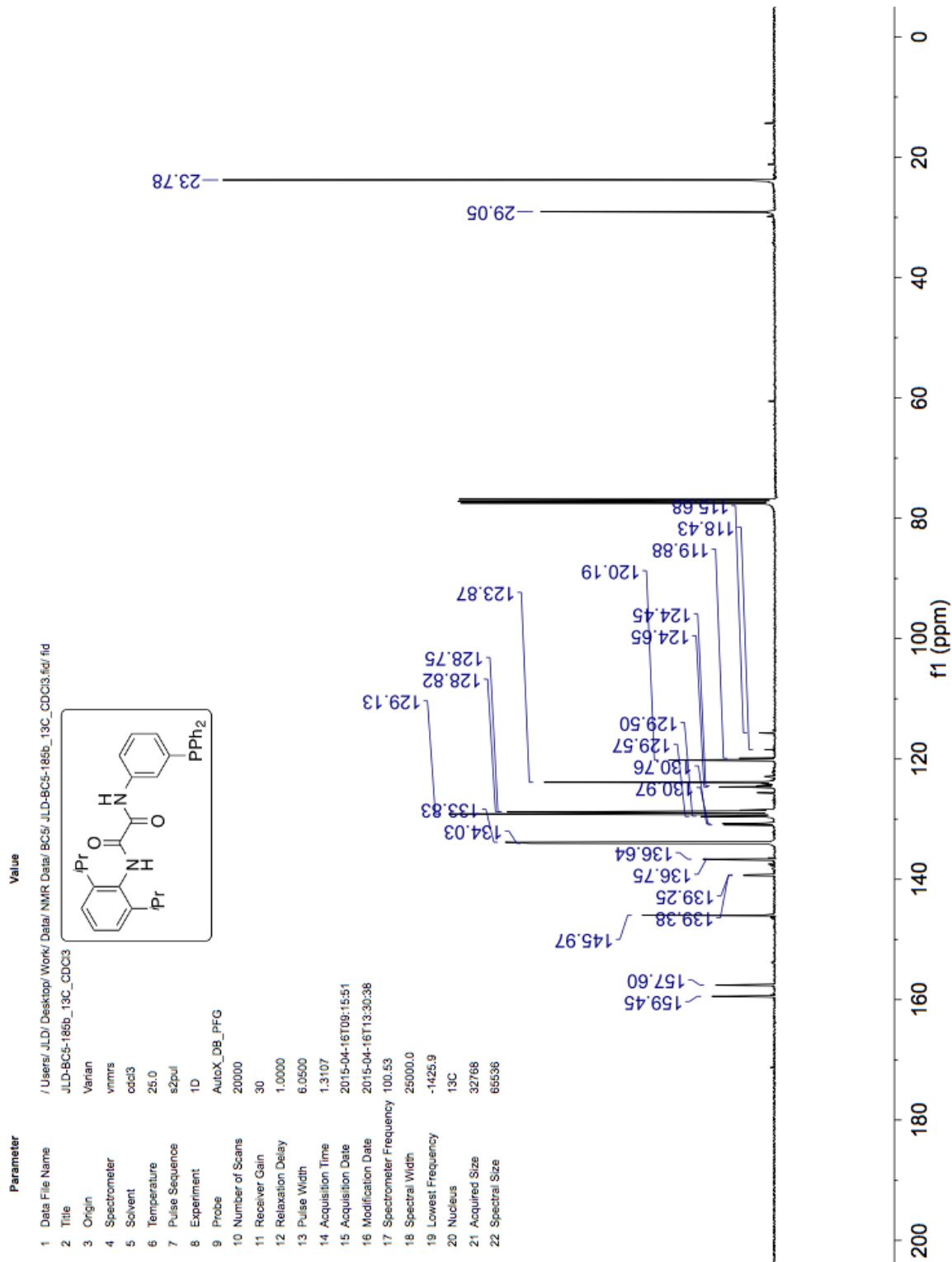
^{13}C NMR Spectrum of N^1 -(2,6-diisopropylphenyl)- N^2 -(3-(diphenylphosphino)phenyl)ethane-1,2-diamine (2.43) in CDCl_3 .



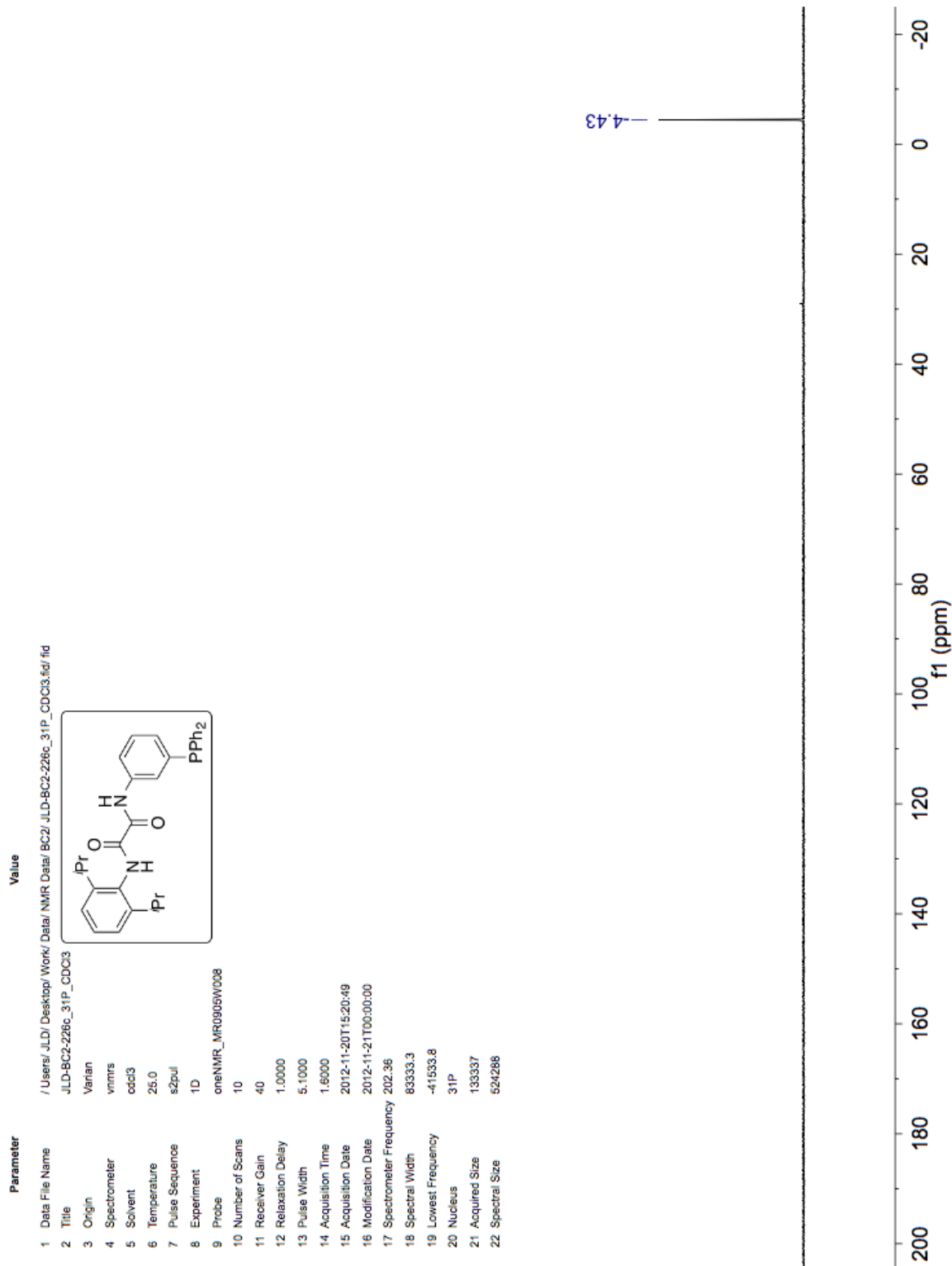
³¹P NMR Spectrum of N¹-(2,6-diisopropylphenyl)-N²-(3-(diphenylphosphino)phenyl)ethane-1,2-diamine (2.43) in CDCl₃.



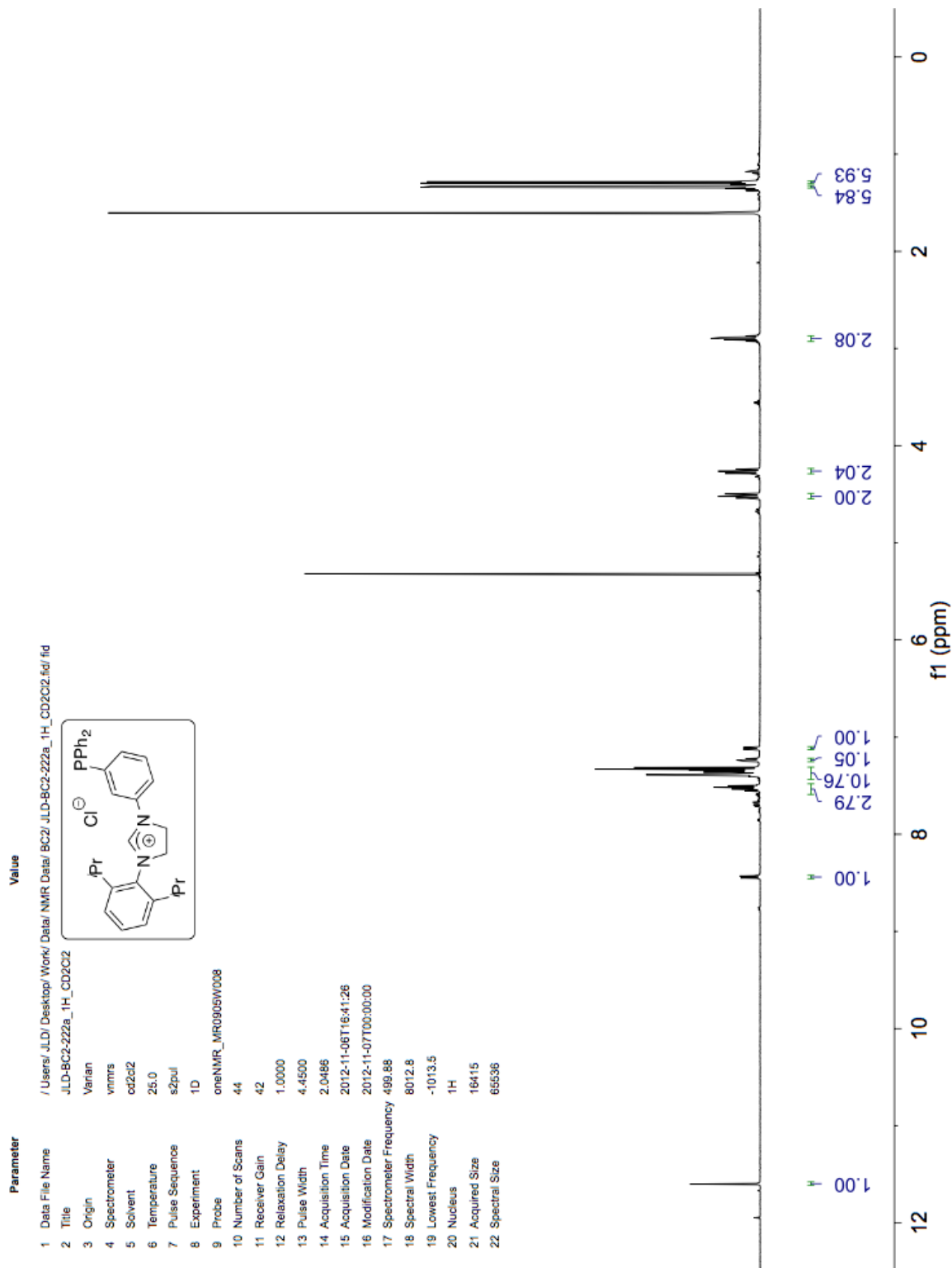
^{13}C NMR Spectrum of N^1 -(2,6-diisopropylphenyl)- N^2 -(3-(diphenylphosphino)phenyl) oxalamide (2.49) in CDCl_3 .



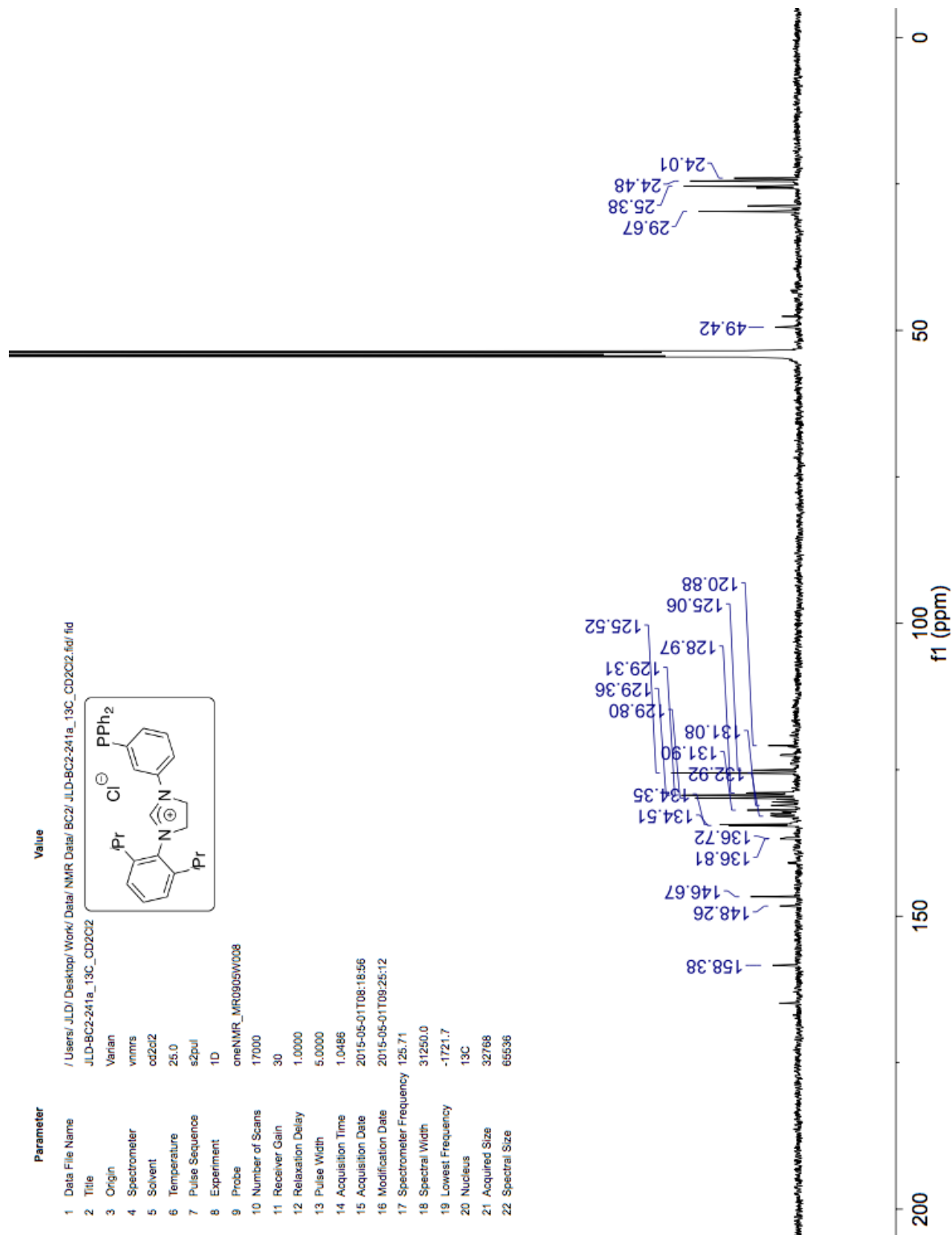
³¹P NMR Spectrum of N¹-(2,6-diisopropylphenyl)-N²-(3-(diphenylphosphino)phenyl) oxalamide (2.49) in CDCl₃.



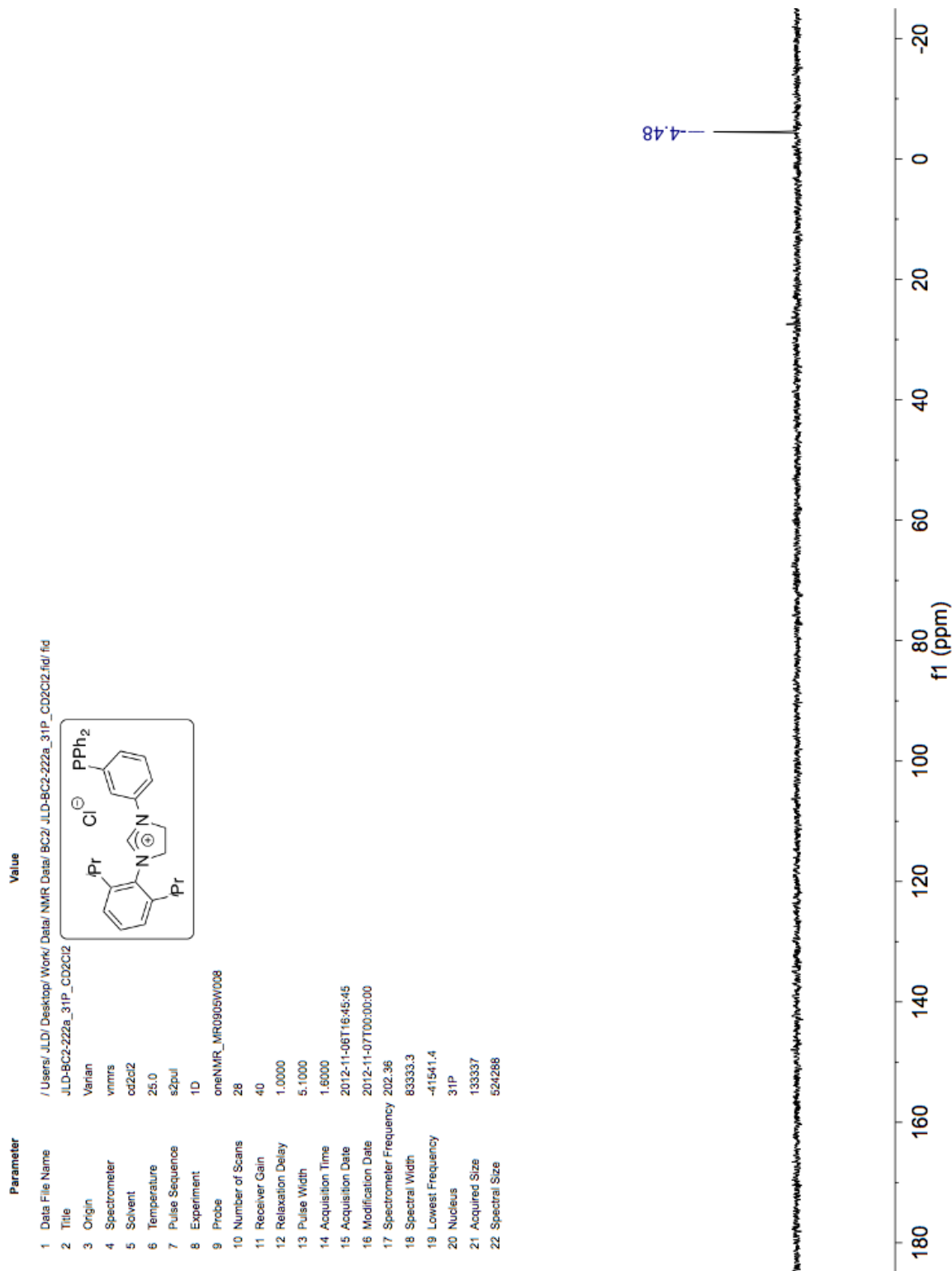
¹H NMR Spectrum of 1-(2,6-diisopropylphenyl)-3-(3-(diphenylphosphino)phenyl)imidazolium chloride (2.51) in CD₂Cl₂.



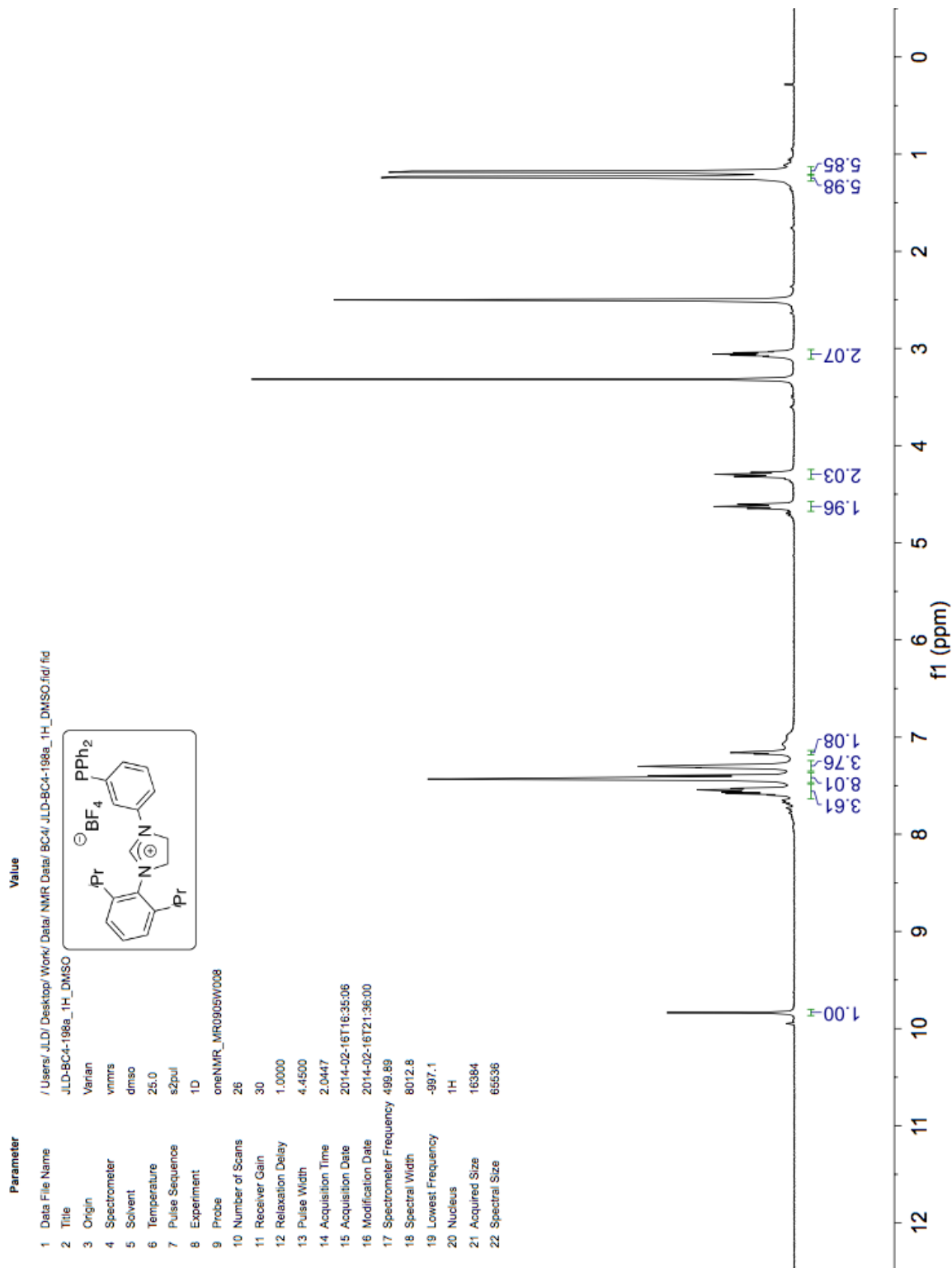
^{13}C NMR Spectrum of 1-(2,6-diisopropylphenyl)-3-(3-(diphenylphosphino)phenyl)imidazolium chloride (2.51) in CD_2Cl_2 .



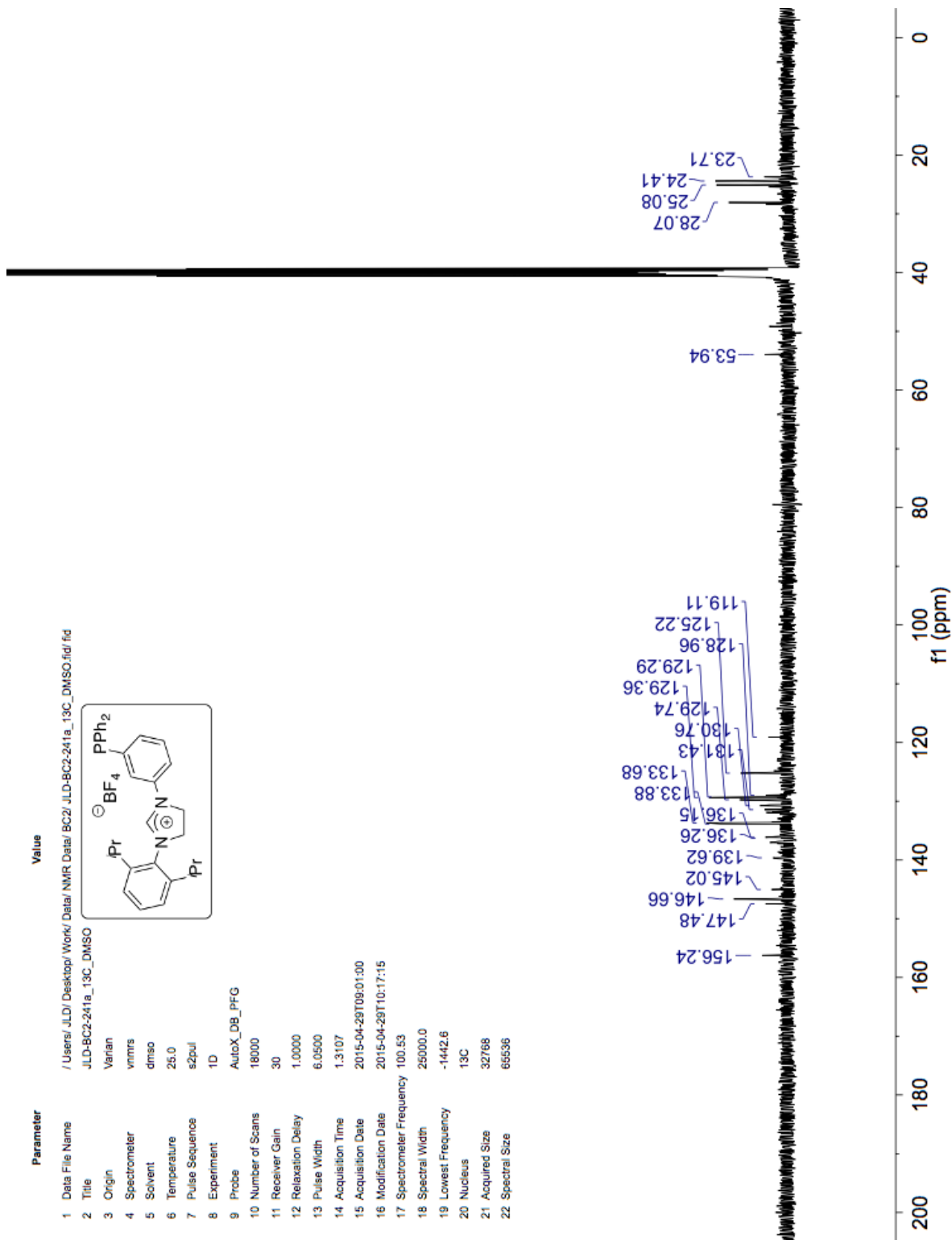
³¹P NMR Spectrum of 1-(2,6-diisopropylphenyl)-3-(3-(diphenylphosphino)phenyl)imidazolium chloride (2.51) in CD₂Cl₂.



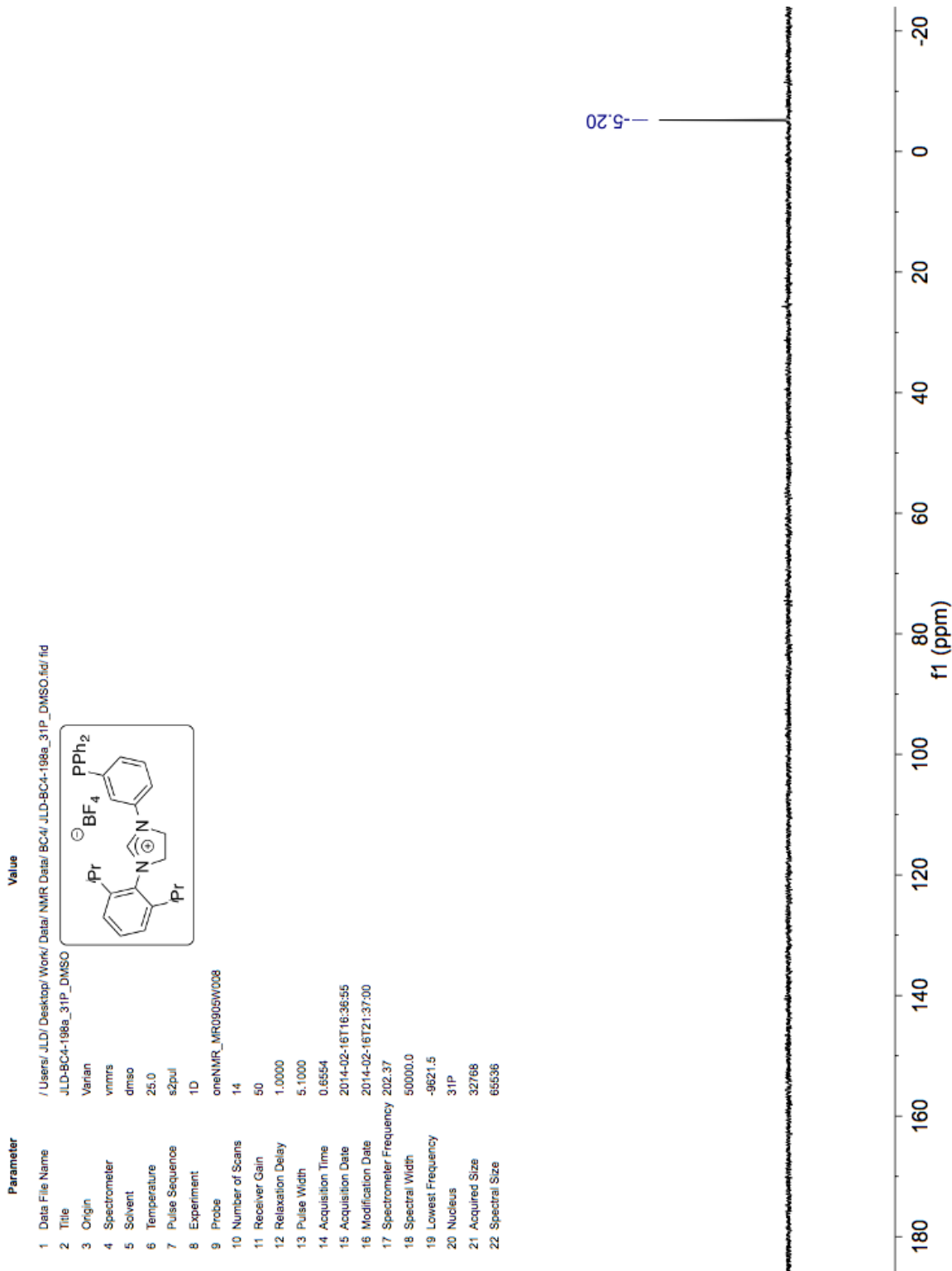
¹H NMR Spectrum of 1-(2,6-diisopropylphenyl)-3-(3-(diphenylphosphino)phenyl)imidazolium tetrafluoroborate (2.52) in DMSO-d₆.



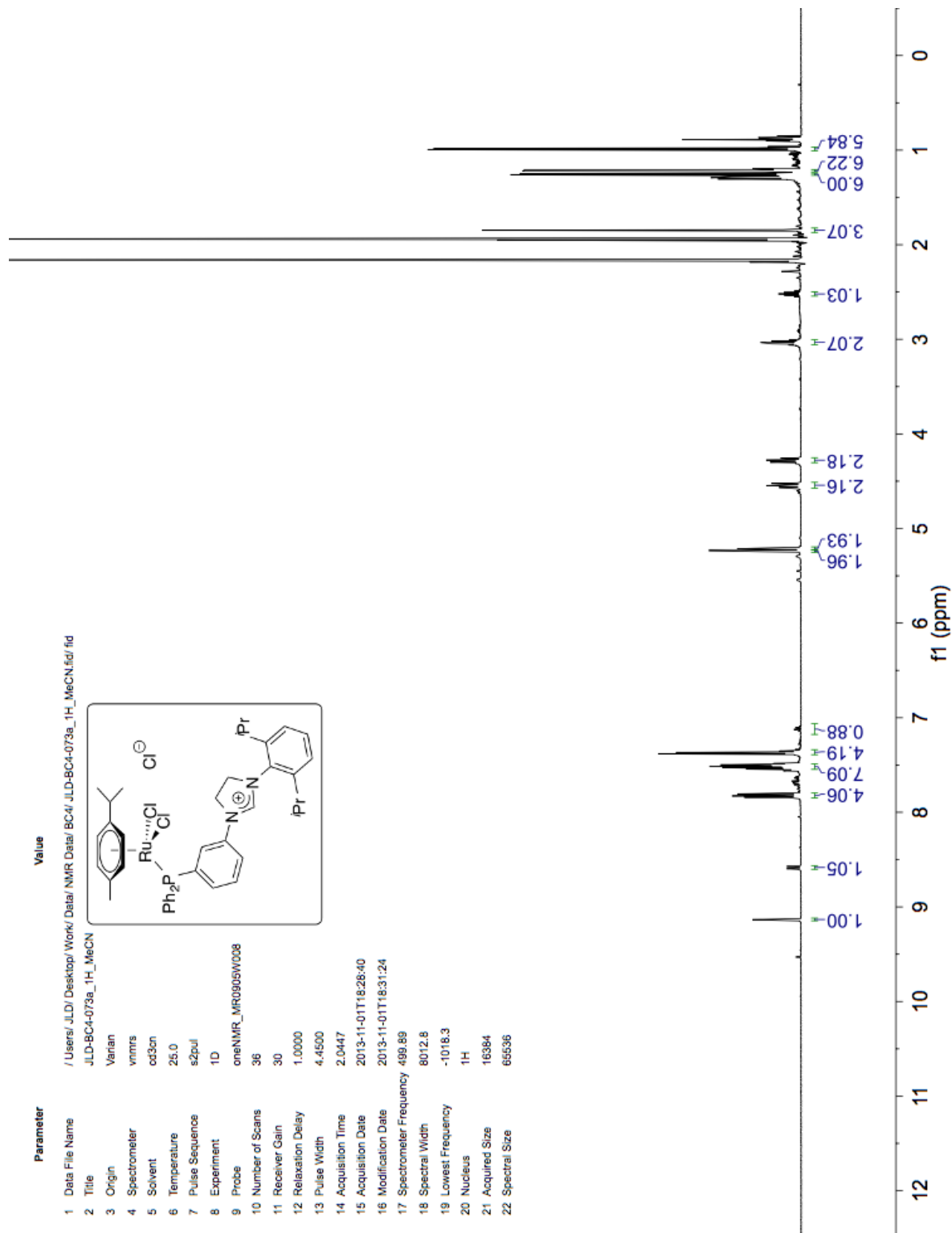
¹³C NMR Spectrum of 1-(2,6-diisopropylphenyl)-3-(3-(diphenylphosphino)phenyl)imidazolium tetrafluoroborate (2.52) in DMSO-*d*₆.



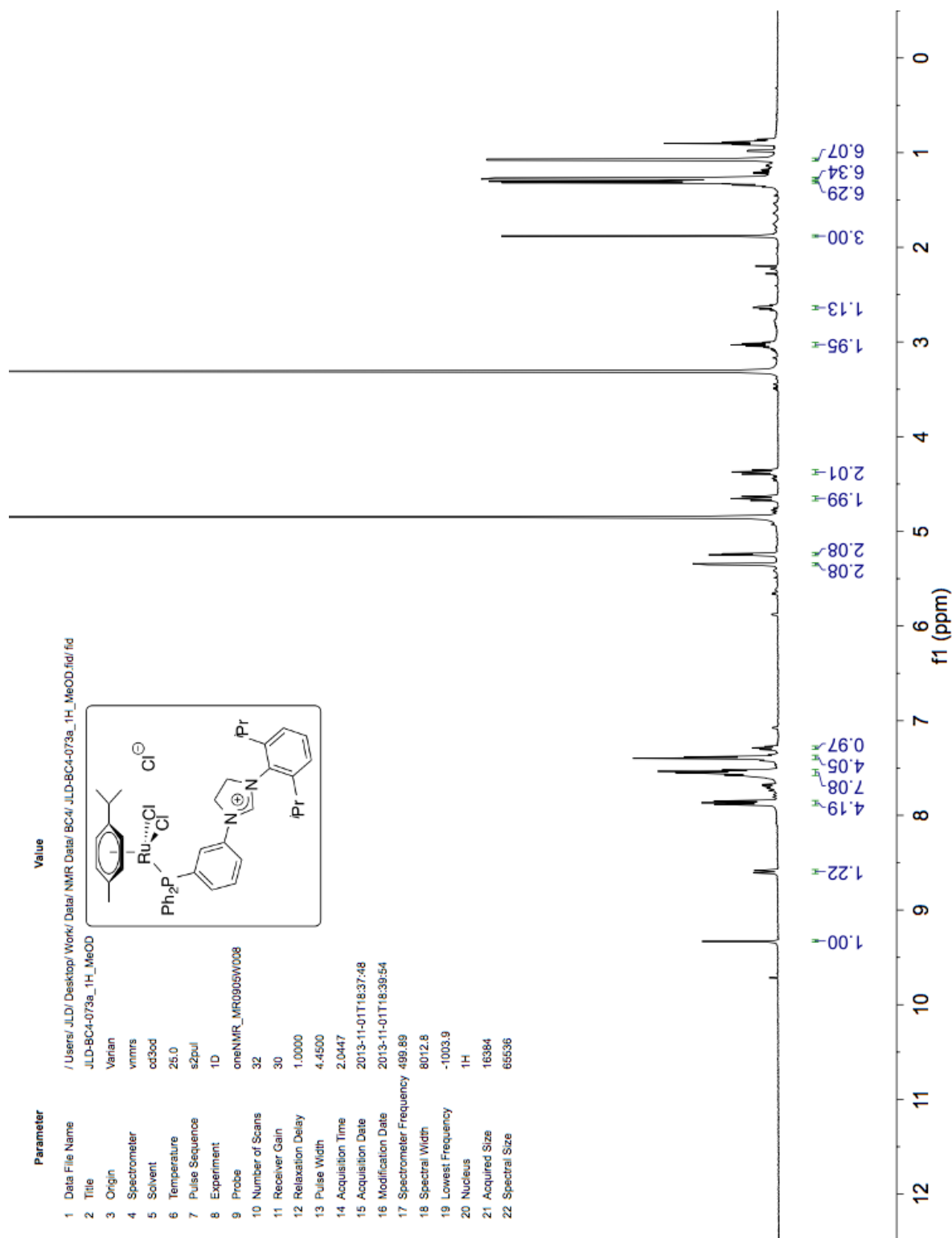
^{31}P NMR Spectrum of 1-(2,6-diisopropylphenyl)-3-(3-(diphenylphosphino)phenyl)imidazolium tetrafluoroborate (2.52) in $\text{DMSO-}d_6$.



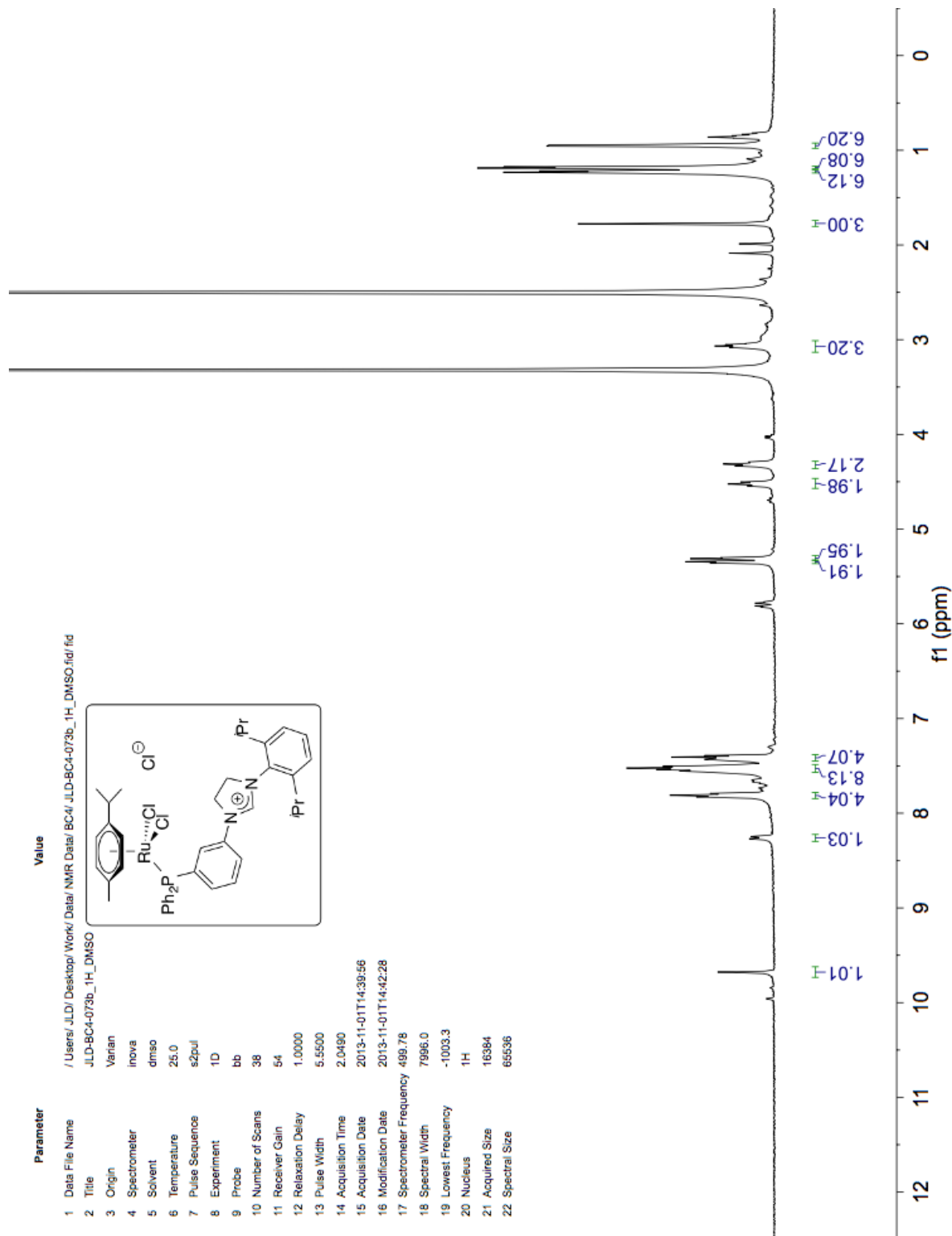
¹H NMR Spectrum of Dichloro(*p*-cymene)(diphenyl-(3-(3-(2,6-diisopropylphenyl)dihydroimidazolium chloride)phenyl))ruthenium (2.53) in MeCN-*d*₃.



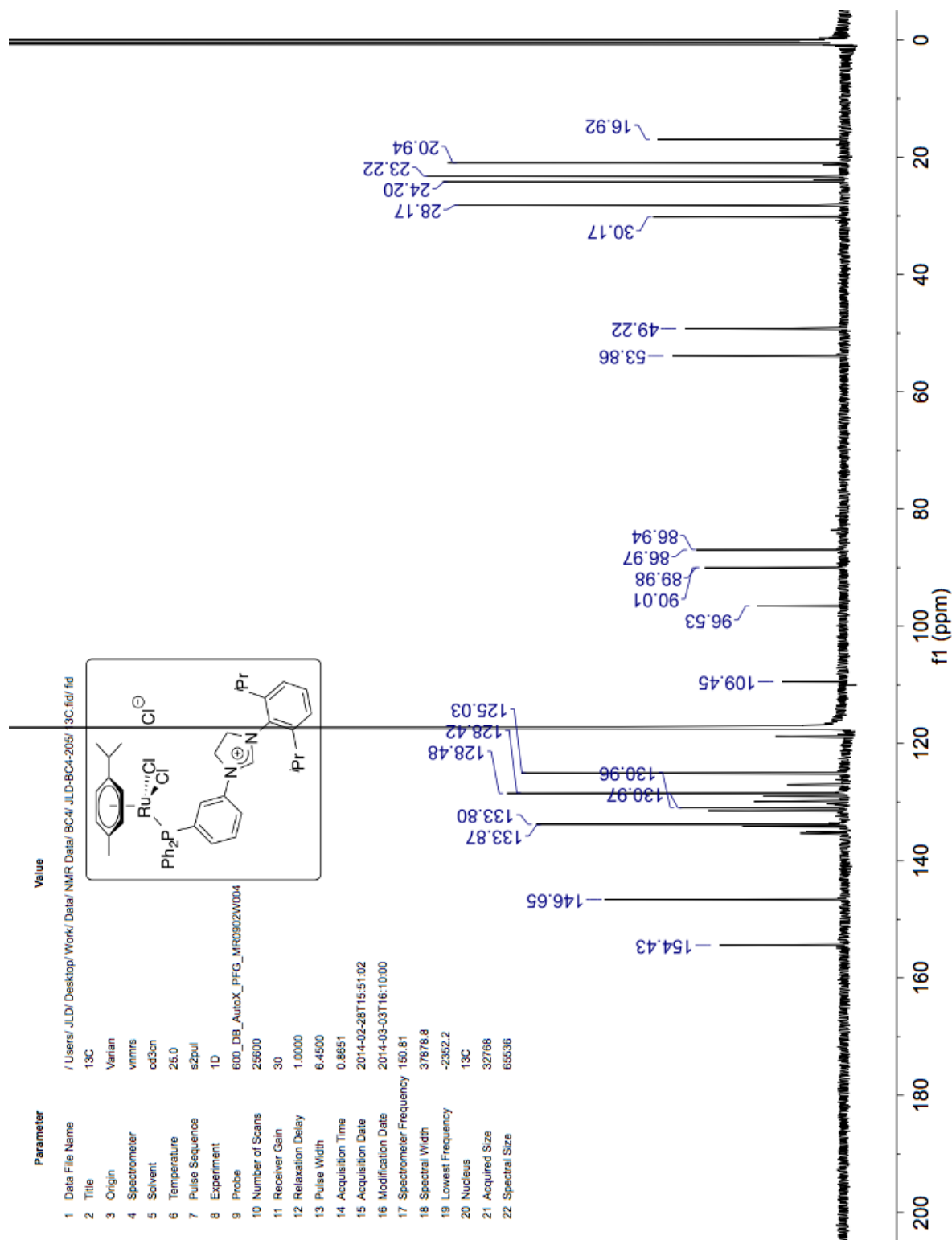
¹H NMR Spectrum of Dichloro(*p*-cymene)(diphenyl-(3-(3-(2,6-diisopropylphenyl)dihydroimidazolium chloride)phenyl))ruthenium (2.53) in MeOD-*d*₄.



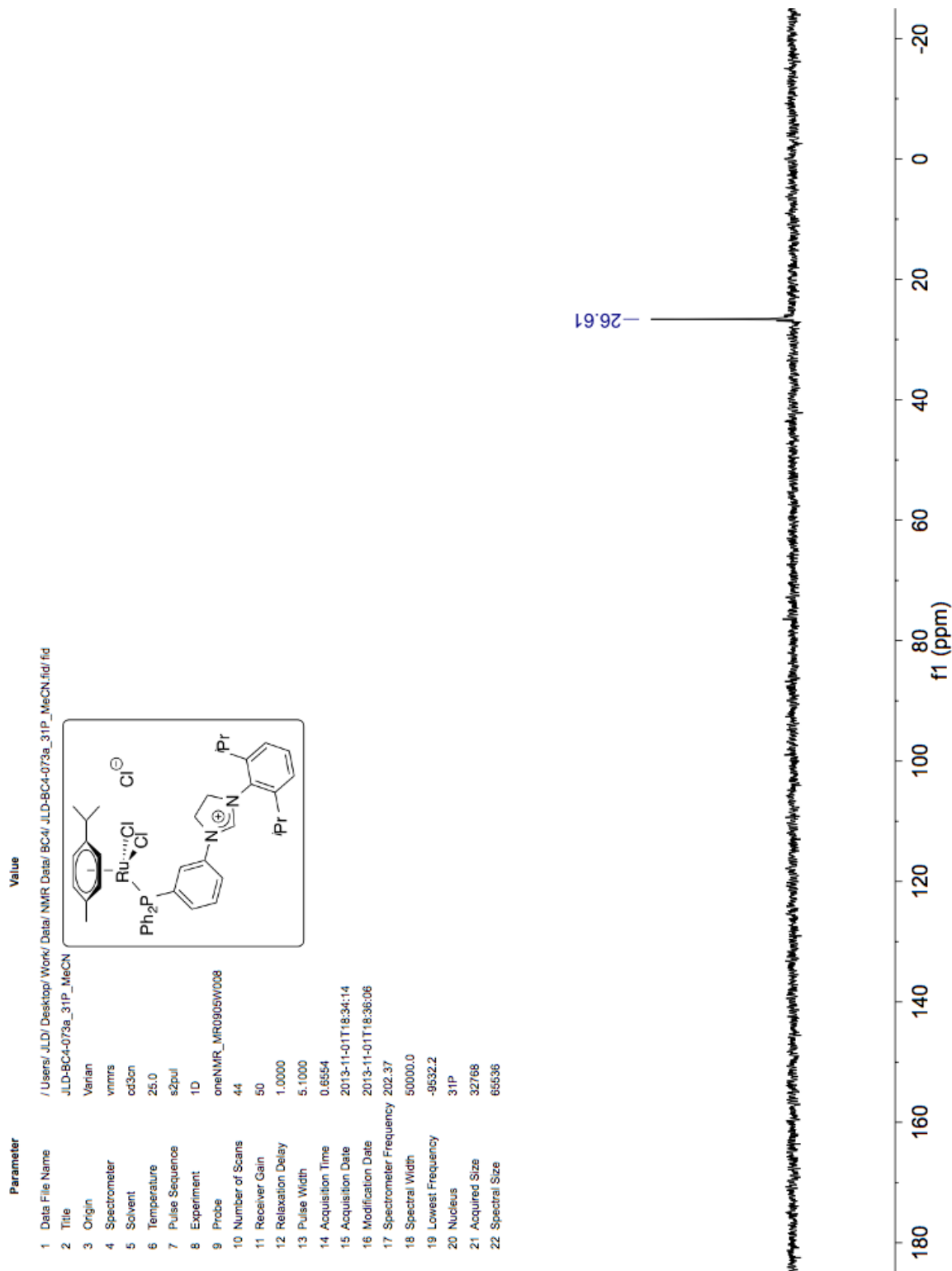
¹H NMR Spectrum of Dichloro(*p*-cymene)(diphenyl-(3-(3-(2,6-diisopropylphenyl)dihydroimidazolium chloride)phenyl))ruthenium (2.53) in DMSO-*d*₆.



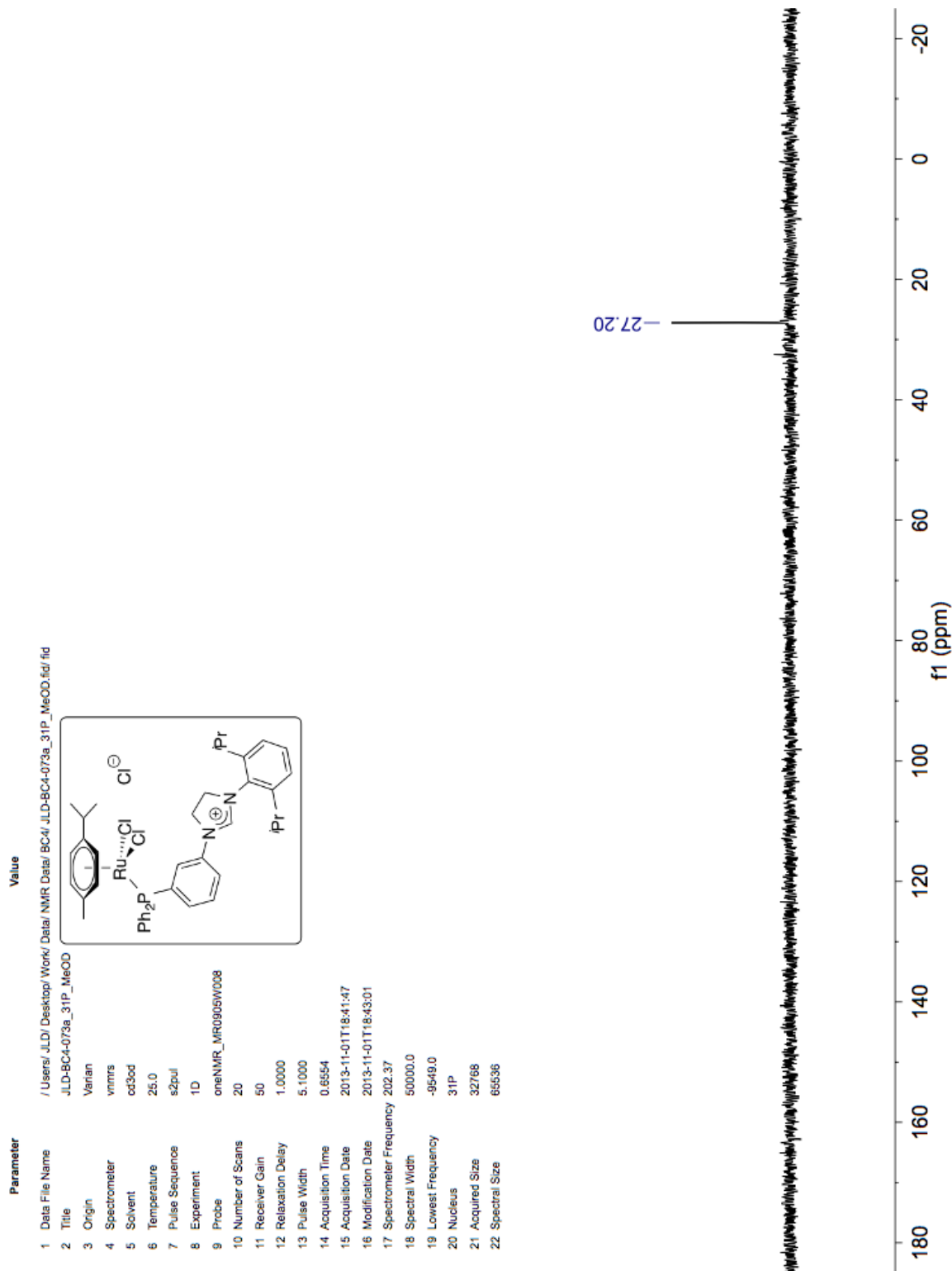
¹³C NMR Spectrum of Dichloro(*p*-cymene)(diphenyl-(3-(3-(2,6-diisopropylphenyl)(dihydroimidazolium chloride)phenyl))ruthenium (2.53) in MeCN-*d*₃.



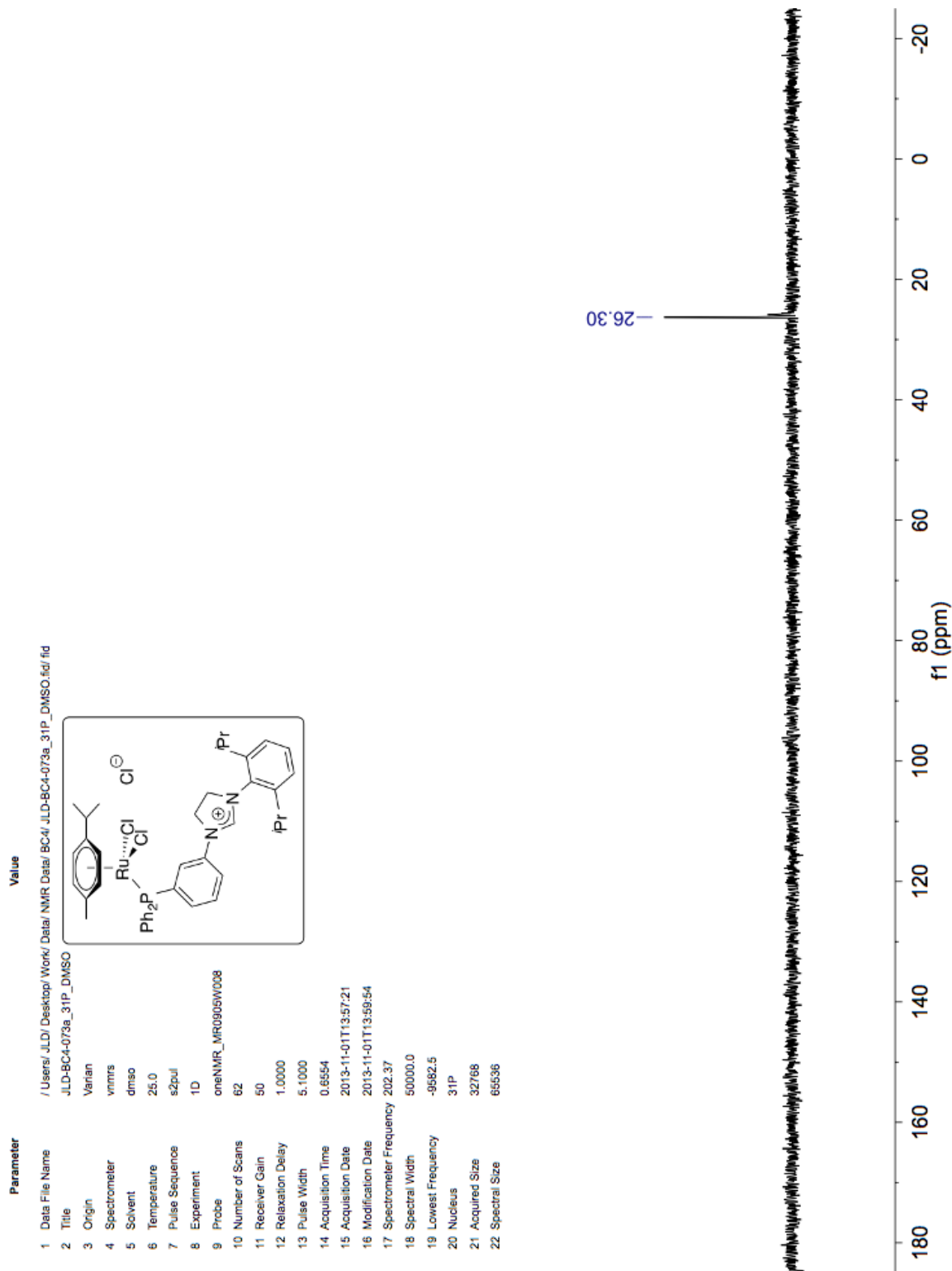
³¹P NMR Spectrum of Dichloro(*p*-cymene)(diphenyl-(3-(3-(2,6-diisopropylphenyl)dihydroimidazolium chloride)phenyl)ruthenium (2.53) in MeCN-*d*₃.



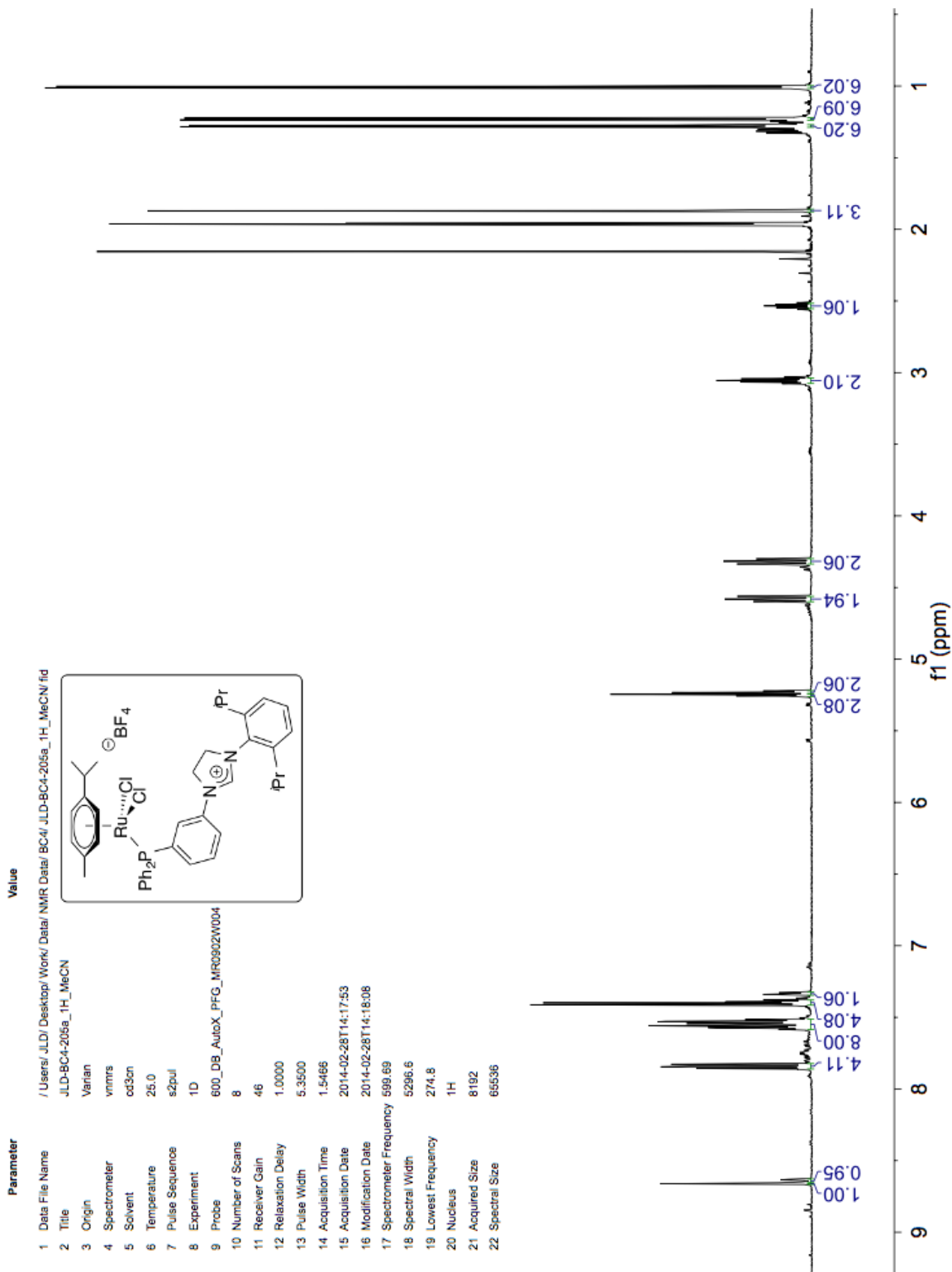
³¹P NMR Spectrum of Dichloro(*p*-cymene)(diphenyl-(3-(3-(2,6-diisopropylphenyl)dihydroimidazolium chloride)phenyl)ruthenium (2.53) in MeOD-*d*₄.



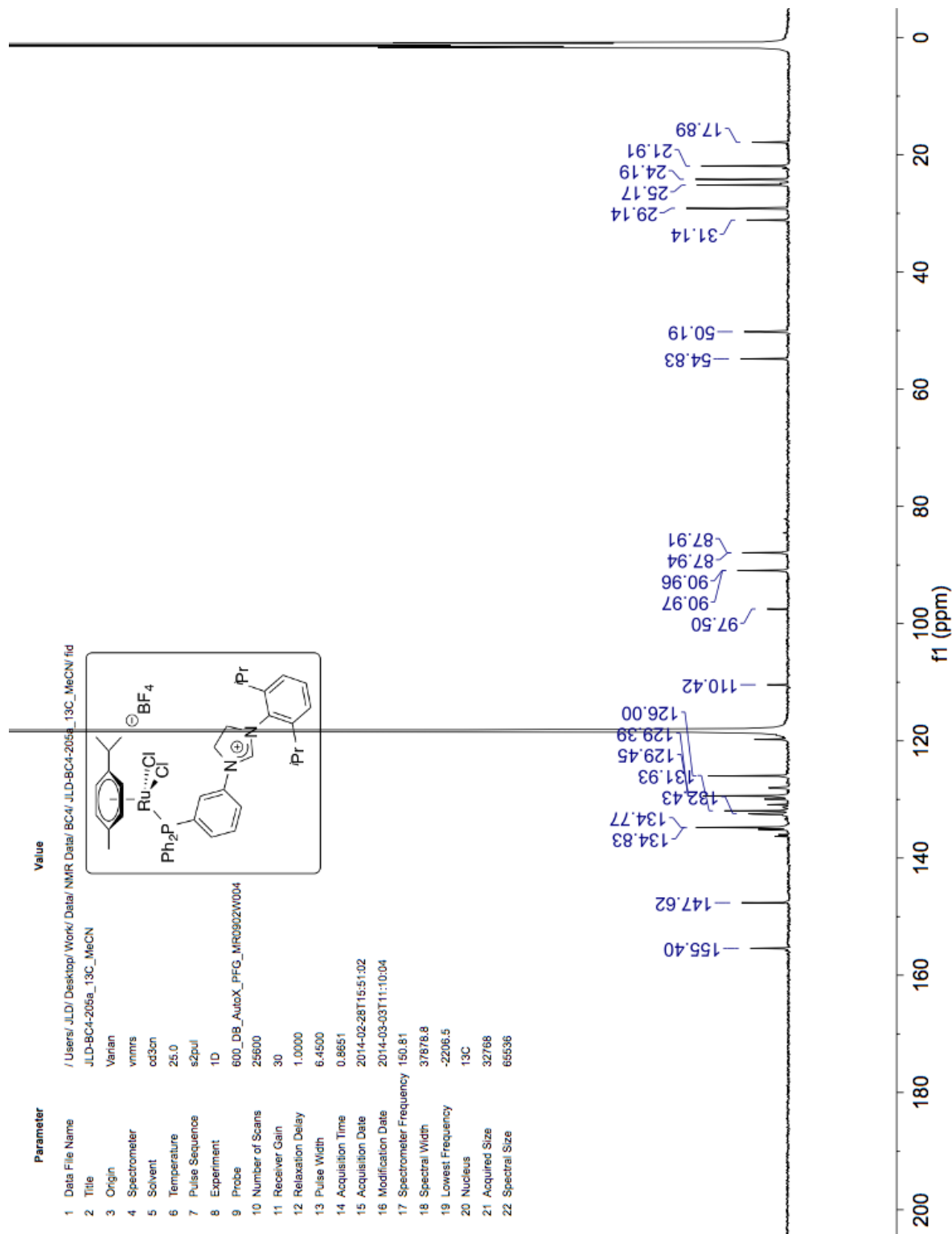
^{31}P NMR Spectrum of Dichloro(*p*-cymene)(diphenyl-(3-(3-(2,6-diisopropylphenyl)dihydroimidazolium chloride)phenyl)ruthenium (2.53) in $\text{DMSO-}d_6$.



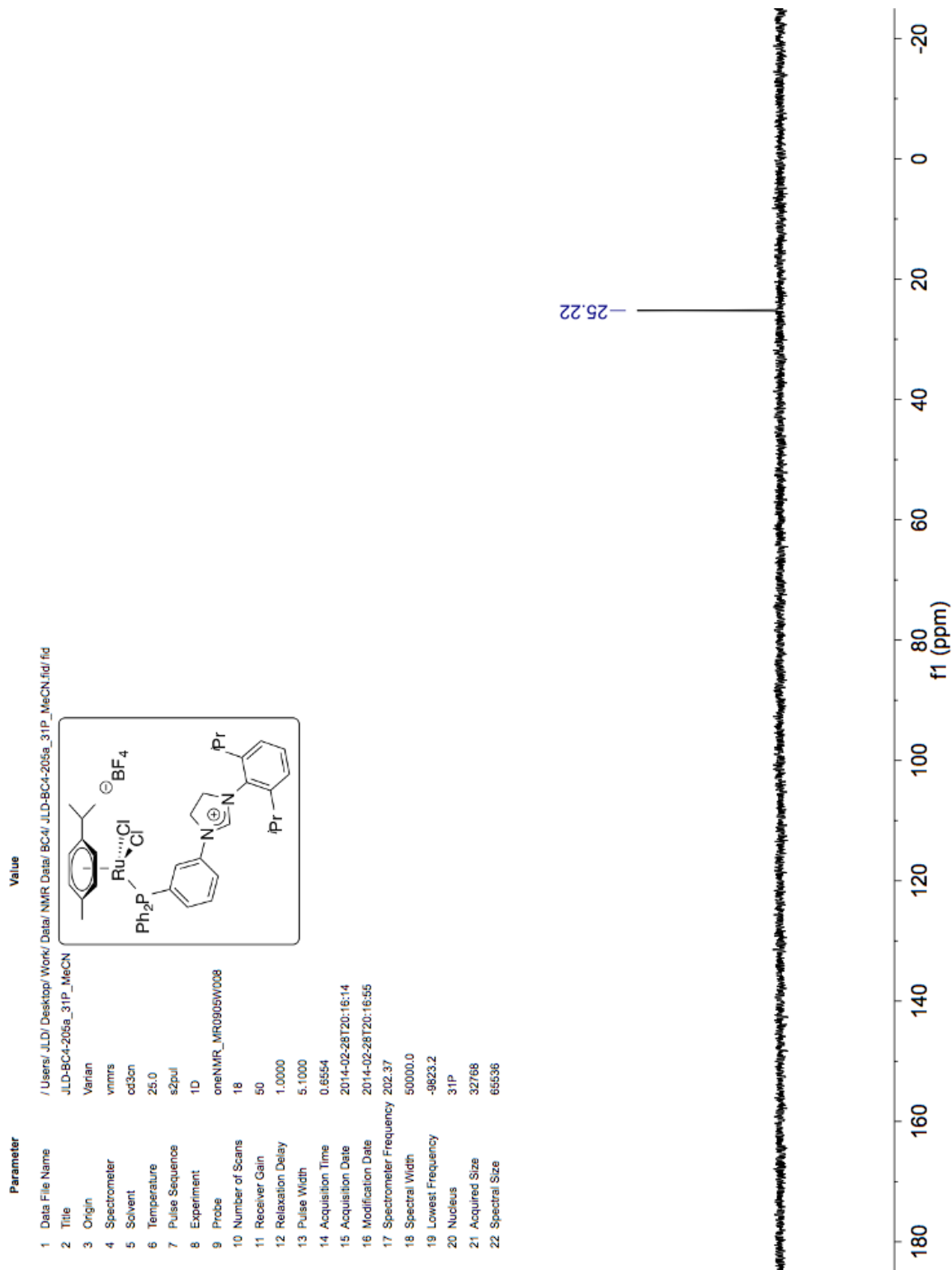
¹H NMR Spectrum of Dichloro(*p*-cymene)(diphenyl-(3-(3-(2,6-diisopropylphenyl)dihydroimidazolium tetrafluoroborate)phenyl))ruthenium (2.54) in MeCN-*d*₃.



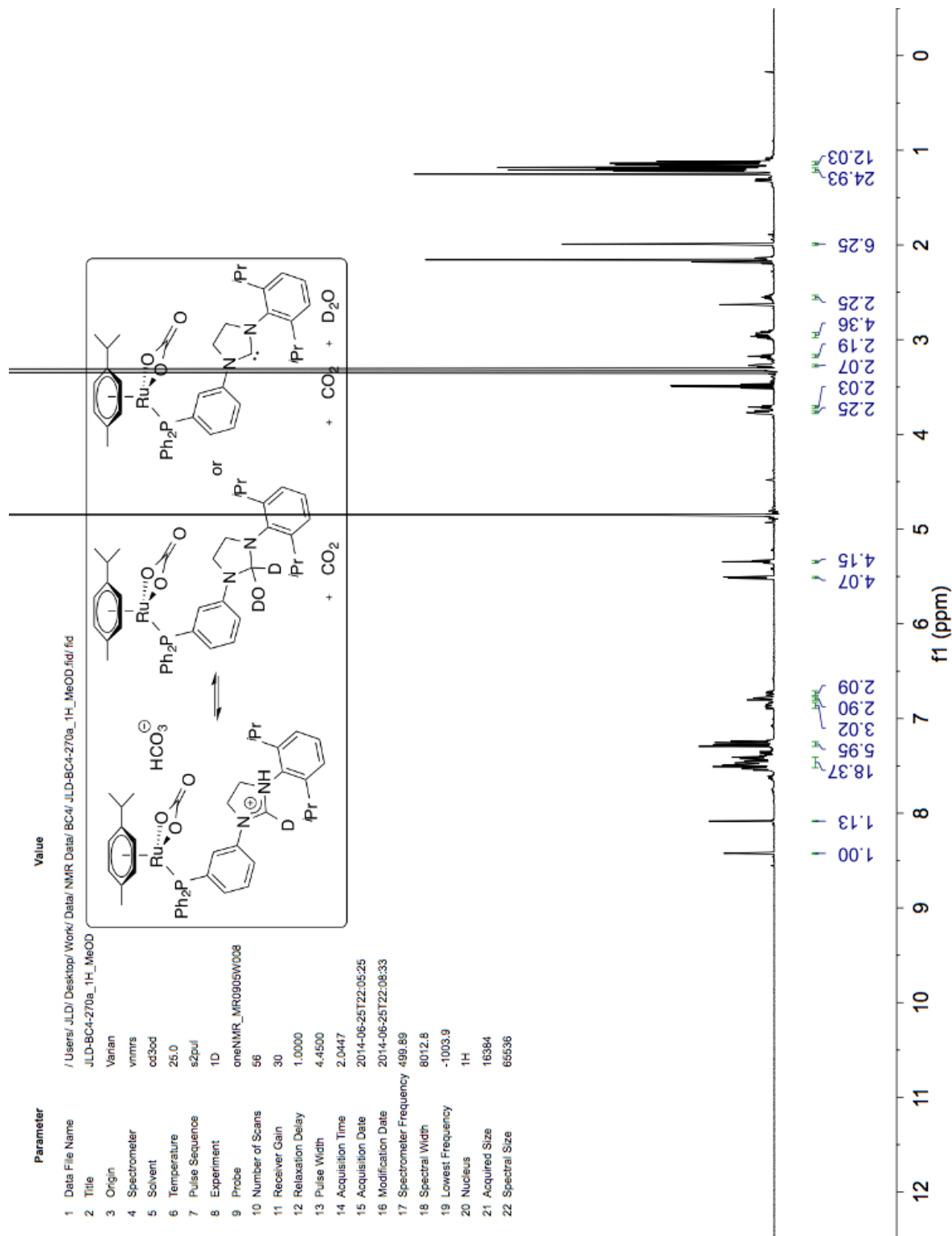
¹³C NMR Spectrum of Dichloro(*p*-cymene)(diphenyl-(3-(3-(2,6-diisopropylphenyl)dihydroimidazolium tetrafluoroborate)phenyl))ruthenium (2.54) in MeCN-*d*₃.



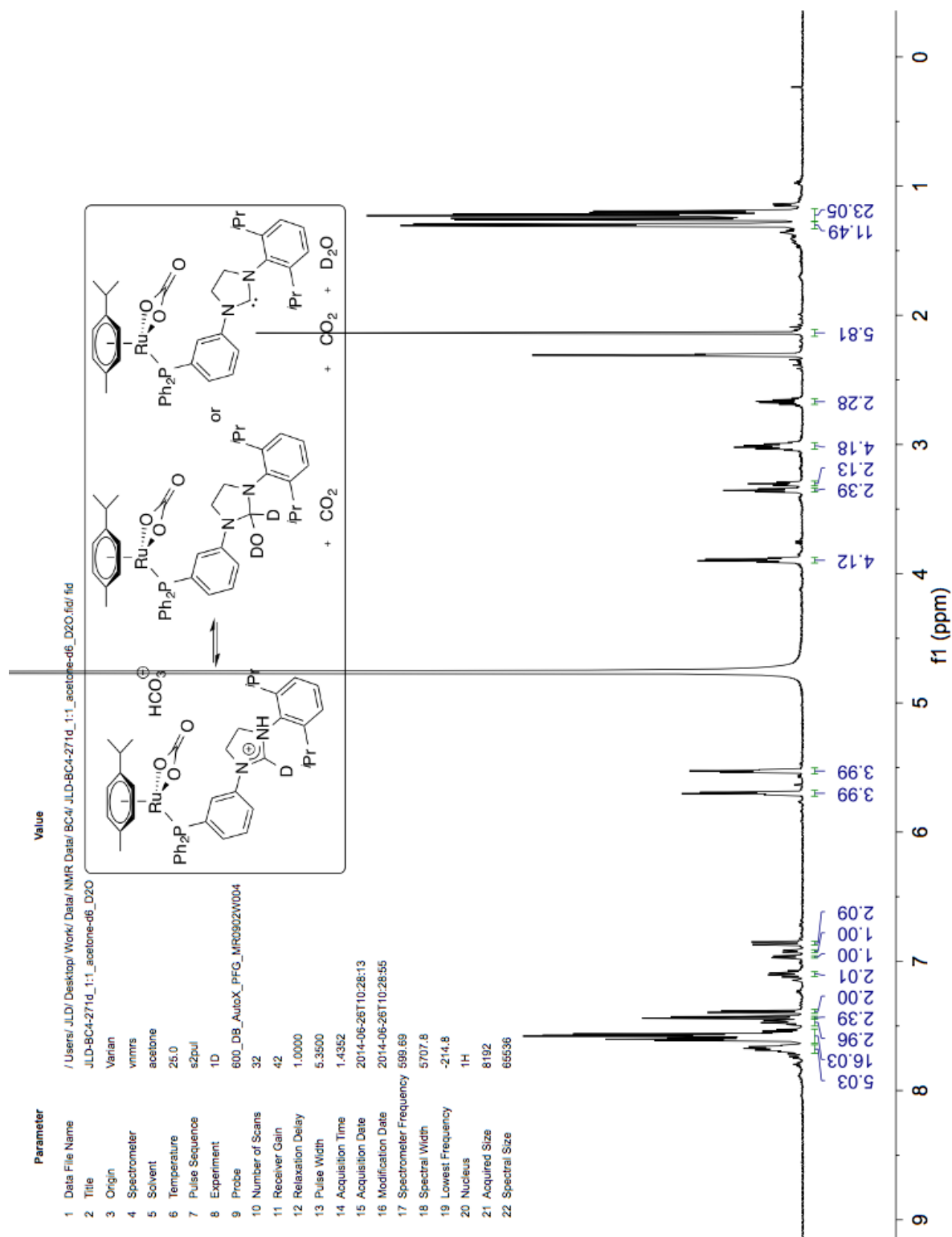
³¹P NMR Spectrum of Dichloro(*p*-cymene)(diphenyl-(3-(3-(2,6-diisopropylphenyl)dihydroimidazolium tetrafluoroborate)phenyl)ruthenium (2.54) in MeCN-*d*₃.



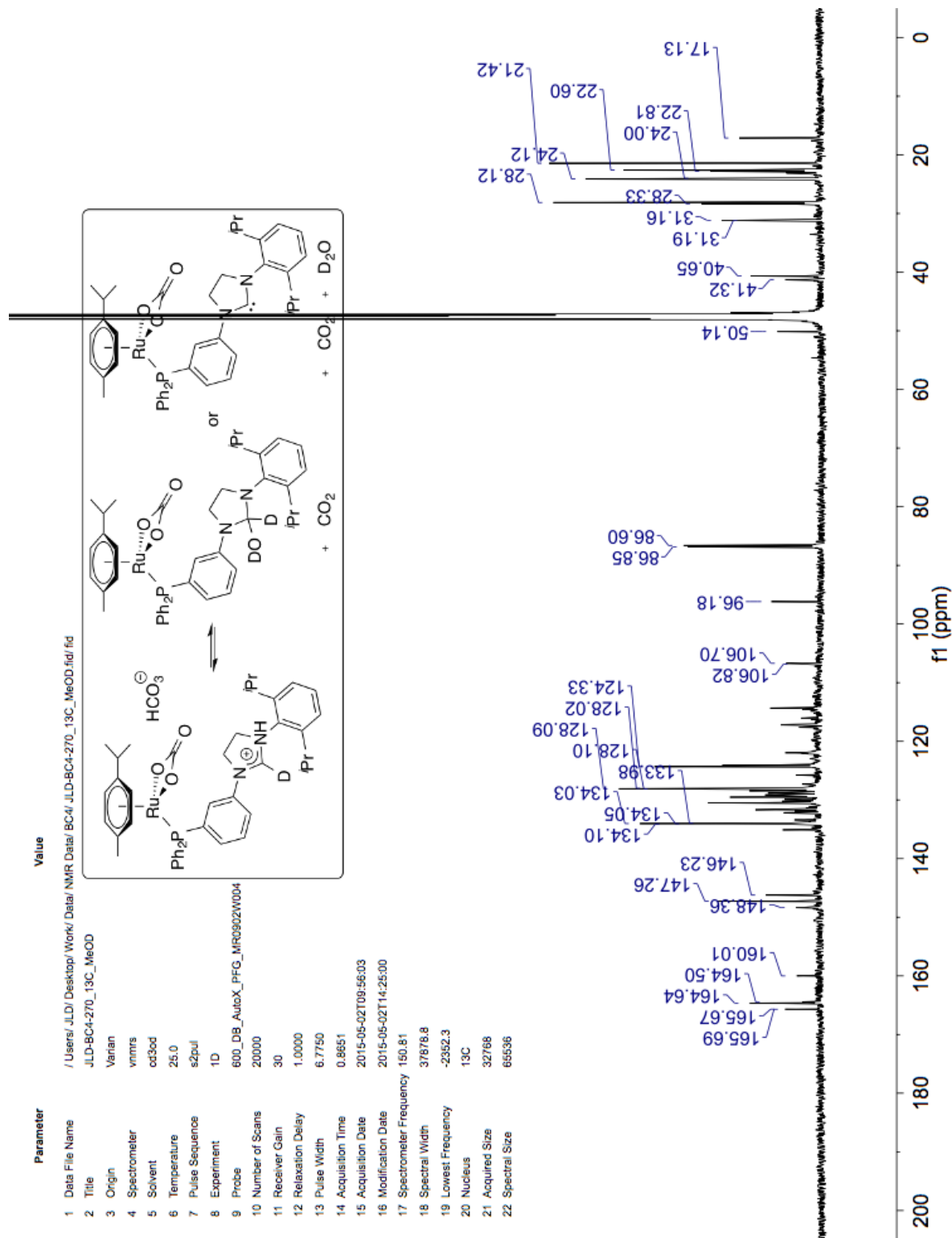
^1H NMR Spectrum of $(\kappa^2\text{-carbonate})(p\text{-cymene})(\text{diphenyl-}(3\text{-}(3\text{-}(2,6\text{-diisopropylphenyl})\text{dihydro-imidazolium bicarbonate})\text{phenyl}))$ ruthenium (2.55) in $\text{MeOD-}d_4$.



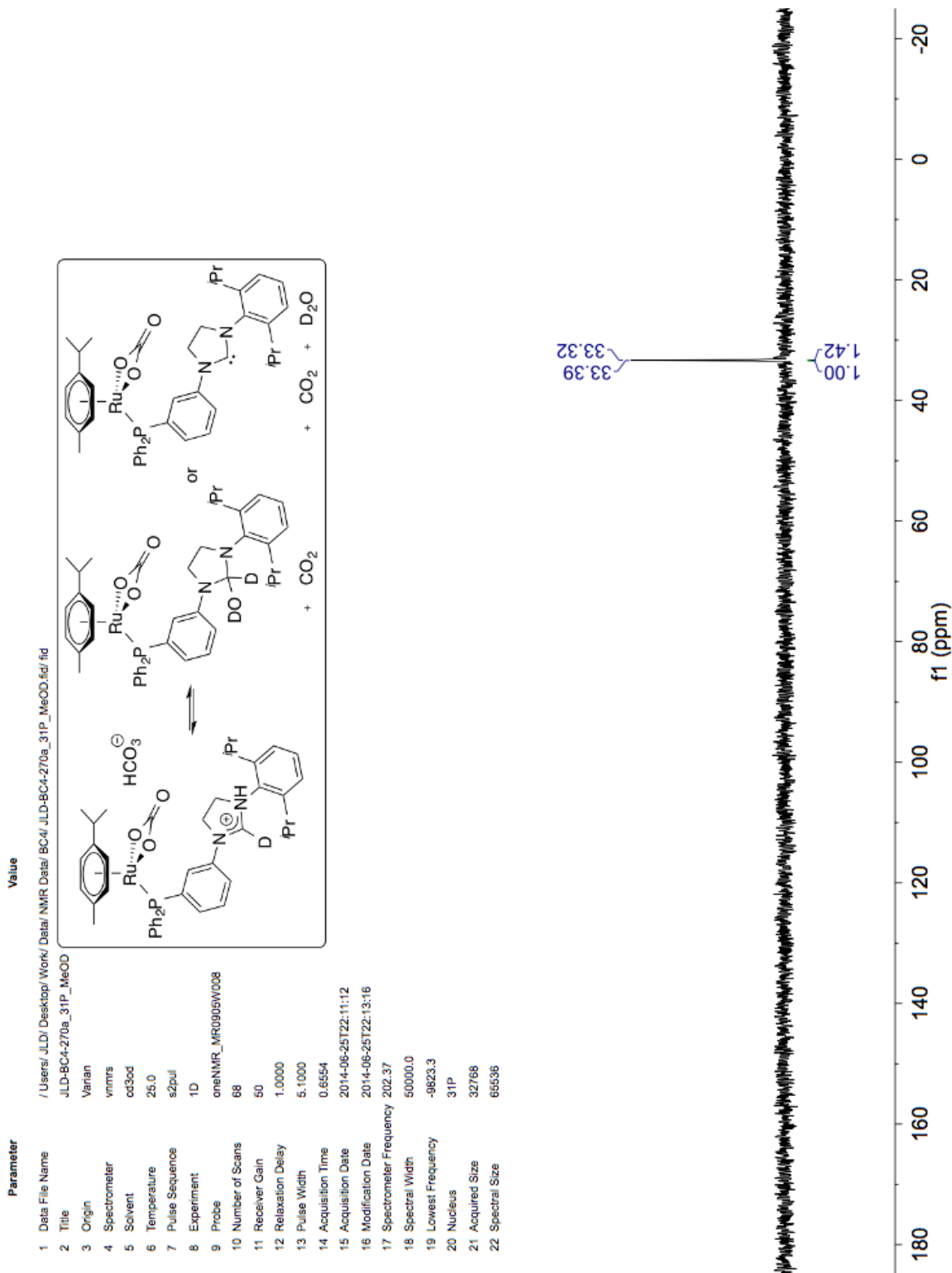
¹H NMR Spectrum of (κ²-carbonate)(*p*-cymene)(diphenyl-(3-(3-(2,6-diisopropylphenyl) dihydro-imidazolium bicarbonate)phenyl)) ruthenium (2.55) in 1:1 acetone-*d*₆/D₂O.



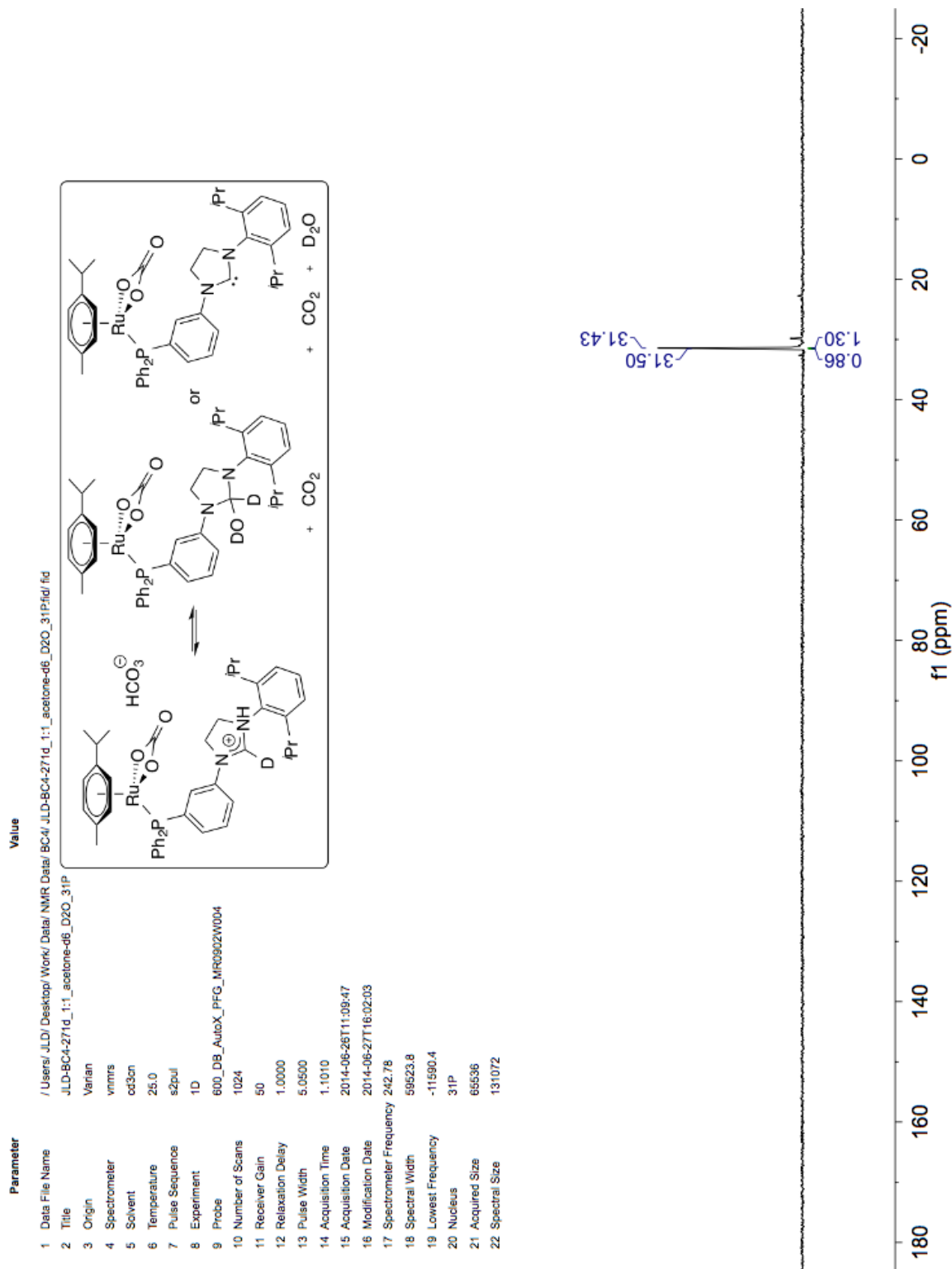
^{13}C NMR Spectrum of (κ^2 -carbonate)(*p*-cymene)(diphenyl-(3-(3-(2,6-diisopropylphenyl) dihydro-imidazolium bicarbonate)phenyl)) ruthenium (2.55) in $\text{MeOD-}d_4$.



^{31}P NMR Spectrum of $(\kappa^2\text{-carbonate})(p\text{-cymene})(\text{diphenyl-}(3\text{-}(3\text{-}(2,6\text{-diisopropylphenyl})\text{dihydro-imidazolium bicarbonate})\text{phenyl}))\text{ ruthenium (2.55)}$ in $\text{MeOD-}d_4$.



³¹P NMR Spectrum of (κ^2 -carbonate)(*p*-cymene)(diphenyl-(3-(3-(2,6-diisopropylphenyl) dihydro-imidazolium bicarbonate)phenyl)) ruthenium (2.55) in 1:1 acetone-*d*₆/D₂O.



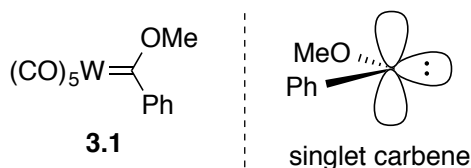
Chapter 3

Chemistry of Iron N-Heterocyclic Carbene Complexes

3.1 Introduction

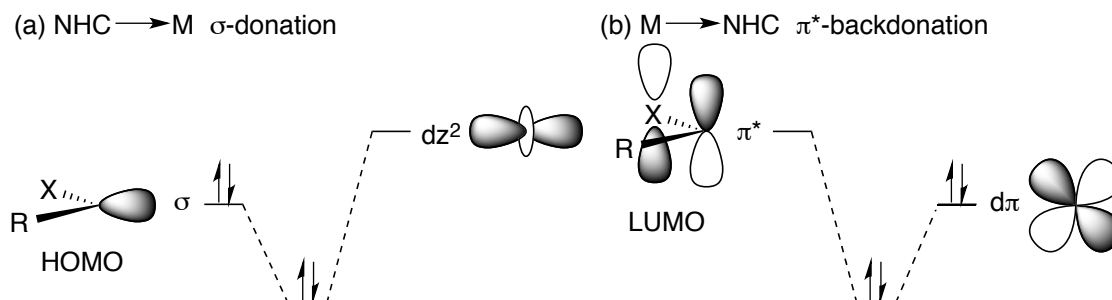
Carbenes are one of the most versatile ligands in organometallic chemistry due to their unique properties. In 1964, Ernst Otto Fischer reported the first example of a transition-metal carbene complex (**3.1**) (Figure 3.1).¹ Since this discovery, carbene ligands containing π -donating substituents (i.e., heteroatoms) are called Fischer carbenes. They are typically in the singlet ground state, which means 2 electrons paired in the carbene lone pair with the p-orbital unoccupied. Fischer-type carbenes prefer the singlet state because the empty p-orbital is stabilized by the neighboring heteroatoms.

Figure 3.1. First example of a Fischer metal-carbene complex and typical ground state



Because of this singlet ground state, they are predominately σ -donors consisting of an interaction between the filled lone pair of the carbene carbon and an empty metal d-orbital (Figure 3.2a). Additionally, Fischer-type carbenes can participate in π -backbonding interactions of a filled metal d-orbital to the empty p-orbital on the carbene carbon (Figure 3.2b).

Figure 3.2. Common binding modes of Fischer-type carbene ligands



These interactions provide the unique bonding character observed in Fischer-type carbenes. They often have significant π -bond character with the carbene carbon being electrophilic in nature. Although metal π -backdonation is present, the direct σ -donation is only partially compensated by the backdonation. Therefore, Fischer-type carbenes are typically found on electron-rich, low oxidation state metal complexes containing mid to late transition metals.

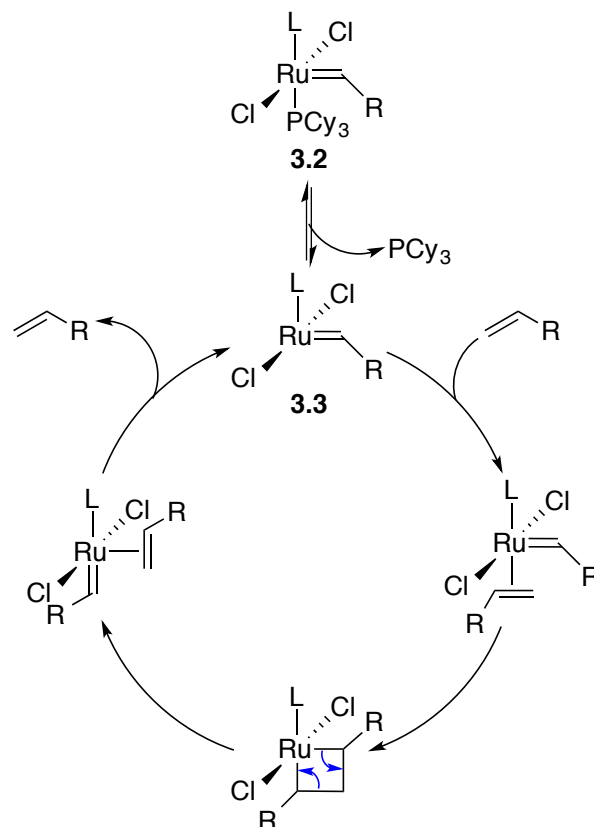
One of the most esteemed examples of Fischer-type carbenes is N-heterocyclic carbenes (NHCs). After isolation of stable NHCs was discovered in 1991 by Arduengo *et al.*,² an extraordinary amount of work focused on the understanding of the coordination chemistry with metal complexes.³ The frontier molecular orbitals are the same as typical Fischer-type carbenes. They are often best viewed as strong σ -donors with minor contributions from π -backdonation from transition metals.³ Since Öfele^{4,5} and Wanzlick⁶ reported the first examples of metal–NHC complexes in the 1960's, numerous studies have been devoted to the synthesis of new NHCs, to their characterization, and to their use as ligands in transition metal complexes.

3.2 Notable Examples of σ -Donating NHC Ligands

3.2.1 Ruthenium Catalyzed Olefin Metathesis

The discovery of metal–NHC complexes spurred extensive investigations to understand the impact these ligands could have on catalysis. One of the most remarkable examples of the usefulness of metal–NHC complexes is in the field of ruthenium-catalyzed olefin metathesis. During the late 1980's and early 1990's, research that led to the development of ruthenium-based catalysts was initiated. In 1995, Grubbs published some of the first well-defined ruthenium-alkylidene complexes, one of which is now known as the first-generation Grubbs catalyst (**3.2**, L = PCy₃, R = Ph) (Scheme 3.1).⁷ These ruthenium-based alkylidene complexes demonstrated high reactivity, had good functional group tolerance, and were stable toward moisture and air.

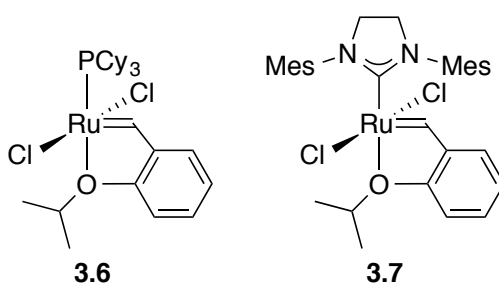
Scheme 3.1. Proposed ruthenium-based alkylidene catalyzed olefin metathesis



Mechanistic studies with this catalyst led the Grubbs' group to conclude that the mechanism first involved dissociation of one phosphine to generate the reactive 14-electron ruthenium intermediate **3.3**.⁸ The group found that more basic phosphines like tricyclohexylphosphine (PCy₃) instead of triphenylphosphine gave higher activity with unstrained and acyclic olefins. They postulated that the higher activity was a result of sterics and electronics of the phosphine ligand. Bulky phosphines should increase phosphine dissociation and stabilize complex **3.3**. Additionally, electron-donating phosphines should increase phosphine dissociation by stabilizing the vacant coordination site *trans* to them. The magnitude of these two effects is manifested in the differences in activities between **3.3** and catalysts containing PPh₃ ligands. However, the two properties must also be balanced as less bulky, basic phosphines (such as

Also in 1999, Hoveyda *et al.* reported other related, very active, and functional-group tolerant ruthenium metathesis catalysts (Figure 3.4). The first-generation catalyst **3.6**¹³ is derived from Grubbs' first-generation catalyst bearing only one phosphine and a chelating alkylidene ligand. The second-generation catalyst **3.7**¹⁴ contains the same chelating alkylidene ligand and a dihydroimidazolium based N-heterocyclic carbene.

Figure 3.4. Hoveyda-Grubbs first and second-generation ruthenium catalysts



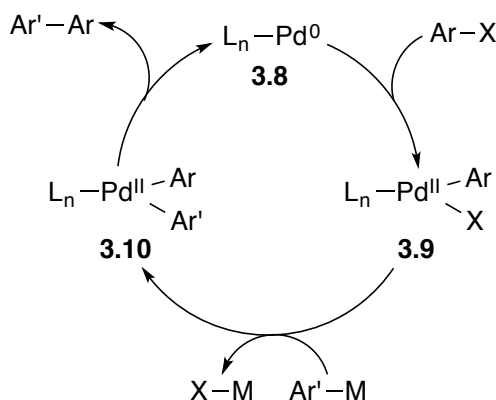
These catalysts are more active than the second-generation Grubbs catalyst because the dissociation of the chelating alkylidene ligand is faster than dissociation of the phosphine. Therefore, the active catalyst remains in the metathesis cycle and side reactions with the phosphine are avoided. They are also especially useful for difficult cases of metathesis of poly-substituted olefins and selective cross-metathesis. The development and activity of these complexes highlights the excellent σ -donating capabilities of N-heterocyclic carbenes.

3.2.2 Palladium Catalyzed C–C Cross Coupling Reactions

Another noteworthy example of the effectiveness of metal–NHC complexes is in palladium catalyzed C–C cross-coupling reactions.^{15, 16} Mono-dentate, bulky, electron-donating tertiary phosphines have historically been employed as ancillary ligands in coupling systems. The importance of careful selection of ancillary ligands can be explained by looking at the generally

accepted mechanism for palladium catalyzed C–C cross-coupling reactions (Scheme 3.2). A zerovalent palladium species **3.8**, stabilized by electron-donating and/or bulky ligand(s), undergoes oxidative addition with an aryl halide to generate palladium(II) complex **3.9**. Addition of an aryl–M reagent, where M is commonly boron, magnesium, tin, silicon, or zinc, results in transmetalation to palladium generate M–X and palladium(II) intermediate **3.10**. Species **3.10** undergoes reductive elimination to couple the aryl groups and regenerate the palladium(0) species **3.8**. The choice of ancillary ligands can affect both the oxidative addition and the reductive elimination steps by stabilizing or destabilizing intermediates during the catalytic cycle.

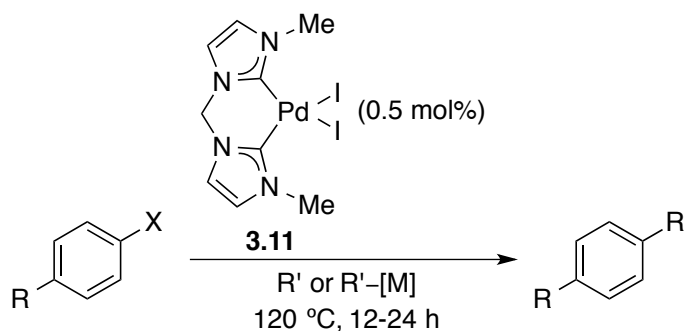
Scheme 3.2. Postulated mechanism for palladium catalyzed cross-coupling reactions



Herrmann and coworkers first introduced Pd–NHC complexes to cross-coupling reactions in 1995.^{17, 18} Previous complexes typically contained phosphine ligands, which commonly have issues due to phosphine dissociation into inactive species. Because of this reason, an excess of ligand is almost always required to control the equilibrium between free and bound phosphine. Herrmann and coworkers demonstrated Heck and Suzuki reactions utilizing a palladium complex bearing a bi-dentate imidazolium ligand (**3.11**) (Table 3.1). Olefination of aryl halides catalyzed by **3.11** demonstrated high activity (entries 1 and 2). The group postulated the high activity was due to the complexes extreme stability to heat, oxygen, and moisture. In

comparison to palladium catalysts containing phosphine ligands, **3.11** (and other Pd–NHC complexes) is much more stable, which should help prevent decomposition of intermediate palladium species like **3.9** and **3.10**. Suzuki cross-coupling of aryl halides with phenylboronic acid resulted in unsymmetrically substituted biaryl compounds in high yields (entries 3-5).

Table 3.1. Pd–NHC catalyzed Heck and Suzuki cross-coupling reactions

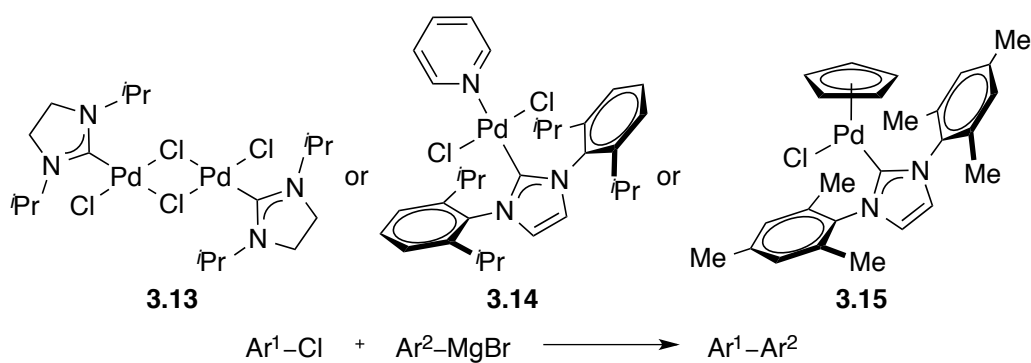


Entry	R	X	R'	[M]	Additive	Yield (%)
1	OMe	Br		N/A	NBu ₄ OAc	95
2	OAc	Cl		N/A	(0.3 equiv.)	60
3	OMe	Br				80
4	OAc	Cl		B(OH) ₂	K ₂ CO ₃ (3 equiv.)	60
5	NO ₂	Br				99

Since their first discovery in 1995, Pd–NHC complexes have become more common for Heck and Suzuki reactions. However, research toward the development of palladium catalysts containing NHCs for Kumada cross-couplings has only recently been reported. Compared to other organometallic cross-coupling reactions, substrate scopes of Pd–NHC catalyzed Kumada reactions have been limited. Predominately only aryl Grignard with aryl halides have been examined. Only a handful of reports have demonstrated well-defined Pd–NHC catalysts (Table 3.2). Reactions catalyzed by **3.12**,¹⁹ **3.13**,²⁰ and **3.14**²¹ proceeded in high yields of the desired cross-coupled product with a variety of substituted aryl halides and Grignard reagents. Similar to

complexes used for Heck and Suzuki cross-coupling reactions, these Pd species are either highly active at low temperatures or stable up to the high temperatures required for reactivity. These results can be attributed to the presence of the NHCs, as their σ -donating capabilities provide strong coordination to the metal center that stabilizes reactive intermediates during the catalytic cycle and helps discourage side reactions.

Table 3.2. Pd–NHC catalyzed Kumada cross-coupling of aryl halides and aryl Grignards

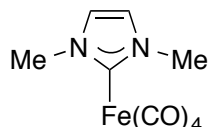


Entry	Cat.	Ar ¹ -Cl	Ar ² -MgBr	Yield (%)
1	3.13			95
2				69
3	3.14			100
4				95
5	3.15			92
6				90

3.3 Reactivity of σ -Donating Iron–NHC Complexes

The reactivity and coordination chemistry of metal–NHC complexes has been studied extensively. Most of these reactions take advantage of NHCs for their excellent σ -donating capabilities. Metathesis and cross-coupling reactions catalyzed by ruthenium- and palladium-NHC complexes, respectively, highlight these σ -donating characteristics. On the other hand, the chemistry of iron–NHC complexes has not been developed to the same extent as other late transition metals. The first isolation of an iron–NHC compound occurred in 1969 (Figure 3.5),²² yet their application in homogeneous catalysis was relatively limited until the last decade.

Figure 3.5. First isolated Fe–NHC complex



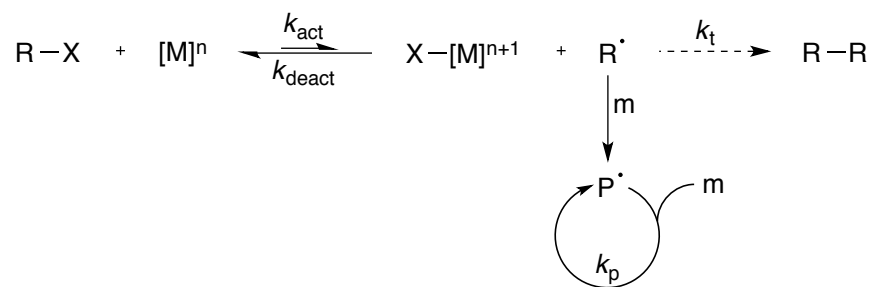
A series of reports published in the last few years have shown that iron–NHC compounds have considerable potential for unique and wide-ranging applications. Iron–NHC catalysis has resulted in numerous applications such as polymerization,^{23–25} C–C bond forming,^{26–28} and reduction reactions.^{29–31} The following sections are designed to highlight important discoveries throughout the history of iron–NHC complexes, while emphasizing the nature of the metal–carbene bond. They are by no means a comprehensive list of all iron–NHC complexes, nor are they representative of all reactions iron–NHC complexes are capable of.

3.3.1 Polymerization Reactions

3.3.1.1 Atom Transfer Radical Polymerization

Atom transfer radical polymerization (ATRP) is among the most effective and most widely used methods of controlled radical polymerization. ATRP allows scientists to easily form polymers by putting together monomers in an organized, piece-by-piece fashion. Such polymerizations demonstrate characteristics of a living and controlled polymerization. They can also be shut down or re-started as desired depending on the reaction conditions. In an ATRP process, a transition metal complex activates a dormant initiator to generate radicals via a one-electron process (Scheme 3.3). Simultaneously, the transition metal is oxidized. After initiation, the radical can react with the monomer, generating polymer with a radical that can react further. Termination typically occurs by radical–radical combination.

Scheme 3.3. General mechanism of a metal mediated ATRP (R–X = initiator–halide, m = monomer, P = polymer)

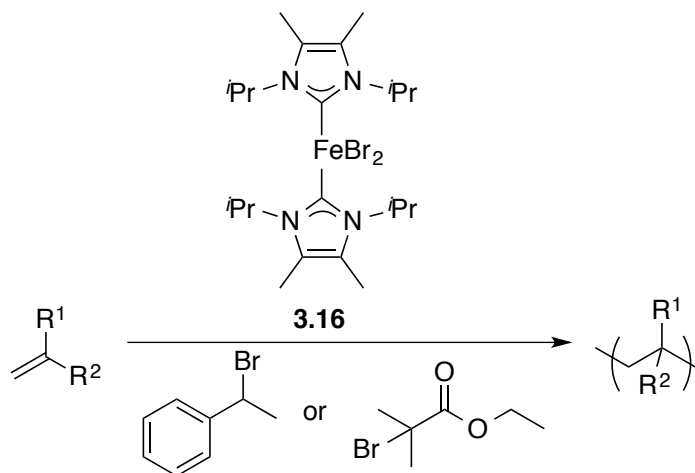


The living character of the polymerization is supported by first-order dependence on the transition metal concentration, a linear increase in polymer molecular weight with conversion, and narrow polydispersity. The key to ATRP is controlling the equilibrium between dormant initiator and activated radical initiator. If $k_{\text{act}} < k_{\text{deact}}$, then the concentration of radicals in solution is low, which is necessary to reduce radical–radical termination events. In addition, it is ideal for

the rate of propagation (k_p) to be faster than the rate of termination (k_t) so that polymerization occurs instead of termination.

Since 1995 when Sawamoto³² and Matyjaszewski³³ independently discovered ATRP, it has become an important method for the synthesis of polymers. ATRP mediated by an iron–NHC complex dates back to a report by Grubbs and coworkers in 2000.²³ The group postulated that the substitution of commonly used phosphine or amine ligands with N-heterocyclic carbenes would be beneficial. In addition to being excellent electron donating ligands, they are less toxic than many phosphines and amines and are easy to prepare and handle. Synthesis of the iron–NHC complex **3.16** was achieved through addition of the iron salt FeBr_2 (or FeCl_2) to the imidazol-2-ylidene ligand. The homogenous ATRP of styrene initiated with 1-phenylethyl bromide and **3.16** provided polystyrene with high conversion of styrene (Table 3.3, entry 1).

Table 3.3. Iron–NHC mediated ATRP of styrene and methyl methacrylate



Entry	R ¹	R ²	PDI ^a
1	Ph	H	1.14
2	CO ₂ Me	Me	1.47

^aPDI = polydispersity index, M_w/M_n

The rate of polymerization is among the highest reported for metal mediated ATRP in organic solvents. The number average molecular weight (M_n) increased linearly over time and agreed with theoretical molecular weights ($M_n(\text{exp.}) = 3400 \text{ g/mol}$, $M_n(\text{theo.}) = 4000 \text{ g/mol}$) demonstrating good control. In addition, a narrow polydispersity index (1.14) was achieved. The ATRP of methyl methacrylate using complex **3.16** and ethyl 2-bromoisobutyrate as the initiator produced poly(methyl methacrylate) in high conversion (entry 2). Results were similar to that of polystyrene with slightly broader polydispersity (1.47).

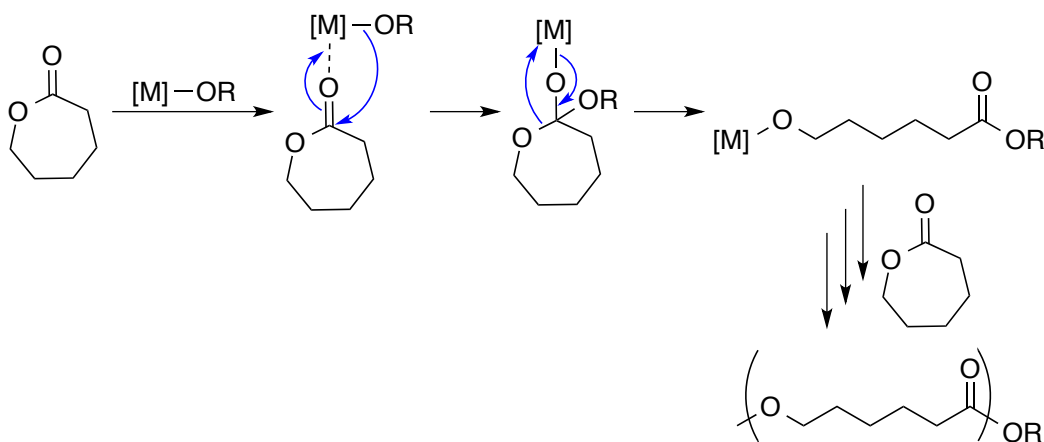
The polymerization rates rival copper based systems and yield polymers with narrow polydispersity. The increased electron-donating ability of the NHC ligands plays an important role on the activity of ATRP catalysts. The group postulated that the high Lewis basicity of the imidazol-2-ylidene may lower the redox potential of the iron(II) complexes facilitating halide abstraction from any dormant polymer chains. This would shift the equilibrium toward growing polymer radicals and therefore increase the rate of polymerization. Importantly, the increased rate of polymerization (and increased concentration of radicals) does not compromise the control. The ATRP reactions can also be performed using *in situ* prepared complexes from iron salts and the free N-heterocyclic carbene ligand, but a slight decrease in the activity was observed. To date this iron–NHC complex is the only example that has been shown to mediate ATRP reactions.

3.3.1.2 Ring-Opening Polymerization

Ring-opening polymerization (ROP), a form of chain-growth polymerization, differs from ATRP in that the reactive species can be radical, anionic, or cationic. In the ring-opening polymerization of lactones, the mechanism proceeds via anionic ring-opening polymerization that involves nucleophilic reagents and metal–alkoxide complexes (Scheme 3.4). Ring opening is triggered by coordination of the monomer to the metal catalyst through the carbonyl group. This coordination facilitates the insertion of the metal–alkoxide into the carbonyl by increasing the

nucleophilicity of the metal–alkoxide and electrophilicity of the carbonyl group. The newly formed metal species can then coordinate a new monomer, the metal–alkoxide can insert, and the polymerization can propagate.

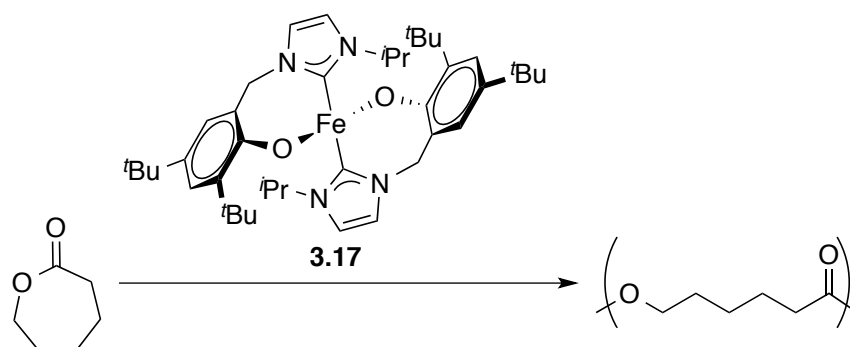
Scheme 3.4. General mechanism of a metal initiated ring-opening polymerization of ϵ -caprolactone



In 2006, Shen *et al.* reported an iron–NHC complex that was active for the ring-opening polymerization of ϵ -caprolactone.²⁴ Iron complex **3.17** was synthesized from a mixture of FeBr₂, sodium hexamethyldisilazane (NaHMDS), and the imidazolium chloride salt of the ligand. Iron complex **3.17** was used for the ROP of ϵ -caprolactone in toluene at 80 °C (Table 3.4). The starting material conversion increased by increasing the polymerization time, while the M_n of the obtained polymer decreased. The molecular weight distribution of the polymer slightly broadened as the polymerization time increased. The poor control on M_n as well as the decrease in M_n over time indicates that there are inter- or intramolecular transesterification events occurring during the polymerization reaction. The iron–NHC complex **3.17** could not be efficiently inhibiting these transesterifications over the course of the ϵ -caprolactone polymerization. Since the polymerization of ϵ -caprolactone initiated with iron–alkoxides typically proceeds via the

coordination-insertion mechanism described in Scheme 3.6, the group postulated the process with complex **3.17** should be similar. According to this mechanism, the poly(ϵ -caprolactone) obtained should contain a unit of the aryl-oxo-functionalized imidazolium ligand at one end of the polymer chain. Therefore, the group synthesized small chain ϵ -caprolactone oligomers and observed the presence of phenyl and imidazolium peaks in the ^1H NMR spectrum of the polymer.

Table 3.4. Activity of 3.17 for the ROP of ϵ -caprolactone

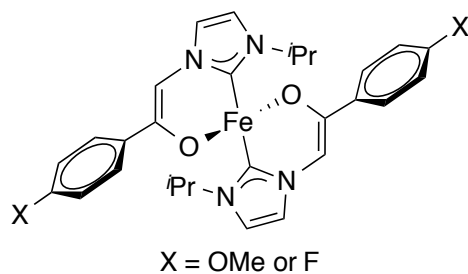


Entry	Time (h)	Conv. (%)	M_n (kg/mol)	PDI ^a
1	0.5	20	12.2	2.1
2	1	31	8.6	1.9
3	2	45	4.7	2.3
4	3	66	4.6	2.1
5	12	100	4.0	3.1

^aPDI = polydispersity index, M_w/M_n

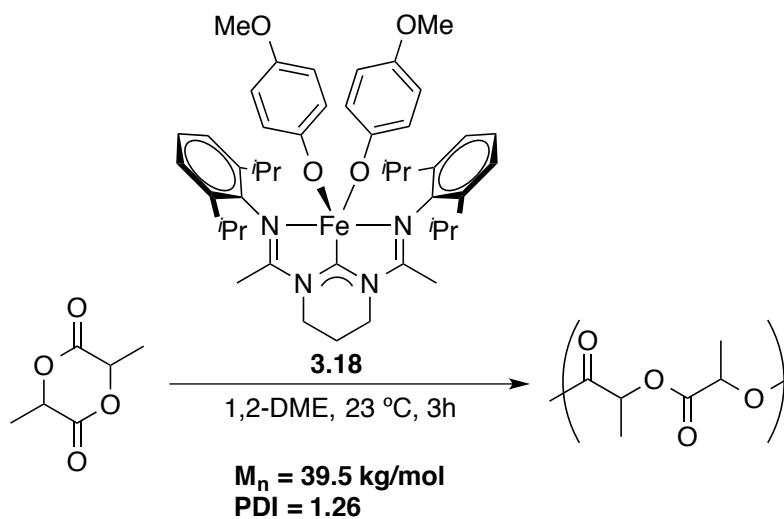
Following their initial report, Shen and coworkers published two other iron–NHC complexes for the ROP of ϵ -caprolactone (Figure 3.6).³⁴ Both complexes demonstrated higher reactivity and the reaction time could be reduced to 9 hours instead of 12. However, the polydispersities were still broad and the issues concerning transesterification could not be solved.

Figure 3.6. Iron–NHC complexes used for the ring-opening polymerization of ϵ -caprolactone



In 2014, our group reported the preparation of high molecular weight poly(lactic acid) produced by an efficient iron catalyst bearing a bis(amidinato)-N-heterocyclic carbene ligand.²⁵ Hilan Z. Kaplan and Cesar M. Manna investigated the reactivity iron bis(alkoxide) complex **3.18** with (*rac*)-lactide (Scheme 3.5). The rate of the polymerization observed for **3.18** was similar to that observed for other iron complexes.³⁵ However, the M_n observed was significantly higher, which was attributed to the presence of the strong σ -donating capabilities of the NHC ligand.

Scheme 3.5. Polymerization of (*rac*)-lactide catalyzed by iron–NHC complex **3.18**

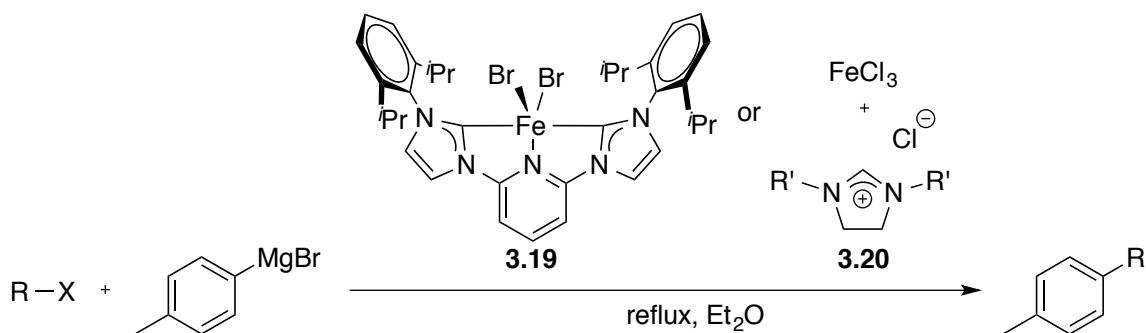


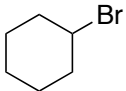
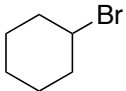
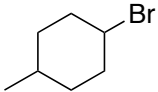
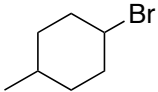
3.3.2 C–C Bond Forming Reactions

3.3.2.1 Kumada Cross-Coupling

Cross-coupling reactions have become one of the most useful and well-established methods for forming C–C bonds. In this area, palladium, nickel, and copper catalysts are the most widely used for the synthesis of complex and functionalized organic molecules. The first example using an iron catalyst was reported in 1971 by Kochi and coworkers, who presented the reaction of alkenyl halides with alkyl Grignards in the presence of catalytic amounts of FeCl_3 .³⁶ Since then, iron-based catalysts have become extremely efficient and valuable for cross-coupling reactions of Grignard reagents with primary and secondary alkyl halides. Although the potential of NHC ligands in coupling reactions is evident by the success of palladium catalysts (See 3.2.2), the use of iron catalysts bearing NHC ligands is only recently emerging.

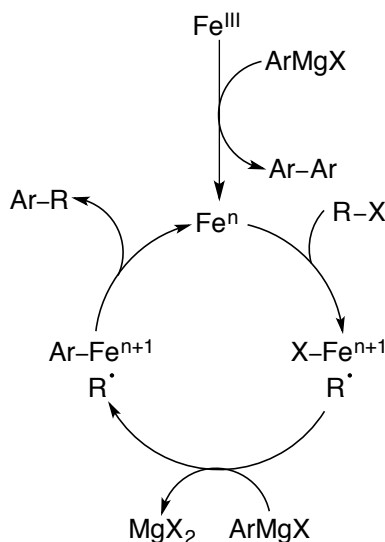
In 2006, Bedford *et al.* reported the first example of an iron–NHC complex in the reaction of aryl Grignards and bromoalkanes (Table 3.5).²⁶ The group demonstrated that a well-defined iron–NHC complex **3.19** can catalyze the cross-coupling of *p*-tolylmagnesium bromide and a range of secondary and primary bromoalkanes. The authors also showed that a series of complexes formed *in situ* from FeCl_3 and a dihydroimidazolium salt (**3.20**) gave high yields of the desired cross-coupling products. Within the series of dihydroimidazolium salts, 1,3-bis(*tert*-butyl)dihydroimidazolium chloride gave the best result (entry 4). These complexes showed only small amounts (15% or less) of 4,4'-bitolyl resulting from homo-coupling of the aryl Grignard. Additionally, almost no products due to homo-coupling, β -H elimination, or H-atom abstraction of the starting material were observed (less than 3% total in all reactions). These complexes also outperformed phosphine, phosphite, and arsine ligands.

Table 3.5. First example of iron–NHC catalyzed Kumada Coupling

Entry	R-X	Cat./R'	Yield (%)
1		3.19	94
2		3.20 ^t Bu	97
3		3.20 /Cy	87
4		3.20 /Mes	45
5		3.19	89
6		3.20 ^t Bu	81
7	octyl-Br	3.19	71
8	octyl-Br	3.20 ^t Bu	73

The authors also proposed a mechanism based on previous reports of Kumada cross-coupling reactions by Kochi,³⁷ Fürstner,³⁸ and Nakamura (Scheme 3.6).³⁹ The active iron species is formed upon reduction of iron(III) to a lower oxidation state iron(n) (n = 0, 1, or 2). The active iron species then reacts with the alkyl halide by the transfer of a single electron to generate an alkyl radical and an X-iron(n+1) species. They propose that the alkyl radical could be free or associated to the iron center. Transmetalation with the Grignard reagent generates an iron-aryl complex, which is then attacked by the radical to form the product and regenerate the catalyst. The group believed that the superiority over other ligands was attributed to the greater electron donating ability of NHCs relative to phosphines, resulting in a more strongly reducing iron center.

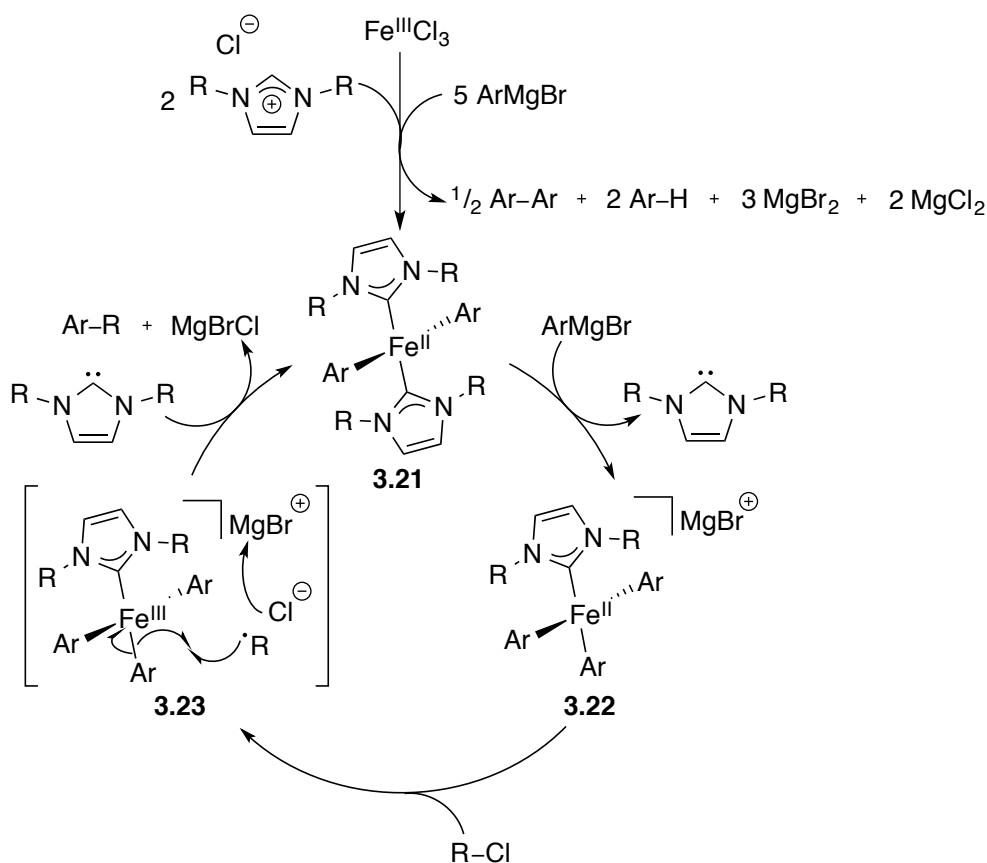
Scheme 3.6. Proposed mechanism of iron–NHC catalyzed Kumada cross-coupling by Bedford



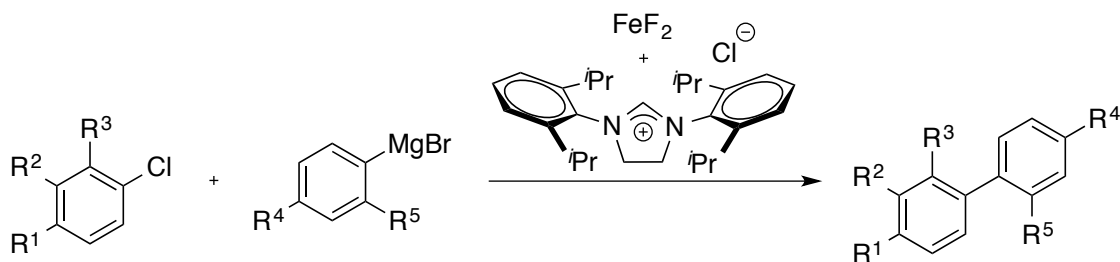
Recently, Nakamura and coworkers reported the cross-coupling of primary, secondary, and tertiary chloroalkanes, which are more challenging substrates than bromoalkanes.²⁷ For a selective coupling, the group found that slow addition of the Grignard reagent was crucial to avoid β -H elimination products. The group noticed that the consumption of starting material only started to occur after addition of at least 5 equivalence of Grignard relative to the amount of FeCl_3 . Based on these results, Nakamura *et al.* proposed a slightly different mechanism specific to each species formed along the catalytic cycle (Scheme 3.7). Similar to the mechanism proposed by Bedford, Nakamura suggested that the active Fe^{II} species **3.21** is generated by the reduction of the Fe^{III} salt in the presence of ArMgBr and an imidazolium chloride salt. The neutral species **3.21** reacts with an additional equivalence of ArMgBr to dissociate one NHC ligand and form the anionic iron(II) intermediate **3.22**. Species **3.22** can undergo single electron transfer (SET) with the alkyl chloride to afford an alkyl radical and iron(III) complex **3.23**. After elimination of the desired cross-coupling product and association of an NHC ligand, the active iron species **3.21** is regenerated. Therefore, the initial consumption of 5 equivalence of ArMgBr

is necessary to deprotonate the ligand precursor salts (2 equiv.) and form the reduced iron(II)-biaryl species **3.21** (3 equiv.).

Scheme 3.7. Proposed mechanism of Kumada cross-coupling by Nakamura



In 2009, Nakamura *et al.* also reported aryl-aryl cross-coupling catalyzed by *in situ* generated iron–NHC complexes from dihydroimidazolium chlorides and FeF₃ or FeF₄ salts.²⁸ Typically, aryl-aryl cross-coupling reactions are difficult due to the formation of homo-coupling products. Remarkably, the system developed by Nakamura and coworkers eliminated Grignard homo-coupling side reactions. Such reactions show high efficiencies of coupling various Grignard reagents with both electron-withdrawing and electron-donating substituted aryl chlorides (Table 3.6).

Table 3.6. Aryl-aryl cross-coupling reactions catalyzed by an *in situ* generated iron–NHC

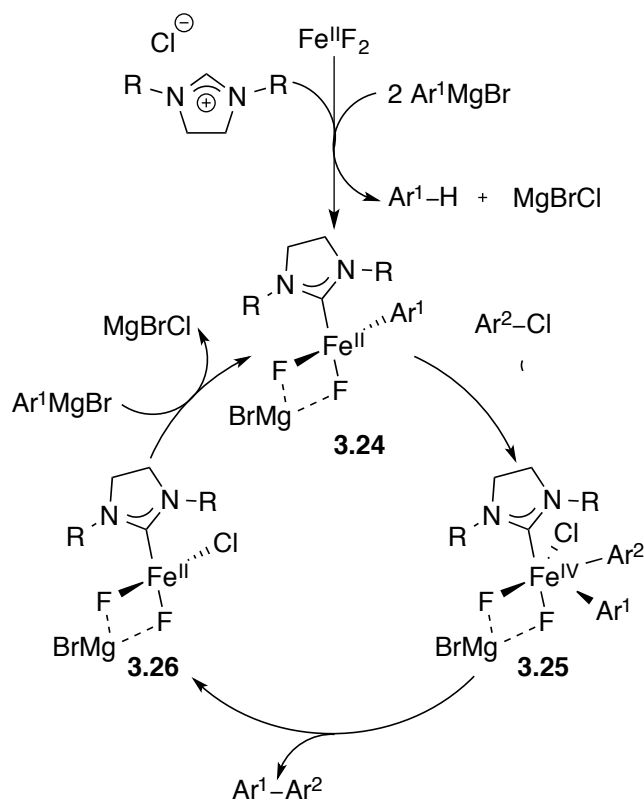
Entry	Aryl halide			Grignard		Yield (%)
	R ¹	R ²	R ³	R ⁴	R ⁵	
1	OMe	H	H	Me	H	92
2	F	H	H	OMe	H	91
3	F	F	H	OMe	H	81
4	H	H	1-butene	Me	H	18
5	H	H	OMe	H	Me	90
6	H	NMe ₂	H	H	H	94

The remarkable success of this iron species is believed to be a combination of the persistent NHC and the fluoride anion ligated throughout the reaction. Reactions with mono-dentate or bi-dentate phosphines instead of the dihydroimidazolium chloride salt achieved yields of only 5%. Reactions were also highly dependent on the identity of the dihydroimidazolium salt. NHCs with less bulky (1,3-bis(mesityl)dihydroimidazolium) or more weakly binding (unsaturated) than 1,3-bis(2,6-diisopropylphenyl)dihydroimidazolium led to lower yields. This suggests that the NHC remains ligated to the metal center and is necessary to stabilize coordinatively unsaturated iron centers during catalysis. Analogous fluoride-free reactions using FeCl₃ led to significant quantities of homo-coupled bi-aryl products, which highlights the importance of fluoride coordination to iron throughout the catalytic cycle.

The proposed mechanism starts with the synthesis of the heteroleptic metalate iron(II) complex **3.24**, which can then undergo oxidative addition with the aryl halide (Scheme 3.8). The newly formed iron(IV) species **3.25** can then undergo reductive elimination to form the desired aryl-aryl product and iron complex **3.26**. The active species **3.24** is regenerated by

transmetalation with the aryl Grignard reagent. The process is extremely practical for achieving high yielding unsymmetrical bi-aryl products with exceptional cross-coupling selectivity. Additionally, it highlights the ability of iron–NHC complexes to catalyze cross-coupling reactions.

Scheme 3.8. Proposed mechanism for aryl-aryl cross-coupling with FeF_2 precursor

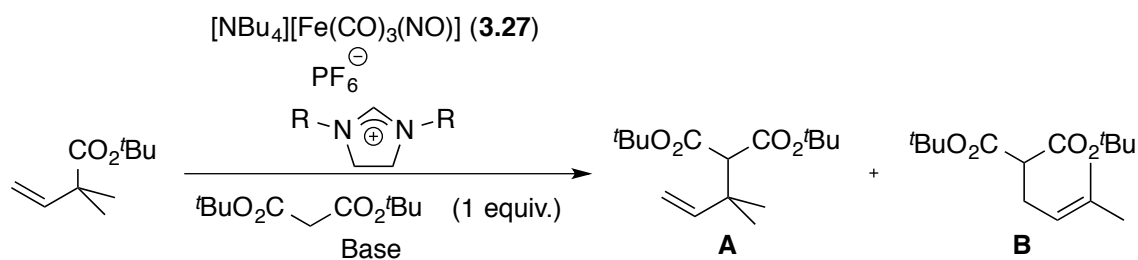


3.3.2.2 Allylic Alkylation

In addition to cross-coupling reactions, a lot of research has been focused on allylic alkylation reactions as versatile tools for the formation of C–C bonds. The reaction is typically catalyzed by molybdenum, ruthenium, palladium, and iridium transition metal systems. Recently, iron has proven to be a suitable metal for this type of catalysis. In 2006, Plietker *et al.* reported the use of $[\text{NBu}_4][\text{Fe}(\text{CO})_3\text{NO}]$ (**3.27**) with a combination of different phosphine ligands for the

alkylation of allylic carbonates with pro-nucleophiles.⁴⁰ Without the addition of exogenous base, the allylated compounds were synthesized in moderate to excellent yields (53-92%) and high regioselectivity (98:2). In 2008, Plietker and coworkers developed an allylic alkylation catalyzed by iron complexes with NHC ligands.⁴¹ The group demonstrated that a variety of dihydroimidazolium salts could be utilized as ligands using iron complex **3.27** (Table 3.7). The reaction of malonate with a Michael donor led to the formation of two possible products (**A** and **B**). Product **A** resulted from *ipso*-substitution, while product **B** was formed through a σ - π - σ isomerization mechanism, which is rare for iron-catalyzed reactions. Interestingly, the regioselectivity of the addition of the malonate nucleophile was controlled using specific NHC ligands. With the *tert*-butyl substituted dihydroimidazolium ligand, the *ipso*-substitution product **A** was predominately formed (entry 1). However, with the 2,4,6-trimethylphenyl substituted dihydroimidazolium ligand, the regioselectivity observed was inverted, and isomer **B** was obtained as the major product.

Table 3.7. Imidazolium and dihydroimidazolium based ligands for allylic alkylation reactions

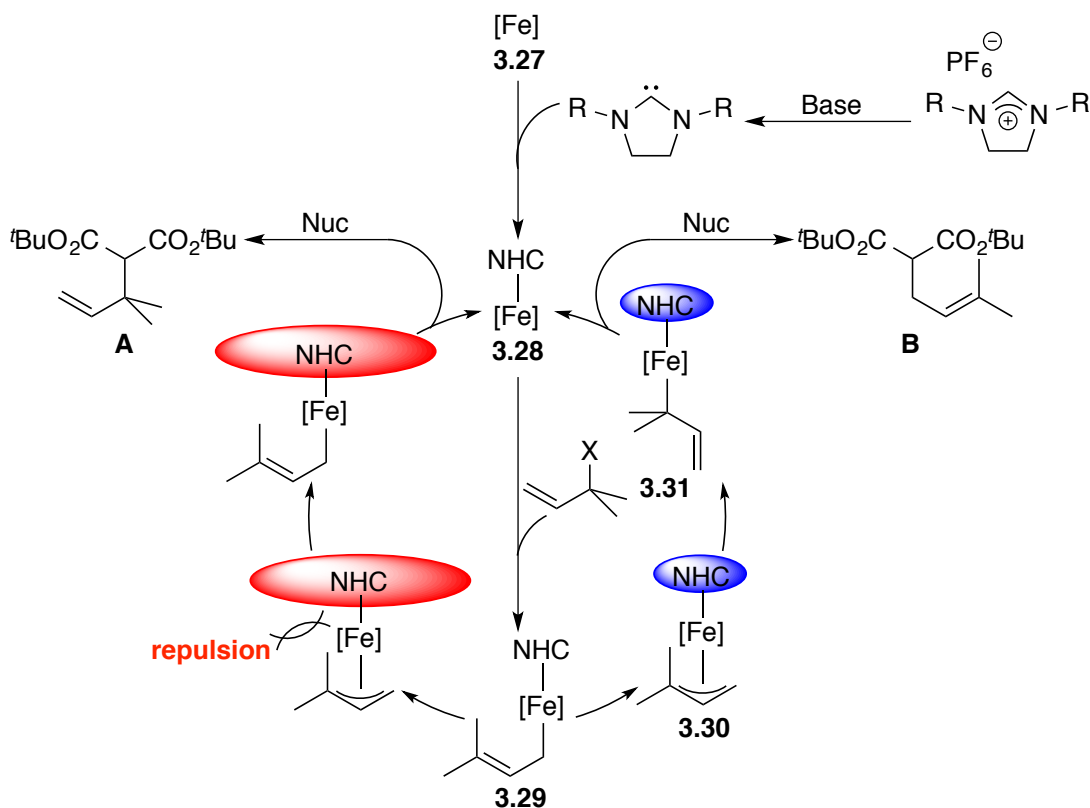


Entry	R	Base	A:B Ratio	Conv. (%)
1	<i>t</i> Bu		91:9	74
2	<i>i</i> Pr	NaNH ₂	84:17	68
3	4-MeOPh		73:37	12
4	2,6- <i>i</i> Pr ₂ Ph	KO ^{<i>t</i>} AM ^{<i>a</i>}	33:67	38
5	2,4,6-Me ₃ Ph		9:91	98

^{*a*}KO^{*t*}AM = potassium 2-methylbutan-2-olate

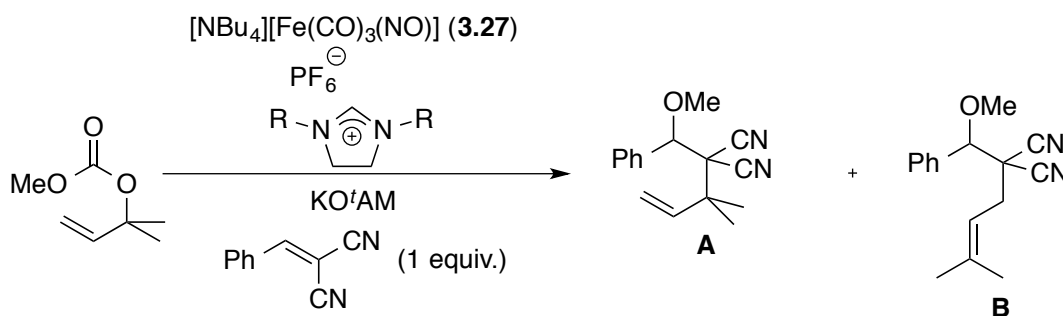
The regioselectivity differences could be explained by looking at the mechanism of this allylic alkylation (Scheme 3.9). Addition of base to a dihydroimidazolium salt and iron complex **3.27** would generate a new iron complex **3.28**. A σ -allyl species **3.29**, which can be formed upon treatment of **3.28** with the starting material, can react via two subsequent routes to give **A** or **B**. Species **3.29** can participate in a direct substitution reaction with the nucleophile to form product **A** via an S_N2' elimination, or can isomerize to π -allyl complex **3.30**. If the NHC ligand is sterically encumbered ($R = t\text{Bu}$), this isomerization to π -allyl complex **3.30** would be disfavored and product **A** would form preferentially. If the NHC ligand allows this isomerization ($R = \text{planar aryl groups}$), then formation of a different σ -allyl species **3.31** and substitution with the nucleophile will preferentially form product **B**.

Scheme 3.9. Proposed mechanism for iron–NHC catalyzed allylic alkylation



The same group continued to publish on the allylic alkylation with iron–NHC complexes.^{42, 43} They have been able to control product formations and use various allyl carbonates and nucleophiles to provide a wide array of complex products. In addition, the group demonstrated regioselective alkoxylation using activated double bonds (Scheme 3.10). A broad variety of functional groups were tolerated on the aryl group of the Michael acceptor or on the allylic carbonate. Products were formed in good yields and typically 99:1 (or 1:99) regioselectivity of **A** to **B** depending on the NHC ligand used allowing for complete control of the products formed. This reaction, again, highlights the unique ability for the strong σ -donating N-heterocyclic carbene ligand to stabilize intermediate iron centers, promoting selective reactivity.

Scheme 3.10. Regioselective alkoxylation of activated alkenes



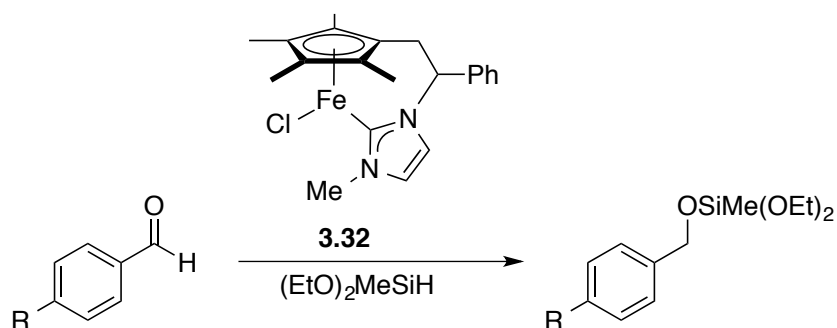
3.3.3 Reduction Reactions

3.3.3.1 Hydrosilylation

The selective reduction of double bonds is a fundamental strategy in chemical synthesis. Although typically catalyzed by ruthenium, rhodium, palladium, iridium and platinum, since the 1980's iron catalyzed reductions have become more successful. However, the first example of an iron–NHC species was a pendant NHC–Cp piano stool complex (3.32) reported in 2010 by Royo and coworkers (Scheme 3.11).³⁰ Hydrosilylation of *p*-substituted benzaldehydes catalyzed by

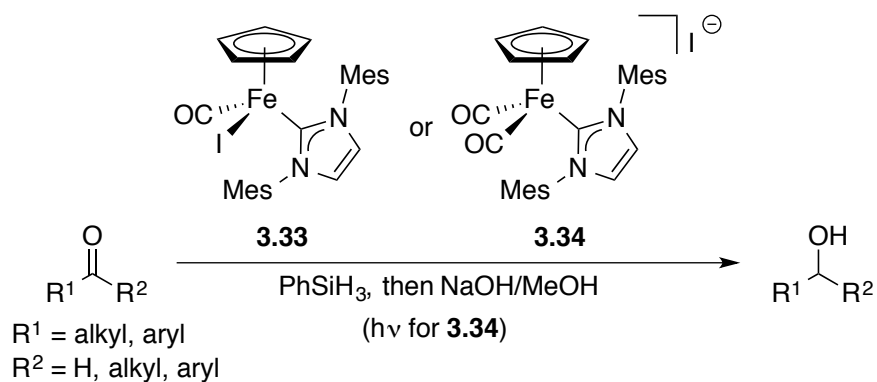
3.32 proceeded in almost quantitative yields. However, alkyl-substituted aldehydes or ketones were not converted.

Scheme 3.11. Hydrosilylation of benzaldehyde derivatives catalyzed by 3.32



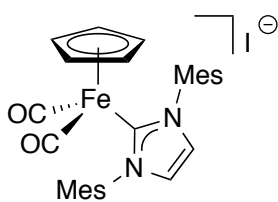
In 2011, Darcel and coworkers published a variety of ketone and aldehyde reductions using well-defined piano stool iron–NHC complexes (Scheme 3.12).²⁹ Iron complex **3.33** was active for hydrosilylation with various silanes producing over 20 examples of alcohols with alkyl, aryl, or H substitutions. Complex **3.34** was active for hydrosilylation under visible light irradiation.

Scheme 3.12. Iron–NHC reduction of ketones and aldehydes



Under these conditions, better activities and increased rates were observed for acetophenone derivatives with nitrile, amine, or alkene functional groups. Reactions utilizing catalysts without NHC ligands (such as $\text{CpFe}(\text{CO})_2$ or $\text{CpFe}(\text{CO})\text{I}$) demonstrated yields of less than 10% desired product. This supports that NHC ligands have a significant influence on the activity. Additionally, piano stool iron complex **3.34** is active for the reduction of amides, esters, and imines by hydrosilylation under irradiation (Table 3.8).⁴⁴⁻⁴⁶ Complex **3.34** is efficient for the reduction of various secondary and tertiary amides to the corresponding amines in 77-98% yields (entries 1 and 2). The reaction was suitable for both aromatic and aliphatic amides. With primary amides, the reduction did not lead to the corresponding amine, but instead to nitrile compounds.

Table 3.8. Reduction of amides, esters, and imines via hydrosilylation catalyzed by 3.34



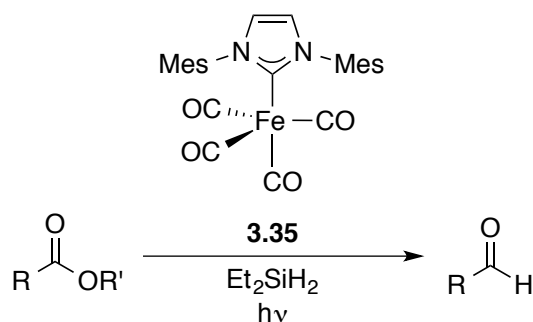
Starting Material $\xrightarrow[\text{PhSiH}_3, h\nu]{\mathbf{3.34}}$ Product

Entry	Starting Material	Product	Conv. (%)
1	$\text{R}-\overset{\text{O}}{\parallel}{\text{C}}-\text{NR}'_2$	$\text{R}-\text{CH}_2-\text{NR}'_2$	77-98
2	$\text{R}-\overset{\text{O}}{\parallel}{\text{C}}-\text{NH}_2$	$\text{R}-\text{C}\equiv\text{N}$	73-98
3	$\text{R}-\overset{\text{O}}{\parallel}{\text{C}}-\text{OR}'$	$\text{R}-\text{CH}_2-\text{OR}' + \text{R}-\text{CH}_2-\text{OH}$	46-49
4	$\text{R}''-\text{N}=\text{C}(\text{R})-\text{R}'$	$\text{R}''-\text{NH}-\text{CH}(\text{R})-\text{R}'$	57-95

Complex **3.34** reduced esters to their corresponding ethers and alcohols in 46-49% with selectivities of 2:3. The authors noted that iron–NHC complex **3.34** was less active compared to its PCy₃ analogue. However, reactions catalyzed by **3.34** gave higher selectivity in favor of the ether, while in the case of the phosphine, the alcohol was preferred. The reduction of imines yielded the corresponding amines in 57-95 % yields. Various functional groups were tolerated, such as halogens, ketones, esters, and alkenes. The mechanism(s) of these hydrosilylation reactions is still unclear, but the ability of the NHC ligand to stabilize coordinatively unsaturated iron complexes is undoubtedly important.

Darcel and coworkers reported another example of the selective reduction of esters catalyzed by a iron(0)–NHC complex (**3.35**) (Scheme 3.13).⁴⁷ A broad variety of substrates were used such as alkyl, benzyl, and phenyl substituted esters; all which proceed in yields of 65-95%. High selectivities for the reduction to the corresponding aldehydes were observed when a secondary silane was used. When tertiary or primary silanes were used, either no reduction, or selective reduction to the alcohol took place.

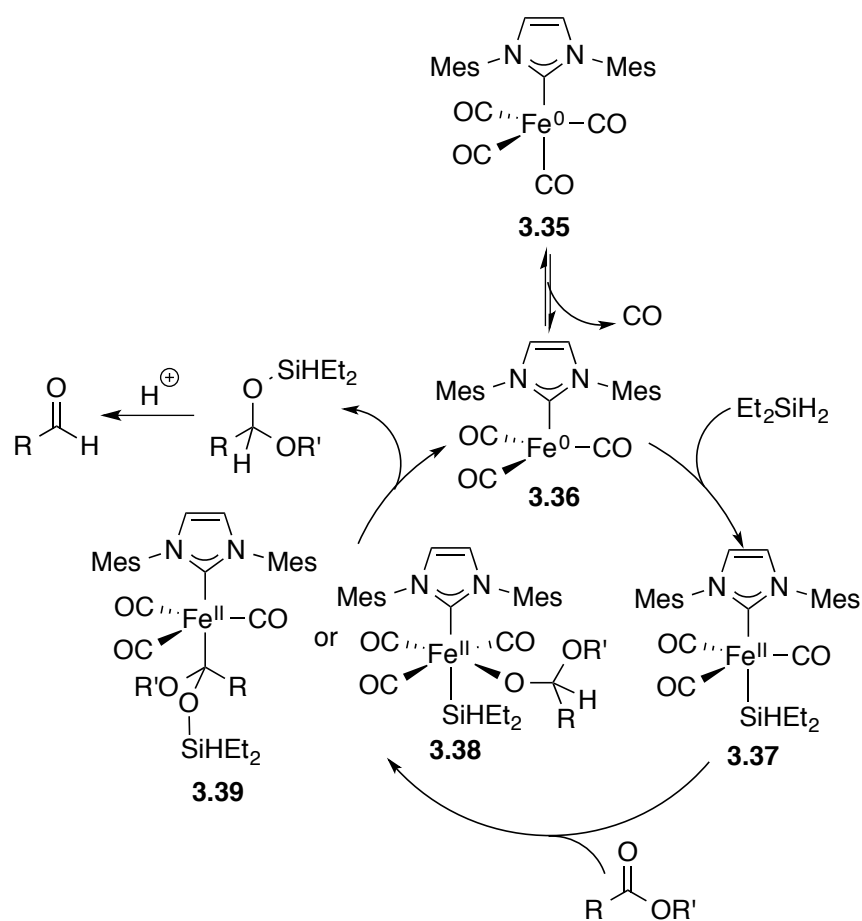
Scheme 3.13. Reduction of esters to aldehydes via hydrosilylation catalyzed by 3.35



The group also explored the mechanism for iron–NHC **3.35** catalyzed reduction of esters (Scheme 3.14). The mechanism starts with the formation of a 16-electron species **3.36** by dissociation of one CO ligand. Oxidative addition of Et₂SiH₂ yields iron(II) **3.37**. Addition of the

ester can generate either complex **3.38** or **3.39** depending on whether the Fe–H or Fe–Si bond inserts into the carbonyl of the ester. Reductive elimination of **3.38** or **3.39** regenerates the active species **3.36** and forms a silylacetal, which upon addition of acid be converted into the aldehyde. Again, the σ -donating capabilities of the NHC ligand stabilize the low oxidation state intermediates in the catalytic cycle, facilitating excellent reactivity.

Scheme 3.14. Proposed mechanism for the iron–NHC **3.35 catalyzed reduction of esters**

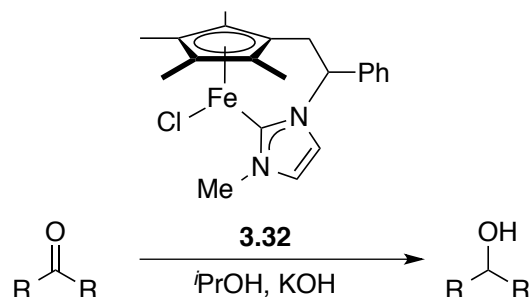


3.3.3.2 Hydrogenation

Apart from reduction via hydrosilylation, reduction with dihydrogen is also a useful synthetic tool for the production of complex organic molecules. Additionally, transfer

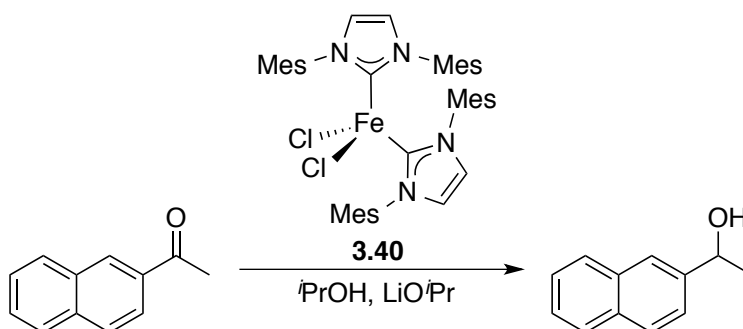
hydrogenation can also be particularly useful. In 2010, Royo and coworkers utilized the iron–NHC pendant piano stool complex **3.32** for the reduction of ketones to their corresponding alcohols (Scheme 3.15).³⁰ Reduction of acetophenone, benzophenone, and cyclohexanone in the presence of 2-propanol and KOH gave the desired products in 85-100%.

Scheme 3.15. Transfer hydrogenation of ketones catalyzed by 3.32



In 2012, Glorius *et al.* reported one additional example of transfer hydrogenation catalyzed by an iron–NHC complex (Scheme 3.16).⁴⁸ Reduction of 2'-acetonaphthone proceeded in the presence of LiO^iPr in isopropanol in up to 98% yield.

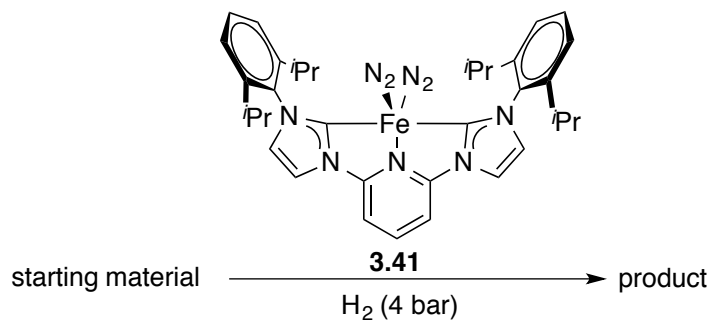
Scheme 3.16. Transfer hydrogenation of 2'-acetonaphthone catalyzed by 3.40



Chirik and coworkers demonstrated reduction of olefins with dihydrogen in 2012 using a low valent iron(0) complex **3.41** (Table 3.9).³¹ The reaction tolerates a variety of functional

groups, including esters, which often cause catalyst deactivation in other systems. This reactivity is attributed to the bulky aryl substituents on the stable tri-dentate bis(N-heterocyclic carbene)pyridine ligand. Although reduction of one tetra-substituted substrate was demonstrated, no conversion was observed with tetramethylethylene (entries 9 and 10). When the bis(N-heterocyclic carbene)pyridine ligand was replaced with a bis(imino)pyridine ligand, almost all reactions proceeded in lower yields, demonstrating the importance of the electron donating NHC ligand.

Table 3.9. Hydrogenation of olefins catalyzed by 3.41

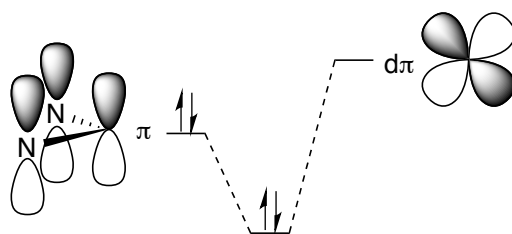


Entry	Starting Material	Product	R	Conv. (%)
1			<i>i</i> Pr	89
2			Me	>95
3			<i>i</i> Pr	>95
4			Me	35
5			<i>i</i> Pr	20
6			Me	>95
7			<i>i</i> Pr	4
8			Me	68
9		N/A	<i>i</i> Pr	0
10		N/A	Me	0

3.4 π -Bonding and Single Electron Bonding in Metal–NHC Complexes

While much of the reactivity of metal–NHC complexes exemplifies the excellent σ -donation of the NHC ligand, π -donation and single electron donation from the carbene are also possible. In 2006, Jacobsen and coworkers reported a computational assessment of σ and π -contributions in a series of metal–NHC complexes.⁴⁹ Through a combination of orbital interactions, steric interactions, and bond enthalpy, the authors calculated the amount of π -bonding in over thirty metal–NHC complexes. For all complexes (iron, ruthenium, osmium, or gold) studied the authors reported at least a 10% contribution to the metal–NHC bond from π -bonding interactions (Figure 3.7). This π -bonding interaction would consist between the filled π -symmetric orbital on the carbene carbon and an empty metal d-orbital. Although no examples have been isolated to date, this theoretical study demonstrates the potential for π -bonding interactions to occur between transition metals and NHCs.

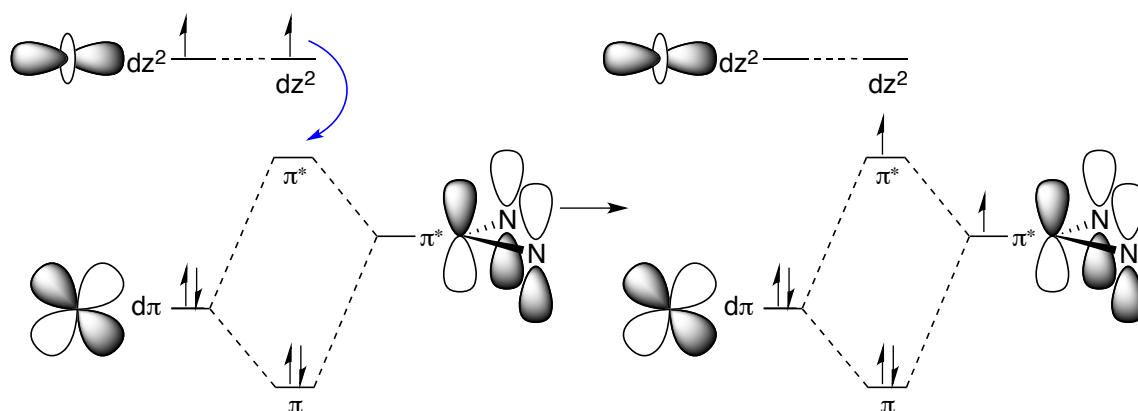
Figure 3.7. π -bonding interactions in metal–NHC complexes



Also possible are single electron contributions, referred to as non-innocent ligands. Jørgensen first introduced the concept of a non-innocent ligand in 1966, in which he established that “ligands are innocent when they allow oxidation states of the central atoms to be defined.”⁵⁰ Essentially, a non-innocent ligand is one that will be easily oxidized or reduced by one or more electrons (Figure 3.8). Upon addition of the carbene to the metal center, the carbene π^* -

antibonding orbital mixes with a d-orbital from the metal to generate bonding and antibonding molecular orbitals. This interaction increases the ligand field splitting to such an extent that the vacant π^* -antibonding molecular orbital is actually lower in energy than the metal d_{z^2} orbital. When the metal d_{z^2} orbital is filled and is the highest occupied molecular orbital (HOMO), intramolecular electron transfer from the metal to the carbene can occur. Additionally, the same phenomenon can occur by the external addition of an oxidant or reductant, where the ligand can donate or accept an electron, respectively.

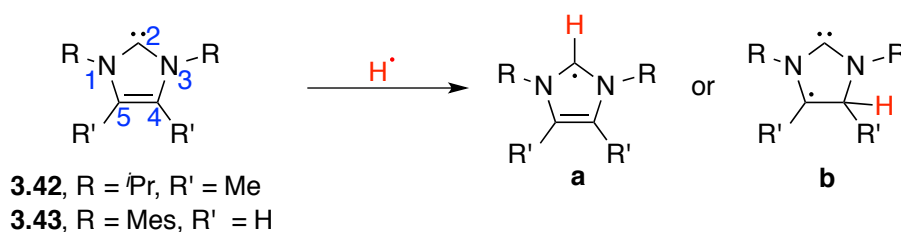
Figure 3.8. Molecular orbital mixing diagrams for metal–NHC bonding with redox non-innocent ligands



The ability for ligands to be redox non-innocent inherently changes the nature of the metal–carbene interaction. The carbene would gain radical character, thus becoming more nucleophilic and more reactive in nature. Although NHCs are typically potent σ -donors, they do have the ability to accept electron density from the metal center. However, to date there have been few reports of complexes displaying redox non-innocence at the N-heterocyclic carbene carbon. While there are no isolated NHC complexes that demonstrate non-innocence, a theoretical study of reactions of imidazol-2-ylidenes with a hydrogen atom suggests this type of reactivity is possible. In 2002, Clyburne, Percival, and coworkers computed the potential for the

addition of a radical to stable NHCs (Table 3.10).⁵¹ The addition of a hydrogen atom to carbenes **3.42** and **3.43** could occur at (a) the carbene carbon to produce **3.42a** or **3.43a**, or (b) the alkene carbon to produce **3.42b** or **3.43b**. The group computed the structures of the carbenes and their corresponding radicals using DFT calculations.

Table 3.10. Selected bond lengths (Å) and angles (°) calculated for carbenes **3.42** and **2.43** and their radicals



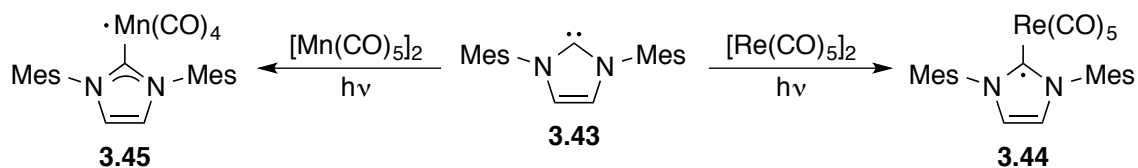
Entry	Parameter	3.42	3.42a	3.42b	3.43	3.43a	3.43b
1	N1–C2			1.386			1.397
2	N3–C2	1.377	1.430	1.358	1.392	1.431	1.367
3	N1–C5			1.414			1.411
4	N3–C4	1.415	1.418	1.496	1.411	1.409	1.504
5	C4–C5	1.367	1.363	1.505	1.357	1.356	1.491
6	N1–C2–N3	102.4	104.6	104.8	101.2	104.0	103.6

For radicals **3.42a** and **3.43a**, the N1(N3)–C2 bond lengths (entries 1 and 2) and N1–C2–N3 (entry 6) bond angle were found to be larger than those in the parent carbenes. The lengthening of the N1(N3)–C2 bonds makes sense as the character of these bonds became more σ in nature. Because the p-orbital on the carbene carbon is now filled, the donation from the nitrogen lone pairs decreases, lengthening the bond. The C4–C5 bond lengths (entry 5) remained approximately the same, indicating there is no delocalization throughout the ring. The structure of **3.42b** and **3.43b** were found to be considerably different from those of the parent carbenes. The C4–C5 bond was significantly longer due to the change from π to σ bonding at the site of addition. Spin density calculations on complex **3.42a** indicated that the majority of the unpaired

spin density (74.9%) is localized on C2, with 9.3% on each of the adjacent nitrogen atoms. In **3.42b**, most of the unpaired spin density is localized on C4 (83.3%), with a small amount of delocalization onto N1 (7.3%), N3 (6.3%), and C2 (7.8%).

With the exception of that one study, very little is known about the addition of a radical to a carbene to yield a new radical. In 2007, Tumanskii, Apeloig, and coworkers investigated the potential for one-electron processes to be used with metal–NHC complexes (Scheme 3.17).⁵² Photolysis of $[\text{Re}(\text{CO})_5]_2$ ($\lambda > 300$ nm) generates a rhenium centered radical $\cdot\text{Re}(\text{CO})_5$ that can react with free NHC **3.43** to generate radical adduct **3.44**. Complex **3.44** is persistent at room temperature for several days. The electron paramagnetic resonance (EPR) spectrum showed hyperfine coupling to the rhenium metal center, the imidazole nitrogen atoms, and two protons. The formation of **3.44** was also supported by matrix-assisted laser desorption/ionization time of flight (MALDI-TOF) mass spectrometry.

Scheme 3.17. Reactivity of NHC 3.43 with rhenium and manganese upon UV irradiation

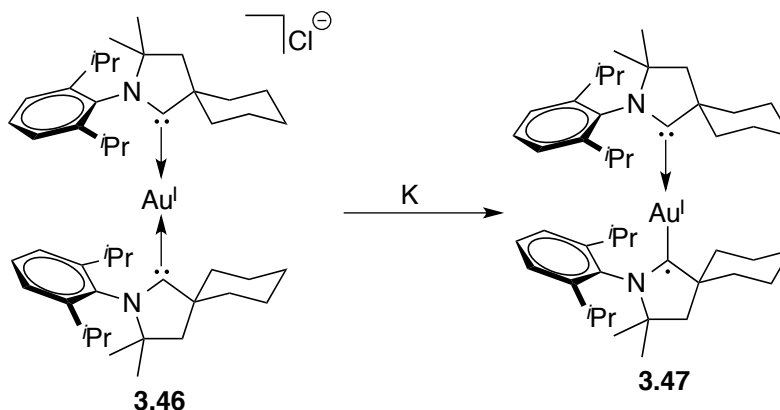


Reaction of free NHC **3.43** with $[\text{Mn}(\text{CO})_5]_2$ under UV irradiation ($\lambda > 300$ nm) led to a different type of product. The EPR spectrum showed hyperfine coupling with only the manganese nucleus. This result suggests that the product is a Mn-centered radical in which one of the carbonyl ligands has been substituted by carbene **3.43**. Complex **3.45** is persistent at room temperature for up to 16 hours. The difference in reactivity between $[\text{Re}(\text{CO})_5]_2$ and $[\text{Mn}(\text{CO})_5]_2$ may result from the known two orders of magnitude faster substitution of CO in manganese carbonyl complexes than analogous rhenium carbonyl complexes.⁵³ The calculated spin density

of **3.44** indicates that 53% of the spin density is localized on the central carbon atom of the NHC ligand and 34% on the other atoms of the imidazol-2-ylidene ring. In contrast, 85% of the spin density is localized on the manganese atom in **3.45**.

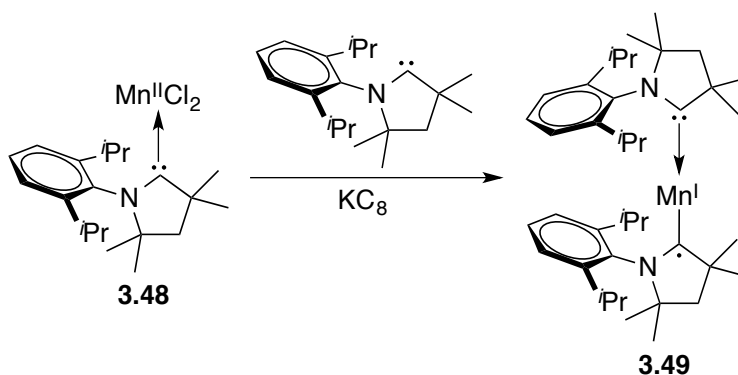
In contrast to Arduengo-type N-heterocyclic carbenes, cyclic(alkyl)(amino)carbenes (CAACs) have recently been shown to demonstrate redox non-innocent properties. In 2013, Bertrand *et al.* reported the isolation of mononuclear gold complexes bearing two CAAC ligands.⁵⁴ A bis(CAAC)Au^ICl complex (**3.46**) was reduced in an attempt to isolate the corresponding gold(0) species (Scheme 3.18). The gold–carbene bond length in **3.47** (1.991(2) Å) is slightly shorter than in the gold(I) precursor (2.0321(11) Å). Additionally, the carbon–nitrogen bond of the CAAC ligand (1.344(3) Å) is longer than in the gold(I) precursor (1.304(2) Å). Both changes indicate significant π -backdonation of the unpaired electron from gold to the ligands. Natural bond order (NBO) analysis showed that the spin density in **3.47** is mainly localized on the carbene carbons (60%) and the nitrogen atoms (20%), while only 17% is localized on the gold metal center. In effect, the result is a gold center that has significantly more gold(I) character than gold(0) due to the ligand reduction. A similar phenomenon occurs when utilizing mononuclear copper complexes with CAAC ligands,⁵⁵ but does not occur in iron or cobalt complexes.⁵⁶

Scheme 3.18. Reduction of bis(CAAC)Au^ICl complex 3.46 with potassium



In analogy to the bis(CAAC)Au **3.47** example, Roesky, Frenking, Dittrich, and coworkers reported similar reactivity with manganese⁵⁷ and zinc complexes⁵⁸ bearing CAAC ligands. Upon reduction of (CAAC)MnCl₂ (**3.48**) with KC₈ in the presence of additional CAAC ligand, bis(CAAC)Mn (**3.49**) was isolated (Scheme 3.19). The magnetic moment at room temperature of 4.15 μ_B is close to the spin only value for an S = 3/2 system, not the value common for a two-coordinate manganese compound (5.92 μ_B, S = 5/2). This result indicated that complex **3.49** contains a covalent bond between the carbene carbon atom and the central manganese atom, leaving a radical center at the carbene moiety. Further investigations established that the data best represented an antiferromagnetic coupling between a manganese(I) center (S = 2) and one radical spin (S = 1/2) that is delocalized on the two carbene carbon atoms.

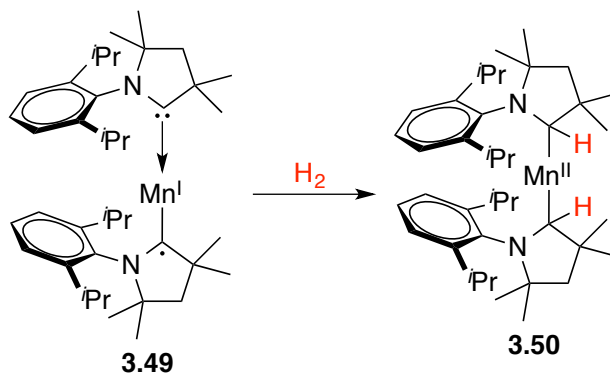
Scheme 3.19. Reduction of (CAAC)MnCl₂ complex 3.48 with potassium graphite



Reactivity studies of the two-coordinate manganese complex **3.49** revealed some interesting results. Complex **3.49** acts as an effective dihydrogen splitter at room temperature. In fact, a molecule of hydrogen was split homolytically by the two radical centers connected by the manganese center to produce **3.50** (Scheme 3.20). In comparison to frustrated Lewis pair chemistry, the group tested the use of the free CAAC ligand for H₂ splitting. Indeed, the free CAAC ligand does cleave dihydrogen at 35 °C for 5 hours. In comparison, complex **3.49**, where

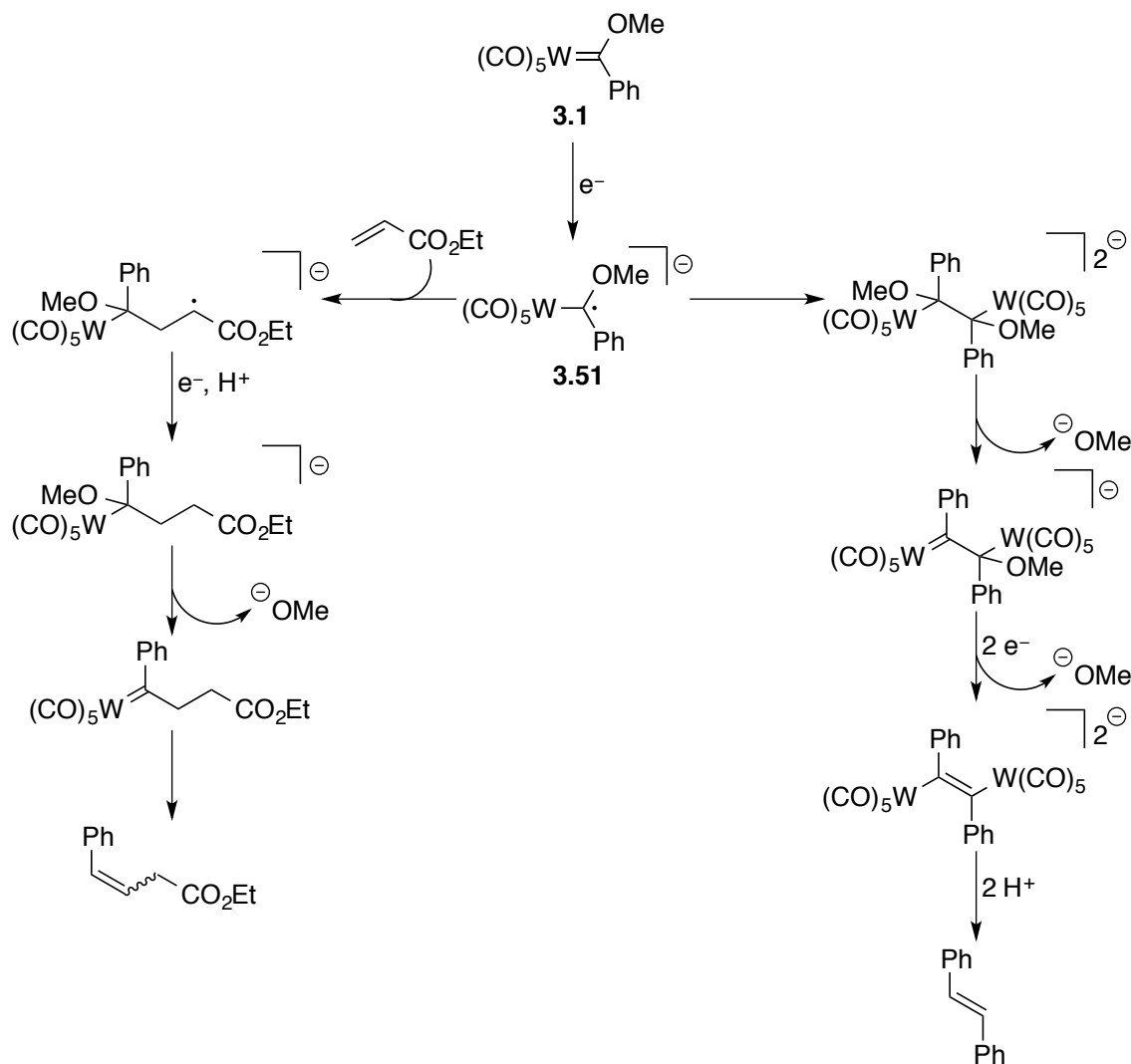
the CAAC is bound to Mn as a delocalized radical, cleaves H₂ at 25 °C within a few seconds. Such an activation of H₂ or other small molecules could be extremely useful for a variety of applications.

Scheme 3.20. Homolytic cleavage of H₂ to generate manganese complex 3.50



Additionally, Fischer-type carbenes, especially those of paramagnetic, first-row transition metals, have demonstrated redox non-innocent behavior.⁵⁹ Reactive Fischer-type carbene complexes are key intermediates in several catalytic reactions such as olefin metathesis, cyclopropanation, and C–H bond insertion. However, up until recently their potential redox non-innocence has received considerably much less attention. The lowest unoccupied molecular orbital (LUMO) of Fischer-type carbene complexes is carbene carbon centered, which makes it possible to form carbon-centered radicals upon one-electron reduction of these complexes. In 1976, Casey *et al.* showed that one-electron reduction of group 6 transition metal carbene complexes lead to the formation of carbon-centered radical anions, as evidenced by EPR spectroscopy (Scheme 3.21).⁶⁰ Recently, the radical reactivity of these complexes has been investigated for stoichiometric transformations. Carbon-centered radicals such as tungsten complex **3.51** have been employed in C–C bond forming reactions to undergo dimerization or radical addition to electron-poor olefins.

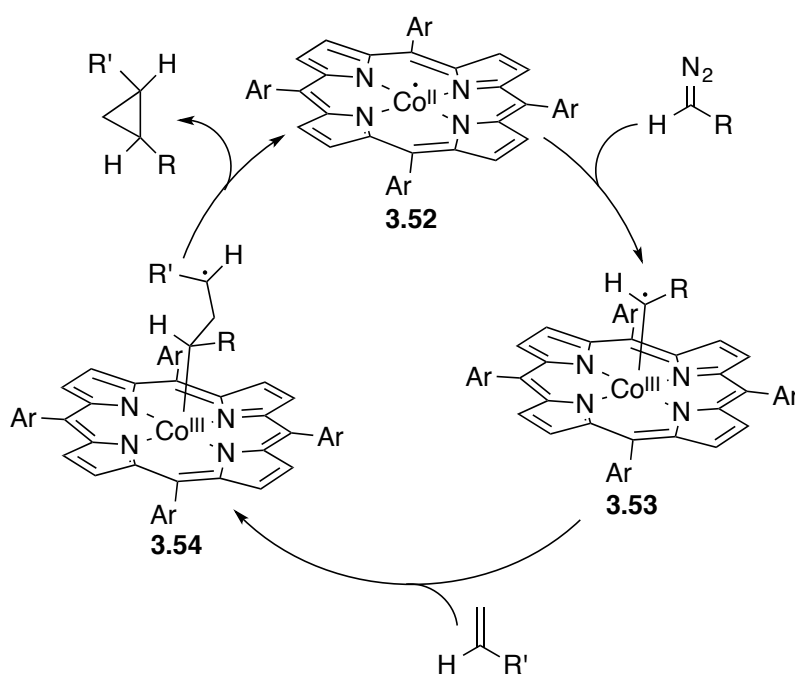
Scheme 3.21. Synthesis and stoichiometric reactivity of tungsten carbene 3.51



Fischer-type carbene ligands also demonstrate redox non-innocence at paramagnetic metal(II) complexes of group 9 transition metals. For example, $\text{Co}^{\text{II}}(\text{porphyrin})$ (**3.52**) is an effective catalyst for olefin cyclopropanation (Scheme 3.22).⁶¹⁼⁶⁴ Reactions catalyzed by **3.52** (or variants of this complex) demonstrate unprecedented reactivity, stereocontrol, and ability to effect cyclopropanation with near stoichiometric amounts of alkenes, avoiding carbene dimer formation. The remarkable reactivity of this complex differs significantly from typical copper and rhodium based systems that generate electrophilic Fischer-type carbene intermediates. Based on EPR and

DFT studies, the catalytically active cobalt carbene complex has a strong carbon-radical character. The mechanism for cyclopropanation involves the reaction of cobalt(II) species **3.52** with a diazo-compound to generate the carbon-centered radical species **3.53**. Addition of radical species **3.53** to the olefin generates complex **3.54**, which can undergo cyclopropane ring closure to form the desired product. The last step is describe as a radical-type C–C bond coupling with simultaneous hemolytic splitting of the Co–C bond to regenerate cobalt(II) species **3.52**.

Scheme 3.22. Carbene-centered radical mechanism for cyclopropanation of olefins



This phenomenon causes the carbene to lose its typical Fischer-type carbene character and gain radical character, thus becoming more nucleophilic in nature. Given the similarities between Arduengo-type NHCs and Fischer-type carbenes in that both are potent σ -donors and have the ability to accept electron density from the metal center, it is interesting that to date there have been few reports of complexes displaying redox non-innocence at the N-heterocyclic carbene carbon.

3.5 References

1. Fischer, E. O.; Maasbol, A. *Angew. Chem. Int. Ed. Engl.* **1964**, *3*, 580.
2. Arduengo, A. J.; Harlow, R. L.; Kline, M. *J. Am. Chem. Soc.* **1991**, *113*, 361.
3. Jacobsen, H.; Correa, A.; Poater, A.; Costabile, C.; Cavallo, L. *Coord. Chem. Rev.* **2009**, *253*, 687.
4. Öfele, K. *J. Organomet. Chem.* **1968**, *12*, P42.
5. Öfele, K.; Herberhold, M. *Angew. Chem. Int. Ed. Engl.* **1970**, *9*, 739.
6. Wanzlick, H. W.; Schönherr, H. *J. Angew. Chem. Int. Ed. Engl.* **1968**, *7*, 141.
7. Schwab, P.; France, M. B.; Ziller, J. W.; Grubbs, R. H. *Angew. Chem. Int. Ed. Engl.* **1995**, *34*, 2039.
8. Dias, E. L.; Nguyen, S. T.; Grubbs, R. H. *J. Am. Chem. Soc.* **1997**, *119*, 3887.
9. Scholl, M.; Trnka, T. M. M. J. P.; Grubbs, R. H. *Tetrahedron Lett.* **1999**, *40*, 2247.
10. Huang, J.; Stevens, E. D.; Nolan, S. P.; Petersen, J. L. *J. Am. Chem. Soc.* **1999**, *121*, 2674.
11. Scholl, M.; Ding, S.; Lee, C. W.; Grubbs, R. H. *Org. Lett.* **1999**, *1*, 953.
12. Grubbs, R. H. *Tetrahedron* **2004**, *60*, 7117.
13. Kingsburg, J. S.; Harrity, J. P. A.; Bonitatebus, P. J.; Hoveyda, A. H. *J. Am. Chem. Soc.* **1999**, *121*, 791.
14. Garber, S. B.; Kingsbury, J. S.; Gray, B. L.; Hoveyda, A. H. *J. Am. Chem. Soc.* **2000**, *122*, 8168.
15. Hillier, A. C.; Grasa, G. A.; Viciu, M. S.; Lee, H. M.; Yang, C.; Nolan, S. P. *J. Organomet. Chem.* **2002**, *653*, 69.
16. Fortman, G. C.; Nolan, S. P. *Chem. Soc. Rev.* **2011**, *40*, 5151.
17. Herrmann, W. A.; Elison, M.; Fischer, J.; Köcher, C.; Artus, G. R. *J. Angew. Chem. Int. Ed. Engl.* **1995**, *34*, 2371.
18. Herrmann, W. A.; Reisinger, C. P.; Spiegler, M. *J. Organomet. Chem.* **1998**, *557*, 93.
19. Hartmann, C. E.; Nolan, S. P. . C. C. S. J. *Organometallics* **2009**, *28*, 2915.
20. Nasielski, J.; Hadei, N.; Achonduh, G.; Kantchev, E. A. B.; O'Brien, C. J.; Lough, A.; Organ, M. G. *Chem. Eur. J.* **2010**, *16*, 10844.
21. Jin, Z.; Gu, X. P.; Qiu, L. L.; Wu, G. P.; Song, H. B.; Fang, J. X. *J. Organomet. Chem.* **2011**, *696*, 489.
22. Öfele, K. *Angew. Chem. Int. Ed. Engl.* **1969**, *8*, 916.
23. Louie, J.; Grubbs, R. H. *Chem. Commun.* **2000**, 1479.
24. Chen, M. Z.; Sun, H. M.; Li, W. F.; Wang, Z. G.; Shen, Q.; Zhang, Y. *J. Organomet. Chem.* **2006**, *691*, 2489.
25. Manna, C. M.; Z., K. H.; Li, B.; Byers, J. A. *Polyhedron* **2014**, *84*, 160.
26. Bedford, R. B.; Betham, M.; Bruce, D. W.; Danopoulos, A. A.; Frost, R. M.; Hird, M. *J. Org. Chem.* **2006**, *71*, 1104.
27. Ghorai, S. K.; Jin, M.; Hatakeyama, T.; Nakamura, M. *Org. Lett.* **2012**, *14*, 1066.
28. Hatakeyama, T.; Hashimoto, S.; Ishizuka, K.; Nakamura, M. *J. Am. Chem. Soc.* **2009**, *131*, 11949.
29. Jiang, F.; Bézier, D.; Sortais, J. B.; Darcel, C. *Adv. Synth. Catal.* **2011**, *353*, 239.

30. Kandepi, V. V. K. M.; Cardoso, J. M. S.; Peris, E.; Royo, B. *Organometallics* **2010**, *29*, 2777.
31. Yu, R. P.; Darmon, J. M.; Hoyt, J. M.; Margulieux, G. W.; Turner, Z. R.; Chirik, P. J. *ACS Catal.* **2012**, *2*, 1760.
32. Kato, M.; Kamigaito, M.; Sawamoto, M.; Higashimura, T. *Macromol.* **1995**, *28*, 1721.
33. Wang, J. S.; Matyjaszewski, K. *J. Am. Chem. Soc.* **1995**, *117*, 5614.
34. Wang, Y.; Sun, H.; Tao, X.; Shen, Q.; Zhang, Y. *Chin. Sci. Bull.* **2007**, *52*, 3193.
35. Biernesser, A. B.; Li, B.; Byers, J. A. *J. Am. Chem. Soc.* **2013**, *135*, 16553.
36. Tamura, M.; Kochi, J. K. *J. Am. Chem. Soc.* **1971**, *93*, 1487.
37. Smith, R. S.; Kochi, J. K. *J. Org. Chem.* **1976**, *41*, 502.
38. Fürstner, A.; Leitner, A.; Méndez, M.; Krause, H. *J. Am. Chem. Soc.* **2002**, *124*, 13856.
39. Nakamura, M.; Matsuo, K.; Ito, S.; Nakamura, E. *J. Am. Chem. Soc.* **2004**, *126*, 3686.
40. Plietker, B. *Angew. Chem. Int. Ed.* **2006**, *45*, 1469.
41. Plietker, B.; Dieskau, A.; Möws, K.; Jatsch, A. *Angew. Chem. Int. Ed.* **2008**, *47*, 198.
42. Holzwarth, M.; Dieskau, A.; Tabassam, M.; Plietker, B. *Angew. Chem. Int. Ed.* **2009**, *48*, 7251.
43. Dieskau, A. P. H. M. S.; Plietker, B. *Chem. Eur. J.* **2012**, *18*, 2423.
44. Bézier, D.; Venkanna, G. T.; Sortais, J. B.; Darcel, C. *ChemCatChem* **2011**, *3*, 1747.
45. Misal Castro, L. C.; Sortais, J. B.; Darcel, C. *Chem. Commun.* **2012**, *48*, 151.
46. Bézier, D.; Venkanna, G. T.; Misal Castro, L. C.; Zhang, J.; Roisnel, T.; Sortais, J. B.; Darcel, C. *Adv. Synth. Catal.* **2012**, *354*, 1879.
47. Li, H.; Misal Castro, L. C.; Zheng, J.; Roisnel, T.; Dorcet, V.; Sortais, J. B.; Darcel, C. *Angew. Chem. Int. Ed.* **2013**, *52*, 8045.
48. Hashimoto, T.; Urban, S.; Hoshino, R.; Ohki, Y.; Tatsumi, K.; Glorius, F. *Organometallics* **2012**, *31*, 4189.
49. Jacobsen, H.; Correa, A.; Costabile, C.; Cavallo, L. *J. Organomet. Chem.* **2006**, *691*, 4350.
50. Jørgensen, C. K. *Coord. Chem. Rev.* **1966**, *1*, 164.
51. McKenzie, I.; Brodovitch, J. C.; Percival, P. W.; Ramnial, T.; Clyburne, J. A. C. *J. Am. Chem. Soc.* **2002**, *125*, 11565.
52. Tumanskii, B.; Sheberla, D.; Molev, G.; Apeloig, Y. *Angew. Chem. Int. Ed.* **2007**, *46*, 7408.
53. Atwood, J. D.; Brown, T. L. *J. Am. Chem. Soc.* **1976**, *98*, 3160.
54. Weinberger, D. S.; Melaimi, M.; Moore, C. E.; Rheingold, A. L.; Frenking, G.; Jerabek, P.; Bertrand, G. *Angew. Chem. Int. Ed.* **2013**, *52*, 8964.
55. Weinberger, D. S.; SK, N. A. M. K. C.; Melaimi, M.; Bertrand, G.; Stückl, A. C.; Roesky, H. W.; Dittrich, B.; Semeshko, S.; Schwederski, B.; Kaim, W.; Jerabek, P.; Frenking, G. *J. Am. Chem. Soc.* **2014**, *136*, 6235.
56. Ung, G.; Rittle, J.; Soleilhavoup, M.; Bertrand, G.; Peters, J. C. *Angew. Chem. Int. Ed.* **2014**, *53*, 8427.
57. Samuel, P. P.; Mondal, K. C.; Roesky, H. W.; Hermann, M.; Frenking, G.; Demeshko, S.; Meyer, F.; Stückl, A. C.; Christian, J. H.; Dalal, N. S.; Ungur, L.; Chibotaru, L. F.; Pröpper, K.; Meents, A.; Dittrich, B. *Angew. Chem. Int. Ed.* **2013**, *52*, 11817.
58. Singh, A. P.; Samuel, P. P.; Roesky, H. W.; Schwarzer, M. C.; Frenking, G.; Sidhu, N. S.; Dittrich, B. *J. Am. Chem. Soc.* **2013**, *135*, 7324.
59. Dzik, W. I.; Zhang, X. P.; de Bruin, B. *Inorg. Chem.* **2011**, *50*, 9896.

60. Krusic, P. J.; Klabunde, U.; Casey, C. P.; Block, T. F. *J. Am. Chem. Soc.* **1976**, *98*, 2015.
61. Penoni, A.; Wanke, R.; Tollari, S.; Gallo, E.; Musella, D.; Ragaini, F.; Demartin, F.; Cenini, S. *Eur. J. Inorg. Chem.* **2003**, 1452.
62. Chen, Y.; Ruppel, J. V.; Zhang, X. P. *J. Am. Chem. Soc.* **2007**, *129*, 12074.
63. Zhu, S.; Perman, J. A.; Zhang, X. P. *Angew. Chem. Int. Ed.* **2008**, *47*, 8460.
64. Zhu, S. F.; Xu, X.; Perman, J. A.; Zhang, X. P. *J. Am. Chem. Soc.* **2010**, *132*, 12796.

Chapter 4

Reactivity of Bis(amidinato)-N-Heterocyclic Carbene Iron Complexes

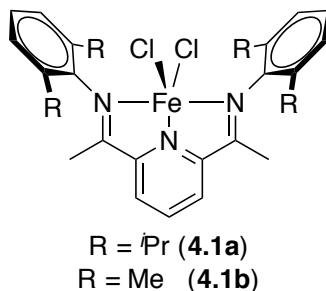
4.1 Introduction

Over the past few decades, the development of highly active and selective transition metal catalysts for the preparation of industrial chemicals and pharmaceuticals has attracted considerable attention. Noble-metals such as ruthenium, rhodium, palladium, iridium, and platinum have demonstrated remarkable activities for a variety of useful chemical transformations. However, their cost, toxicity, and scarcity warrant the development of cheap, non-toxic, and earth abundant alternatives. Recently, there has been an increasing effort to develop base-metal catalysts into useful and practical replacements for noble-metal catalysts.¹ Such systems utilizing iron have been shown to be active for oxidation, reduction, hydrogenation, cycloaddition, polymerization, and coupling reactions.² However, very few of these catalysts have been adopted for the preparation of industrial chemicals and pharmaceuticals; therefore, the field of base-metal catalysis remains underdeveloped.

4.1.1 Bis(imino)pyridine Iron Complexes

While the metal employed largely influences the expectations for catalytic activity, the importance of supporting ligands in tuning the reactivity of any given complex is vital. In particular, complexes bearing bis(imino)pyridine (PDI) ligands (**4.1**) have been shown to be exceptionally useful for a diverse series of chemical transformations (Figure 4.1).

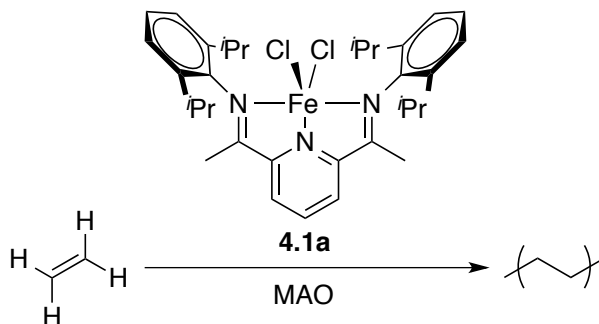
Figure 4.1. Bis(imino)pyridine iron complexes



4.1.1.1 Reactivity

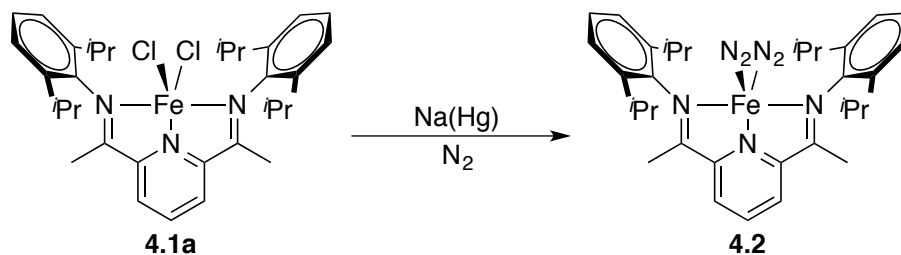
In the late 1990's, Gibson³ and Brookhart⁴ showed that iron and cobalt complexes containing bis(imino)pyridine (PDI, pyridyldiimine) ligands were extremely active and long-lived catalysts for the polymerization of ethylene (Scheme 4.1). These catalysts are robust and extremely active for polymerization to linear, high-density polyethylene. In fact, these complexes rivaled efficiencies of most of the potent early transition metal metallocenes complexes.⁵ Simple modifications to the aryl groups on the imine moieties enabled control of the number molecular weight (M_n) of the polymer. For example, catalysts bearing 2,6-diisopropylphenyl groups (**4.1a**) produced higher molecular weight polymer than catalysts bearing 2,6-dimethylphenyl groups (**4.1b**). Additional modifications in the reaction conditions enabled the selective production of olefin dimers, oligomers, polymers,^{6, 7} and cyclotrimers⁸ (when acetylene was used as the monomer feedstock).

Scheme 4.1. Polymerization of ethylene facilitated by iron complex 4.1a



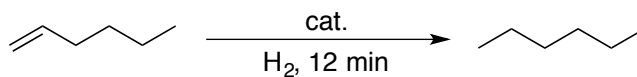
In 2004, Chirik *et al.* further demonstrated the usefulness of complexes bearing PDI ligands by the isolation of a bis(dinitrogen) complex **4.2** (Scheme 4.2).⁹ Complex **4.2** was generated by reduction of the parent dichloride **4.1a** with sodium mercury amalgam under a nitrogen atmosphere. The complex was shown to be active for a variety of organic transformations.

Scheme 4.2. Preparation of bis(dinitrogen) 4.2 by reduction of dichloride complex 4.1a



Complex **4.2** proved to be a competent catalyst for the hydrogenation of olefins at low loadings (0.3 mol%) and low pressures of hydrogen. In fact, the iron-based catalyst outperformed some of the more active noble-metal complexes for the hydrogenation of 1-hexene (Table 4.1).¹⁰ Under conditions optimized for the iron system, **4.2** showed a higher TOF as compared to Pd/C, Wilkinson's catalyst, and Crabtree's catalyst. Additionally, complex **4.2** is active for the hydrogenation of functionalized and hindered olefins.¹¹ While the catalyst tolerates functional groups such as ketones and esters, mono-substituted amines and other Lewis bases dramatically decrease catalytic turnover.

Table 4.1. Comparison of iron complex 4.2 with noble-metal catalysts for the hydrogenation of 1-hexene

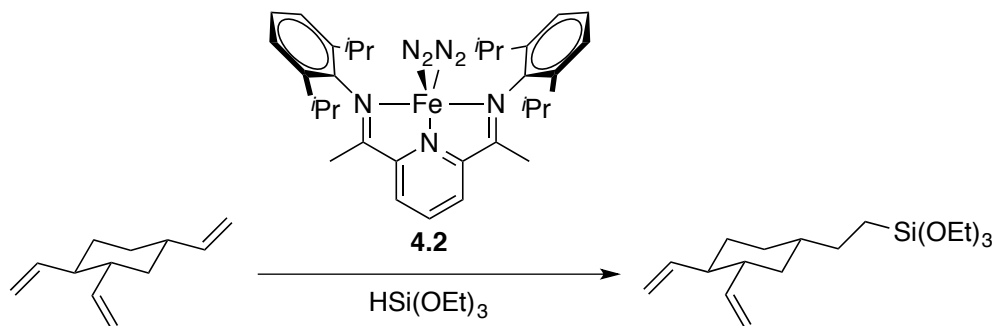


Entry	Cat.	TOF (h ⁻¹)
1	4.2	1800
2	10% Pd/C	370
3	RhCl(PPh ₃) ₃ (2.34)	10
4	[Ir(cod)(PCy ₃)pyr]PF ₆	75

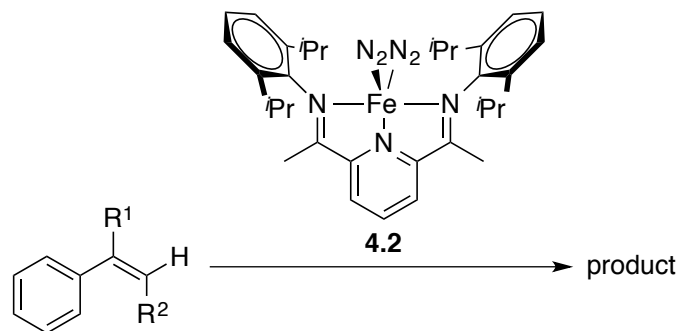
Chirik's reduced iron complex **4.2** has also been applied to hydrosilylation of alkenes.¹² Although precious metal catalysts such as platinum and rhodium conventionally carry out

hydrosilylation, Chirik *et al.* reported an iron-catalyzed variant. The regioselective hydrosilylation of 1,2,4-trivinylcyclohexane with tertiary silanes is an important transformation in the production of low rolling resistance tires.¹³ Iron catalyst **4.2** exhibited selectivity for the mono-hydrosilylation of the alkene that far exceeded results obtained with commercially used platinum compounds (Scheme 4.3). Furthermore, the catalytic hydrosilylation proceeded with high anti-Markovnikov selectivity, and with internal olefins, addition of PhSiH₃ *trans*-2-hexene furnished exclusively terminally silylated products.

Scheme 4.3. Selective hydrosilylation of 1,2,4-trivinylcyclohexane catalyzed by 4.2

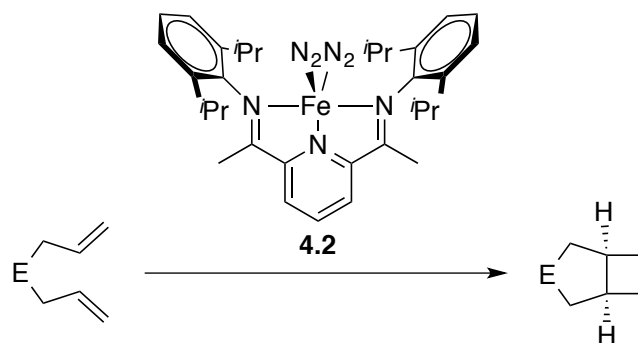


Encouraged by these results, Chirik extended the scope of olefin functionalization reactions to include the hydroboration of terminal, internal, and geminal olefins.¹⁴ Such reactions are useful for applications in organic synthesis such as Suzuki cross-coupling reactions.^{15, 16} Reactions catalyzed by **4.2** offer distinct advantages in substrate scope and selectivity over the previously reported noble and base-metal catalysts. Additionally, the catalyst is effective in the absence of organic solvents, thereby minimizing waste and facilitating product isolation. Interestingly, the hydroboration of styrene derivatives catalyzed by **4.2** generated the anti-Markovnikov products exclusively in high yields (Table 4.2). This selectivity is challenging due to poor regioselectivity and competitive dehydrogenative borylation.

Table 4.2. Anti-Markovnikov hydroboration of styrene derivatives catalyzed by complex 4.2

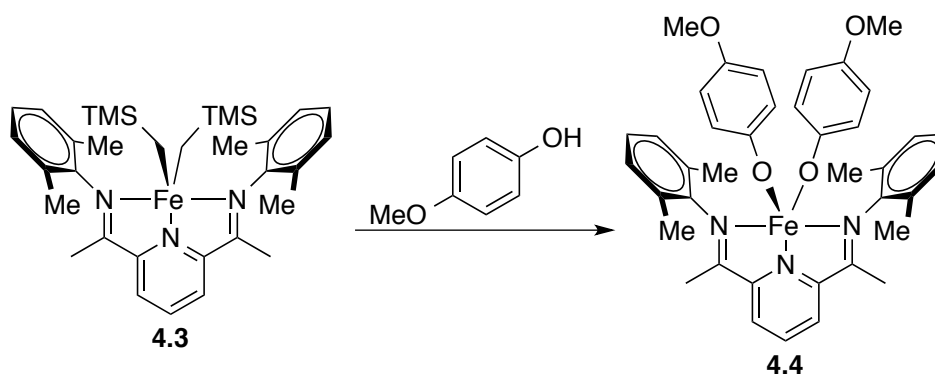
Entry	R ¹	R ²	Product
1	H	H	
2	Me	H	
4	H	Me	

The Chirik group also demonstrated the use of complex **4.2** for the intramolecular $[2\pi+2\pi]$ cycloaddition of α,ω -dienes for the direct construction of strained four-membered rings.¹⁷ While thermally forbidden,¹⁸ photochemical methods, use of strained olefins, activated π systems, and transition metal reagents have been employed to circumvent the constraints of orbital symmetry.¹⁹ The group demonstrated a series of di-olefins that undergo $[2\pi+2\pi]$ cycloaddition at room temperature using complex **4.2** as the catalyst precursor (Table 4.3). The iron catalyst is tolerant of amine and ester functional groups (entries 5 and 6). In the absence of light, the reaction yields did not change, suggesting a thermal process. In 2011, Chirik also published the coupling of two different partners in an intramolecular fashion.²⁰

Table 4.3. $[2\pi+2\pi]$ cycloaddition of α,ω -dienes catalyzed by **4.2**

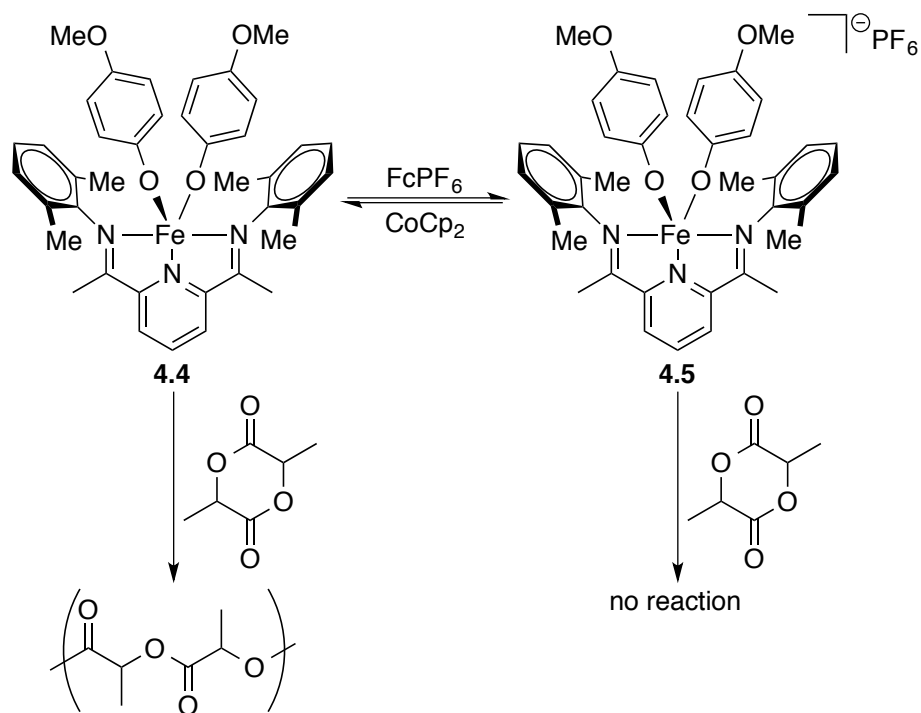
Entry	E	Time (min)	Conv. (%)
1	CH ₂	300	92
2	SiMe ₂	300	0
3	NH	300	0
4	NBn	26	90
5	N ^t Bu	<5	>95
6	C(CO ₂ Et) ₂	141	>95

In 2013, our laboratory demonstrated the use of iron complexes bearing a bis(imino)pyridine ligand for the polymerization of (*rac*)-lactide.²¹ Starting from a bis(alkyl) iron complex **4.3**, Ashley B. Biernesser synthesized an iron bis(alkoxide) complex **4.4** (Scheme 4.4). Iron species **4.4**, either isolated or generated *in situ*, is an active polymerization catalyst for producing poly(lactic acid) with very low polydispersities (PDI < 1.2).

Scheme 4.4. Synthesis of iron bis(alkoxide) bis(imino)pyridine complex **4.4**

The catalysis demonstrated several hallmarks of a living polymerization such as a linear dependence of M_n on conversion, narrow molecular weight distributions, and linear polymer growth upon sequential addition of lactide monomer. We also noted an interesting feature of the catalytic system: simple oxidation of the active species completely but reversibly generated an iron complex (**4.5**) that was inactive for lactide polymerization. The lactide polymerization reaction could be switched on and off by reversibly reducing and oxidizing the metal center, respectively (Scheme 4.5). We proposed the special properties of iron complexes supported by bis(imino)pyridine ligands explains the versatility of the complexes and that the electronic and steric properties will be useful for polymerization and copolymerization reactions in the future.

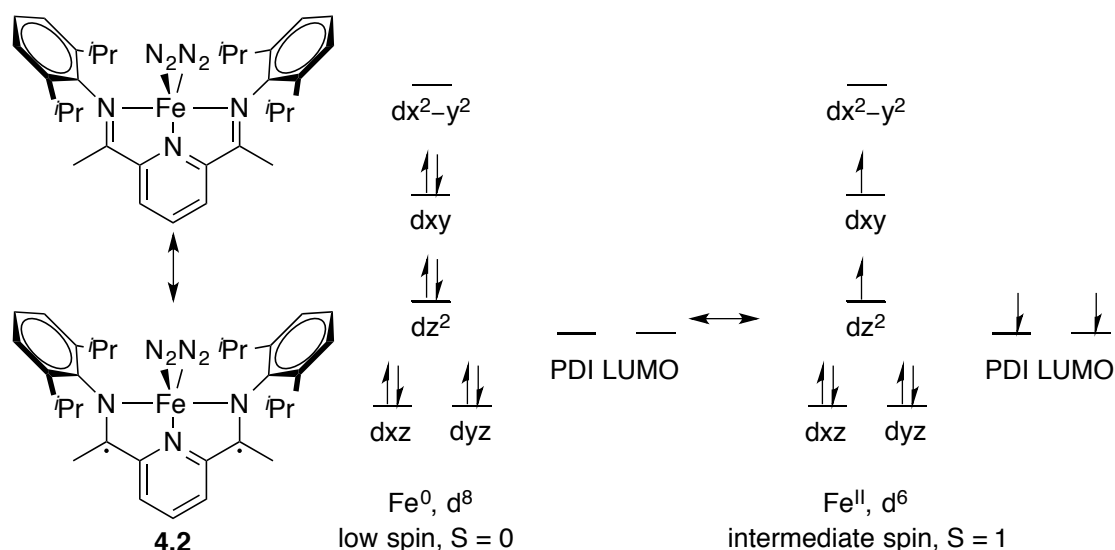
Scheme 4.5. Polymerization of lactide to poly(lactide acid) with iron bis(imino)pyridine complexes 4.4 and 4.5



4.1.1.2 Electronic Structure and its Effect on Reactivity

Due to such remarkable activity in a variety of catalytic transformations, the electronic structure of the bis(imino)pyridine ligand framework has been studied extensively. In 2004, Chirik and coworkers first demonstrated the effectiveness of iron complex **4.2** as a competent catalyst for hydrogenation, and subsequently hydrosilylation, hydroboration, and cycloaddition reactions. Additionally, the group studied the electron structure through a combination of X-ray crystallography, SQUID magnetometry, Mössbauer spectroscopy, and DFT calculations.^{9, 22} Complex **4.2** is thought to be a hybrid resonance structure between a low spin iron(0) complex and an intermediate spin ($S = 1$) iron(II) center coupled to a doubly anionic, triplet bis(imino)pyridine ligand (Figure 4.2).

Figure 4.2. Representative electronic structure of bis(imino)pyridine iron complex 4.2

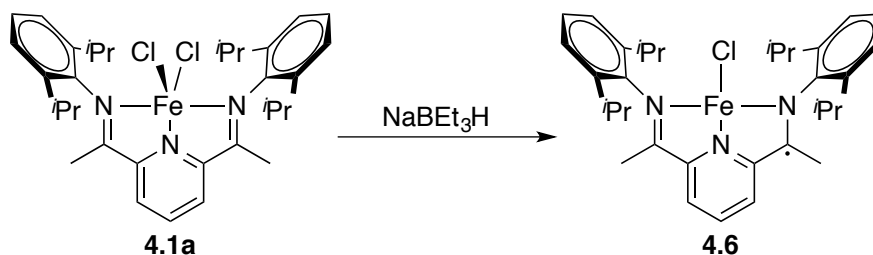


In the solution phase, iron complex **4.2** is in equilibrium with an iron complex with a singly bound dinitrogen molecule, which the authors believe is unambiguously an intermediate spin ($S = 1$) iron(II) center coupled to a doubly anionic, triplet bis(imino)pyridine ligand with a

magnetic moment similar to the value expected for 2 unpaired electrons. Evidence for a two-electron reduction of the ligand was first indicated by X-ray crystallography. The C–N bond distances of the imine moieties were elongated to 1.333 Å from 1.280 Å in the parent dichloride complex **4.1a**, which indicates a reduction in the C–N bond order. The Mössbauer spectrum featured an isomer shift of 0.39 mm/s and a quadrupole splitting of 0.53 mm/s . These values are consistent with an intermediate spin ($S = 1$) iron(II) center, and are not in agreement with those expected for an iron(0) center (isomer shift = 0 mm/s). To corroborate these experimental results, unrestricted broken symmetry (BS) DFT calculations carried out supported the hypothesis that the bis(imino)pyridine was acting as a redox non-innocent ligand that had been doubly reduced on the iron center.

In support of this redox activity, the parent dichloride complex **4.1a** was reduced with one electron to a formally iron(I) complex (**4.6**). The Chirik group observed that the bis(imino)pyridine ligand had been singly reduced (Scheme 4.6).^{23,24}

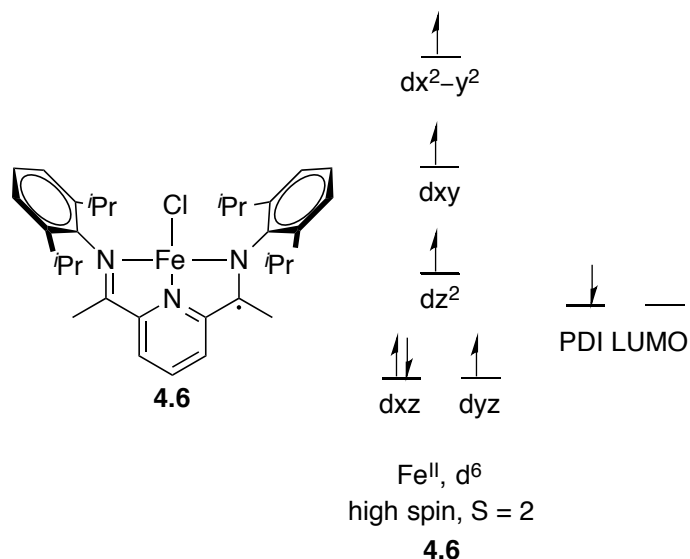
Scheme 4.6. Synthesis of bis(imino)pyridine iron complex **4.6**



Similar to bis(dinitrogen) complex **4.2**, lengthening of the C–N bond was observed crystallographically from 1.280 Å in the parent dichloride complex **4.1a** to 1.301 and 1.313 Å in complex **4.6**. These values support a reduction, but to a lesser extent than in the doubly reduced species **4.3**. The Mössbauer spectrum showed an isomer shift of 0.77 mm/s and a quadrupole splitting of 0.73 mm/s , which unambiguously indicate a high spin ($S = 2$) iron center. The solution

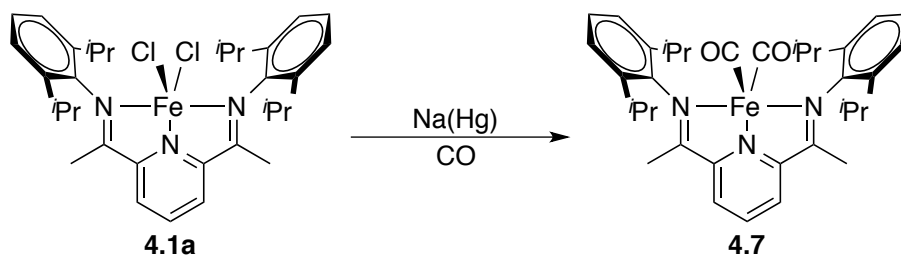
state magnetic moment was measured to be $4.0 \mu_B$, which corresponds to the calculated spin only value of $3.9 \mu_B$ for a species with 3 total unpaired electrons ($S = 3/2$). Based on these results, the group postulated that complex **4.6** is best represented as a high spin iron(II) center antiferromagnetically coupled to a singlet, anionic ligand (Figure 4.3).

Figure 4.3. Representative electronic structure of bis(imino)pyridine iron complex 4.6



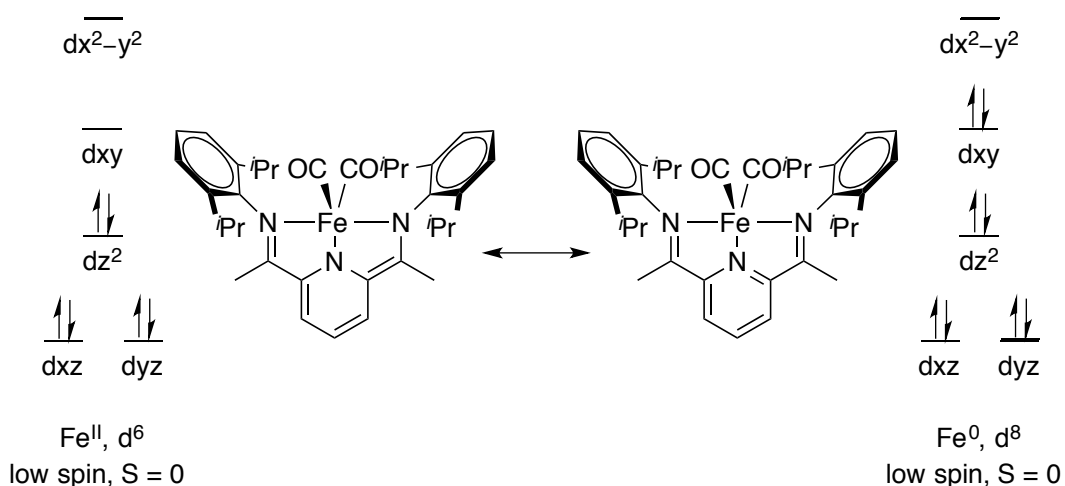
The addition of sodium mercury amalgam under an atmosphere of carbon monoxide generated a diamagnetic iron species (**4.7**) (Scheme 4.7).²⁵

Scheme 4.7. Synthesis of bis(imino)pyridine iron complex 4.7



Based on spectroscopic and computational studies, the Chirik group established that the ground state for this molecule can be described either as a low spin iron(II) compound with a singlet dianionic chelate or as a traditional low spin ($S=0$) iron(0) d^8 complex with a neutral bis(imino)pyridine ligand (Figure 4.4). The reason for the ambiguity derives from the DFT computed HOMO of the compound, which is 68% bis(imino)pyridine in character with a large contribution from the iron center. Unlike the bis(dinitrogen) compound **4.2**, **4.7** exhibits no spectroscopic evidence for the mixing of low-lying higher-spin excited states, and therefore, the electronic structure can be considered a hybrid of the iron(0) and iron(II) centers.

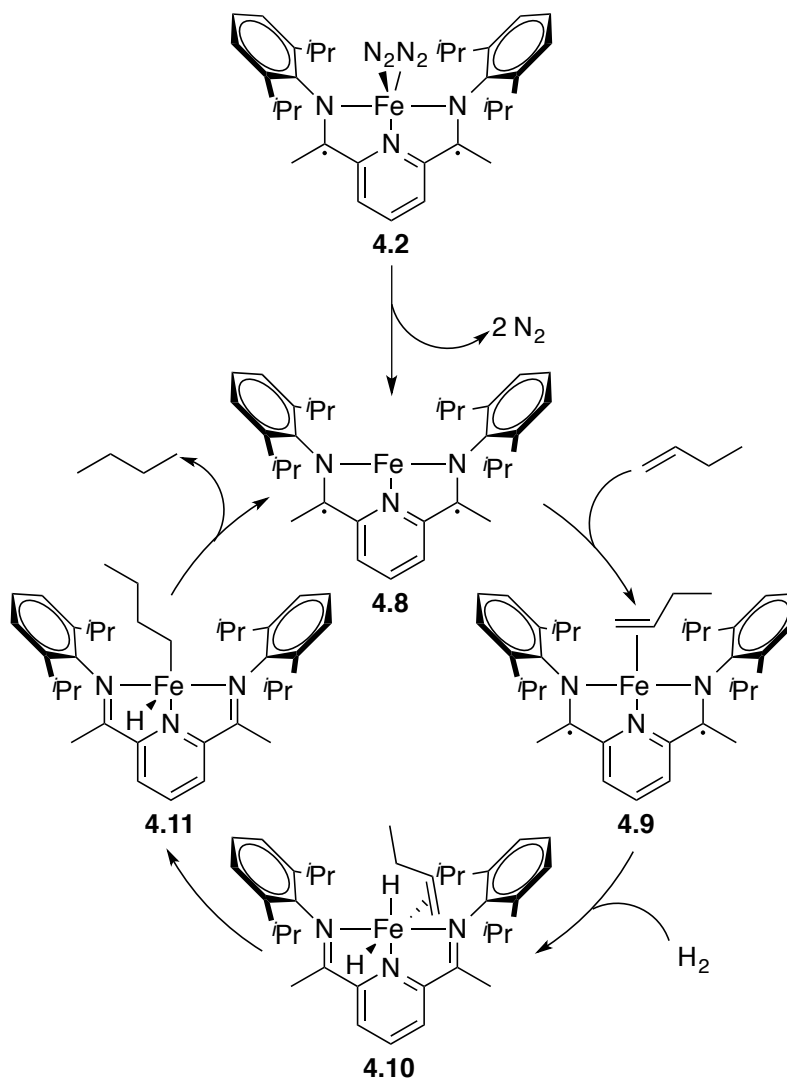
Figure 4.4. Representative electronic structure of bis(imino)pyridine iron complex 4.7



The ability of the bis(imino)pyridine ligand to accept one or two electrons has been shown to be of importance with regard to catalysis. First row transition metals can undergo both one and two-electron processes, but commonly proceed by one-electron pathways; therefore, pairing a redox active metal to a redox non-innocent ligand presents an opportunity for controlled two electron events. The Chirik group has used this strategy in the context of iron

bis(imino)pyridine catalyzed reactions. For example, an interesting mechanism for the iron-catalyzed hydrogenation of olefins was proposed (Scheme 4.8).

Scheme 4.8. Proposed mechanism for the hydrogenation of olefins catalyzed by bis(imino)pyridine iron complex 4.2

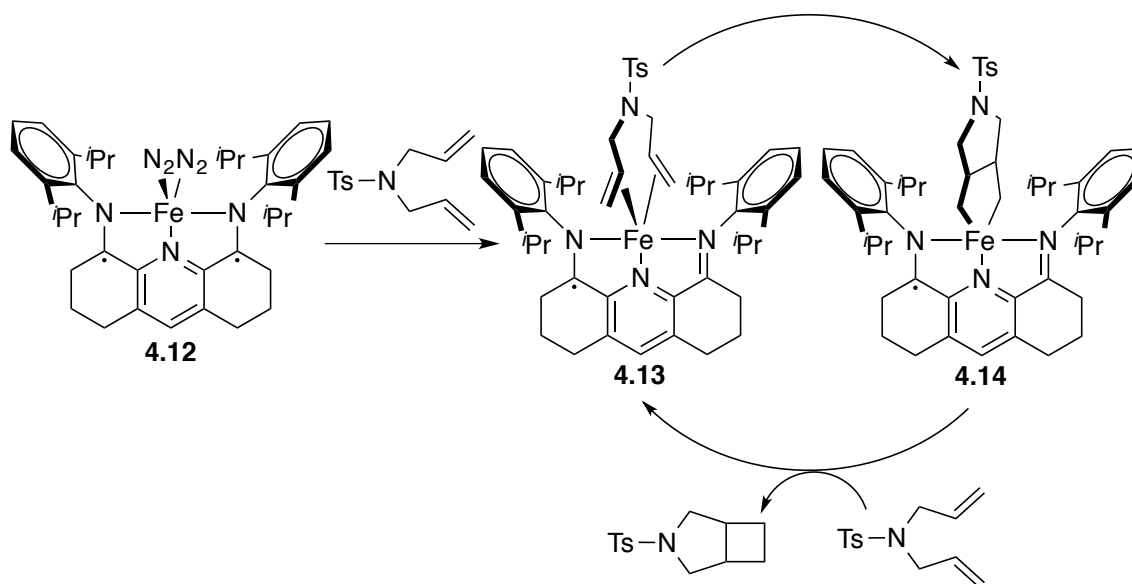


Loss of two equivalents of dinitrogen from 4.2 (relative to the catalyst) was observed by a Toepler pump experiment, which would lead to the coordinatively unsaturated complex 4.8. Coordination of the olefin would generate species 4.9, which can undergo oxidative addition of

H₂ to give 18-electron complex **4.10**. Insertion of the Fe–H bond into the bound olefin would form the iron-alkyl intermediate **4.11**. Upon reductive elimination to form the alkane product, the active catalytic species **4.8** would be regenerated. Formally, the iron complex would undergo oxidative addition from the starting iron(0) to an iron(II) complex, and then after reductive elimination would reform an iron(0) species. However, because the complex contains the redox active bis(imino)pyridine ligand, the iron center remains an iron(II) species, while the ligand gets oxidized and reduced by two electrons.

Another interesting reaction that highlights the redox non-innocent nature of the bis(imino)pyridine ligand is the [2 π +2 π] cycloaddition of α,ω -dienes (Scheme 4.9).²⁶ The Chirik group studied the mechanism by isolating intermediates and characterizing by X-ray crystallography, Mössbauer spectroscopy, and DFT calculations.

Scheme 4.9. Proposed mechanism for the [2 π +2 π] cycloaddition of α,ω -dienes catalyzed by bis(imino)pyridine iron complex **4.11**



They synthesized bis(dinitrogen) iron complex **4.12**, which is analogous to **4.2**, to be sure that dissociation of one of the two imine arms of the ligand could not occur during their mechanistic studies. Similar to **4.2**, complex **4.12** is an intermediate spin ($S = 1$) iron center coupled to a doubly reduced bis(imino)pyridine ligand. Upon addition of a diene (N,N-diallyl-4-methylbenzenesulfonamide) and displacement of the dinitrogen ligands, complex **4.13** was isolated and determined to be a high spin ($S = 3/2$) iron(I) center paired with a singly reduced PDI ligand. Oxidative addition of the diene generated metallacyclopentane **4.14**. Complex **4.14** is best described as an intermediate spin ($S = 3/2$) iron(III) coupled with a singly reduced ligand. Reductive elimination closes the cycle and forms the bicyclic product (3-tosyl-3-azabicyclo[3.2.0]heptane).

The ability for the bis(imino)pyridine framework to serve as a redox non-innocent ligand enables unique catalytic activity that other base-metal catalyst do not demonstrate. It is clear from these studies that the redox activity of the ligand can assist in the stabilization of various oxidation states of iron while also facilitating reactivity that mimics that of noble-metals.

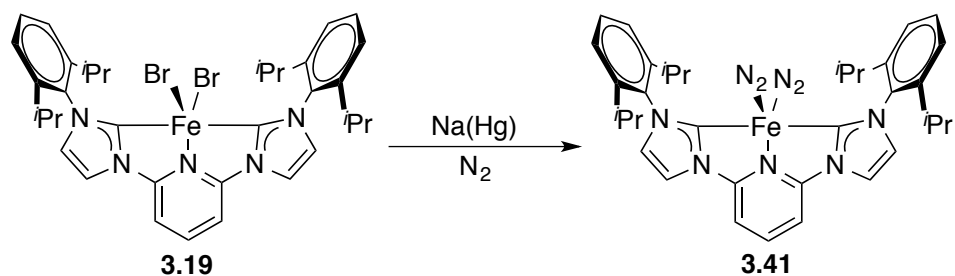
4.1.2 Modifications to the Bis(imino)pyridine Ligand Structure

A significant amount of work has been done to elucidate how the steric and electronic structures of the bis(imino)pyridine framework affect the reactivity of iron complexes bearing the ligand. Much of the focus has been on the steric properties of ligand and its implications on the reactivity of the complexes. For example, reactions such as ethylene polymerization, hydrogenation, hydrosilylation, and hydroboration are extremely sensitive to the steric bulk about the N-aryl portion of the ligand. Common modifications include substitutions at the 2- and 6-positions of the N-aryl groups. Considerably less has been done to probe the electronic contributions and donor effects of the ligand framework. Despite the large number of

perturbations that have been done to the N-aryl groups, these electronic modifications can mostly be attributed to subtle inductive effects.

In contrast, Danopoulos and coworkers synthesized an analogous complex to **4.1a** that replaced the two imine moieties with significantly more σ -donating N-heterocyclic carbenes (**3.19**).²⁷ The authors wondered how the modification of the bis(imino)pyridine framework to a bis(N-heterocyclic carbene)pyridine ligand would affect the reactivity of the complex. In 2005, Danopoulos was able to isolate the corresponding bis(dinitrogen) complex (**3.41**) from addition of sodium mercury amalgam to the parent dibromide **3.19** (Scheme 4.10). As an analogy to the bis(imino)pyridine complexes, Gibson *et al.* tested complex **3.19** for its ability to catalyze the polymerization of ethylene with MAO.²⁸ While titanium, vanadium, and chromium complexes bearing bis(N-heterocyclic carbene)pyridine ligands were active, cobalt and iron complexes demonstrated no production of polyethylene under the conditions studied.

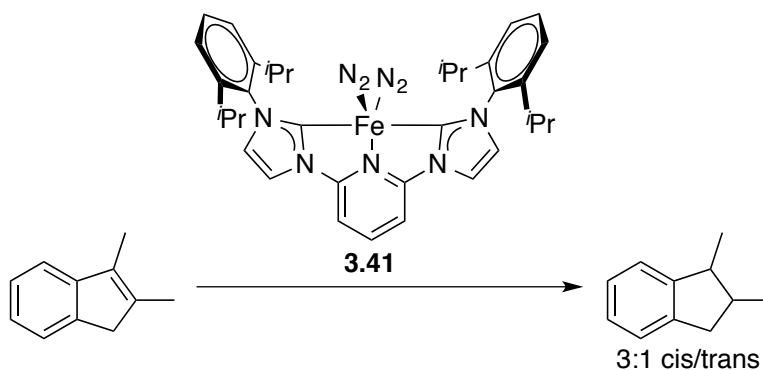
Scheme 4.10. Synthesis of bis(N-heterocyclic carbene)pyridine iron complex 3.41



Additionally, in 2012, Chirik and coworkers explored the use of the bis(dinitrogen) complex **3.41** for the hydrogenation of olefins (See Chapter 3).¹³ The group found that the increased donating ability of the bis(N-heterocyclic carbene)pyridine ligand significantly increased the catalytic activity as compared to the bis(imino)pyridine framework. In fact,

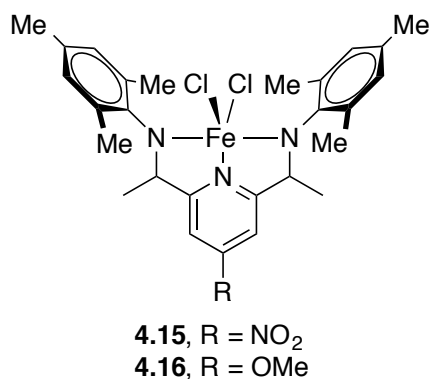
complex **3.41** in the presence of H₂ hydrogenated a tetra-substituted olefin, which is still a remaining challenge for even the most active noble-metal complexes (Scheme 4.11).²⁹

Scheme 4.11. Hydrogenation of a tetra-substituted olefin catalyzed by iron complex 3.41



Furthermore, a few reports have demonstrated modifications to the central pyridine of the ligand framework. In 2010, Mohammadi *et al.* synthesized and studied resonance withdrawing (**4.15**) and donating (**4.16**) groups in the para-position of the pyridine ring (Figure 4.5).³⁰

Figure 4.5. Para-substituted bis(imino)pyridine iron complexes

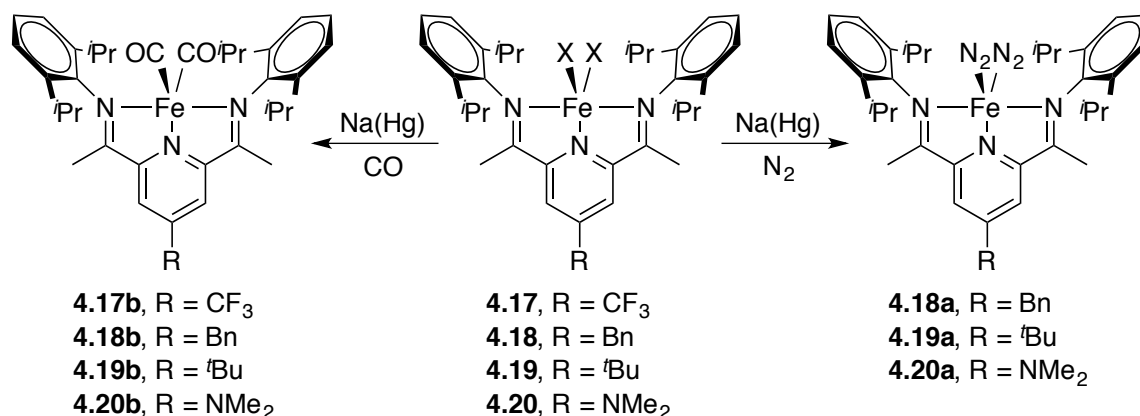


The group tested these complexes for the polymerization of ethylene based on results Brookhart had previously observed.³¹ Brookhart's group noticed that the reaction catalyzed by

various nickel complexes was extremely effected by the electronic properties of the catalyst. In fact, lowering the electron density at the metal center through the addition of electron withdrawing groups produced more active catalysts. This supports the fact that early transition metals have typically demonstrated higher activities than late transition metals. Mohammadi and coworkers demonstrated that complex **4.15** with an electron withdrawing nitro group in the para-position had a higher activity than that of **4.16**. However, even though it was more active, complex **4.15** had lower thermal stability and a shorter lifetime as compared to **4.16**.

In 2012, Chirik *et al.* also reported the synthesis and characterization of a variety of para-substituted bis(imino)pyridine compounds (**4.17-4.20**) (Scheme 4.12).³² Despite not investing any catalytic activities, the group investigated the electronic properties of the complexes by isolating the corresponding bis(dinitrogen) (**4.17a-4.20a**) and dicarbonyl (**4.18b-4.20b**) compounds. (The corresponding bis(dinitrogen) complex from addition of Na(Hg) amalgam of **4.17** was not generated, but instead a mixture of free bis(imino)pyridine ligand and one-electron reduction to an iron–chloride species similar to iron **4.6**.)

Scheme 4.12. Bis(dinitrogen) and dicarbonyl iron complexes bearing a para-substituted PDI ligand (X = Br or Cl)



The group explored the influence of the 4-substitution on the electronic properties by evaluating each using electrochemical, vibrational, and Mössbauer spectroscopy. The introduction of para-substitution does not influence the redox activity of the PDI ligand. The bis(dinitrogen) species are best described as intermediate spin ($S = 1$) iron(II) centers coupled to doubly anionic, triplet bis(imino)pyridine ligands similar to **4.2**. The diamagnetic dicarbonyl species are best considered as a hybrid of iron(0) and iron(II) centers as in **4.7**. However, the remote substituents do have a measurable influence on the electronic properties of the metal. The carbonyl stretching frequencies are sensitive to the identity of the para-substituent, with the most electron poor member of the series, **4.17b** ($R = CF_3$), exhibiting the highest stretching frequencies while the most electron rich member, **4.20b** ($R = NMe_2$), has the lowest values (Table 4.4). There is little difference between the stretching frequencies of the parent compound **4.7** and the alkyl-substituted derivatives **4.18b** ($R = Bn$) and **4.19b** ($R = ^iBu$).

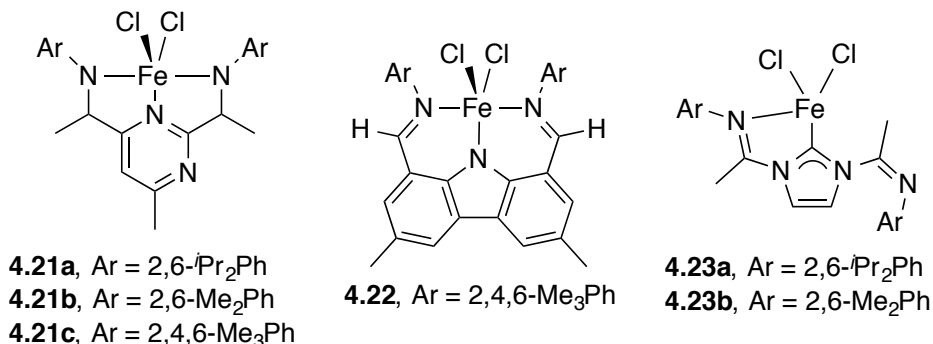
Table 4.4. Carbonyl stretching frequencies of bis(imino)pyridine dicarbonyl complexes

Entry	Complex	$\nu(CO)$ (cm^{-1})
1	4.17b ($R = CF_3$)	1925, 1983
2	4.7	1914, 1974
3	4.18b ($R = Bn$)	1913, 1972
4	4.19b ($R = ^iBu$)	1911, 1971
5	4.20b ($R = NMe_2$)	1906, 1965

In addition to simple substitutions on the pyridine ring, a few reports have replaced the central pyridine with various heterocycles. In 2003, Gibson *et al.* reported the synthesis and characterization of pyrimidine-based complexes (**4.21**) with various N-aryl substituents and a carbazole-based complex (**4.22**) (Figure 4.6).³³ Pyrimidine-based complexes afforded active polymerization catalysts upon activation with MAO, although the activity was substantially

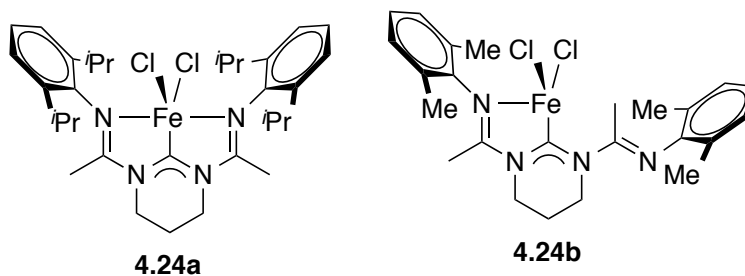
reduced compared to the pyridine analogues. The authors attributed this to the reduced catalytic stability under typical polymerization conditions.

Figure 4.6. Iron complexes bearing ligands with modifications to the central donor of the bis(imino)pyridine ligand



In 2012, Lavoie and Thagfi published the synthesis, characterization, and ethylene polymerization of iron complexes bearing 1,3-bis(imino)-*N*-heterocyclic carbene ligands (**4.23**) (Figure 4.6).³⁴ Although designed as a tri-dentate ligand comparable to the bis(imino)pyridine framework, the ligand coordinated to iron (and cobalt and chromium) in a bi-dentate mode through the carbene carbon and one of the two imine nitrogen atoms. The complexes were tested for the polymerization of ethylene and were completely inactive.

Notably absent from the literature, as of early 2012, was a tri-dentate bis(amidinato)-*N*-heterocyclic carbene analogue to the bis(imino)pyridine ligand. Our laboratory³⁵ and Lavoie³⁶ independently synthesized iron complexes bearing bis(amidinato)-*N*-heterocyclic carbene ligands (Figure 4.7). We hypothesized that having an *N*-heterocyclic carbene as the central donor could have significant impacts on the reactivity of such iron complexes. Placement of a strong *trans*-influencing ligand opposite the reactive coordination sites would effectively weaken the bond between the metal and any bound substrates. Additionally, the increased donating ability of a carbene over a pyridine ligand could better stabilize higher oxidation states of the iron center.

Figure 4.7. Bis(amidinato)-N-heterocyclic carbene iron complexes

We reported tri-dentate chelation by a bis(amidinato)-4,5,6-trihydropyrimid-2-ylidene ligand with 2,6-diisopropylaryl N-substituted groups (**4.24a**). Interestingly, Lavoie reported bi-dentate chelation when the ligand contained a 2,6-dimethylphenyl substituted ligand (**4.24b**). However, Lavoie's group obtained minimal characterization for complex **4.24b**. The group proposed a bi-dentate coordination mode because two stretching frequency bands in the imine region of the IR spectrum were observed with values strongly suggesting coordination of only one amidinato nitrogen atom. Attempts to grow crystals to unambiguously determine the coordination mode of the ligand were not successful.

Our group obtained a crystal structure of **4.24a** supporting a penta-coordinate iron structure. Analysis of the X-ray crystallographic data revealed complex **4.24a** contains one of the shortest iron–NHC bond reported to date, which combined with the short iron–amidine bond lengths leads to a more sterically congested coordination environment relative to that of the analogous bis(imino)pyridine complex **4.1a**. Since this initial discovery, our group has explored the origin of the unique structural and electronic properties of complex **4.24a**. The following sections represent a combination of work done by Hilan Z. Kaplan, Cesar M. Manna, and myself. They are designed to highlight my work, as well as the unique features of iron complexes bearing bis(amidinato)-N-heterocyclic carbene ligands.

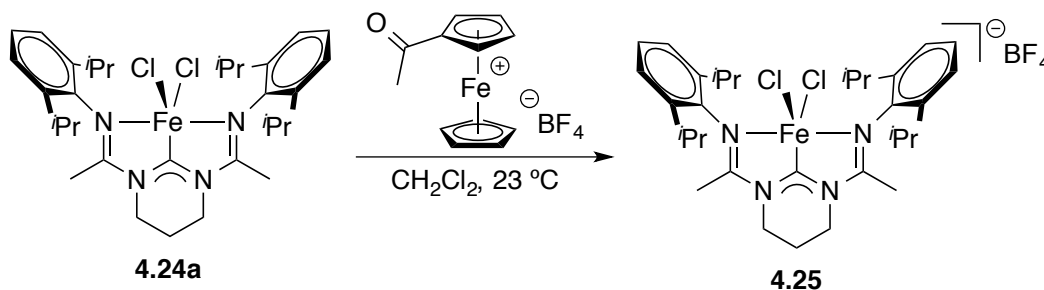
4.2 Synthesis and Characterization of Complexes Bearing Bis(amidinato)-N-heterocyclic Carbene Ligands

4.2.1 Introduction

4.2.1.1 Iron(II) and Iron(III) Complexes

In our 2012 publication, we reported the synthesis and characterization of iron complex **4.24a** bearing a bis(amidinato)-N-heterocyclic carbene.³⁵ A high spin iron(II) configuration was assigned to the complex based on the solution magnetic moment (μ_{eff}), which was measured to be $5.0 \mu_{\text{B}}$ ($X \cdot T = 3.1 \text{ cm}^3 \cdot \text{K/mol}$) in THF and $4.6 \mu_{\text{B}}$ ($X \cdot T = 2.7 \text{ cm}^3 \cdot \text{K/mol}$) in CH_2Cl_2 at $25 \text{ }^\circ\text{C}$ using Evans' method.^{37,38} One electron oxidation of **4.24a** was possible using acetylferrocenium tetrafluoroborate in CH_2Cl_2 to form complex **4.25** (Scheme 4.13). The magnetic moment in THF at $25 \text{ }^\circ\text{C}$ was measured to be $5.0 \mu_{\text{B}}$ ($X \cdot T = 3.1 \text{ cm}^3 \cdot \text{K/mol}$), which is too low for a high spin iron(III) complex and too high for an intermediate spin iron(III) complex.

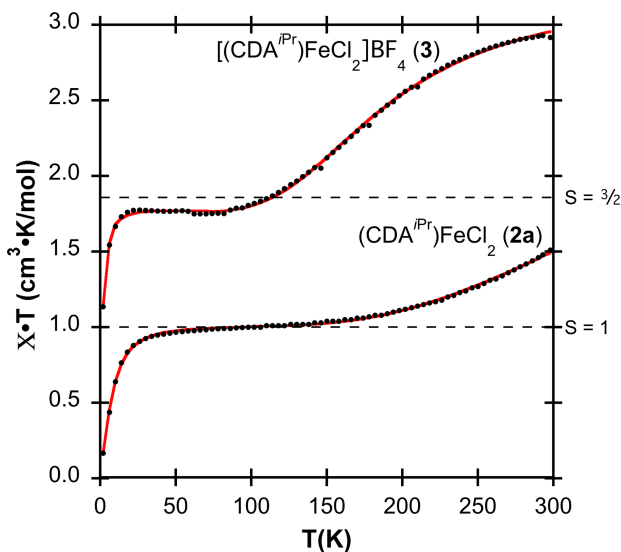
Scheme 4.13. Synthesis of cationic iron(III) complex 4.25



Hilan Z. Kaplan obtained dc-magnetic susceptibility data for polycrystalline samples of **4.24a** and **4.25** from 2 K to 300 K (Figure 4.8). The samples demonstrated complicated magnetic behavior as a function of temperature. At low temperatures, both complexes had low magnetic moments that increased rapidly to a plateau at intermediate temperatures. Upon further heating, the magnetic moment once again underwent a gradual increase until the sample reached the

maximum temperature achievable by the experimental setup. The plateau at $X \cdot T$ for **4.24a** occurred from 30 K to 150 K and at $1.00 \text{ cm}^3 \cdot \text{K/mol}$ is the same as the spin only value expected for an $S = 1$ metal complex. Above 150 K, the increase in magnetic moment suggests a spin state change from an $S = 1$ to an $S = 2$ ground state. The plateau at $X \cdot T$ for **4.25** emerged at 25 K and persisted up to 100 K, and at $1.78 \text{ cm}^3 \cdot \text{K/mol}$ is slightly lower than the value for an $S = 3/2$ spin state ($1.88 \text{ cm}^3 \cdot \text{K/mol}$). The best fit of the high temperature data ($>100 \text{ K}$) suggest a higher spin state characterized by $X \cdot T = 3.31 \text{ cm}^3 \cdot \text{K/mol}$. This value is significantly lower than the spin only value expected for a high spin $S = 5/2$ iron(III) center ($4.39 \text{ cm}^3 \cdot \text{K/mol}$), which we currently cannot definitively explain.

Figure 4.8. Variable temperature solid-state dc-magnetization data for **4.24a** and **4.25** using SQUID. Filled symbols represent experimental data, and solid line represents the simulation, which was obtained from a combination of two models: below 100 K, the data were fit to intermediate spin iron complexes with significant contributions from zero-field splitting (for $S = 1$ in **4.24a**: $g_{iso} = 2.01$, $|D| = 26 \text{ cm}^{-1}$, $|E| = 6 \text{ cm}^{-1}$; for $S = 3/2$ in **4.25**: $g_{iso} = 1.95$, $|D| = 4 \text{ cm}^{-1}$, $|E| = 1 \text{ cm}^{-1}$) and above 100 K, the data was fit using $X = 1[1 + \exp\{(\Delta H/R)(1/T - 1/T_c)\}]$ to calculate the high spin fraction in a spin transition occurring at a spin transition temperature (T_c) according to the Sorai domain model (for **4.24a**: $T_c = 563 \text{ K}$; $\Delta H = 705 \text{ cm}^{-1}$; for **4.25**: $T_c = 199 \text{ K}$; $\Delta H = 502 \text{ cm}^{-1}$).³⁹



To gain further insight, **4.24a** and **4.25** were analyzed by variable temperature zero-field ^{57}Fe Mössbauer spectroscopy by Hilan Z. Kaplan and Matthew J. T. Wilding at Harvard University. At low temperatures, the Mössbauer spectrum features isomer shift and quadrupole splitting values that are inconsistent with a high spin iron(II) species, which one might anticipate in analogy to the related bis(imino)pyridine iron system (**4.1a**). The observed values are more consistent with an intermediate spin ($S = 1$) iron(II) center as suggested by the SQUID measurements. Minimal changes in the Mössbauer spectrum between 100 and 150 K are consistent with either rapid interconversion between $S = 1$ and $S = 2$ spin states or a quantum admixed $S = 1,2$ spin state at elevated temperatures. The Mössbauer spectrum of **4.25** at low temperatures demonstrated isomer shifts that were more consistent with an intermediate spin $S = 3/2$ iron(III) species than a high spin $S = 5/2$ complex. As was the case with **4.24a**, small differences observed upon warming the sample to 298 K can be explained by a statistical distribution of quantum admixed spin states.

As a final experiment directed towards understanding the spin transitions that appear to occur in these complexes, Hilan Z. Kaplan and Bo Li carried out variable temperature X-ray crystallographic experiments.⁴⁰ Consistent with a change in spin state were considerable changes in metal-ligand bond distances in **4.24a** and **4.25** upon increasing the temperature (Table 4.5). For example, the iron-carbene bond length in **4.24a** elongated from the abnormally short 1.812(2) Å to 1.882(3) Å at 100 and 250 K, respectively. Additionally, the average iron-imine bond distances extended from 2.026(4) Å to 2.104(4) Å. These significant increases in bond length on the order of 0.07-0.08 Å are common for complexes of iron that undergo spin transitions.^{41, 42}

To corroborate our experimental results, we carried out unrestricted DFT calculations on both **4.24a** and **4.25**. Intermediate ($S = 1$ and $3/2$) and high spin ($S = 2$ and $5/2$) configurations were calculated to be close in energy (*ca.* 5 kcal/mol) for both **4.24a** and **4.25**, but a low spin state configuration ($S = 1/2$) considered for **4.25** was significantly higher in energy (> 15 kcal/mol).

Comparing calculated and experimental metal–ligand bond lengths supports intermediate spin state assignments for **4.24a** and **4.25** at low temperatures (<100 K). At elevated temperatures (>100 K), the experimental bond lengths move towards what is calculated for a high spin state structure (Table 4.5). Also consistent with this assignment were the Mössbauer parameters, which were calculated to be close to the experimental values observed at low temperature for the intermediate spin state electronic configuration.

Table 4.5. Selected bond lengths (Å) and Mössbauer parameters ($^{mm}/s$) for **4.24a and **4.25****

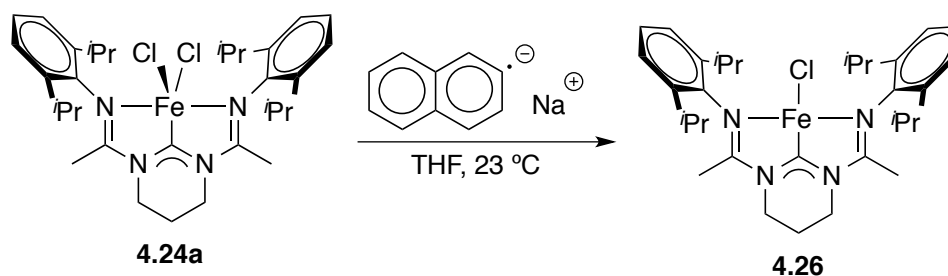
	4.24a				4.25			
	Exp.		Calc.		Exp.		Calc.	
	100 K	250 K	S = 1	S = 2	80 K	298 K	S = $^3/2$	S = $^5/2$
Fe–carbene	1.812(2)	1.882(3)	1.823	2.024	1.908(2)	2.033(2)	1.904	2.105
Fe–imine	2.026(4)	2.104(4)	2.071	2.284	2.031(9)	2.142(12)	2.1202	2.262
δ	0.31	0.40	0.42	0.70	0.18	0.21	0.32	0.33
$ \Delta E_Q $	2.14	1.93	2.17	1.43	2.21	1.58	2.78	1.67

Based on our magnetic, spectroscopic, crystallographic, and computational investigations, we hypothesized that the electronic features of the complexes were due to the excellent σ -donating capabilities of the CDA ligands. Instead of featuring a high spin configuration common in the bis(imino)pyridine iron(II) complex **4.1a**, the CDA ligand encourages the formation of an intermediate spin state configuration at low temperatures and a spin equilibrium complex at elevated temperatures. We reasoned that these capabilities could be beneficial for stabilizing high oxidation state iron complexes, so future reactivity is geared toward investigating these complexes for their ability to support high oxidation state iron intermediates during the catalytic aziridination of olefins (See 4.3.1)

4.2.2 Synthesis and Electronic Structure of a Formally Iron(I)-CDA Complex

Hilan Z. Kaplan carried out the one-electron reduction of **4.24a** using sodium naphthalide in THF to form iron mono-chloride **4.26** (Scheme 4.14). The structure of the complex was then characterized by X-ray diffraction as well as Mössbauer spectroscopy and DFT calculations.

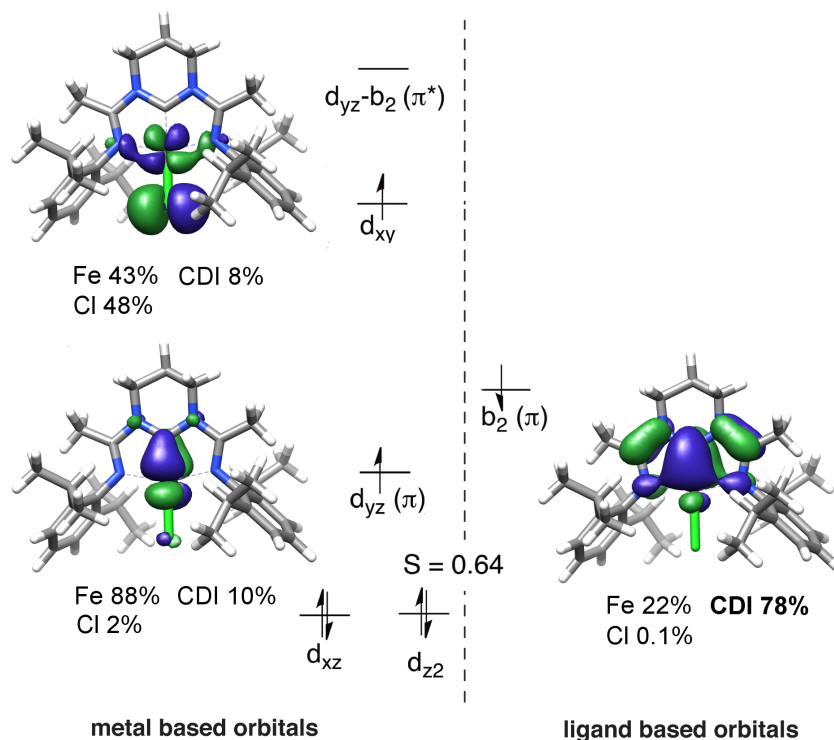
Scheme 4.14. Synthesis of iron mono-chloride complex 4.26



To gain insight on the electronic structure of **4.26**, Hilan Z. Kaplan and Matthew J. T. Wilding at Harvard University obtained a zero-field ^{57}Fe Mössbauer spectrum. Although the spectrum features three unique doublets, suggesting that three distinct iron centers were present in the sample, the major component is consistent with a low spin iron(I) or intermediate spin iron(II) configuration instead of high spin iron(I).^{43,44} Crystals suitable for X-ray crystallography were obtained for **4.26**. The most striking feature of the structure is the iron–carbene bond, which at 1.791(3) Å, is the shortest of all the previously synthesized iron–CDA complexes. Additionally, the distance between the carbon of the NHC and the nitrogen atom in the ring lengthens slightly while bonds between the nitrogens on the NHC ring and the imine carbons shorten. On one hand, the observed changes to the ligand may be an indication of increased backdonation from the metal into the ligand π^* -antibonding orbitals, but on the other hand, they are on par with changes observed in the reduction of bis(imino)pyridine compound **4.1a**.^{9, 23, 24}

We carried out unrestricted DFT calculations on **4.26** adopting the broken symmetry (BS) approach used by Wieghardt, Chirik, and coworkers for calculations of bis(imino)pyridine complexes to calculate the most likely electronic configuration of **4.26**.^{45,46} Low spin ($S = 1/2$) and high spin ($S = 3/2$) configurations were considered for **4.26**. When calculations were carried out with a closed shell ligand configuration normal convergence was not observed. Instead, the calculations spontaneously converged to broken symmetry solutions where one electron resides on the ligand. Although the calculations predict that the high spin configuration is slightly lower in energy than the intermediate spin (*ca.* 5 kcal/mol), the calculated and experimental metal–ligand bond lengths agree better for the intermediate spin situation. The BS solution was evident from population of a molecular orbital containing a small amount of special overlap ($S = 0.64$), which is illustrated in the qualitative molecular orbital diagram for **4.26** in Figure 4.9.

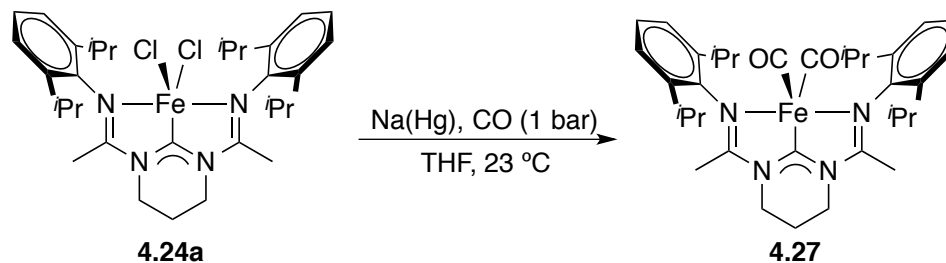
Figure 4.9. Qualitative molecular orbital diagram of 4.26 obtained from the BS(2,1) solution of an unrestricted DFT calculation. Illustrated are the molecular orbitals that are involved in the anti-ferromagnetic coupling as well as the SOMO.



One orbital contains significant electron density on the metal d_{yz} orbital, while the other contains significant electron density on a ligand-centered orbital corresponding to the b_2 irreducible representation in the C_{2v} point group. Population of the ligand orbital with this symmetry would lead to the short metal–carbene bond distances and the deviations from normal ligand bond distances observed in the complex. This description is consistent with the bis(amidinato)-N-heterocyclic carbene acting as a redox non-innocent ligand where the unpaired electron on the ligand participates in an antiferromagnetic interaction with the iron(II) metal center. This interaction is reminiscent of bonding in the bis(imino)pyridine iron mono-chloride complex **4.6** (Figure 4.3), except that in **4.26** the metal orbital is the π -symmetric d_{yz} orbital rather than the σ -symmetric d_{z^2} orbital for the bis(imino)pyridine complex. The b_2 orbital on the CDA ligand is suited for a π -backdonation interaction from the metal d_{yz} orbital, contributing to the shortening of the metal–NHC carbon bond.

Hilan Z. Kaplan also investigated the two-electron reduction of **4.24a** using Na(Hg) amalgam under an atmosphere of CO to form iron dicarbonyl **4.27** (Scheme 4.15). The structure of the complex was characterized by X-ray diffraction, Mössbauer spectroscopy and DFT calculations.

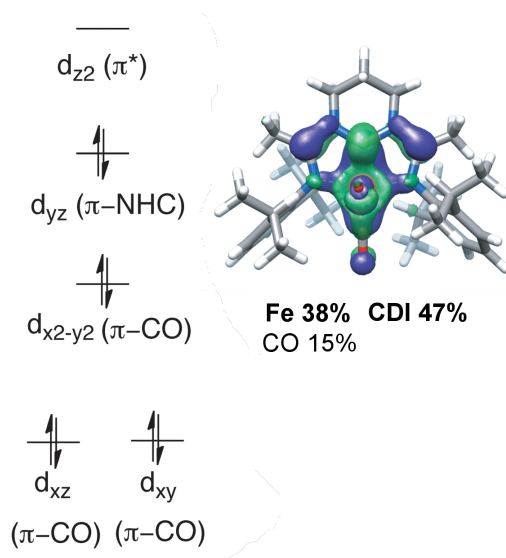
Scheme 4.15. Synthesis of iron dicarbonyl complex 4.27



To gain insight on the electronic structure of **4.27**, Hilan Z. Kaplan and Matthew T. J. Wilding at Harvard University obtained zero-field ^{57}Fe Mössbauer spectrum was obtained at 90 K. The spectrum features isomer shift and quadrupole splitting value that are significantly lower than typical iron dichloride complexes and are consistent with the strongly π -acidic nature of the carbonyl ligands. Interestingly, Mössbauer fitting parameters are almost identical with the analogous bis(imino)pyridine iron dicarbonyl complex **4.7**⁴⁷ and correspond well to a low spin iron(0) oxidation state. This closed shell character agrees well with the diamagnetic nature of the compound observed by ^1H NMR spectroscopy. We carried out unrestricted DFT calculations on **4.27** (B3LYP/def2-TZVP(f) on iron and the primary coordination sphere; B3LYP/def2-SV(P) for all others). Low spin ($S = 1$) and high spin ($S = 2$) configurations were considered for **4.27**. The bond metrics predicted for the low spin ($S = 1$) electronic configuration are in agreement with the experimental data. These results suggest that the best descriptor for the electronic state of the complex is a low spin iron(0).

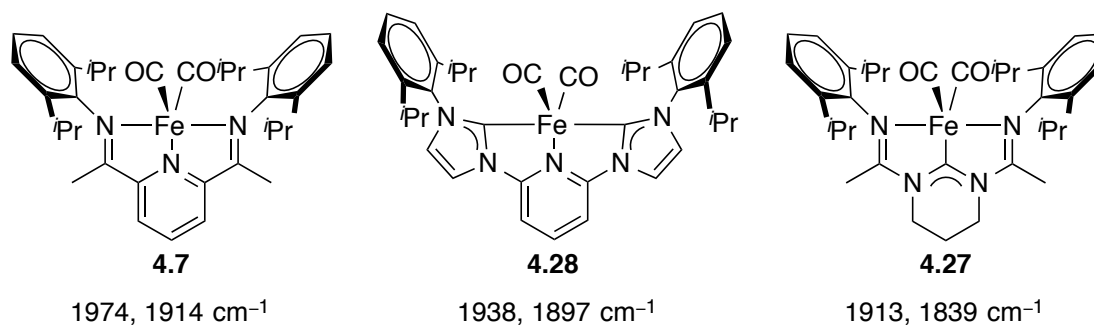
The DFT calculations best described the electronic state as a low spin iron(0), however, the ligand bond distances suggest some contribution from an electronic structure with a reduced ligand. For the bis(imino)pyridine iron dicarbonyl complex **4.7**, Chirik *et al.* proposed a hybrid of iron(0) and iron(II) centers (Figure 4.4). This conclusion was based on the DFT computed HOMO of the compound, which is 68% bis(imino)pyridine in character with a large contribution from the iron center with no spectroscopic evidence for the mixing of low-lying higher-spin excited states. The molecular orbital diagram in Figure 4.10 illustrates the π -bonding in complex **4.27**, which is manifested in the HOMO of the complex. Significant contributions from the metal d_{yz} orbital (38%) and the b_2 orbital of the NHC ligand (47%) demonstrate a high degree of covalency in this interaction.

Figure 4.10. Qualitative molecular orbital diagram of 4.27 obtained from an unrestricted DFT calculation



To assess the impact of NHC donating abilities versus ligand framework, the IR stretching frequencies of the carbonyl ligands were compared for the bis(amidinato)-N-heterocyclic carbene, bis(imino)pyridine, and bis(N-heterocyclic carbene)pyridine complexes (Figure 4.11). Complex **4.27** contains a more electron rich metal center compared to the corresponding bis(imino)pyridine dicarbonyl complex **4.7** as evidenced by the significantly lower IR stretching frequency observed for **4.27** ($\nu = 1913$ and 1839 cm^{-1}).

Figure 4.11. IR stretching frequencies of iron dicarbonyl complexes

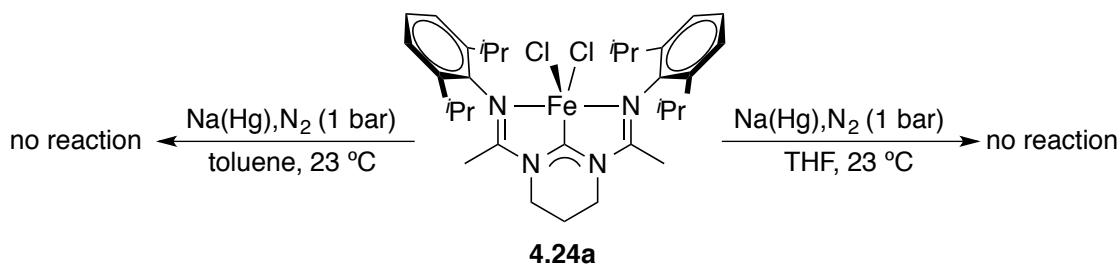


The iron center is also more electron-rich compared to the bis(N-heterocyclic carbene) dicarbonyl compound **4.28** reported by Danopoulos and coworkers ($\nu = 1938$ and 1897 cm^{-1}).⁴⁸ Clearly it is not only the donating ability of the NHC, but also its location as the central donor in the pincer ligand or the saturated nature of the NHC that provides these unique features.

4.2.3 Synthesis of a Bis(dinitrogen) Formally Iron(0)-CDA Complex

Analogous to the work Chirik and coworkers reported in 2004, we attempted the synthesis of a bis(dinitrogen)-bis(amidinato)-N-heterocyclic carbene complex.⁹ Following the procedure Chirik's group developed for the preparation of bis(dinitrogen) complex **4.2**, iron dichloride complex **4.24a** was treated with excess sodium mercury amalgam in toluene under an atmosphere of nitrogen (Scheme 4.16). However, in contrast the bis(imino)pyridine complex, there was no reaction with the CDA. This difference in reactivity is most likely due to the poor solubility of **4.24a** in toluene. Therefore, sodium mercury amalgam was added to complex **4.24a** in THF under an atmosphere of nitrogen and unfortunately no reaction occurred.

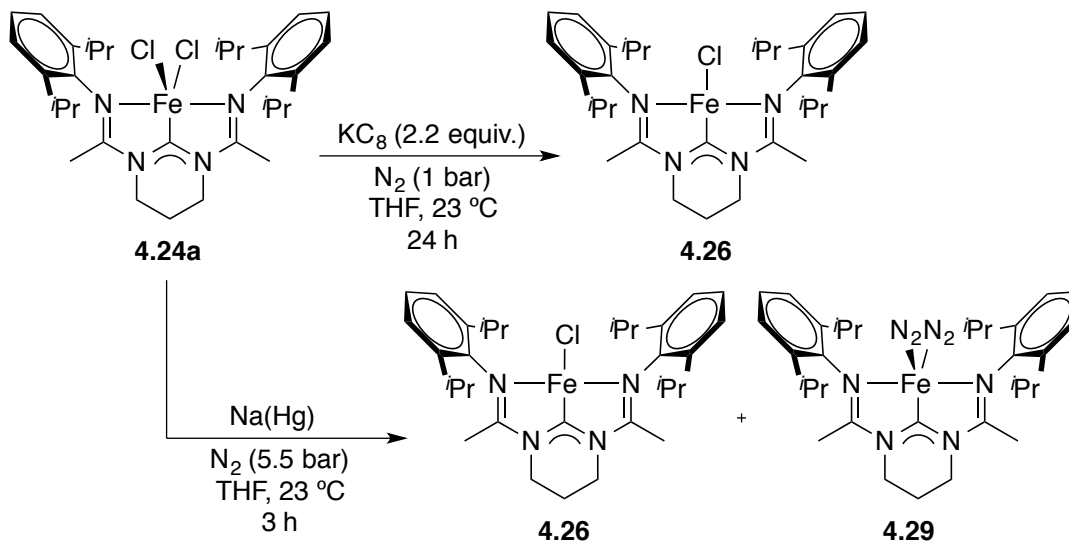
Scheme 4.16. Treatment of iron complex 4.24a with sodium mercury amalgam under an atmosphere of nitrogen



Next, we explored the use of potassium graphite, a commonly used reductant for first row transition metal complexes. Treatment of iron complex **4.24a** with potassium graphite under an atmosphere of nitrogen in THF generated the singly reduced iron mono-chloride compound **4.26**

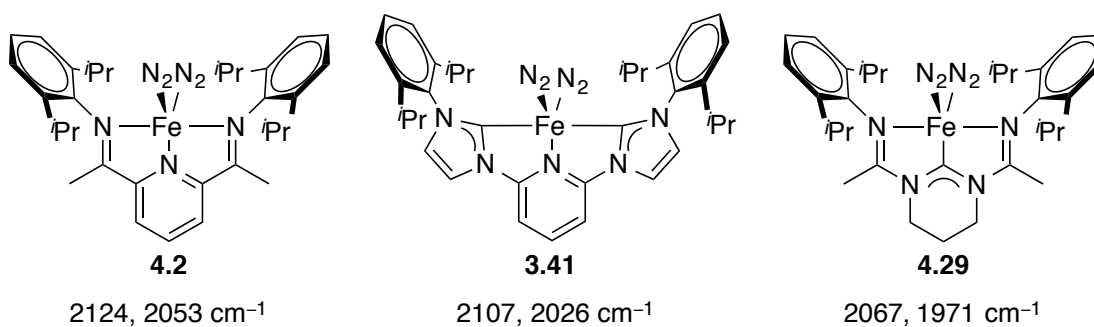
in low yield (Scheme 4.17). Under higher pressures of nitrogen and sodium mercury amalgam, Hilan Z. Kaplan isolated a mixture of the singly reduced compound **4.26** and the bis(dinitrogen)-bis(amidinato)-N-heterocyclic carbene complex (**4.29**).

Scheme 4.17. Reduction of iron dichloride complex 4.24a



The IR spectrum of the mixture of **4.26** and **4.29** contained two very strong and distinct stretches at 2067 and 1071 cm^{-1} , which is characteristic of symmetric and asymmetric stretches from metal-bound dinitrogen molecules (Figure 4.12).

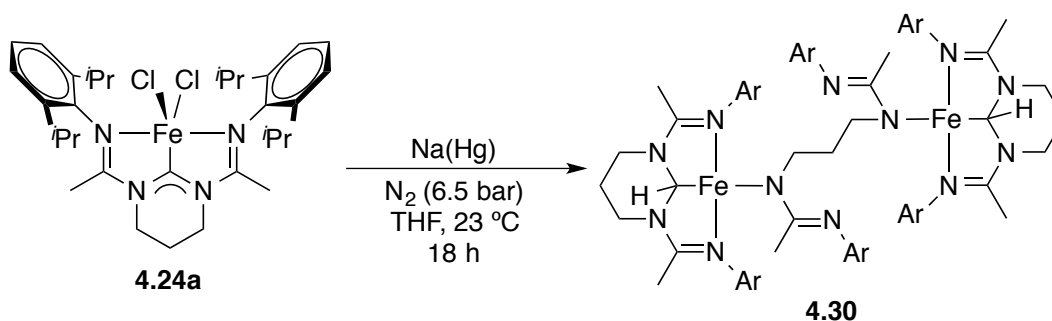
Figure 4.12. IR stretching frequencies of iron bis(dinitrogen) complexes



Similar to the iron dicarbonyl complexes, we can compare the bis(dinitrogen) complexes for the bis(amidinato)-N-heterocyclic carbene, bis(imino)pyridine, and bis(N-heterocyclic carbene)pyridine complexes. Once again, the complex that contains the CDA ligand (**4.29**) contains a more electron rich metal center compared to the corresponding bis(imino)pyridine and bis(N-heterocyclic carbene)pyridine containing complexes (**4.2** and **3.44**, respectively).

Assuming the presence of **4.26** was the result of an incomplete reaction, the same transformation was attempted with an increase in pressure and reaction time (6.5 bar and 18 hours). Unfortunately, instead of **4.29**, Hilan Z. Kaplan isolated the bridged dimer **4.30** identified it by X-ray crystallography (Scheme 4.18). Interestingly, the dimer is bridged by a ligand that has lost the carbene-carbon of the NHC, which is perhaps a result of hydrolysis by water. Additionally, a new C–H bond was formed between a hydrogen atom and the carbene carbon of the CDA ligand. The bond metrics support this change as the carbene carbon now adopts a tetrahedral geometry.

Scheme 4.18. Reduction of 4.24a with Na(Hg) at 6.5 bar N₂ for 18 hours



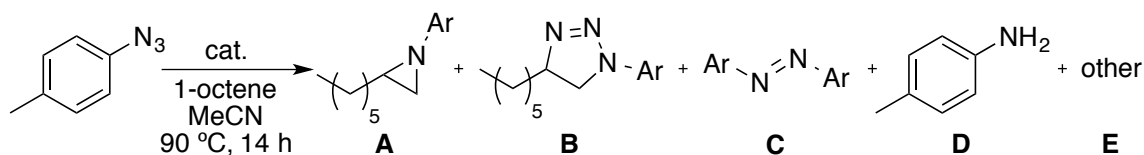
4.3 Catalytic and Stoichiometric Reactivity of Complexes Bearing Bis(amidinato)-N-heterocyclic Carbene Ligands

Based on our magnetic, spectroscopic, crystallographic, and computational investigations, we hypothesized that the electronic features of CDA complexes were due to the excellent σ -donating capabilities of the bis(amidinato)-N-heterocyclic carbene ligand. We reasoned that these capabilities could be beneficial for a variety of chemical transformation so we undertook investigations into the reactivity of these complexes with azides, hydrides, alkyl reagents, and ethylene.

4.3.1 Aziridination and Azide Homo-coupling

Based on our characterization studies of iron(II) **4.24a** and iron(II) **4.25** complex bearing CDA ligands, the formation of intermediate spin state configurations at low temperatures and spin equilibrium complexes at elevated temperatures was hypothesized. We reasoned that these capabilities could be beneficial for stabilizing high oxidation state iron complexes, so we undertook an investigation into the reactivity of iron bis(amidinato)-N-heterocyclic carbene **4.24a** with aryl azides in the presence of 1-octene (Table 4.6).

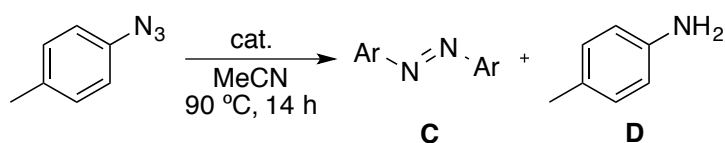
Table 4.6. Aziridination of 1-octene with *p*-tolylazide



Entry	Cat.	Conv. (%)	A	B	C	D	E
1	N/A	44	23	13	0	0	8
2	4.24a	80	25	27	6	20	3
3	4.1a	78	18	31	3	14	12
4	FeCl ₂	79	26	28	2	11	11

Unfortunately, reactions catalyzed by **4.24a** at 50 °C demonstrated no conversion of either starting material. At higher temperatures, the conversion of *p*-tolylazide was 80% and aziridines was observed. However, the quantity of aziridine produced was not significantly above the background reaction that occurs without an iron catalyst (entries 1 and 2). Additionally, bis(imino)pyridine complex **4.1a** and FeCl₂ showed similar results under these conditions. A by-product in reactions using **4.24a** at 90 °C was the homo-dimerization of *p*-tolylazide to form 1,2-di-*p*-tolylidiazene (**C**), which did not occur in the absence of the iron catalyst (Table 4.7, entry 1). Since the catalytic homo-coupling of azides to give diazenes often proceeds through high oxidation state iron–imido intermediates, we speculated that the formation of a diazene product was an indicator that such an intermediate was forming.

Table 4.7. Catalytic homo-coupling of *p*-tolylazide



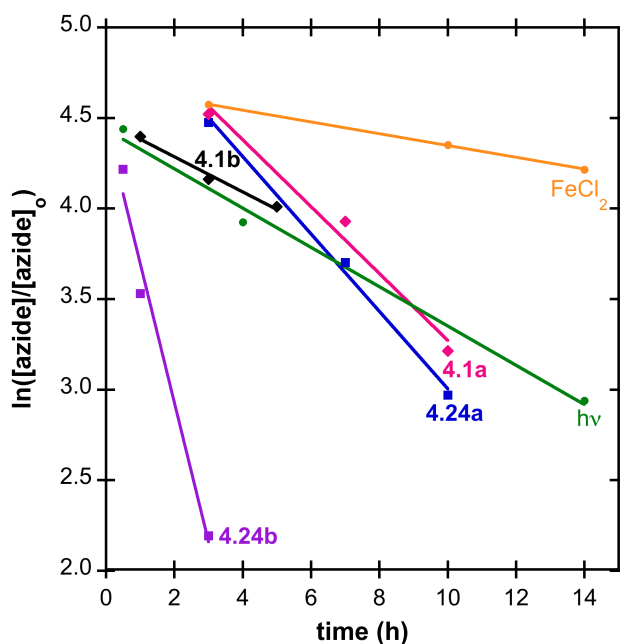
Entry	Cat.	Conv. (%)	C:D	k_{obs} ($\times 10^{-5} \text{ s}^{-1}$)
1	N/A	0	N/A	N/A
2	FeCl ₂	32	1:2	0.903
3	4.1a	78	3:1	5.13
4	4.24a	86	4:1	5.94
5	4.1b	91	6:1	2.69
6	4.24b	91	10:1	21.4

In order to rule out ligand dissociation, a comparison of aryl azide homo-coupling was made using iron-CDA complex **4.24a**, iron-PDI complex **4.1a**, and FeCl₂. After 14 hours, FeCl₂, **4.1a**, and **4.24a** demonstrated significantly different reactivity resulting in 32%, 78%, and 86% conversion of *p*-tolylazide, respectively. Whereas reactions with FeCl₂ (entry 2) produced only 11% diazene and 21% *p*-toluidine (1:2 selectivity), reactions catalyzed by **4.1a** (entry 3) gave

58% diazene and 20% *p*-toluidine (3:1 selectivity) and reactions catalyzed by **4.24a** (entry 4) gave 68% yield of the diazene with *p*-toluidine (18%) as the only by-product (4:1 selectivity).

Envisioning a mechanism where a metal–nitrene interacts with an equivalent of azide to liberate the diazene product, we surmised that a decrease in steric bulk around the iron center would lead to a more efficient reaction. Consistent with this hypothesis were reactions carried out with the less sterically encumbered bis(imino)pyridine complex **4.1b** and bis(amidinato)-N-heterocyclic carbene complex **4.24b** (entries 5 and 6), which both proceed with 91% conversion and greater formation of the diazene product (6:1 and 10:1 selectivity). Kinetic measurements revealed that the rate of azide conversion for **4.24b** was nearly five times faster than both **4.1b** and **4.24a**, and over an order of magnitude faster than FeCl₂ (Table 4.6, Figure 4.13).

Figure 4.13. Reaction rates for diazene homo-coupling (catalyst: orange circle = FeCl₂, blue squares = 4.24a, pink diamonds = 4.1a, purple squares = 4.24b, black diamonds = 4.1b, green circles = hv)



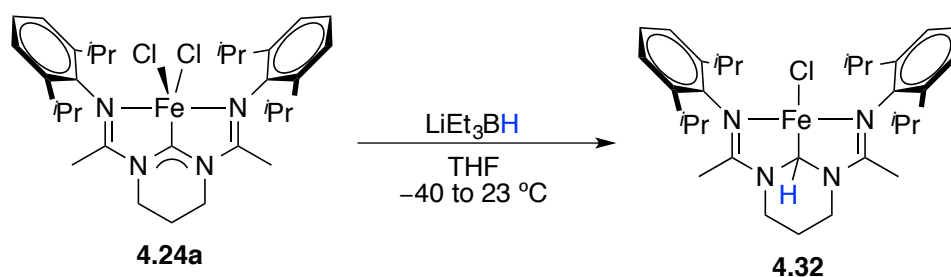
4.3.2 Redox and Chemical Non-Innocence of CDA Ligands

The data obtained from the synthesis and characterization of iron-CDA complexes prompted us to investigate the ability for the CDA ligand to be redox or chemically non-innocent. We've already demonstrated the redox non-innocence of bis(amidinato)-N-heterocyclic carbene mono-chloride complex **4.27**, but understanding the full reactivity profile of CDA containing iron complexes would allow us to design future catalytic reactions. The generation of ligand radicals can lead to interesting ligand-centered reactivity, especially in the field of organometallic chemistry, where redox non-innocent ligands offer ample opportunities for new and fast transformations (See Chapter 3). On one hand, redox non-innocent spectator ligands can be used as electron reservoirs to facilitate two-electron reactivity for transition metals that have a tendency to react via one-electron pathways (such as cheap, first-row transition metals). On the other hand, redox non-innocent ligands can also be used to generate reactive ligand radicals to impose controlled ligand-centered radical-type reactivity in catalysis.

4.3.2.1 Reactivity with Super Hydride

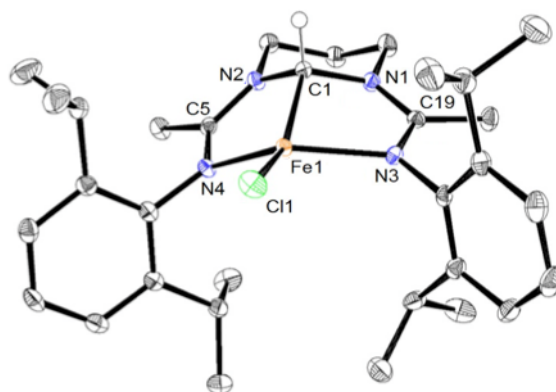
Hilan Z. Kaplan treated iron dichloride complex **4.24a** with one equivalent of Super Hydride (LiEt_3BH) and isolated iron complex **4.32** (Scheme 4.20). Interestingly, the solid-state structure of **4.32** clearly revealed that a new C–H bond was formed between the hydride and the carbene carbon of the CDA ligand, effectively transforming the carbene to an alkyl group.

Scheme 4.20. Addition of Super Hydride to iron dichloride complex 4.24a



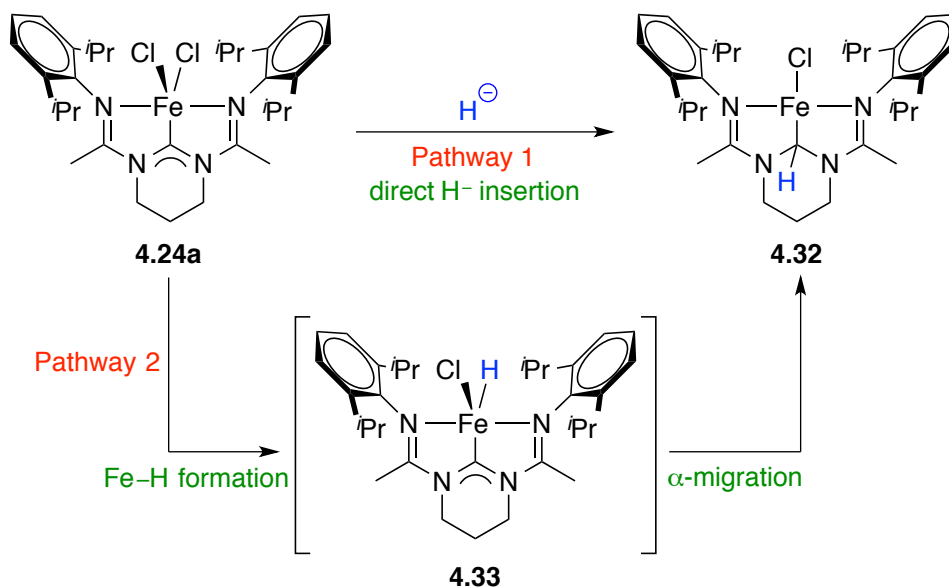
The X-ray crystal structure and bond metrics of **4.32** supported this assignment (Figure 4.14). The carbene carbon used to be planar with the nitrogens in the NHC ring, but now the carbene carbon adopts a tetrahedral geometry. These changes in structure are evident by the $\text{N}(1)\text{--C}(1)\text{--N}(2)$ angle of $109.0(1)^\circ$. Additionally, the bond distances between the nitrogens in the NHC ring and the carbene carbon lengthen, which is evidence of the double bond character in the carbene structure being reduced to single bond character.

Figure 4.14. Crystal structure of **4.32** recorded at 100 K at the 50% probability level. Hydrogen atoms (except the relevant $\text{C}(1)\text{--H}$) and solvent molecules were omitted for clarity.



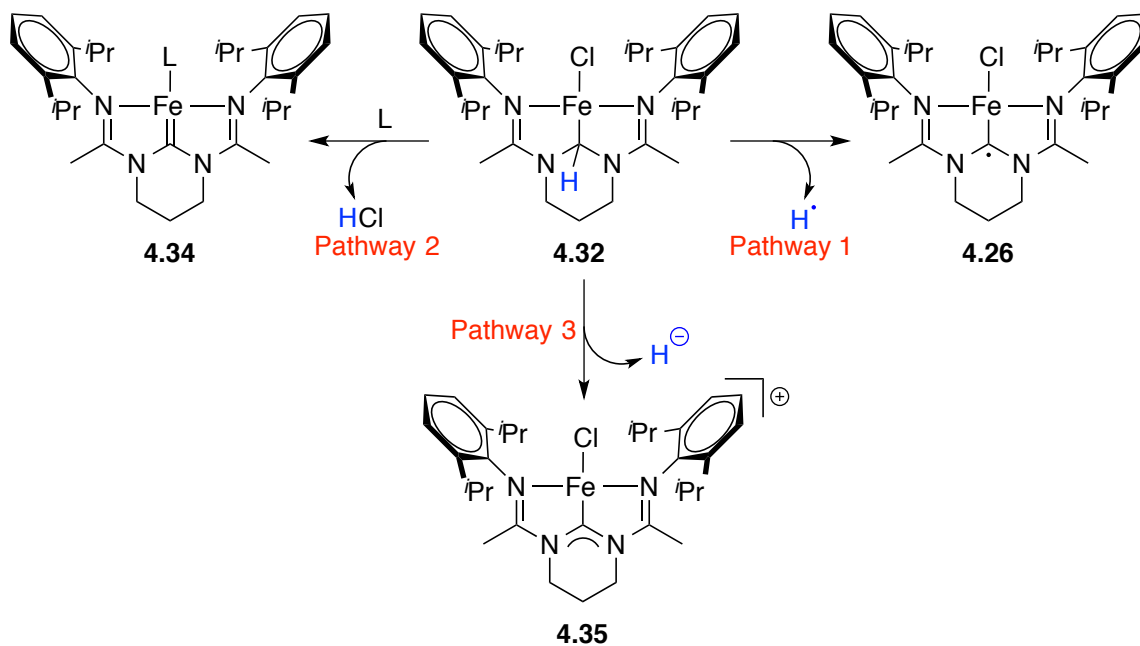
The mechanism for the formation of **4.32** is interesting as there are two plausible pathways for the reaction to occur (Scheme 4.21). In pathway 1, a hydride could be directly delivered from LiEt_3BH to the electrophilic carbene carbon to form **4.32**. In pathway 2, a hydride could be added to the iron center to form iron–hydride intermediate **4.33**, followed by α -migration of the hydride to the carbene carbon. Although an α -migration such as this is not common for NHCs, it is routine for metal bound olefins (as in hydrogenation), carbonyl ligands and Fischer-type carbenes.

Scheme 4.21. Possible pathways for the formation of iron complex 4.32



The formation of complex 4.32 led us to wonder what the nature of the newly formed C–H bond is (Scheme 4.22).

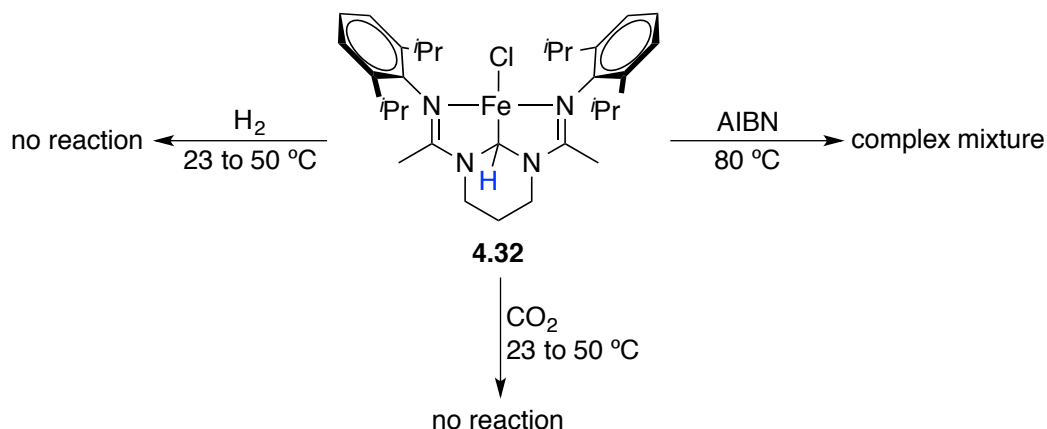
Scheme 4.22. Possible reactivity of the C–H bond in complex 4.32



It is possible to envision the C–H bond behaving in at three ways: (1) an H[•] donor to generate the intermediate spin mono-chloride iron(II) complex **4.26**,⁴⁹ (2) a proton source to form a Schrock-type carbene complex **4.34**,⁵⁰ or (3) a hydride to formally oxidize the complex to species **4.35**.⁵¹ None of these pathways are novel for transition metal complexes, but are not typical for Arduengo-type N-heterocyclic carbenes.

To investigate the nature of this bond, we explored the reactivity of **4.32** with several compounds that could accept a hydrogen atom, a proton, or a hydride (Scheme 4.23). Treatment of complex **4.32** with azobisisobutyronitrile (AIBN), a commonly used radical initiator, led to a complex mixture of various iron containing products. Addition of CO₂ or H₂ yielded no reaction.

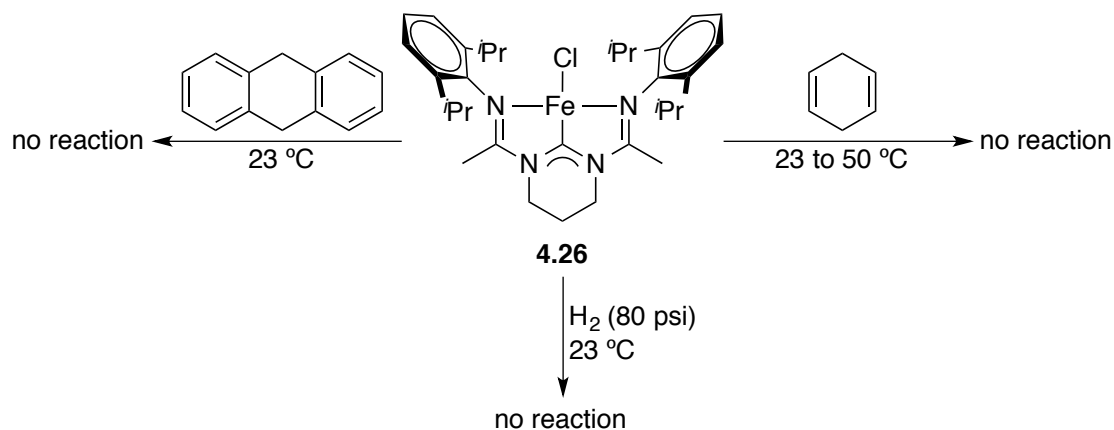
Scheme 4.23. Reactivity of iron complex 4.32



We also explored the reactivity of the intermediate spin mono-chloride iron(II) complex **4.26** because if pathway 1 was proceeding, then maybe this process is reversible. Therefore, we treated complex **4.26** with several compounds that could donate a hydrogen atom, a proton, or a hydride (Scheme 4.24). Addition of cyclohexadi-1,4-ene or 9,10-dihydroanthracene, commonly used hydrogen atom donors, or H₂ showed no conversion of the starting complex **4.26**. Unfortunately, complexes **4.26** and **4.32** are both extremely sensitive and rapidly decompose in

the presence of trace amounts of water or other impurities, which has hindered the progress of these investigations.

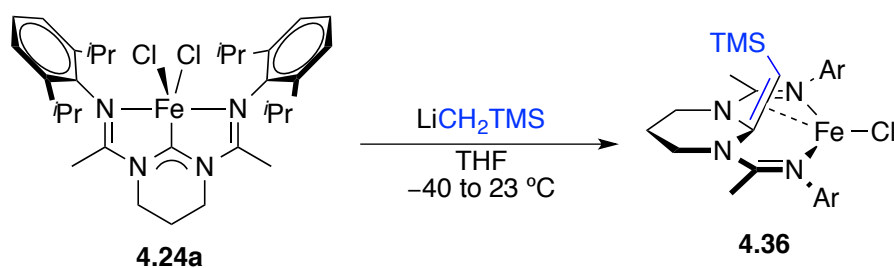
Scheme 4.24. Reactivity of iron complex 4.26



4.3.2.2 Reactivity with an Alkyl Lithium Reagent

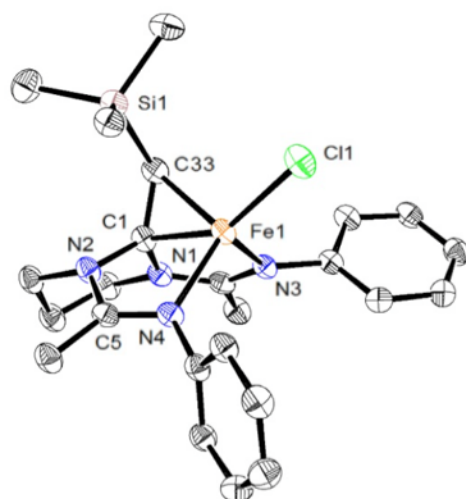
Hilan Z. Kaplan treated iron dichloride complex **4.24a** with one equivalent of LiCH_2TMS resulted in the formation of a new iron complex (**4.36**) (Scheme 4.25). Interestingly, the solid-state structure of **4.36** clearly revealed that the nucleophile (LiCH_2TMS) formed a new bond with the carbene ligand rather than the iron center. Additionally, the high resolution mass spectroscopy of complex **4.36** agreed with this assignment.

Scheme 4.25. Addition of LiCH_2TMS to iron dichloride complex 4.24a



The X-ray crystal structure and bond metrics of **4.36** supported this structural assignment (Figure 4.15). Analysis of the bond lengths from the crystal structure suggests that a β -hydride elimination occurred in addition to the newly formed C–C bond with the carbene carbon. Both C(1) of the heterocycles and C(33) of the added alkyl group form bonds with the iron center. Additionally, the C(1)–C(33) bond length is 1.408(4) Å, which is too short to be a single bond. Further evidence for the C(1)–C(33) bond having double bond character is the hybridization of C(33), which is much closer to sp^2 than sp^3 .

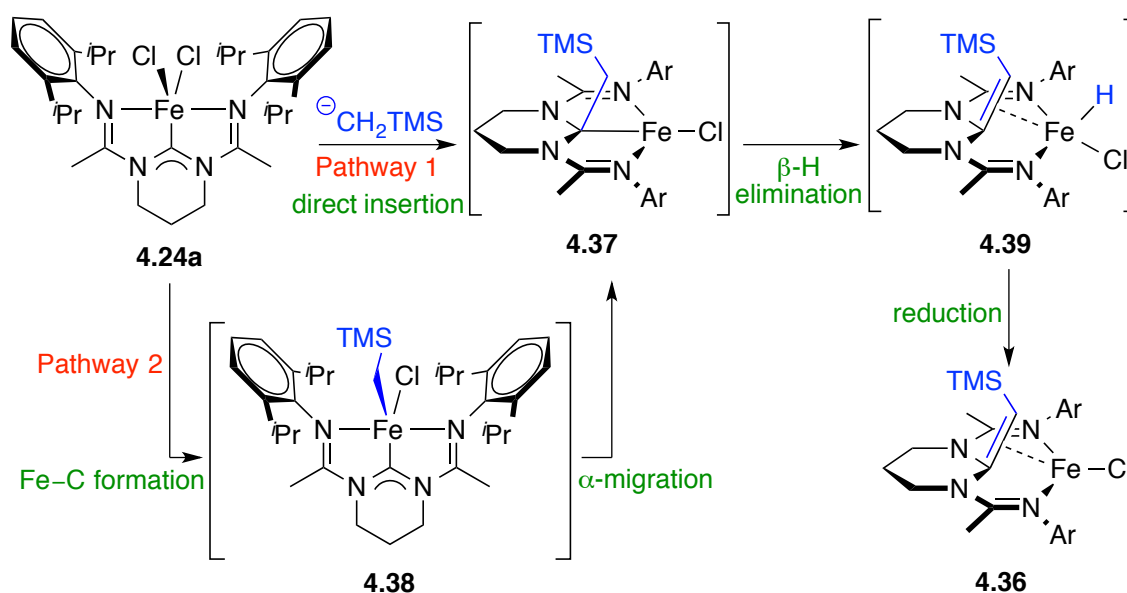
Figure 4.15. Crystal structure of **4.36** recorded at 100 K at the 50% probability level. Hydrogen atoms, isopropyl groups, and solvent molecules were omitted for clarity.



Similar to iron complex **4.32**, the mechanism for the formation of **4.36** is interesting as there are two pathways for the reaction to occur (Scheme 4.26). In pathway 1, the alkyl group could be directly delivered from LiCH_2TMS to the electrophilic carbene carbon to form **4.37**. In pathway 2, the alkyl group could be added to the iron center to form iron–alkyl intermediate **4.38**, followed by α -migration of the alkyl group to the carbene carbon. Intermediate **4.37** could then undergo β -hydride elimination to form iron complex **4.29**, which upon reduction would generate

complex **4.36**. Although the presence of a metal–hydride has been observed via IR of the crude reaction mixture ($\nu = 1953 \text{ cm}^{-1}$), X-ray crystallography is not able to resolve iron–hydrogen bonds. Unfortunately, the isolated yields of **4.36** are low (around 30%), and the complex is extremely sensitive and rapidly decomposes in the presence of trace amounts of water or other impurities.

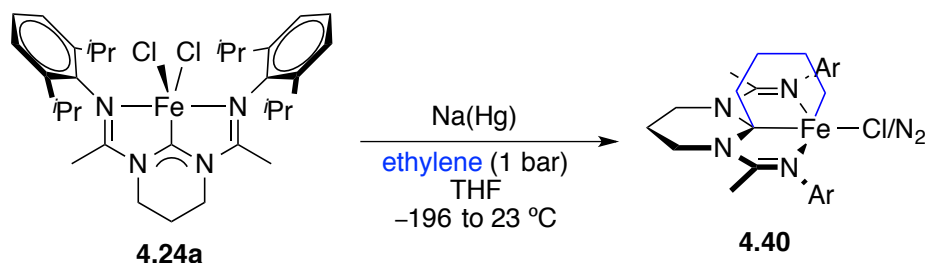
Scheme 4.26. Possible pathways for the formation of iron complex 4.36



4.3.2.3 Reactivity with Ethylene

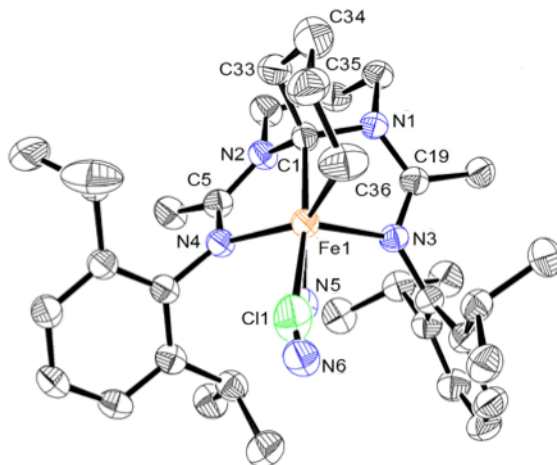
Treatment of iron dichloride complex **4.24a** with excess sodium mercury amalgam under an atmosphere of ethylene resulted in the formation of a new iron complex (**4.40**) (Scheme 4.27). Interestingly, the solid-state structure of **4.40** clearly revealed that two equivalents of the nucleophile (ethylene) formed a new bond with the carbene ligand and the iron center.

Scheme 4.27. Addition of Na(Hg) to iron dichloride complex 4.24a under an atmosphere of ethylene



The X-ray crystal structure and bond metrics of **4.40** supported this structural assignment (Figure 4.16). Analysis of the bond lengths from the crystal structure suggests that the complex contains a bridged six-membered ring across the iron–carbene bond.

Figure 4.16. Crystal structure of 4.40 recorded at 100 K at the 50% probability level. Hydrogen atoms and solvent molecules were omitted for clarity.



The unique reactivity of **4.24a** toward ethylene is reflected by the bond metrics of **4.40**. A new C–C bond was formed between the carbene carbon and a carbon in ethylene, effectively transforming it from a carbene to an alkyl. The Fe(1)–C(1) bond distance elongates from the short 1.812(2) Å to 2.000(2) Å, a value consistent with iron–alkyl bonds (Table 4.9).⁵² As expected,

the N(2)–C(1) bond lengthens significantly as the double bond character in the carbene is reduced to single bonds, elongating from 1.360(3) Å to 1.470(3) Å. Additionally, all of the C–C bond distances in the six-membered bridged ring have significant single bond character.

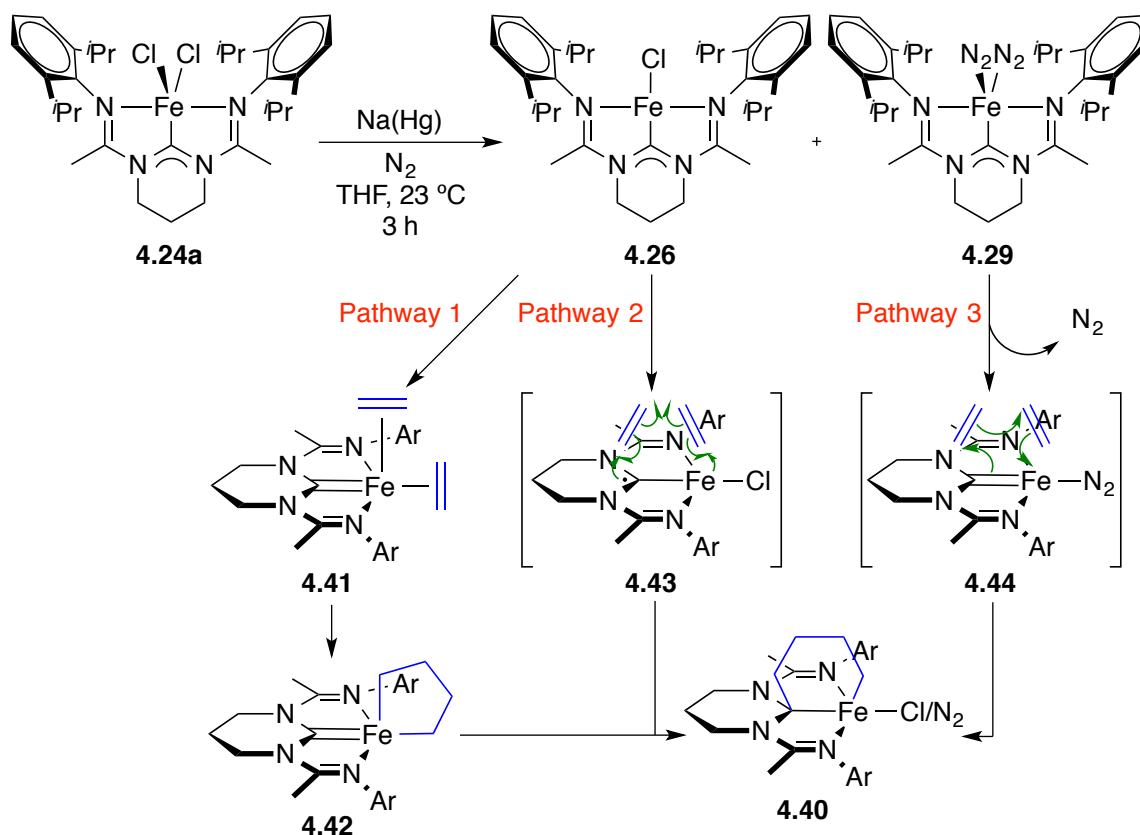
Table 4.9. Selected experimental bond lengths (Å) for 4.40

	Length
Fe(1)–C(1)	2.000(2)
Fe(1)–N(4)	2.116(2)
Fe(1)–C(36)	2.063(3)
N(4)–C(5)	1.307(3)
N(2)–C(1)	1.470(3)
C(1)–C(33)	1.530(4)
C(33)–C(34)	1.500(4)
C(34)–C(35)	1.488(5)
C(35)–C(36)	1.505(4)

Similar to iron complexes **4.32** and **4.36**, the mechanism for the formation of **4.40** is interesting as there is more than one possible pathway for the reaction to occur (Scheme 4.28). According to our previous results, addition of sodium mercury amalgam under nitrogen atmosphere (in a glove box) should convert **4.24a** to a mixture of the corresponding iron monochloride complex **4.26** and bis(dinitrogen) complex **4.29**. In pathway 1, loss of chloride or nitrogen ligands with association of two molecules of ethylene would generate complex **4.41**. Oxidative coupling of the ethylene molecules would generate metallacyclopentane species **4.42**, which could undergo α -migration to form the six-membered ring structure **4.40**. In pathway 2, the redox activity of the bis(amidinato)-N-heterocyclic carbene could facilitate one-electron cycloaddition to generate the six-membered ring structure **4.40**. In pathway 3, loss of one equivalent of dinitrogen could open up the coordination sphere so that a two-electron cycloaddition could occur, utilizing the π -bonding character of the iron–carbene bond. Additionally, binding of the ethylene molecules could occur to generate **4.41** prior to

cycloaddition, as is common in olefin hydrogenation catalyzed by bis(imino)pyridine iron complexes (Scheme 4.8).

Scheme 4.28. Possible pathways for the formation of iron complex 4.40



Although the complex was isolated and crystallized, **4.40** is extremely sensitive and rapidly decomposes in the presence of trace amounts of water or other impurities. In fact, to date the complex has only successfully been synthesized a total of four times by Hilan Z. Kaplan and myself. Attempts to alter the reaction conditions (i.e., time, temperature, solvent, reductant, glassware, stir bars), demonstrated no change to the outcome, which unfortunately precluded further investigations into complex **4.40** and its future stoichiometric or catalytic reactivity.

4.4 Conclusions

While N-heterocyclic carbenes have become ubiquitous in transition metal catalysis, the electronic consequences of their binding to first row transition metals, especially to iron, remains underexplored. Considering the renewed interest in base metals for chemical catalysis and the usefulness of N-heterocyclic carbene ligands have demonstrated for organocatalysis, the investigations we've presented have provided significant insight into the electronic consequences that may result by ligating NHCs to iron. We've synthesized iron complexes supported by CDA ligands in multiple oxidation states and through a combination of magnetic, spectroscopic, crystallographic, and computational methods, we have been able to characterize the bonding in most of these complexes.

A characteristic feature in the bonding of iron–CDA complexes is a π -interaction between a metal-based orbital and a ligand-centered orbital with large contributions from the empty p-orbital of the NHC carbon. In the dicarbonyl complex **4.27**, this interaction is manifested as a π -backbond, which highlights the π -accepting capabilities of CDA ligands. Increasing the oxidation state of the complex by a single electron changes the π -interaction such that complex it is best described as an antiferromagnetic interaction between the metal and the ligand. Although this kind of interaction has been observed for complexes of bis(imino)pyridine ligands, this is the first isolated example demonstrating this behavior for an Arduengo-type N-heterocyclic carbene. Further increasing the oxidation state by one-electron leads to complex **4.24a**, which increases the covalency in the iron–carbene bond to the point that it has significant π -character. This increased metal–ligand orbital overlap may contribute to the spin equilibrium situation (or quantum admixed spin states) in **4.24a**. One more increase in oxidation state results in a complex (**4.25**) that exhibits a similar spin equilibrium situation (or quantum admixed spin states), but has significantly less one-electron interactions.

The bonding in CDA iron complexes is particularly interesting when compared to the analogous bis(imino)pyridine or bis(N-heterocyclic carbene)pyridine complexes of iron. We believe that the unique features exhibited in CDA complexes are caused by the extended π -framework of the CDA ligand coupled with the electronegativity of the iron center leading to excellent orbital overlap and energy matching. We also demonstrated these distinctive characteristics through a variety of catalytic and stoichiometric transformations. As compared to bis(imino)pyridine iron complexes, the better σ -donating capabilities of the NHC ligand dramatically changed the reactivity for the polymerization of (*rac*)-lactide and the homo-coupling of *p*-tolylazide. Additionally, stoichiometric reactions with Super hydride, an alkyl lithium reagent, and with ethylene resulted in unusual reactivity at the carbene carbon rather than the metal center as commonly observed for metal–NHC complexes. These types of reactivity open up the door to a number of processes that evoke redox and chemically non-innocent ligands.

Future efforts in the group will be directed toward discovering new reactions by applying iron–CDA complexes as catalysts for a variety of reactions involving multiple oxidation states of iron. Although the low oxidation state complexes are extremely sensitive to trace amounts of water or other impurities, we have started to investigate the use of more soluble complexes so solvents like pentane and toluene (that are typically easier to dry) can be used. Preliminary results suggest these complexes are active for the hydrogenation of primary and secondary olefins. Additionally, bis(amidinato)-N-heterocyclic complexes of cobalt could be prepared and investigated as a comparison to the iron complexes we've previously synthesized.

4.5 Experimental

4.5.1 General Considerations

Unless otherwise stated, all reactions were carried out in oven-dried glassware in a nitrogen atmosphere glove box or using standard Schlenk line techniques.⁵³ Solvents were used after passage through a solvent purification system similar to the one reported by Grubbs⁵⁴ under a blanket of argon. Particularly air-sensitive manipulations were performed using solvent that was then degassed by briefly exposing the solvent to vacuum. Unless otherwise stated, all work-up and purification procedures were carried out with reagent grade solvents (purchased from Fisher Scientific, Inc.) in air. Organic reagents were purchased from Sigma-Aldrich, TCI America, or Fisher Scientific. Benzene-*d*₆ and dichloromethane-*d*₂ were purchased from Cambridge Isotope Laboratories and were vacuum distilled from Na/benzophenone and CaH₂, respectively. Compounds (2,6-diacetylpyridinebis(2,6-diisopropylanil)iron dichloride (**4.1a**),⁴ (2,6-diacetylpyridinebis(2,6-dimethylanil)iron dichloride (**4.1b**),⁴ and N,N-1,3-bis[1-(2,6-diisopropylphenylimino)ethyl]4,5,6-trihydropyrimid-2-ylidene iron dichloride (**4.24a**)³⁵ were prepared according to the known literature procedures.

¹H NMR spectra were recorded on a Varian VNMRS (500 MHz) or INOVA (500 MHz) spectrometer. For diamagnetic compounds, NMR spectra are reported as follows: chemical shift, multiplicity (s = singlet, d = doublet, t = triplet, pent = pentet, hept = heptet, m = multiplet), coupling constants (Hz), and integration. For paramagnetic compounds, NMR spectra are reported as follows: chemical shift (peak width at half height). Infrared spectra for air and water sensitive compounds were recorded in a glove bag filled with nitrogen or argon and were recorded on a Bruker Alpha-p spectrometer. Magnetic moments were determined by Evans' method according to the procedure published by Gibson and coworkers.⁵⁵ High-resolution mass spectra were obtained at the Boston College Mass Spectrometry Facility using ESI+ or MALDI ionization mode.

Variable temperature (2–300 K) magnetization data were recorded in a 1 T magnetic field on a MPMS-XL Quantum Design SQUID magnetometer. Values for magnetic susceptibility were corrected for the underlying diamagnetic increment by using tabulated Pascal constants. The magnetic data at low temperature (<100 K) were fit using Eckhard Bill's julX program to obtain zero-field splitting parameters.⁵⁶ At temperatures >100 K, the data was modeled using Sorai's⁵⁷ model as described in the text.

⁵⁷Fe Mössbauer spectra were measured on liquid nitrogen cooled samples at zero magnetic field with a constant acceleration spectrometer (SEE Co., Edina, MN). Solid or crystalline samples were prepared as Paratone-N mulls in a glove box and frozen in liquid nitrogen prior to handling in air. Isomer shifts are quoted relative to Fe foil at room temperature. Data was processed, simulated, and analyzed using a package written by E.R.K. for IGOR Pro 6 (Wavemetrics, Lake Oswego, OR).

Selected single crystals suitable for X-ray crystallographic analysis were used for structural determination. The X-ray intensity data were measured at 100(2) K (Oxford Cryostream 700) on a Bruker Kappa APEX Duo diffractometer system equipped with a sealed Mo-target X-ray tube ($\lambda = 0.71073 \text{ \AA}$) and a high brightness I μ S copper source ($\lambda = 1.54178 \text{ \AA}$). The crystals were mounted on a goniometer head with paratone oil. The detector was placed at a distance of 5.000 cm from the crystal. For each experiment, data collection strategy was determined by APEX software package and all frames were collected with a scan width of 0.5° in ω and ϕ with an exposure time of 10 or 20 s/frame.

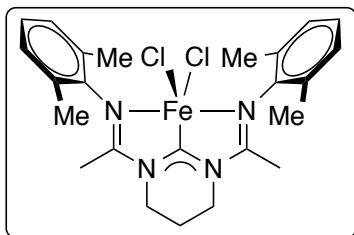
The frames were integrated with the Bruker SAINT Software package using a narrow-frame integration algorithm to a maximum 2θ angle of 56.54° (0.75 \AA resolution) for Mo data and 136.50° (0.83 \AA resolution) for Cu data. The final cell constants are based upon the refinement of the XYZ-centroids of several thousand reflections above $20 \sigma(I)$. Analysis of the data showed negligible decay during data collection. Data were corrected for absorption effects using the

empirical method (SADABS). The structures were solved and refined by full-matrix least squares procedures on $|F^2|$ using the Bruker SHELXTL (version 6.12) software package. All hydrogen atoms were included in idealized positions for structure factor calculations except those forming hydrogen bonds or on a chiral center. Anisotropic displacement parameters were assigned to all non-hydrogen atoms, except those disordered.

All DFT calculations were carried out in an analogous fashion described by Wieghardt, Chirik, and coworkers for the related bis(imino)pyridine complexes⁵⁸ using the ORCA open access software package.⁵⁹ Spin unrestricted Kohn-Shalm geometry optimizations were carried out starting from coordinates obtained from the crystal structures of compounds #. Calculations were carried out using the B3LYP functional. The triple-d quality basis sets def2-TZVP developed by Ahlrichs^{60,61} with one set of polarization functions were used on the metal, on the nitrogen atoms, and on all atoms attached to the metal. For all remaining carbon and hydrogen atoms, a double- ξ quality def2-SV(P) basis set also developed by Ahlrichs⁶⁰ was used that also included a polarizing set of d-functions on the carbon atoms. Appropriate auxiliary basis sets were chosen to match the orbital basis sets.⁶²⁻⁶⁴ The RIJCOSX⁶⁵⁻⁶⁷ approximation was used to accelerate the calculations. We have adopted the broken-symmetry (BS) approach by Ginsberg⁶⁸ and Noodleman⁶⁹ where BS(m,n)⁷⁰ denotes m (n) electrons that are spin up (spin down) at the two interacting fragments. Molecular orbital pictures and spin density plots were generated using Chimera.⁷¹ Nonrelativistic single-point calculations were carried out on the optimized geometry to predict Mössbauer isomer shifts (δ) and quadropole splittings ($|\Delta E_Q|$). The ORCA “CoreProp” basis set CP(PPP) was used for iron.⁷² This basis set is based on the TurboMole DZ basis set developed by Ahlrichs and coworkers and obtained from the basis set library under <ftp://chemi.uni-karlsruhe.de/pub/basen>. The Ahlrichs (2d2fg,3p2df) polarization functions used were obtained from the TurboMole basis set library under <ftp://chemie.uni-karlsruhe.de/pub/basen>. All other basis sets were the same as those used in the geometry optimization calculations.

4.5.2 Experimental Procedures

N,N-1,3-bis[1-(2,6-dimethylphenylimino)ethyl]4,5,6-trihydropyrimid-2-ylidene iron



dichloride (4.24b). (Performed by Aristidis Vasilopoulos.) In

an inert atmosphere glove box, anhydrous iron(II) chloride (133 mg, 1.05 mmol, 1.05 equiv.) was suspended in THF (15 mL)

and cooled to $-40\text{ }^{\circ}\text{C}$. To the cold suspension was then added

drop wise to a precooled ($-40\text{ }^{\circ}\text{C}$) solution of sodium bis(trimethylsilyl)amide (195 mg, 1.05

mmol, 1.05 equiv.) in THF (10 mL) and the mixture was held at $-40\text{ }^{\circ}\text{C}$ and agitated occasionally

for twelve hours. The mixture was then warmed to $23\text{ }^{\circ}\text{C}$ for twenty minutes, during which time

most of the remaining solid dissolved. The orange/brown solution was re-cooled to $-40\text{ }^{\circ}\text{C}$,

filtered through Celite, and added to a precooled ($-40\text{ }^{\circ}\text{C}$) suspension of 1,3-bis[1-(2,6-

dimethylphenylimino)ethyl]-4,5,6-trihydropyrimidinium chloride (414 mg, 1.00 mmol, 1.00

equiv.) in THF (10 mL). The suspension was allowed to gradually warm to $23\text{ }^{\circ}\text{C}$, during which

time it turned bright pink in color. The reaction mixture was allowed to stir at $23\text{ }^{\circ}\text{C}$ for twenty-

four hours and was then concentrated *in vacuo*. The crude solid was dissolved in CH_2Cl_2 , filtered

through Celite, and was washed with THF. The crude residue was recrystallized from a mixture

of CH_2Cl_2 and pentane at $-40\text{ }^{\circ}\text{C}$ to deliver the title compound **4.24b** as a bright pink red solid

(331 mg, 66%). ^1H NMR (CD_2Cl_2 , 500 MHz) δ 22.82 (262.7 Hz), 18.93 (225.9 Hz), 10.51 (319.4

Hz), 7.02 (94.3 Hz), 6.86 (73.3 Hz), 6.65 (40.2 Hz), 6.58 (60.3 Hz), 4.13 (78.1 Hz), 3.80 (214.5

Hz), 2.03 (65.7 Hz), 1.66 (112.4 Hz), 1.28 (50.0 Hz), 0.99 (130.1 Hz), 0.87 (42.9 Hz), 0.45 (427.2

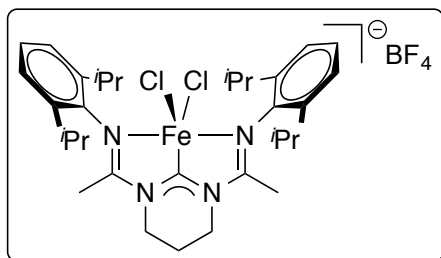
Hz), 0.39 (162.2 Hz), -13.16 (240.3 Hz), -31.05 (526.2 Hz), -39.52 (462.1 Hz). Spectroscopic

data were in agreement with the reported literature values.³⁶ IR (neat): 1631, 1590, 1473, 1377,

1291, 1203, 1092, 1060, 1033, 1010, 817, 768 cm^{-1} . HRMS (ESI+) for $\text{C}_{24}\text{H}_{30}\text{ClFeN}_4$ $[\text{M}]^+$:

Calcd. 465.15084, Found 465.15202.

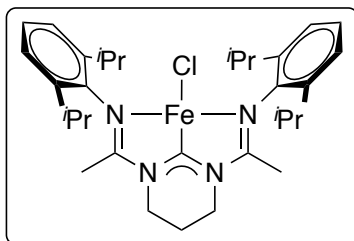
{N,N-1,3-bis[1-(2,6-diisopropylphenylimino)ethyl]4,5,6-trihydropyrimid-2-



ylidene}iron dichloride tetrafluoroborate (4.25).

(Performed by Hilan Z. Kaplan.) In an inert atmosphere glove box, **2a** (50.0 mg, 0.0815 mmol, 1.00 equiv.) was suspended in CH₂Cl₂ (2.0 mL) and a solution of acetylferrocenium tetrafluoroborate (25.7 mg, 0.0815 mmol, 1.00 equiv.) in CH₂Cl₂ (2.0 mL) was added drop wise. Immediately upon addition, the reaction mixture changed from dark blue to a deep red. The solution was allowed to stir for 15 minutes at 25 °C and was concentrated *in vacuo*. The crude solid was washed with pentane (5 x 10 mL) and was again dried *in vacuo*. The crude residue was recrystallized from 2:3:2 Et₂O/CH₂Cl₂/THF v/v at -40 °C to deliver the title compound **4.25** as dark red crystals suitable for X-ray crystallography (41.9 mg, 73%). ¹H NMR (CD₂Cl₂, 500 MHz) δ 77.58 (745.4 Hz), 60.25 (768.5 Hz), 39.06 (269.0 Hz), 7.52 (2853.2 Hz), 5.70 (358.3 Hz), 3.72 (95.9 Hz), 3.41 (11.7 Hz), 1.83 (13.9 Hz), 1.26 (14.8 Hz), 1.13 (9.4 Hz), 0.86 (14.5 Hz), -34.50 (216.3 Hz). IR (neat): 1627, 1517, 1264, 1204, 1043, 1026, 1008, 816, 803 cm⁻¹. μ_{eff} = 5.0 μ_B at 25 °C (Evans' method). HRMS (MALDI) for C₃₂H₄₆Cl₂FeN₄ [M]⁺: Calcd. 612.2449, Found 612.2450.

{N,N-1,3-bis[1-(2,6-diisopropylphenylimino)ethyl]4,5,6-trihydropyrimid-2-

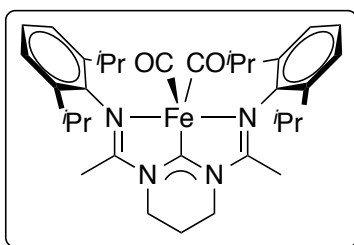


ylidene}iron chloride (4.26).

In an inert atmosphere glove box, a solution of sodium naphthalide in THF was prepared by stirring naphthalene (68.9 mg, 0.538 mol, 1.10 equiv.) and freshly cut sodium metal (22.5 mg, 0.978 mmol, 2.00 equiv.) in THF (16.2 mL) for 12 hours. The dark green solution was then cooled to -40 °C, filtered, and added to a precooled (-40 °C) suspension of **4.24a** (300 mg, 0.489 mmol, 1.00 equiv.) in THF (34.4 mL). The reaction was allowed to warm to 23 °C and was stirred for 24 hours. The reaction

mixture was then filtered through Celite, and concentrated *in vacuo*. The crude red solid was washed with pentane (3 x 20 mL) and Et₂O (15 mL), and dried *in vacuo* to deliver the title compound **4.26** as a reddish brown solid (181 mg, 64%). Crystals suitable for X-ray crystallography were grown from a toluene solution layered with hexanes at 23 °C. ¹H NMR: Decomposition before obtaining spectrum. IR (neat): 1526, 1424, 1407, 1322, 795, 768 cm⁻¹ (under N₂). HRMS (MALDI) for C₃₂H₄₆Cl₁FeN₄ [M]⁺: Calcd. 577.2760, Found 577.2783.

{N,N-1,3-bis[1-(2,6-diisopropylphenylimino)ethyl]4,5,6-trihydropyrimid-2-



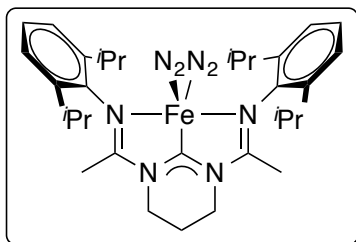
ylidene}iron dicarbonyl (4.27**).** (Performed by Hilan Z.

Kaplan.) In an inert atmosphere glove box, mercury (5.20 g, 26.2 mmol, 115 equiv.) was weighed into a 50 mL round bottom flask. THF (12.2 mL) was added followed by freshly cut sodium

metal (26.2 mg, 1.14 mmol, 5.00 equiv.). The biphasic mixture immediately turned grey and cloudy and was allowed to stir for 1 hour at 23 °C. A solution of **4.24a** (140 mg, 0.228 mmol, 1.00 equiv.) in THF (10.6 mL) was then added via pipette. The flask was sealed with a 180° joint and removed from the glove box. The reaction mixture was free-pump-thawed, backfilled with 1 atmosphere of carbon monoxide gas, and allowed to warm to 23 °C. After 5 minutes at 23 °C, the mixture turned a deep green, and after 10 minutes, the color changed to a yellow/brown. The reaction was allowed to stir for a total of 2 hours at 23 °C, after which it was thoroughly degassed, and taken back into the glove box. The crude reaction was filtered through Celite, and concentrated *in vacuo* to afford a dark yellow solid. Recrystallization from THF layered with pentane (~1:4 THF:pentane v/v) at -40 °C delivered the title compound **4.27** as bright orange crystals (67.3 mg, 49%). Crystals suitable for X-ray crystallography were grown from a vapor diffusion of pentane into a saturated benzene solution at 23 °C. ¹H NMR (C₆D₆, 500 MHz) δ 7.15-7.12 (m, 6H), 3.25 (hept, *J* = 6.8 Hz, 4H), 2.99 (t, *J* = 5.6 Hz, 4H), 1.59 (s, 6H), 1.55 (d, *J* = 6.6

Hz, 12H), 1.40 (pent, $J = 5.6$ Hz, 2H), 1.11 (d, $J = 7.1$ Hz, 12H); ^{13}C NMR: Decomposition before obtaining spectrum. IR (neat): 1913, 1839, 1522, 1425, 768, 625, 593 cm^{-1} (under N_2). HRMS (MALDI) for $\text{C}_{32}\text{H}_{46}\text{FeN}_4\text{O}_2$ $[\text{M}]^+$: Calcd. 598.2970, Found 298.2972.

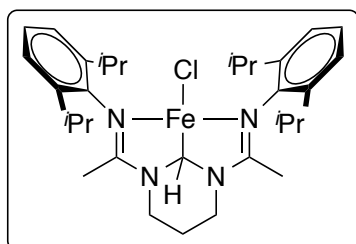
{N,N-1,3-bis[1-(2,6-diisopropylphenylimino)ethyl]4,5,6-trihydropyrimid-2-



ylidene}iron bis(dinitrogen) (4.29) (as a mixture with 4.26).

(Performed by Hilan Z. Kaplan.) In an inert atmosphere glove box, mercury (1.13 g, 5.62 mmol, 115 equiv.) was weighed into a Fisher-Porter tube. THF (3.2 mL) was added followed by freshly cut sodium metal (5.6 mg, 0.25 mmol, 5.0 equiv.). The biphasic mixture immediately turned grey and cloudy and was allowed to stir for 1 hour at 23 °C. A solution of **4.24a** (30 mg, 0.049 mmol, 1.0 equiv.) in THF (1.5 mL) was then added via pipette. The tube was sealed, removed from the glove box, and pressurized to 5.5 bar nitrogen. After 30 seconds, the reaction mixture turned brown/orange. After 4 hours, the reaction was taken back into the glove box. The crude reaction was washed with pentane, filtered through Celite, and concentrated *in vacuo* to afford a brown/orange solid. Crystals suitable for X-ray crystallography were grown from a vapor diffusion of pentane into a saturated diethyl ether solution at -40 °C. ^1H NMR: Decomposition before obtaining spectrum. IR (neat): 2957, 2070, 1974, 1686, 1561, 1459, 1359, 1320, 1211, 780, 481 cm^{-1} (under Ar).

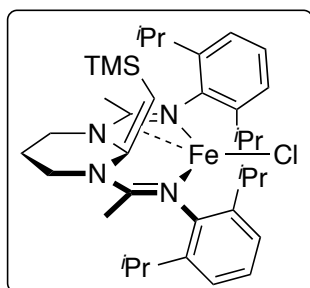
{N,N-1,3-bis[1-(2,6-diisopropylphenylimino)ethyl]4,5,6-trihydropyrimidyl}iron



chloride (4.32). (Performed by Hilan Z. Kaplan.) In an inert atmosphere glove box, **4.24a** (202 mg, 0.329 mmol, 1.00 equiv.) was suspended in THF (16 mL) and the mixture was cooled to -40 °C. A solution of LiBEt_3H in THF (0.329 mL, 0.329 mmol,

1.00 M, 1.00 equiv.) was then added drop wise, and the reaction was allowed to warm to 23 °C. Within minutes of the addition, the reaction turned bright green and homogenous. The solution was allowed to stir for 1 hour, and was then filtered through Celite, and concentrated *in vacuo* to afford a light green solid. The crude residue was recrystallized from benzene layered with hexane (1:1 v/v) to afford the title compound **4.32** as bright green crystals suitable for X-ray crystallography (114 mg, 60%). ¹H NMR: Decomposition before obtaining spectrum. IR (neat): 1591, 1430, 1288, 1259, 1023, 778, 687 cm⁻¹ (under N₂). μ_{eff} = 5.2 μ_B at 25 °C (Evans' method). HRMS (MALDI) for C₃₂H₄₇ClFeN₄ [M]⁺: Calcd. 578.2839, Found 578.2814.

{N,N-1,3-bis[1-(2,6-diisopropylphenylimino)ethyl]-2-(2-

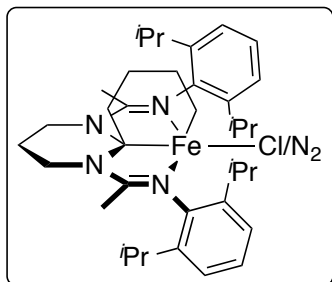


(trimethylsilyl)methylene)4,5,6-trihydropyrimidyl}iron chloride

(4.36). (Performed by Hilan Z. Kaplan.) In an inert atmosphere glove box, **4.24a** (50 mg, 0.082 mmol, 1.0 equiv.) was suspended in THF (4.1 mL) and the mixture was cooled to -40 °C. A solution of LiCH₂TMS in pentane (82 μL, 0.82 mmol, 1.0 M, 1.00 equiv.) was

added to the suspension and the mixture was allowed to warm to 23 °C, during which time the mixture turned from purple to deep red. After 3 hours of stirring, the reaction was concentrated *in vacuo*. The crude red solid was dissolved in benzene, filtered through Celite, and layered with hexanes to deliver red/brown crystals of the title compound **4.36** that were suitable for X-ray crystallography (15 mg, 28%). ¹H NMR: Decomposition before obtaining spectrum. IR (neat): 2960, 2864, 1554, 1417, 1378, 833, 767 cm⁻¹ (under N₂). HRMS (MALDI) for C₃₆H₅₆ClFeN₄Si [M]⁺: Calcd. 663.3312, Found 663.3330.

{N,N-1,3-bis[1-(2,6-diisopropylphenylimino)ethyl]-2-(κ²-butane)4,5,6-



trihydropyrimidyl}iron chloride or dinitrogen (**4.40**). In an

inert atmosphere glove box, mercury (1.17 g, 5.85 mmol, 115 equiv.) was added to a 25 mL round bottom flask. THF (2.0 mL) was added followed by freshly cut sodium (0.0055 g, 0.24 mmol, 5.0 equiv.). The biphasic mixture immediately turned grey and cloudy and was allowed to stir for 1 hour. A suspension of **4.24a** (0.0301 g, 0.0490 mmol, 1.00 equiv.) in THF (3 mL) was then added drop wise. The flask was sealed with a 180° joint and removed from the glove box. The purple reaction mixture was freeze-pump-thawed with liquid N₂ and the flask was backfilled with 1 bar of ethylene (at which point the ethylene began to condense on top of the frozen reaction mixture). The reaction was allowed to warm to 23 °C. After 5 minutes at 23 °C, the mixture turned deep red, and after 15 minutes, the color changed to orange/brown. The reaction was allowed to stir for a total of 2 hours at 23 °C, after which it was thoroughly degassed, and taken back into the glove box. The crude reaction was filtered through Celite, and concentrated *in vacuo* to afford an orange oil. Recrystallization from pentane, followed by recrystallization from diethyl ether afforded the title compound **4.40** as bright orange crystals suitable for X-ray crystallography (0.0293 g, 94%). ¹H NMR: Decomposition before obtaining spectrum. IR (neat): 2958, 1552, 1423, 1406, 1386, 1358, 1322, 1252, 1099, 936, 794, 767 cm⁻¹ (under N₂). HRMS: Decomposition before obtaining data.

4.6 References

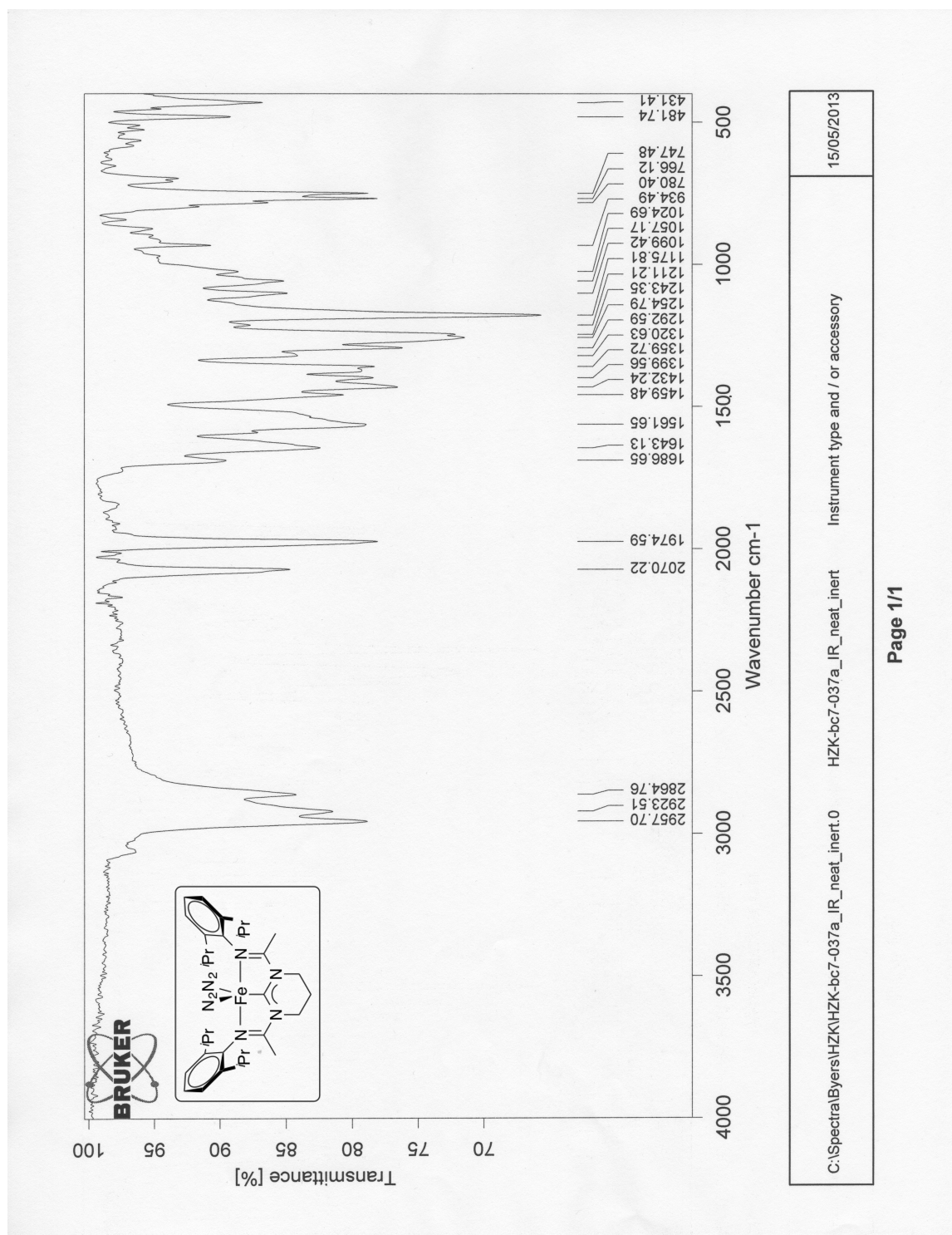
1. Chirik, P. J.; Wieghardt, K. *Science* **2010**, *327*, 794.
2. Bolm, C.; Legros, J.; Paih, J. L.; Zani, L. *Chem. Rev.* **2004**, *104*, 6217.
3. Small, B. L.; Brookhart, M.; Bennett, A. M. A. *J. Am. Chem. Soc.* **1998**, *120*, 4049.
4. Britovsek, G. J. P.; Bruce, M.; Gibson, V. C.; Kimberley, B. S.; Maddox, P. J.; Mastroianni, S.; McTavish, S. J.; Redshaw, C.; Solan, G. A.; Sromberg, S.; White, A. J. P.; Williams, D. J. *J. Am. Chem. Soc.* **1999**, *121*, 8728.
5. Spaleck, W.; Küber, F.; Winter, A.; Rohrmann, J.; Bachmann, B.; Antberg, M.; Dolle, V.; Paulus, E. F. *Organometallics* **1994**, *13*, 954.
6. Gibson, V. C.; Solan, G. A. *Top. Organomet. Chem.* **2009**, *26*, 107.
7. Bianchini, C. G. G.; Rios, I. G.; Matovani, G.; Meli, A.; Segarra, A. M. *Coord. Chem. Rev.* **2006**, *250*, 1391.
8. Karpiniec, S. S.; McGuinness, D. S.; Britovsek, G. J. P.; Patel, J. *Organometallics* **2008**, *27*, 1470.
9. Bart, S. C.; Lobkovsky, E.; Chirik, P. J. *J. Am. Chem. Soc.* **2004**, *126*, 13794.
10. Crabtree, R. H. *Acc. Chem. Res.* **1979**, *12*, 351.
11. Trovitch, R. J.; Lobkovsky, E.; Bill, E.; Chirik, P. J. *Organometallics* **2007**, *27*, 1470.
12. Tondreau, A. M.; Atienza, C. C. H.; Weller, K. J.; Nye, S. A.; Lewis, K. M.; Delis, J. G. P.; Chirik, P. J. *Science* **2012**, *335*, 567.
13. Yu, R. P.; Darmon, J. M.; Hoyt, J. M.; Margulieuz, G. W.; Turner, Z. R.; Chirik, P. J. *ACS Catal.* **2012**, *2*, 1760.
14. Obligacion, J. V.; Chirik, P. J. *Org. Lett.* **2013**, *15*, 2680.
15. Suzuki, A. *Angew. Chem. Int. Ed.* **2011**, *50*, 6722.
16. Chemier, S. R.; Trauner, D.; Danishefsky, S. J. *Angew. Chem. Int. Ed.* **2001**, *40*, 4544.
17. Bouwkamp, M. W.; Bowman, A. C.; Lobkovsky, E.; Chirik, P. J. *J. Am. Chem. Soc.* **2006**, *128*, 13340.
18. Woodward, R. B.; Hoffmann, R. *Angew. Chem. Int. Ed. Engl.* **1969**, *8*, 781.
19. Crimmins, M. T. *Comprehensive Organic Synthesis*; Trost, B. M.; Fleming, I.; Paquette, L. A., Eds.; Pergamon: Oxford, 1991; Vol. 5.
20. Russel, S. K.; Lobkovsky, E.; Chirik, P. J. *J. Am. Chem. Soc.* **2011**, *133*, 8858.
21. Biernesser, A. B.; Li, B.; Byers, J. A. *J. Am. Chem. Soc.* **2013**, *135*, 16553.
22. Stieber, S. C. E.; Milsman, C.; Hoyt, J. M.; Turner, Z. R.; Finkelstein, K. D.; Wieghardt, K.; DeBeer, S.; Chirik, P. J. *Inorg. Chem.* **2012**, *51*, 3770.
23. Bart, S. C.; Chlopek, K.; Bouwkamp, M. W.; Lobkovsky, E.; Neese, F.; Wieghardt, K.; Chirik, P. J. *J. Am. Chem. Soc.* **2006**, *128*, 13901.
24. Bouwkamp, M. W.; Bart, S. C.; Hawrelak, E. J.; Trovitch, R. J.; Lobkovsky, E.; Chirik, P. J. *J. Am. Chem. Soc.* **2005**, *127*, 9660.
25. Tondreau, A. M.; Milsman, L. E.; Chirik, P. J. *Inorg. Chem.* **2011**, *50*, 9888.
26. Hoyt, J. M.; Sylvester, K. T.; Semperoni, S. P.; Chirik, P. J. *J. Am. Chem. Soc.* **2013**, *135*, 4862.
27. Danopoulos, A. A.; Tsoureas, N.; Wright, J.; Light, M. *Organometallics* **2004**, *23*, 166.
28. McGuinness, D. S.; Gibson, V. C.; Steed, J. W. *Organometallics* **2004**, *23*, 6288.

29. Wüstenberg, B.; Pfaltz, A. *Adv. Synth. Catal.* **2008**, *350*, 174.
30. Zohuri, G. H.; Seyedi, S. M.; Sandaroods, R.; Damavandi, S.; Mohammadi, A. *Catal. Lett.* **2010**, *140*, 160.
31. Svejda, S. A.; Brookhart, M. *Organometallics* **1999**, *18*, 65.
32. Darmon, J. M.; Turner, Z. R.; Lobkovsky, E.; Chirik, P. J. *Organometallics* **2012**, *31*, 2275.
33. Britovsek, G. J. P.; Gibson, V. C.; Hoarau, O. D.; Spitzmeser, S. K.; White, A. J. P.; Williams, D. J. *Inorg. Chem.* **2003**, *42*, 3465.
34. Thagfi, J. A.; Lavoie, G. G. *Organometallics* **2012**, *31*, 2463.
35. Kaplan, H. Z.; Li, B.; Byers, J. A. *Organometallics* **2012**, *31*, 7343.
36. Thagfi, J. A.; Lavoie, G. G. *Organometallics* **2012**, *31*, 7351.
37. Evans, D. F. *J. Chem. Soc.* **1959**, 2003.
38. Schubert, E. M. *J. Chem. Educ.* **1992**, *69*, 62.
39. Kahn, O. *Molecular Magnetism*; VCH Publishers, Inc.: New York, NY, 1993.
40. Mossin, S.; Tran, B. L.; Adhikari, D.; Pink, M.; Heinemann, F. W.; Sutter, J.; Szilagy, R. K.; Meyer, K.; Mindiola, D. J. *J. Am. Chem. Soc.* **2012**, *134*, 13651.
41. Broeckx, W.; Overbergh, N.; Samyn, C.; Smets, G.; L'Abbé, G. *Tetrahedron* **1971**, *27*, 3527.
42. Sha, C. K.; Ouyang, S. L.; Hsieh, D. Y.; Chang, R. C.; Chang, S. C. *J. Org. Chem.* **1986**, *51*, 1490.
43. Stoian, S. A.; Yu, Y.; Smith, J. M.; Hollard, P. L.; Bominaar, E. L.; Münck, E. *Inorg. Chem.* **2005**, *44*, 4915.
44. Yu, Y.; Sadique, A. R.; Smith, J. M.; Dugan, T. R.; Cowley, R. E.; Brennessel, W. W.; Flaschnriem, C. J.; Bill, E.; Cundari, T. R.; Hollard, P. L. *J. Am. Chem. Soc.* **2008**, *130*, 6624.
45. Bowman, A. C.; Milsman, C.; Bill, E.; Turner, Z. R.; Lobkovsky, E.; DeBeer, S.; Wieghardt, K.; Chirik, P. J. *J. Am. Chem. Soc.* **2011**, *133*, 17353.
46. Scepaniak, J. J.; Harris, T. D.; Vogel, C. S.; Sutter, J.; Meyer, K. S. *J. Am. Chem. Soc.* **2011**, *133*, 3824.
47. Bart, S. C.; Lobkovsky, E.; Bill, E.; Wieghardt, K.; Chirik, P. J. *Inorg. Chem.* **2007**, *46*, 7055.
48. Danopoulos, A. A.; Pugh, D.; Smith, H.; Saßmannshausen, J. *Chem. Eur. J.* **2009**, *15*, 5491-5502.
49. Buford, R. J.; Piers, W. E.; Parvez, M. *Eur. J. Inorg. Chem.* **2013**, *22*, 3826.
50. Gutsulyak, D. V.; Piers, W. E.; Borau-Garcia, J.; Parvez, M. *J. Am. Chem. Soc.* **2013**, *135*, 11776.
51. Horn, M.; Mayr, H.; Lacôte, E.; Merling, E.; Deaner, J.; Wells, S.; McFadden, T.; Curran, D. P. *Org. Lett.* **2012**, *14*, 82.
52. Cámpora, J.; Naz, A. M.; Palma, P.; Álvarez, E. *Organometallics* **2005**, *24*, 4878.
53. Burger, J. B.; Bercaw, J. E. *New Developments in the Synthesis, Manipulation, and Characterization of Organometallic Compounds*; American Chemical Society: Washington, D.C., 1987.
54. Pangborn, A. B.; Giardello, M. A.; Grubbs, R. H.; Rose, R. K.; Timmers, F. J. *Organometallics* **1996**, *15*, 1518.
55. Britovsek, G. J. P.; Gibson, V. C.; Spitzmesser, S. K.; Tellmann, K. P.; White, A. J. P.; Williams, D. J. *J. Am. Chem., Dalton Trans.* **2002**, 1159.
56. Bill, E. julX version 1.5, MPI for Chemical Energy Conversion. **2013**.

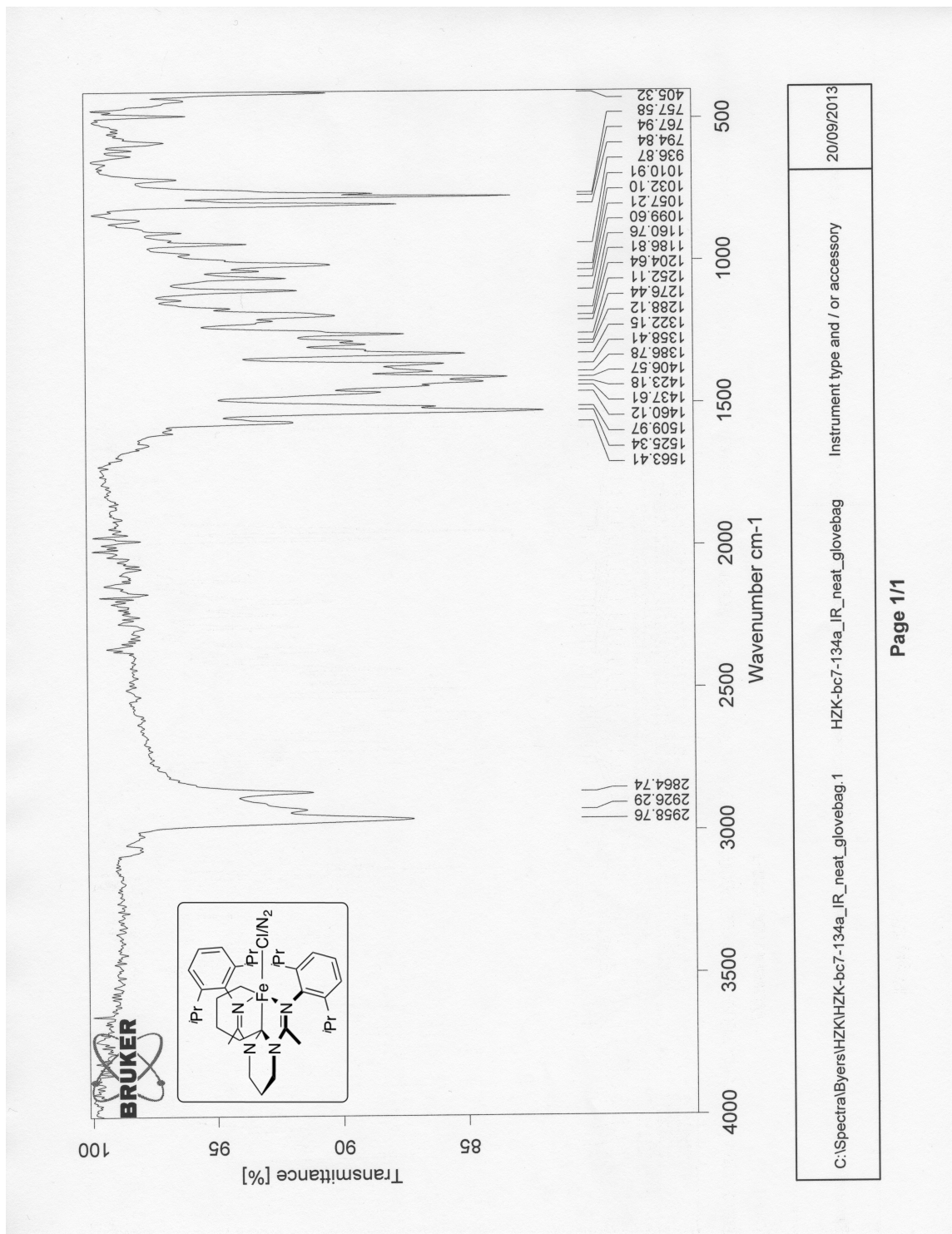
57. Kahn, O. In *Molecular Magnetism*; VCH Publishers, Inc.: New York, N.Y., 1993.
58. Bart, S.; Krzystof, C.; Eckhard, B.; Boukamp, M. W.; Lobkovsky, E.; Neese, F.; Wieghardt, K.; Chirik, P. J. *J. Am. Chem. Soc.* **2006**, *128*, 13901.
59. Neese, F. Orca: an ab initio, DFT and Semiempirical Electronic Structure Package, Version 2.8, Revision 2287. Institut für Physikalische and Theoretische Chemie, Universität Bonn: Bonn Germany, 2010.
60. Schäfer, A.; Horn, H.; Ahlrichs, R. *J. Chem. Phys.* **1992**, *97*, 2571.
61. Weigend, F.; Ahlrichs, R. *Phys. Chem. Chem. Phys.* **2005**, *7*, 3297.
62. Eichkorn, K.; Weigend, F.; Treutler, O.; Ahlrichs, R. *Theor. Chem. Acc.* **1997**, *97*, 119.
63. Eichkorn, K.; Treutler, O.; Öhm, H.; Häser, M.; Ahlrichs, R. *Chem. Phys. Lett.* **1995**, *240*, 283.
64. Eichkorn, K.; Treutler, O.; Öhm, H.; Häser, M.; Ahlrichs, R. *Chem. Phys. Lett.* **1995**, *242*, 652.
65. Neese, F.; Wennmobs, F.; Hansen, A.; Becker, U. *Chem. Phys.* **2009**, *356*, 98.
66. Kossmann, S.; Neese, F. *Chem. Phys. Lett.* **2009**, *481*, 240.
67. Neese, F. *J. Comput. Chem.* **2003**, *24*, 1740.
68. Ginsberg, A. P. *J. Am. Chem. Soc.* **1980**, *102*, 111.
69. Noodleman, L.; Peng, C. Y.; Case, D. A.; Mouesca, J. M. *Coord. Chem. Rev.* **1995**, *144*, 199.
70. Kirchner, B.; Wennmobs, F.; Ye, S.; Neese, F. *Curr. Opin. Chem. Biol.* **2007**, *11*, 134.
71. Pettersen, E. F.; Goddard, T. D.; Huang, C. C.; Couch, G. S.; Greenblatt, D. M.; Meng, E. C.; Ferrin, T. E. *J. Comput. Chem.* **2004**, *25*, 1605.
72. Neese, F. *Inorg. Chim. Acta* **2002**, *337*, 181.
73. Maltempo, M. M. *J. Chem. Phys.* **1974**, *61*, 2540.
74. Dolphin, H. D.; Sams, J. R.; Tsin, T. B. *Inorg. Chem.* **1977**, *16*, 711.
75. Manna, C. M.; Z., K. H.; Li, B.; Byers, J. A. *Polyhedron* **2014**, *84*, 160.

4.7 Spectra

IR Spectrum of {N,N-1,3-bis[1-(2,6-diisopropylphenylimino)ethyl]4,5,6-trihydropyrimid-2-ylidene}iron bis(dinitrogen) (4.29).



IR Spectrum of {N,N-1,3-bis[1-(2,6-diisopropylphenylimino)ethyl]-2-(κ^2 -butane)4,5,6-trihydropyrimidyl}iron chloride or dinitrogen (4.40).



C:\Spectral\Byers\HZK\HZK-bc7-134a_IR_neat_glovebag.1 HZK-bc7-134a_IR_neat_glovebag Instrument type and / or accessory 20/09/2013

Appendix

X-ray Crystallographic Data

**A.1 Data for (κ^2 -carbonate)(*p*-cymene)(triphenylphosphine)ruthenium (2.40)
at 100 K**

Figure A.1. ORTEP plot of 2.40 with thermal ellipsoids represented at the 50% probability level. Hydrogen atoms and solvent molecules were excluded for clarity.

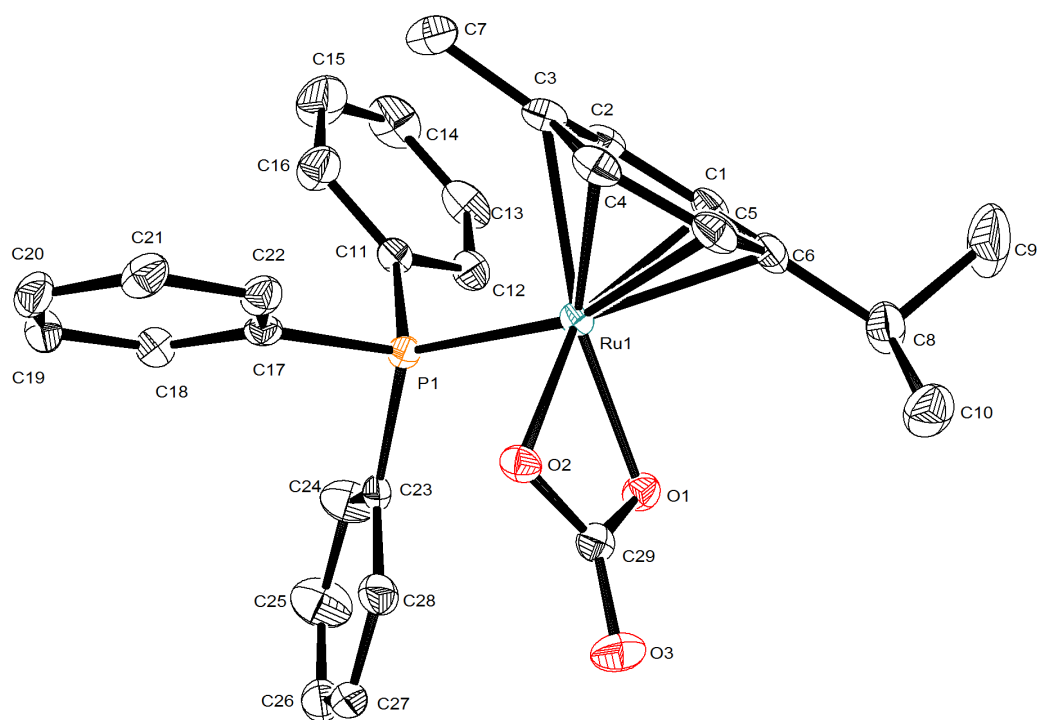


Table A.1. Crystal data and structure refinement for C₂₉H₃₁O₄PRu (2.40).

	100 K
Identification code/CCDC	C ₂₉ H ₃₁ O ₄ PRu /959394
Empirical formula	C ₂₉ H ₃₁ O ₄ PRu
Formula weight	575.58
Temperature	100(2) K
Wavelength	1.54178 Å
Crystal system	Monoclinic
Space group	P 2 ₁ /c
Unit cell dimensions	a = 9.0094(3) Å α = 90° b = 14.3971(4) Å β = 94.3520(10)° c = 21.0729(6) Å γ = 90°
Volume	2725.47(14) Å ³
Z	4
Density (calculated)	1.403 Mg/m ³
Absorption coefficient	5.463 mm ⁻¹
F(000)	1184
Crystal size	0.20 × 0.16 × 0.10 mm ³
Theta range for data collection	3.72 to 69.88°
Index ranges	-10 ≤ h ≤ 10, 0 ≤ k ≤ 17, 0 ≤ l ≤ 25
Reflections collected	4890
Independent reflections	4890 [R _{int} = 0.0000]
Completeness to θ = 32.15/66.36°	98.5%
Absorption correction	Semi-empirical from equivalents
Max. and min. transmission	0.6111 and 0.4079
Refinement method	Full-matrix least-squares on F ²
Data / restraints / parameters	4890 / 2 / 322
Goodness-of-fit on F ²	1.140
Final R indices [I > 2σ(I)]	R ₁ = 0.0236, ωR ₂ = 0.0539
R indices (all data)	R ₁ = 0.0238, ωR ₂ = 0.0540
Extinction coefficient	na
Largest diff. peak and hole	0.820 and -0.437 e.Å ⁻³

Table A.2. Atomic coordinates ($\times 10^4$) and equivalent isotropic displacement parameters ($\text{\AA}^2 \times 10^3$) for $\text{C}_{29}\text{H}_{31}\text{O}_4\text{PRu}$ (2.40). $U(\text{eq})$ is defined as one third of the trace of the orthogonalized U_{ij} tensor.

	x	y	z	U(eq)
Ru(1)	4346(1)	1141(1)	3733(1)	13(1)
P(1)	4313(1)	503(1)	2709(1)	14(1)
O(1)	6662(2)	1214(1)	3820(1)	18(1)
O(2)	5494(2)	-46(1)	4076(1)	18(1)
O(3)	7958(2)	76(1)	4348(1)	26(1)
C(1)	3724(2)	2604(1)	3783(1)	20(1)
C(2)	2536(2)	2126(1)	3457(1)	20(1)
C(3)	1850(2)	1346(2)	3731(1)	20(1)
C(4)	2457(2)	1045(2)	4331(1)	21(1)
C(5)	3608(2)	1544(2)	4681(1)	21(1)
C(6)	4259(2)	2329(1)	4414(1)	20(1)
C(7)	524(2)	876(2)	3401(1)	27(1)
C(8)	5554(3)	2851(2)	4737(1)	27(1)
C(9)	4998(4)	3798(2)	4947(2)	60(1)
C(10)	6341(3)	2345(2)	5298(1)	32(1)
C(11)	3344(2)	1232(1)	2104(1)	18(1)
C(12)	4000(3)	2074(2)	1944(1)	23(1)
C(13)	3295(3)	2654(2)	1494(1)	31(1)
C(14)	1910(3)	2430(2)	1214(1)	39(1)
C(15)	1235(3)	1613(2)	1383(1)	43(1)
C(16)	1957(3)	1011(2)	1818(1)	30(1)
C(17)	3357(2)	-621(1)	2649(1)	17(1)
C(18)	3237(2)	-1119(2)	2077(1)	22(1)
C(19)	2520(3)	-1970(2)	2038(1)	26(1)
C(20)	1902(2)	-2333(2)	2571(1)	26(1)
C(21)	2016(2)	-1846(2)	3139(1)	24(1)
C(22)	2752(2)	-996(2)	3181(1)	20(1)
C(23)	6053(2)	213(1)	2352(1)	17(1)
C(24)	6349(3)	460(2)	1736(1)	33(1)
C(25)	7636(3)	150(2)	1479(1)	42(1)
C(26)	8633(3)	-408(2)	1831(1)	32(1)
C(27)	8357(3)	-653(2)	2442(1)	30(1)
C(28)	7079(3)	-338(2)	2702(1)	25(1)
C(29)	6782(2)	394(1)	4096(1)	17(1)
O(1S)	437(2)	8906(1)	4616(1)	39(1)

Table A.3. Bond lengths [Å] and angles [°] for C₂₉H₃₁O₄PRu (2.40).

Ru(1)-O(1)	2.0833(14)	C(11)-C(12)	1.399(3)
Ru(1)-O(2)	2.0984(13)	C(12)-C(13)	1.383(3)
Ru(1)-C(1)	2.184(2)	C(12)-H(12A)	0.9500
Ru(1)-C(4)	2.198(2)	C(13)-C(14)	1.377(4)
Ru(1)-C(2)	2.205(2)	C(13)-H(13A)	0.9500
Ru(1)-C(5)	2.229(2)	C(14)-C(15)	1.382(4)
Ru(1)-C(6)	2.238(2)	C(14)-H(14A)	0.9500
Ru(1)-C(3)	2.268(2)	C(15)-C(16)	1.387(3)
Ru(1)-P(1)	2.3440(5)	C(15)-H(15A)	0.9500
P(1)-C(11)	1.822(2)	C(16)-H(16A)	0.9500
P(1)-C(17)	1.832(2)	C(17)-C(22)	1.393(3)
P(1)-C(23)	1.837(2)	C(17)-C(18)	1.399(3)
O(1)-C(29)	1.316(3)	C(18)-C(19)	1.384(3)
O(2)-C(29)	1.320(3)	C(18)-H(18A)	0.9500
O(3)-C(29)	1.237(3)	C(19)-C(20)	1.394(3)
C(1)-C(2)	1.408(3)	C(19)-H(19A)	0.9500
C(1)-C(6)	1.435(3)	C(20)-C(21)	1.384(3)
C(1)-H(1A)	1.0000	C(20)-H(20A)	0.9500
C(2)-C(3)	1.426(3)	C(21)-C(22)	1.391(3)
C(2)-H(2A)	1.0000	C(21)-H(21A)	0.9500
C(3)-C(4)	1.407(3)	C(22)-H(22A)	0.9500
C(3)-C(7)	1.498(3)	C(23)-C(28)	1.386(3)
C(4)-C(5)	1.421(3)	C(23)-C(24)	1.391(3)
C(4)-H(4A)	1.0000	C(24)-C(25)	1.390(3)
C(5)-C(6)	1.409(3)	C(24)-H(24A)	0.9500
C(5)-H(5A)	1.0000	C(25)-C(26)	1.378(4)
C(6)-C(8)	1.506(3)	C(25)-H(25A)	0.9500
C(7)-H(7A)	0.9800	C(26)-C(27)	1.376(4)
C(7)-H(7B)	0.9800	C(26)-H(26A)	0.9500
C(7)-H(7C)	0.9800	C(27)-C(28)	1.388(3)
C(8)-C(10)	1.517(3)	C(27)-H(27A)	0.9500
C(8)-C(9)	1.531(3)	C(28)-H(28A)	0.9500
C(8)-H(8A)	1.0000	O(1S)-H(1O)	0.865(18)
C(9)-H(9A)	0.9800	O(1S)-H(2O)	0.856(18)
C(9)-H(9B)	0.9800		
C(9)-H(9C)	0.9800	O(1)-Ru(1)-O(2)	63.00(5)
C(10)-H(10A)	0.9800	O(1)-Ru(1)-C(1)	101.93(7)
C(10)-H(10B)	0.9800	O(2)-Ru(1)-C(1)	152.93(7)
C(10)-H(10C)	0.9800	O(1)-Ru(1)-C(4)	140.00(7)
C(11)-C(16)	1.383(3)	O(2)-Ru(1)-C(4)	97.66(7)

C(1)-Ru(1)-C(4)	79.64(8)	C(6)-C(1)-H(1A)	119.5
O(1)-Ru(1)-C(2)	135.00(7)	Ru(1)-C(1)-H(1A)	119.5
O(2)-Ru(1)-C(2)	161.79(7)	C(1)-C(2)-C(3)	121.6(2)
C(1)-Ru(1)-C(2)	37.40(8)	C(1)-C(2)-Ru(1)	70.49(12)
C(4)-Ru(1)-C(2)	66.58(8)	C(3)-C(2)-Ru(1)	73.82(12)
O(1)-Ru(1)-C(5)	105.80(7)	C(1)-C(2)-H(2A)	118.7
O(2)-Ru(1)-C(5)	94.33(7)	C(3)-C(2)-H(2A)	118.7
C(1)-Ru(1)-C(5)	67.06(8)	Ru(1)-C(2)-H(2A)	118.7
C(4)-Ru(1)-C(5)	37.42(8)	C(4)-C(3)-C(2)	117.1(2)
C(2)-Ru(1)-C(5)	78.70(8)	C(4)-C(3)-C(7)	121.4(2)
O(1)-Ru(1)-C(6)	89.34(7)	C(2)-C(3)-C(7)	121.5(2)
O(2)-Ru(1)-C(6)	116.19(7)	C(4)-C(3)-Ru(1)	68.95(12)
C(1)-Ru(1)-C(6)	37.85(8)	C(2)-C(3)-Ru(1)	69.05(11)
C(4)-Ru(1)-C(6)	67.28(8)	C(7)-C(3)-Ru(1)	134.26(15)
C(2)-Ru(1)-C(6)	67.47(8)	C(3)-C(4)-C(5)	121.9(2)
C(5)-Ru(1)-C(6)	36.77(8)	C(3)-C(4)-Ru(1)	74.36(12)
O(1)-Ru(1)-C(3)	168.54(7)	C(5)-C(4)-Ru(1)	72.48(12)
O(2)-Ru(1)-C(3)	124.68(7)	C(3)-C(4)-H(4A)	118.8
C(1)-Ru(1)-C(3)	67.46(8)	C(5)-C(4)-H(4A)	118.8
C(4)-Ru(1)-C(3)	36.69(8)	Ru(1)-C(4)-H(4A)	118.8
C(2)-Ru(1)-C(3)	37.13(8)	C(6)-C(5)-C(4)	120.57(19)
C(5)-Ru(1)-C(3)	66.69(8)	C(6)-C(5)-Ru(1)	71.93(11)
C(6)-Ru(1)-C(3)	79.55(8)	C(4)-C(5)-Ru(1)	70.10(12)
O(1)-Ru(1)-P(1)	92.52(4)	C(6)-C(5)-H(5A)	119.0
O(2)-Ru(1)-P(1)	88.27(4)	C(4)-C(5)-H(5A)	119.0
C(1)-Ru(1)-P(1)	115.95(6)	Ru(1)-C(5)-H(5A)	119.0
C(4)-Ru(1)-P(1)	123.17(6)	C(5)-C(6)-C(1)	118.0(2)
C(2)-Ru(1)-P(1)	92.96(6)	C(5)-C(6)-C(8)	123.47(19)
C(5)-Ru(1)-P(1)	160.60(6)	C(1)-C(6)-C(8)	118.35(19)
C(6)-Ru(1)-P(1)	153.09(6)	C(5)-C(6)-Ru(1)	71.29(12)
C(3)-Ru(1)-P(1)	96.10(6)	C(1)-C(6)-Ru(1)	69.06(11)
C(11)-P(1)-C(17)	105.27(9)	C(8)-C(6)-Ru(1)	127.39(15)
C(11)-P(1)-C(23)	102.88(9)	C(3)-C(7)-H(7A)	109.5
C(17)-P(1)-C(23)	100.53(9)	C(3)-C(7)-H(7B)	109.5
C(11)-P(1)-Ru(1)	112.96(7)	H(7A)-C(7)-H(7B)	109.5
C(17)-P(1)-Ru(1)	112.49(7)	C(3)-C(7)-H(7C)	109.5
C(23)-P(1)-Ru(1)	120.90(7)	H(7A)-C(7)-H(7C)	109.5
C(29)-O(1)-Ru(1)	92.43(12)	H(7B)-C(7)-H(7C)	109.5
C(29)-O(2)-Ru(1)	91.63(11)	C(6)-C(8)-C(10)	114.4(2)
C(2)-C(1)-C(6)	120.47(19)	C(6)-C(8)-C(9)	108.4(2)
C(2)-C(1)-Ru(1)	72.11(12)	C(10)-C(8)-C(9)	110.2(2)
C(6)-C(1)-Ru(1)	73.08(12)	C(6)-C(8)-H(8A)	107.9
C(2)-C(1)-H(1A)	119.5	C(10)-C(8)-H(8A)	107.9

C(9)-C(8)-H(8A)	107.9	C(17)-C(18)-H(18A)	119.6
C(8)-C(9)-H(9A)	109.5	C(18)-C(19)-C(20)	119.8(2)
C(8)-C(9)-H(9B)	109.5	C(18)-C(19)-H(19A)	120.1
H(9A)-C(9)-H(9B)	109.5	C(20)-C(19)-H(19A)	120.1
C(8)-C(9)-H(9C)	109.5	C(21)-C(20)-C(19)	120.0(2)
H(9A)-C(9)-H(9C)	109.5	C(21)-C(20)-H(20A)	120.0
H(9B)-C(9)-H(9C)	109.5	C(19)-C(20)-H(20A)	120.0
C(8)-C(10)-H(10A)	109.5	C(20)-C(21)-C(22)	120.3(2)
C(8)-C(10)-H(10B)	109.5	C(20)-C(21)-H(21A)	119.9
H(10A)-C(10)-H(10B)	109.5	C(22)-C(21)-H(21A)	119.9
C(8)-C(10)-H(10C)	109.5	C(21)-C(22)-C(17)	120.3(2)
H(10A)-C(10)-H(10C)	109.5	C(21)-C(22)-H(22A)	119.9
H(10B)-C(10)-H(10C)	109.5	C(17)-C(22)-H(22A)	119.9
C(16)-C(11)-C(12)	118.6(2)	C(28)-C(23)-C(24)	118.4(2)
C(16)-C(11)-P(1)	122.76(17)	C(28)-C(23)-P(1)	117.87(16)
C(12)-C(11)-P(1)	118.56(16)	C(24)-C(23)-P(1)	123.59(17)
C(13)-C(12)-C(11)	120.5(2)	C(25)-C(24)-C(23)	120.4(2)
C(13)-C(12)-H(12A)	119.8	C(25)-C(24)-H(24A)	119.8
C(11)-C(12)-H(12A)	119.8	C(23)-C(24)-H(24A)	119.8
C(14)-C(13)-C(12)	120.4(2)	C(26)-C(25)-C(24)	120.4(2)
C(14)-C(13)-H(13A)	119.8	C(26)-C(25)-H(25A)	119.8
C(12)-C(13)-H(13A)	119.8	C(24)-C(25)-H(25A)	119.8
C(13)-C(14)-C(15)	119.5(2)	C(27)-C(26)-C(25)	119.8(2)
C(13)-C(14)-H(14A)	120.3	C(27)-C(26)-H(26A)	120.1
C(15)-C(14)-H(14A)	120.3	C(25)-C(26)-H(26A)	120.1
C(14)-C(15)-C(16)	120.5(3)	C(26)-C(27)-C(28)	120.0(2)
C(14)-C(15)-H(15A)	119.7	C(26)-C(27)-H(27A)	120.0
C(16)-C(15)-H(15A)	119.7	C(28)-C(27)-H(27A)	120.0
C(11)-C(16)-C(15)	120.5(2)	C(23)-C(28)-C(27)	121.1(2)
C(11)-C(16)-H(16A)	119.8	C(23)-C(28)-H(28A)	119.4
C(15)-C(16)-H(16A)	119.8	C(27)-C(28)-H(28A)	119.4
C(22)-C(17)-C(18)	118.97(19)	O(3)-C(29)-O(1)	124.10(19)
C(22)-C(17)-P(1)	119.87(16)	O(3)-C(29)-O(2)	123.91(19)
C(18)-C(17)-P(1)	121.15(16)	O(1)-C(29)-O(2)	112.00(17)
C(19)-C(18)-C(17)	120.7(2)	H(1O)-O(1S)-H(2O)	100
C(19)-C(18)-H(18A)	119.6		

Table A.4. Anisotropic displacement parameters ($\text{\AA}^2 \times 10^3$) for $\text{C}_{29}\text{H}_{31}\text{O}_4\text{PRu}$ (2.40). The anisotropic displacement factor exponent takes the form: $-2p^2 [h^2 a^* U^{11} + \dots + 2 h k a^* b^* U^{12}]$.

	U ¹¹	U ²²	U ³³	U ²³	U ¹³	U ¹²
Ru(1)	16(1)	11(1)	13(1)	2(1)	1(1)	1(1)
P(1)	15(1)	13(1)	14(1)	2(1)	0(1)	0(1)
O(1)	17(1)	18(1)	20(1)	1(1)	0(1)	-2(1)
O(2)	19(1)	14(1)	20(1)	3(1)	1(1)	3(1)
O(3)	20(1)	33(1)	25(1)	6(1)	-2(1)	6(1)
C(1)	27(1)	12(1)	20(1)	0(1)	4(1)	6(1)
C(2)	21(1)	19(1)	20(1)	2(1)	3(1)	9(1)
C(3)	17(1)	22(1)	23(1)	0(1)	6(1)	6(1)
C(4)	24(1)	19(1)	22(1)	3(1)	10(1)	5(1)
C(5)	26(1)	22(1)	15(1)	1(1)	6(1)	9(1)
C(6)	25(1)	17(1)	18(1)	-4(1)	1(1)	6(1)
C(7)	18(1)	30(1)	32(1)	4(1)	1(1)	1(1)
C(8)	36(1)	21(1)	24(1)	-4(1)	-3(1)	1(1)
C(9)	80(2)	28(2)	66(2)	-20(1)	-39(2)	15(2)
C(10)	32(1)	37(1)	25(1)	0(1)	-4(1)	0(1)
C(11)	21(1)	17(1)	14(1)	1(1)	1(1)	3(1)
C(12)	27(1)	20(1)	22(1)	0(1)	4(1)	1(1)
C(13)	46(2)	22(1)	26(1)	8(1)	12(1)	8(1)
C(14)	56(2)	32(1)	27(1)	11(1)	-5(1)	16(1)
C(15)	40(2)	39(2)	46(2)	4(1)	-23(1)	8(1)
C(16)	28(1)	24(1)	34(1)	4(1)	-8(1)	0(1)
C(17)	13(1)	15(1)	23(1)	3(1)	-1(1)	2(1)
C(18)	22(1)	21(1)	24(1)	-1(1)	1(1)	1(1)
C(19)	25(1)	21(1)	30(1)	-7(1)	-3(1)	1(1)
C(20)	22(1)	16(1)	38(1)	1(1)	-7(1)	-4(1)
C(21)	20(1)	22(1)	28(1)	7(1)	-3(1)	-3(1)
C(22)	19(1)	20(1)	20(1)	2(1)	-3(1)	1(1)
C(23)	17(1)	14(1)	21(1)	-5(1)	1(1)	-2(1)
C(24)	32(1)	36(1)	32(1)	9(1)	12(1)	8(1)
C(25)	40(2)	47(2)	40(2)	9(1)	23(1)	6(1)
C(26)	20(1)	32(1)	45(2)	-16(1)	10(1)	-5(1)
C(27)	22(1)	30(1)	37(1)	-15(1)	-9(1)	7(1)
C(28)	27(1)	27(1)	21(1)	-6(1)	-2(1)	6(1)
C(29)	20(1)	20(1)	13(1)	0(1)	1(1)	2(1)
O(1S)	31(1)	35(1)	50(1)	-13(1)	-8(1)	7(1)

Table A.5. Hydrogen coordinates ($\times 10^4$) and isotropic displacement parameters ($\text{\AA}^2 \times 10^3$) for $\text{C}_{29}\text{H}_{31}\text{O}_4\text{PRu}$ (2.40).

	x	y	z	U(eq)
H(1A)	4289	3078	3552	24
H(2A)	2298	2260	2995	24
H(4A)	2167	421	4489	26
H(5A)	4110	1257	5072	25
H(7A)	-388	1177	3522	40
H(7B)	515	220	3525	40
H(7C)	576	923	2939	40
H(8A)	6296	2960	4415	33
H(9A)	4473	4112	4583	90
H(9B)	5847	4178	5109	90
H(9C)	4316	3712	5283	90
H(10A)	6712	1746	5155	47
H(10B)	5642	2241	5624	47
H(10C)	7179	2722	5475	47
H(12A)	4936	2248	2148	27
H(13A)	3769	3211	1376	37
H(14A)	1423	2832	908	46
H(15A)	268	1464	1200	52
H(16A)	1496	443	1920	35
H(18A)	3651	-871	1712	26
H(19A)	2449	-2305	1648	31
H(20A)	1403	-2914	2545	31
H(21A)	1589	-2092	3502	28
H(22A)	2843	-671	3574	24
H(24A)	5667	842	1489	39
H(25A)	7831	323	1059	50
H(26A)	9507	-622	1653	39
H(27A)	9041	-1037	2687	36
H(28A)	6904	-502	3126	30
H(1O)	-350(30)	9250(20)	4565(17)	59
H(2O)	820(40)	9120(20)	4972(11)	59

Table A.6. Torsion angles [°] for C₂₉H₃₁O₄PRu (2.40).

O(1)-Ru(1)-P(1)-C(11)	-118.52(8)	O(1)-Ru(1)-C(1)-C(2)1	55.99(12)
O(2)-Ru(1)-P(1)-C(11)	178.61(8)	O(2)-Ru(1)-C(1)-C(2)	-151.34(14)
C(1)-Ru(1)-P(1)-C(11)	-13.95(10)	C(4)-Ru(1)-C(1)-C(2)	-64.79(13)
C(4)-Ru(1)-P(1)-C(11)	80.59(10)	C(5)-Ru(1)-C(1)-C(2)	-101.72(14)
C(2)-Ru(1)-P(1)-C(11)	16.79(9)	C(6)-Ru(1)-C(1)-C(2)	-130.93(19)
C(5)-Ru(1)-P(1)-C(11)	80.46(19)	C(3)-Ru(1)-C(1)-C(2)	-28.56(12)
C(6)-Ru(1)-P(1)-C(11)	-24.99(15)	P(1)-Ru(1)-C(1)-C(2)	57.20(13)
C(3)-Ru(1)-P(1)-C(11)	53.91(9)	O(1)-Ru(1)-C(1)-C(6)	-73.09(13)
O(1)-Ru(1)-P(1)-C(17)	122.46(8)	O(2)-Ru(1)-C(1)-C(6)	-20.4(2)
O(2)-Ru(1)-P(1)-C(17)	59.60(8)	C(4)-Ru(1)-C(1)-C(6)	66.14(13)
C(1)-Ru(1)-P(1)-C(17)	-132.97(9)	C(2)-Ru(1)-C(1)-C(6)	130.93(19)
C(4)-Ru(1)-P(1)-C(17)	-38.43(10)	C(5)-Ru(1)-C(1)-C(6)	29.20(12)
C(2)-Ru(1)-P(1)-C(17)	-102.22(9)	C(3)-Ru(1)-C(1)-C(6)	102.37(14)
C(5)-Ru(1)-P(1)-C(17)	-38.56(19)	P(1)-Ru(1)-C(1)-C(6)	-171.88(10)
C(6)-Ru(1)-P(1)-C(17)	-144.01(14)	C(6)-C(1)-C(2)-C(3)	-1.4(3)
C(3)-Ru(1)-P(1)-C(17)	-65.10(9)	Ru(1)-C(1)-C(2)-C(3)	55.58(18)
O(1)-Ru(1)-P(1)-C(23)	3.88(9)	C(6)-C(1)-C(2)-Ru(1)-	57.00(17)
O(2)-Ru(1)-P(1)-C(23)	-58.99(9)	O(1)-Ru(1)-C(2)-C(1)	-34.26(16)
C(1)-Ru(1)-P(1)-C(23)	108.45(10)	O(2)-Ru(1)-C(2)-C(1)	135.7(2)
C(4)-Ru(1)-P(1)-C(23)	-157.01(10)	C(4)-Ru(1)-C(2)-C(1)	104.11(14)
C(2)-Ru(1)-P(1)-C(23)	139.19(10)	C(5)-Ru(1)-C(2)-C(1)	66.86(13)
C(5)-Ru(1)-P(1)-C(23)	-157.14(18)	C(6)-Ru(1)-C(2)-C(1)	30.13(12)
C(6)-Ru(1)-P(1)-C(23)	97.41(15)	C(3)-Ru(1)-C(2)-C(1)	132.99(18)
C(3)-Ru(1)-P(1)-C(23)	176.32(10)	P(1)-Ru(1)-C(2)-C(1)	-130.82(12)
O(2)-Ru(1)-O(1)-C(29)	-5.96(11)	O(1)-Ru(1)-C(2)-C(3)	-167.25(11)
C(1)-Ru(1)-O(1)-C(29)	150.08(12)	O(2)-Ru(1)-C(2)-C(3)	2.7(3)
C(4)-Ru(1)-O(1)-C(29)	62.04(15)	C(1)-Ru(1)-C(2)-C(3)	-132.99(18)
C(2)-Ru(1)-O(1)-C(29)	170.53(12)	C(4)-Ru(1)-C(2)-C(3)	-28.88(12)
C(5)-Ru(1)-O(1)-C(29)	80.82(12)	C(5)-Ru(1)-C(2)-C(3)	-66.13(13)
C(6)-Ru(1)-O(1)-C(29)	114.12(12)	C(6)-Ru(1)-C(2)-C(3)	-102.86(14)
C(3)-Ru(1)-O(1)-C(29)	128.5(3)	P(1)-Ru(1)-C(2)-C(3)	96.19(12)
P(1)-Ru(1)-O(1)-C(29)	-92.73(11)	C(1)-C(2)-C(3)-C(4)	-3.0(3)
O(1)-Ru(1)-O(2)-C(29)	5.94(10)	Ru(1)-C(2)-C(3)-C(4)	51.07(17)
C(1)-Ru(1)-O(2)-C(29)	-54.89(19)	C(1)-C(2)-C(3)-C(7)	176.01(19)
C(4)-Ru(1)-O(2)-C(29)	-137.09(12)	Ru(1)-C(2)-C(3)-C(7)	-129.93(19)
C(2)-Ru(1)-O(2)-C(29)	-166.1(2)	C(1)-C(2)-C(3)-Ru(1)-	54.06(17)
C(5)-Ru(1)-O(2)-C(29)	-99.60(12)	O(1)-Ru(1)-C(3)-C(4)	-80.4(4)
C(6)-Ru(1)-O(2)-C(29)	-68.69(13)	O(2)-Ru(1)-C(3)-C(4)	48.92(15)
C(3)-Ru(1)-O(2)-C(29)	-164.12(11)	C(1)-Ru(1)-C(3)-C(4)	-103.36(14)
P(1)-Ru(1)-O(2)-C(29)	99.66(11)	C(2)-Ru(1)-C(3)-C(4)	-132.11(19)

C(5)-Ru(1)-C(3)-C(4)	-29.66(13)	C(4)-Ru(1)-C(5)-C(6)	-133.40(19)
C(6)-Ru(1)-C(3)-C(4)	-65.81(13)	C(2)-Ru(1)-C(5)-C(6)	-67.34(13)
P(1)-Ru(1)-C(3)-C(4)	141.04(12)	C(3)-Ru(1)-C(5)-C(6)	-104.29(14)
O(1)-Ru(1)-C(3)-C(2)	51.7(4)	P(1)-Ru(1)-C(5)-C(6)	-133.22(16)
O(2)-Ru(1)-C(3)-C(2)	-178.97(11)	O(1)-Ru(1)-C(5)-C(4)	-160.09(11)
C(1)-Ru(1)-C(3)-C(2)	28.75(12)	O(2)-Ru(1)-C(5)-C(4)-	96.94(12)
C(4)-Ru(1)-C(3)-C(2)	132.11(19)	C(1)-Ru(1)-C(5)-C(4)	103.40(14)
C(5)-Ru(1)-C(3)-C(2)	102.45(14)	C(2)-Ru(1)-C(5)-C(4)	66.06(13)
C(6)-Ru(1)-C(3)-C(2)	66.31(13)	C(6)-Ru(1)-C(5)-C(4)	133.40(19)
P(1)-Ru(1)-C(3)-C(2)	-86.85(12)	C(3)-Ru(1)-C(5)-C(4)	29.12(12)
O(1)-Ru(1)-C(3)-C(7)	165.8(3)	P(1)-Ru(1)-C(5)-C(4)	0.2(2)
O(2)-Ru(1)-C(3)-C(7)	-64.9(2)	C(4)-C(5)-C(6)-C(1)	0.1(3)
C(1)-Ru(1)-C(3)-C(7)	142.8(2)	Ru(1)-C(5)-C(6)-C(1)	52.58(16)
C(4)-Ru(1)-C(3)-C(7)	-113.8(3)	C(4)-C(5)-C(6)-C(8)	-175.5(2)
C(2)-Ru(1)-C(3)-C(7)	114.1(3)	Ru(1)-C(5)-C(6)-C(8)	-123.0(2)
C(5)-Ru(1)-C(3)-C(7)	-143.5(2)	C(4)-C(5)-C(6)-Ru(1)	-52.51(17)
C(6)-Ru(1)-C(3)-C(7)	-179.6(2)	C(2)-C(1)-C(6)-C(5)	2.9(3)
P(1)-Ru(1)-C(3)-C(7)	27.2(2)	Ru(1)-C(1)-C(6)-C(5)	-53.65(17)
C(2)-C(3)-C(4)-C(5)	6.0(3)	C(2)-C(1)-C(6)-C(8)	178.70(19)
C(7)-C(3)-C(4)-C(5)-	172.97(19)	Ru(1)-C(1)-C(6)-C(8)	122.16(18)
Ru(1)-C(3)-C(4)-C(5)	57.15(18)	C(2)-C(1)-C(6)-Ru(1)	56.54(17)
C(2)-C(3)-C(4)-Ru(1)	-51.11(16)	O(1)-Ru(1)-C(6)-C(5)	-118.05(13)
C(7)-C(3)-C(4)-Ru(1)	129.88(19)	O(2)-Ru(1)-C(6)-C(5)	-58.83(14)
O(1)-Ru(1)-C(4)-C(3)	162.25(11)	C(1)-Ru(1)-C(6)-C(5)	131.36(19)
O(2)-Ru(1)-C(4)-C(3)	-141.29(12)	C(4)-Ru(1)-C(6)-C(5)	28.60(13)
C(1)-Ru(1)-C(4)-C(3)	65.99(13)	C(2)-Ru(1)-C(6)-C(5)	101.57(14)
C(2)-Ru(1)-C(4)-C(3)	29.21(13)	C(3)-Ru(1)-C(6)-C(5)	64.82(13)
C(5)-Ru(1)-C(4)-C(3)	131.60(19)	P(1)-Ru(1)-C(6)-C(5)	147.66(12)
C(6)-Ru(1)-C(4)-C(3)	103.46(14)	O(1)-Ru(1)-C(6)-C(1)	110.59(13)
P(1)-Ru(1)-C(4)-C(3)	-48.33(14)	O(2)-Ru(1)-C(6)-C(1)	169.81(11)
O(1)-Ru(1)-C(4)-C(5)	30.65(17)	C(4)-Ru(1)-C(6)-C(1)	-102.77(14)
O(2)-Ru(1)-C(4)-C(5)	87.12(12)	C(2)-Ru(1)-C(6)-C(1)	-29.79(12)
C(1)-Ru(1)-C(4)-C(5)	-65.60(13)	C(5)-Ru(1)-C(6)-C(1)	-131.36(19)
C(2)-Ru(1)-C(4)-C(5)	-102.39(14)	C(3)-Ru(1)-C(6)-C(1)	-66.55(13)
C(6)-Ru(1)-C(4)-C(5)	-28.13(12)	P(1)-Ru(1)-C(6)-C(1)	16.3(2)
C(3)-Ru(1)-C(4)-C(5)	-131.60(19)	O(1)-Ru(1)-C(6)-C(8)	0.25(19)
P(1)-Ru(1)-C(4)-C(5)	-179.93(10)	O(2)-Ru(1)-C(6)-C(8)	59.5(2)
C(3)-C(4)-C(5)-C(6)	-4.7(3)	C(1)-Ru(1)-C(6)-C(8)	-110.3(2)
Ru(1)-C(4)-C(5)-C(6)	53.35(17)	C(4)-Ru(1)-C(6)-C(8)	146.9(2)
C(3)-C(4)-C(5)-Ru(1)	-58.03(18)	C(2)-Ru(1)-C(6)-C(8)	-140.1(2)
O(1)-Ru(1)-C(5)-C(6)	66.51(13)	C(5)-Ru(1)-C(6)-C(8)	118.3(2)
O(2)-Ru(1)-C(5)-C(6)	129.65(12)	C(3)-Ru(1)-C(6)-C(8)	-176.9(2)
C(1)-Ru(1)-C(5)-C(6)	-30.01(13)	P(1)-Ru(1)-C(6)-C(8)	-94.0(2)

C(5)-C(6)-C(8)-C(10)	13.6(3)	C(22)-C(17)-C(18)-C(19)	0.4(3)
C(1)-C(6)-C(8)-C(10)	-162.0(2)	P(1)-C(17)-C(18)-C(19)	179.65(16)
Ru(1)-C(6)-C(8)-C(10)	-77.7(2)	C(17)-C(18)-C(19)-C(20)	0.4(3)
C(5)-C(6)-C(8)-C(9)	-109.9(3)	C(18)-C(19)-C(20)-C(21)	-0.4(3)
C(1)-C(6)-C(8)-C(9)	74.5(3)	C(19)-C(20)-C(21)-C(22)	-0.4(3)
Ru(1)-C(6)-C(8)-C(9)	158.9(2)	C(20)-C(21)-C(22)-C(17)	1.2(3)
C(17)-P(1)-C(11)-C(16)	16.0(2)	C(18)-C(17)-C(22)-C(21)	-1.2(3)
C(23)-P(1)-C(11)-C(16)	120.86(19)	P(1)-C(17)-C(22)-C(21)	179.52(16)
Ru(1)-P(1)-C(11)-C(16)	-107.15(19)	C(11)-P(1)-C(23)-C(28)	179.15(17)
C(17)-P(1)-C(11)-C(12)	-167.28(16)	C(17)-P(1)-C(23)-C(28)	-72.34(18)
C(23)-P(1)-C(11)-C(12)	-62.39(18)	Ru(1)-P(1)-C(23)-C(28)	52.05(19)
Ru(1)-P(1)-C(11)-C(12)	69.60(17)	C(11)-P(1)-C(23)-C(24)	-5.6(2)
C(16)-C(11)-C(12)-C(13)	-2.3(3)	C(17)-P(1)-C(23)-C(24)	102.9(2)
P(1)-C(11)-C(12)-C(13)	-179.21(17)	Ru(1)-P(1)-C(23)-C(24)	-132.76(18)
C(11)-C(12)-C(13)-C(14)	2.7(3)	C(28)-C(23)-C(24)-C(25)	0.6(4)
C(12)-C(13)-C(14)-C(15)	-0.7(4)	P(1)-C(23)-C(24)-C(25)	-174.5(2)
C(13)-C(14)-C(15)-C(16)	-1.7(4)	C(23)-C(24)-C(25)-C(26)	0.2(4)
C(12)-C(11)-C(16)-C(15)	0.0(4)	C(24)-C(25)-C(26)-C(27)	-0.5(4)
P(1)-C(11)-C(16)-C(15)	176.7(2)	C(25)-C(26)-C(27)-C(28)	0.0(4)
C(14)-C(15)-C(16)-C(11)	2.0(4)	C(24)-C(23)-C(28)-C(27)	-1.2(3)
C(11)-P(1)-C(17)-C(22)	-123.35(17)	P(1)-C(23)-C(28)-C(27)	174.25(18)
C(23)-P(1)-C(17)-C(22)	130.04(17)	C(26)-C(27)-C(28)-C(23)	0.9(4)
Ru(1)-P(1)-C(17)-C(22)	0.07(18)	Ru(1)-O(1)-C(29)-O(3)	-170.37(19)
C(11)-P(1)-C(17)-C(18)	57.40(19)	Ru(1)-O(1)-C(29)-O(2)	9.13(16)
C(23)-P(1)-C(17)-C(18)	-49.21(19)	Ru(1)-O(2)-C(29)-O(3)	170.44(19)
Ru(1)-P(1)-C(17)-C(18)	-179.18(15)	Ru(1)-O(2)-C(29)-O(1)	-9.06(16)

Table A.7. Hydrogen bonds for C₂₉H₃₁O₄PRu (2.40) [Å and °].

D-H...A	d(D-H)	d(H...A)	d(D...A)	<(DHA)
O(1S)-H(1O)...O(3)#1	0.865(18)	1.959(19)	2.820(2)	173(3)
O(1S)-H(2O)...O(3)#2	0.856(18)	2.09(2)	2.921(3)	162(3)

Symmetry transformations used to generate equivalent atoms:

#1 $x-1, y+1, z$ #2 $-x+1, -y+1, -z+1$

A.2 Data for {N,N-1,3-bis[1-(2,6-diisopropylphenylimino)ethyl]-2-(κ^2 -butane)4,5,6-trihydropyrimidyl}iron chloride or dinitrogen (4.40) at 100 K

Figure A.2. ORTEP plot of 4.40 with thermal ellipsoids represented at the 50% probability level. Hydrogen atoms, solvent molecules, and counterion were excluded for clarity.

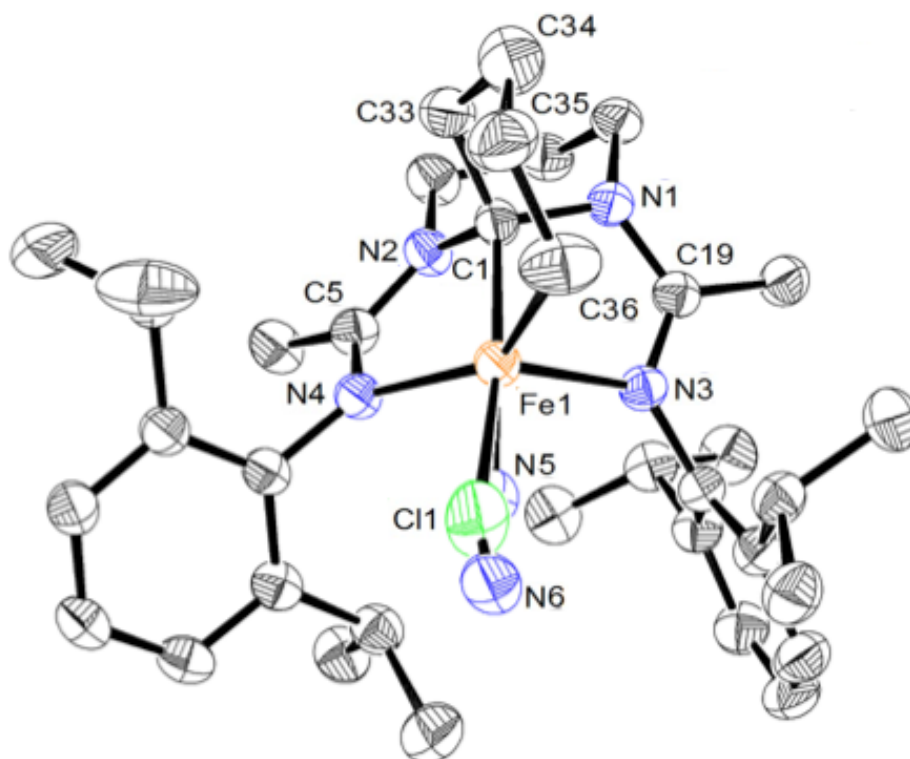


Table A.8. Crystal data and structure refinement for C₄₂H₆₉Cl_{10.25}FeN_{5.50}O_{1.50} (4.40).

	100 K
Identification code/CCDC	C42H69Cl10.25FeN5.50O1.50
Empirical formula	C42 H69 Cl10.25 Fe N5.50 O1.50
Formula weight	739.74
Temperature	100(2) K
Wavelength	1.54178 Å
Crystal system	Monoclinic
Space group	P 2(1)/n
Unit cell dimensions	a = 13.2430(12) Å α = 90° b = 16.6655(15) Å β = 91.366(3)° c = 19.0356(17) Å γ = 90°
Volume	4200.0(7) Å ³
Z	4
Density (calculated)	1.170 Mg/m ³
Absorption coefficient	3.313 mm ⁻¹
F(000)	1307
Crystal size	0.200 x 0.140 x 0.100 mm ³
Theta range for data collection	3.338 to 70.256°
Index ranges	-15 ≤ h ≤ 15, -19 ≤ k ≤ 19, 0 ≤ l ≤ 22
Reflections collected	14207
Independent reflections	7488 [R _{int} = 0.0352]
Completeness to θ = 32.15/66.36°	97.6 %
Absorption correction	Semi-empirical from equivalents
Max. and min. transmission	0.7532 and 0.4396
Refinement method	Full-matrix least-squares on F ²
Data / restraints / parameters	7488 / 26 / 472
Goodness-of-fit on F ²	1.064
Final R indices [I > 2σ(I)]	R ₁ = 0.0565, ωR ₂ = 0.1505
R indices (all data)	R ₁ = 0.0584, ωR ₂ = 0.1529
Extinction coefficient	na
Largest diff. peak and hole	0.799 and -0.589 e.Å ⁻³

Table A.9. Atomic coordinates ($\times 10^4$) and equivalent isotropic displacement parameters ($\text{\AA}^2 \times 10^3$) for $\text{C}_{36}\text{H}_{57}\text{ClFeN}_4\text{Si}$ (4.40). U(eq) is defined as one third of the trace of the orthogonalized U_{ij} tensor.

	x	y	z	U(eq)
Fe(1)	7240(1)	2084(1)	2390(1)	30(1)
N(1)	6033(2)	2527(1)	3516(1)	35(1)
N(2)	7437(2)	1694(1)	3837(1)	33(1)
N(3)	6128(2)	2926(1)	2381(1)	31(1)
N(4)	8415(2)	2429(1)	3100(1)	31(1)
C(1)	6623(2)	1800(2)	3307(1)	32(1)
C(2)	5665(2)	2553(2)	4235(1)	43(1)
C(3)	6517(2)	2370(2)	4763(1)	41(1)
C(4)	7096(2)	1613(2)	4563(1)	38(1)
C(5)	8315(2)	2087(1)	3713(1)	33(1)
C(6)	9133(2)	2062(2)	4272(2)	41(1)
C(7)	9259(2)	2942(2)	2972(1)	34(1)
C(8)	9340(2)	3687(2)	3319(1)	38(1)
C(9)	10102(2)	4209(2)	3118(2)	44(1)
C(10)	10766(2)	4014(2)	2600(2)	48(1)
C(11)	10699(2)	3269(2)	2283(2)	44(1)
C(12)	9959(2)	2720(2)	2464(1)	36(1)
C(13)	8652(2)	3937(2)	3911(1)	41(1)
C(14)	9265(3)	4162(2)	4577(2)	54(1)
C(15)	7951(2)	4627(2)	3700(2)	51(1)
C(16)	9950(2)	1876(2)	2161(1)	36(1)
C(17)	10533(2)	1314(2)	2663(2)	46(1)
C(18)	10371(2)	1814(2)	1421(2)	45(1)
C(19)	5727(2)	3027(2)	3001(1)	34(1)
C(20)	4979(2)	3672(2)	3156(2)	45(1)
C(21)	5706(2)	3320(2)	1773(1)	32(1)
C(22)	4850(2)	2983(2)	1429(1)	35(1)
C(23)	4464(2)	3358(2)	830(1)	38(1)
C(24)	4903(2)	4034(2)	559(1)	40(1)
C(25)	5755(2)	4349(2)	887(1)	39(1)
C(26)	6174(2)	4002(2)	1495(1)	35(1)
C(27)	4368(2)	2213(2)	1683(2)	42(1)
C(28)	4549(4)	1539(2)	1170(2)	77(1)
C(29)	3242(3)	2333(3)	1813(3)	85(1)
C(30)	7077(2)	4404(2)	1851(1)	40(1)
C(31)	6749(2)	5216(2)	2158(2)	49(1)
C(32)	7968(2)	4527(2)	1367(2)	55(1)
C(33)	5906(2)	1080(2)	3295(2)	42(1)

C(34)	6369(3)	290(2)	3107(2)	58(1)
C(35)	6708(3)	276(2)	2368(2)	57(1)
C(36)	7519(3)	882(2)	2221(2)	59(1)
N(5)	7744(4)	2353(3)	1562(2)	35(1)
N(6)	8088(3)	2477(3)	1024(2)	48(1)
Cl(1)	7748(5)	2271(5)	1271(3)	64(2)
O(1S)	7013(2)	8447(1)	676(1)	51(1)
C(1S)	7353(3)	7094(2)	992(2)	64(1)
C(2S)	7799(3)	7878(2)	762(2)	60(1)
C(3S)	7387(3)	9222(2)	506(2)	68(1)
C(4S)	6517(3)	9786(2)	414(2)	63(1)
O(2S)	-309(5)	4990(6)	-19(5)	96(2)
C(6S)	1017(15)	4158(12)	565(10)	183(8)
C(7S)	579(7)	4688(6)	76(6)	84(3)
C(8S)	-703(7)	5395(6)	-609(5)	82(2)
C(9S)	-1684(8)	5677(8)	-615(6)	108(3)

Table A.10. Bond lengths [Å] and angles [°] for C₄₂H₆₉Cl_{10.25}FeN_{5.50}O_{1.50} (4.40).

Fe(1)-N(5)	1.784(5)	C(13)-C(15)	1.527(4)
Fe(1)-C(1)	2.000(2)	C(13)-C(14)	1.535(4)
Fe(1)-N(3)	2.034(2)	C(13)-H(13)	1.0000
Fe(1)-C(36)	2.063(3)	C(14)-H(14A)	0.9800
Fe(1)-N(4)	2.116(2)	C(14)-H(14B)	0.9800
Fe(1)-Cl(1)	2.271(5)	C(14)-H(14C)	0.9800
N(1)-C(19)	1.340(3)	C(15)-H(15A)	0.9800
N(1)-C(2)	1.465(3)	C(15)-H(15B)	0.9800
N(1)-C(1)	1.501(3)	C(15)-H(15C)	0.9800
N(2)-C(5)	1.361(3)	C(16)-C(18)	1.531(4)
N(2)-C(1)	1.470(3)	C(16)-C(17)	1.533(4)
N(2)-C(4)	1.471(3)	C(16)-H(16)	1.0000
N(3)-C(19)	1.316(3)	C(17)-H(17A)	0.9800
N(3)-C(21)	1.432(3)	C(17)-H(17B)	0.9800
N(4)-C(5)	1.307(3)	C(17)-H(17C)	0.9800
N(4)-C(7)	1.433(3)	C(18)-H(18A)	0.9800
C(1)-C(33)	1.530(4)	C(18)-H(18B)	0.9800
C(2)-C(3)	1.524(4)	C(18)-H(18C)	0.9800
C(2)-H(2A)	0.9900	C(19)-C(20)	1.497(4)
C(2)-H(2B)	0.9900	C(20)-H(20A)	0.9800
C(3)-C(4)	1.529(4)	C(20)-H(20B)	0.9800
C(3)-H(3A)	0.9900	C(20)-H(20C)	0.9800
C(3)-H(3B)	0.9900	C(21)-C(26)	1.405(4)
C(4)-H(4A)	0.9900	C(21)-C(22)	1.412(4)
C(4)-H(4B)	0.9900	C(22)-C(23)	1.387(4)
C(5)-C(6)	1.502(4)	C(22)-C(27)	1.517(4)
C(6)-H(6A)	0.9800	C(23)-C(24)	1.375(4)
C(6)-H(6B)	0.9800	C(23)-H(23)	0.9500
C(6)-H(6C)	0.9800	C(24)-C(25)	1.379(4)
C(7)-C(12)	1.405(4)	C(24)-H(24)	0.9500
C(7)-C(8)	1.409(4)	C(25)-C(26)	1.396(4)
C(8)-C(9)	1.393(4)	C(25)-H(25)	0.9500
C(8)-C(13)	1.525(4)	C(26)-C(30)	1.517(4)
C(9)-C(10)	1.376(4)	C(27)-C(28)	1.512(5)
C(9)-H(9)	0.9500	C(27)-C(29)	1.530(4)
C(10)-C(11)	1.382(4)	C(27)-H(27)	1.0000
C(10)-H(10)	0.9500	C(28)-H(28A)	0.9800
C(11)-C(12)	1.390(4)	C(28)-H(28B)	0.9800
C(11)-H(11)	0.9500	C(28)-H(28C)	0.9800
C(12)-C(16)	1.519(4)	C(29)-H(29A)	0.9800

C(29)-H(29B)	0.9800	C(7S)-H(7S1)	0.9900
C(29)-H(29C)	0.9800	C(7S)-H(7S2)	0.9900
C(30)-C(32)	1.528(4)	C(8S)-C(9S)	1.381(12)
C(30)-C(31)	1.540(4)	C(8S)-H(8S1)	0.9900
C(30)-H(30)	1.0000	C(8S)-H(8S2)	0.9900
C(31)-H(31A)	0.9800	C(9S)-H(9S1)	0.9800
C(31)-H(31B)	0.9800	C(9S)-H(9S2)	0.9800
C(31)-H(31C)	0.9800	C(9S)-H(9S3)	0.9800
C(32)-H(32A)	0.9800		
C(32)-H(32B)	0.9800	N(5)-Fe(1)-C(1)	177.77(17)
C(32)-H(32C)	0.9800	N(5)-Fe(1)-N(3)	96.00(15)
C(33)-C(34)	1.500(4)	C(1)-Fe(1)-N(3)	81.96(9)
C(33)-H(33A)	0.9900	N(5)-Fe(1)-C(36)	91.97(16)
C(33)-H(33B)	0.9900	C(1)-Fe(1)-C(36)	89.16(12)
C(34)-C(35)	1.488(5)	N(3)-Fe(1)-C(36)	143.20(13)
C(34)-H(34A)	0.9900	N(5)-Fe(1)-N(4)	102.15(17)
C(34)-H(34B)	0.9900	C(1)-Fe(1)-N(4)	79.44(9)
C(35)-C(36)	1.505(4)	N(3)-Fe(1)-N(4)	109.82(8)
C(35)-H(35A)	0.9900	C(36)-Fe(1)-N(4)	103.42(13)
C(35)-H(35B)	0.9900	C(1)-Fe(1)-Cl(1)	170.7(2)
C(36)-H(36A)	0.9900	N(3)-Fe(1)-Cl(1)	97.33(16)
C(36)-H(36B)	0.9900	C(36)-Fe(1)-Cl(1)	85.9(2)
N(5)-N(6)	1.150(6)	N(4)-Fe(1)-Cl(1)	109.4(2)
O(1S)-C(2S)	1.415(4)	C(19)-N(1)-C(2)	124.3(2)
O(1S)-C(3S)	1.424(4)	C(19)-N(1)-C(1)	117.2(2)
C(1S)-C(2S)	1.502(5)	C(2)-N(1)-C(1)	117.3(2)
C(1S)-H(1S1)	0.9800	C(5)-N(2)-C(1)	116.0(2)
C(1S)-H(1S2)	0.9800	C(5)-N(2)-C(4)	119.4(2)
C(1S)-H(1S3)	0.9800	C(1)-N(2)-C(4)	114.83(19)
C(2S)-H(2S1)	0.9900	C(19)-N(3)-C(21)	120.6(2)
C(2S)-H(2S2)	0.9900	C(19)-N(3)-Fe(1)	112.77(17)
C(3S)-C(4S)	1.494(5)	C(21)-N(3)-Fe(1)	126.22(16)
C(3S)-H(3S1)	0.9900	C(5)-N(4)-C(7)	120.5(2)
C(3S)-H(3S2)	0.9900	C(5)-N(4)-Fe(1)	111.26(17)
C(4S)-H(4S1)	0.9800	C(7)-N(4)-Fe(1)	128.20(16)
C(4S)-H(4S2)	0.9800	N(2)-C(1)-N(1)	107.05(19)
C(4S)-H(4S3)	0.9800	N(2)-C(1)-C(33)	111.1(2)
O(2S)-C(7S)	1.288(11)	N(1)-C(1)-C(33)	108.1(2)
O(2S)-C(8S)	1.400(11)	N(2)-C(1)-Fe(1)	108.64(15)
C(6S)-C(7S)	1.399(15)	N(1)-C(1)-Fe(1)	105.46(15)
C(6S)-H(6S1)	0.9800	C(33)-C(1)-Fe(1)	116.01(18)
C(6S)-H(6S2)	0.9800	N(1)-C(2)-C(3)	110.7(2)
C(6S)-H(6S3)	0.9800	N(1)-C(2)-H(2A)	109.5

C(3)-C(2)-H(2A)	109.5	C(8)-C(13)-C(15)	112.4(2)
N(1)-C(2)-H(2B)	109.5	C(8)-C(13)-C(14)	111.3(2)
C(3)-C(2)-H(2B)	109.5	C(15)-C(13)-C(14)	109.8(2)
H(2A)-C(2)-H(2B)	108.1	C(8)-C(13)-H(13)	107.7
C(2)-C(3)-C(4)	111.7(2)	C(15)-C(13)-H(13)	107.7
C(2)-C(3)-H(3A)	109.3	C(14)-C(13)-H(13)	107.7
C(4)-C(3)-H(3A)	109.3	C(13)-C(14)-H(14A)	109.5
C(2)-C(3)-H(3B)	109.3	C(13)-C(14)-H(14B)	109.5
C(4)-C(3)-H(3B)	109.3	H(14A)-C(14)-H(14B)	109.5
H(3A)-C(3)-H(3B)	107.9	C(13)-C(14)-H(14C)	109.5
N(2)-C(4)-C(3)	109.0(2)	H(14A)-C(14)-H(14C)	109.5
N(2)-C(4)-H(4A)	109.9	H(14B)-C(14)-H(14C)	109.5
C(3)-C(4)-H(4A)	109.9	C(13)-C(15)-H(15A)	109.5
N(2)-C(4)-H(4B)	109.9	C(13)-C(15)-H(15B)	109.5
C(3)-C(4)-H(4B)	109.9	H(15A)-C(15)-H(15B)	109.5
H(4A)-C(4)-H(4B)	108.3	C(13)-C(15)-H(15C)	109.5
N(4)-C(5)-N(2)	118.0(2)	H(15A)-C(15)-H(15C)	109.5
N(4)-C(5)-C(6)	123.9(2)	H(15B)-C(15)-H(15C)	109.5
N(2)-C(5)-C(6)	117.9(2)	C(12)-C(16)-C(18)	114.3(2)
C(5)-C(6)-H(6A)	109.5	C(12)-C(16)-C(17)	109.3(2)
C(5)-C(6)-H(6B)	109.5	C(18)-C(16)-C(17)	110.1(2)
H(6A)-C(6)-H(6B)	109.5	C(12)-C(16)-H(16)	107.6
C(5)-C(6)-H(6C)	109.5	C(18)-C(16)-H(16)	107.6
H(6A)-C(6)-H(6C)	109.5	C(17)-C(16)-H(16)	107.6
H(6B)-C(6)-H(6C)	109.5	C(16)-C(17)-H(17A)	109.5
C(12)-C(7)-C(8)	120.6(2)	C(16)-C(17)-H(17B)	109.5
C(12)-C(7)-N(4)	119.4(2)	H(17A)-C(17)-H(17B)	109.5
C(8)-C(7)-N(4)	119.8(2)	C(16)-C(17)-H(17C)	109.5
C(9)-C(8)-C(7)	118.0(2)	H(17A)-C(17)-H(17C)	109.5
C(9)-C(8)-C(13)	118.8(2)	H(17B)-C(17)-H(17C)	109.5
C(7)-C(8)-C(13)	123.2(2)	C(16)-C(18)-H(18A)	109.5
C(10)-C(9)-C(8)	121.9(3)	C(16)-C(18)-H(18B)	109.5
C(10)-C(9)-H(9)	119.0	H(18A)-C(18)-H(18B)	109.5
C(8)-C(9)-H(9)	119.0	C(16)-C(18)-H(18C)	109.5
C(9)-C(10)-C(11)	119.3(3)	H(18A)-C(18)-H(18C)	109.5
C(9)-C(10)-H(10)	120.3	H(18B)-C(18)-H(18C)	109.5
C(11)-C(10)-H(10)	120.3	N(3)-C(19)-N(1)	117.1(2)
C(10)-C(11)-C(12)	121.4(3)	N(3)-C(19)-C(20)	123.4(2)
C(10)-C(11)-H(11)	119.3	N(1)-C(19)-C(20)	119.5(2)
C(12)-C(11)-H(11)	119.3	C(19)-C(20)-H(20A)	109.5
C(11)-C(12)-C(7)	118.6(3)	C(19)-C(20)-H(20B)	109.5
C(11)-C(12)-C(16)	120.9(2)	H(20A)-C(20)-H(20B)	109.5
C(7)-C(12)-C(16)	120.4(2)	C(19)-C(20)-H(20C)	109.5

H(20A)-C(20)-H(20C)	109.5	C(31)-C(30)-H(30)	108.0
H(20B)-C(20)-H(20C)	109.5	C(30)-C(31)-H(31A)	109.5
C(26)-C(21)-C(22)	120.2(2)	C(30)-C(31)-H(31B)	109.5
C(26)-C(21)-N(3)	120.6(2)	H(31A)-C(31)-H(31B)	109.5
C(22)-C(21)-N(3)	119.1(2)	C(30)-C(31)-H(31C)	109.5
C(23)-C(22)-C(21)	118.6(2)	H(31A)-C(31)-H(31C)	109.5
C(23)-C(22)-C(27)	119.5(2)	H(31B)-C(31)-H(31C)	109.5
C(21)-C(22)-C(27)	121.8(2)	C(30)-C(32)-H(32A)	109.5
C(24)-C(23)-C(22)	121.7(3)	C(30)-C(32)-H(32B)	109.5
C(24)-C(23)-H(23)	119.1	H(32A)-C(32)-H(32B)	109.5
C(22)-C(23)-H(23)	119.1	C(30)-C(32)-H(32C)	109.5
C(23)-C(24)-C(25)	119.5(2)	H(32A)-C(32)-H(32C)	109.5
C(23)-C(24)-H(24)	120.3	H(32B)-C(32)-H(32C)	109.5
C(25)-C(24)-H(24)	120.3	C(34)-C(33)-C(1)	115.8(2)
C(24)-C(25)-C(26)	121.4(2)	C(34)-C(33)-H(33A)	108.3
C(24)-C(25)-H(25)	119.3	C(1)-C(33)-H(33A)	108.3
C(26)-C(25)-H(25)	119.3	C(34)-C(33)-H(33B)	108.3
C(25)-C(26)-C(21)	118.6(2)	C(1)-C(33)-H(33B)	108.3
C(25)-C(26)-C(30)	118.8(2)	H(33A)-C(33)-H(33B)	107.4
C(21)-C(26)-C(30)	122.6(2)	C(35)-C(34)-C(33)	111.9(3)
C(28)-C(27)-C(22)	110.4(2)	C(35)-C(34)-H(34A)	109.2
C(28)-C(27)-C(29)	111.8(3)	C(33)-C(34)-H(34A)	109.2
C(22)-C(27)-C(29)	111.1(3)	C(35)-C(34)-H(34B)	109.2
C(28)-C(27)-H(27)	107.8	C(33)-C(34)-H(34B)	109.2
C(22)-C(27)-H(27)	107.8	H(34A)-C(34)-H(34B)	107.9
C(29)-C(27)-H(27)	107.8	C(34)-C(35)-C(36)	113.4(3)
C(27)-C(28)-H(28A)	109.5	C(34)-C(35)-H(35A)	108.9
C(27)-C(28)-H(28B)	109.5	C(36)-C(35)-H(35A)	108.9
H(28A)-C(28)-H(28B)	109.5	C(34)-C(35)-H(35B)	108.9
C(27)-C(28)-H(28C)	109.5	C(36)-C(35)-H(35B)	108.9
H(28A)-C(28)-H(28C)	109.5	H(35A)-C(35)-H(35B)	107.7
H(28B)-C(28)-H(28C)	109.5	C(35)-C(36)-Fe(1)	119.4(2)
C(27)-C(29)-H(29A)	109.5	C(35)-C(36)-H(36A)	107.5
C(27)-C(29)-H(29B)	109.5	Fe(1)-C(36)-H(36A)	107.5
H(29A)-C(29)-H(29B)	109.5	C(35)-C(36)-H(36B)	107.5
C(27)-C(29)-H(29C)	109.5	Fe(1)-C(36)-H(36B)	107.5
H(29A)-C(29)-H(29C)	109.5	H(36A)-C(36)-H(36B)	107.0
H(29B)-C(29)-H(29C)	109.5	N(6)-N(5)-Fe(1)	175.6(4)
C(26)-C(30)-C(32)	113.6(2)	C(2S)-O(1S)-C(3S)	112.1(3)
C(26)-C(30)-C(31)	109.3(2)	C(2S)-C(1S)-H(1S1)	109.5
C(32)-C(30)-C(31)	109.8(2)	C(2S)-C(1S)-H(1S2)	109.5
C(26)-C(30)-H(30)	108.0	H(1S1)-C(1S)-H(1S2)	109.5
C(32)-C(30)-H(30)	108.0	C(2S)-C(1S)-H(1S3)	109.5

H(1S1)-C(1S)-H(1S3)	109.5	H(6S1)-C(6S)-H(6S2)	109.5
H(1S2)-C(1S)-H(1S3)	109.5	C(7S)-C(6S)-H(6S3)	109.5
O(1S)-C(2S)-C(1S)	108.9(3)	H(6S1)-C(6S)-H(6S3)	109.5
O(1S)-C(2S)-H(2S1)	109.9	H(6S2)-C(6S)-H(6S3)	109.5
C(1S)-C(2S)-H(2S1)	109.9	O(2S)-C(7S)-C(6S)	134.6(12)
O(1S)-C(2S)-H(2S2)	109.9	O(2S)-C(7S)-H(7S1)	103.5
C(1S)-C(2S)-H(2S2)	109.9	C(6S)-C(7S)-H(7S1)	103.5
H(2S1)-C(2S)-H(2S2)	108.3	O(2S)-C(7S)-H(7S2)	103.5
O(1S)-C(3S)-C(4S)	109.0(3)	C(6S)-C(7S)-H(7S2)	103.5
O(1S)-C(3S)-H(3S1)	109.9	H(7S1)-C(7S)-H(7S2)	105.3
C(4S)-C(3S)-H(3S1)	109.9	C(9S)-C(8S)-O(2S)	120.2(9)
O(1S)-C(3S)-H(3S2)	109.9	C(9S)-C(8S)-H(8S1)	107.3
C(4S)-C(3S)-H(3S2)	109.9	O(2S)-C(8S)-H(8S1)	107.3
H(3S1)-C(3S)-H(3S2)	108.3	C(9S)-C(8S)-H(8S2)	107.3
C(3S)-C(4S)-H(4S1)	109.5	O(2S)-C(8S)-H(8S2)	107.3
C(3S)-C(4S)-H(4S2)	109.5	H(8S1)-C(8S)-H(8S2)	106.9
H(4S1)-C(4S)-H(4S2)	109.5	C(8S)-C(9S)-H(9S1)	109.5
C(3S)-C(4S)-H(4S3)	109.5	C(8S)-C(9S)-H(9S2)	109.5
H(4S1)-C(4S)-H(4S3)	109.5	H(9S1)-C(9S)-H(9S2)	109.5
H(4S2)-C(4S)-H(4S3)	109.5	C(8S)-C(9S)-H(9S3)	109.5
C(7S)-O(2S)-C(8S)	128.5(7)	H(9S1)-C(9S)-H(9S3)	109.5
C(7S)-C(6S)-H(6S1)	109.5	H(9S2)-C(9S)-H(9S3)	109.5
C(7S)-C(6S)-H(6S2)	109.5		

Table A.11. Anisotropic displacement parameters ($\text{\AA}^2 \times 10^3$) for $\text{C}_{42}\text{H}_{69}\text{Cl}_{10.25}\text{FeN}_{5.50}\text{O}_{1.50}$ (4.40). The anisotropic displacement factor exponent takes the form: $-2p^2[h^2 a^* U^{11} + \dots + 2hka^* b^* U^{12}]$.

	U ¹¹	U ²²	U ³³	U ²³	U ¹³	U ¹²
Fe(1)	30(1)	31(1)	29(1)	1(1)	3(1)	2(1)
N(1)	37(1)	37(1)	30(1)	2(1)	4(1)	6(1)
N(2)	32(1)	38(1)	30(1)	5(1)	2(1)	-1(1)
N(3)	32(1)	32(1)	31(1)	1(1)	4(1)	3(1)
N(4)	32(1)	28(1)	32(1)	-1(1)	3(1)	-1(1)
C(1)	29(1)	34(1)	32(1)	2(1)	0(1)	3(1)
C(2)	48(2)	50(2)	32(1)	3(1)	11(1)	9(1)
C(3)	49(2)	46(2)	29(1)	2(1)	5(1)	-2(1)
C(4)	42(1)	43(2)	31(1)	5(1)	3(1)	-2(1)
C(5)	36(1)	31(1)	33(1)	-1(1)	3(1)	1(1)
C(6)	38(2)	50(2)	36(1)	3(1)	-2(1)	-4(1)
C(7)	32(1)	33(1)	36(1)	2(1)	0(1)	-2(1)
C(8)	40(1)	35(1)	38(1)	-3(1)	0(1)	-3(1)
C(9)	46(2)	35(1)	51(2)	-4(1)	-1(1)	-6(1)
C(10)	42(2)	42(2)	59(2)	4(1)	4(1)	-11(1)
C(11)	38(1)	45(2)	50(2)	2(1)	10(1)	-3(1)
C(12)	33(1)	35(1)	40(1)	1(1)	1(1)	-1(1)
C(13)	46(2)	38(1)	39(1)	-7(1)	2(1)	-4(1)
C(14)	63(2)	58(2)	41(2)	-11(1)	-5(1)	-3(2)
C(15)	58(2)	48(2)	47(2)	-10(1)	3(1)	7(1)
C(16)	33(1)	37(1)	39(1)	-2(1)	5(1)	1(1)
C(17)	48(2)	41(2)	48(2)	-3(1)	-2(1)	8(1)
C(18)	39(2)	51(2)	45(2)	-3(1)	7(1)	2(1)
C(19)	35(1)	34(1)	34(1)	-1(1)	4(1)	0(1)
C(20)	50(2)	46(2)	40(2)	2(1)	9(1)	14(1)
C(21)	34(1)	31(1)	30(1)	1(1)	5(1)	6(1)
C(22)	34(1)	38(1)	34(1)	2(1)	4(1)	4(1)
C(23)	37(1)	41(2)	36(1)	1(1)	0(1)	3(1)
C(24)	48(2)	38(1)	35(1)	6(1)	-1(1)	8(1)
C(25)	50(2)	31(1)	38(1)	4(1)	4(1)	2(1)
C(26)	40(1)	29(1)	36(1)	-2(1)	4(1)	5(1)
C(27)	34(1)	48(2)	42(2)	13(1)	-2(1)	-4(1)
C(28)	124(4)	41(2)	67(2)	1(2)	19(2)	-26(2)
C(29)	40(2)	99(3)	117(4)	54(3)	12(2)	-7(2)
C(30)	46(2)	32(1)	41(1)	0(1)	-1(1)	-1(1)
C(31)	60(2)	32(1)	54(2)	-4(1)	-7(1)	-2(1)
C(32)	51(2)	56(2)	58(2)	-3(2)	4(1)	-9(2)
C(33)	46(2)	40(2)	39(1)	4(1)	-1(1)	-6(1)

C(34)	61(2)	48(2)	65(2)	-5(2)	-9(2)	-2(2)
C(35)	50(2)	43(2)	78(2)	2(2)	9(2)	-3(1)
C(36)	76(2)	36(2)	67(2)	-8(2)	17(2)	-8(2)
N(5)	36(2)	32(2)	38(3)	-5(2)	9(2)	11(1)
N(6)	46(2)	68(3)	31(2)	7(2)	14(2)	16(2)
Cl(1)	48(2)	111(4)	33(3)	0(3)	17(2)	25(2)
O(1S)	50(1)	47(1)	55(1)	10(1)	7(1)	-1(1)
C(1S)	69(2)	54(2)	69(2)	10(2)	-11(2)	2(2)
C(2S)	55(2)	57(2)	69(2)	6(2)	2(2)	3(2)
C(3S)	68(2)	58(2)	79(2)	18(2)	25(2)	-3(2)
C(4S)	80(2)	50(2)	59(2)	6(2)	23(2)	5(2)

Table A.12. Hydrogen coordinates ($\times 10^4$) and isotropic displacement parameters ($\text{\AA}^2 \times 10^3$) for $\text{C}_{42}\text{H}_{69}\text{Cl}_{10.25}\text{FeN}_{5.50}\text{O}_{1.50}$ (4.40).

	x	y	z	U(eq)
H(2A)	5116	2155	4287	52
H(2B)	5385	3092	4332	52
H(3A)	6232	2298	5235	50
H(3B)	6989	2830	4786	50
H(4A)	7685	1539	4887	46
H(4B)	6652	1137	4602	46
H(6A)	9759	2281	4085	62
H(6B)	9246	1505	4421	62
H(6C)	8929	2383	4676	62
H(9)	10165	4715	3345	53
H(10)	11265	4388	2461	57
H(11)	11169	3129	1934	53
H(13)	8221	3465	4028	49
H(14A)	9729	3724	4701	82
H(14B)	8805	4255	4964	82
H(14C)	9653	4652	4490	82
H(15A)	8355	5087	3551	77
H(15B)	7546	4782	4103	77
H(15C)	7503	4456	3312	77
H(16)	9232	1690	2137	44
H(17A)	11237	1491	2708	68
H(17B)	10510	766	2477	68
H(17C)	10224	1325	3126	68
H(18A)	10045	2217	1117	67
H(18B)	10236	1277	1232	67
H(18C)	11101	1910	1441	67
H(20A)	5292	4068	3474	68
H(20B)	4390	3435	3378	68
H(20C)	4767	3936	2717	68
H(23)	3880	3141	601	46
H(24)	4623	4283	150	48
H(25)	6064	4812	694	47
H(27)	4703	2065	2141	50
H(28A)	4229	1670	715	116
H(28B)	4257	1041	1351	116
H(28C)	5277	1468	1113	116
H(29A)	2887	2446	1367	128
H(29B)	3154	2786	2135	128
H(29C)	2965	1845	2022	128

H(30)	7309	4055	2251	48
H(31A)	6535	5575	1774	73
H(31B)	7319	5457	2420	73
H(31C)	6186	5132	2474	73
H(32A)	8150	4013	1155	82
H(32B)	8547	4737	1640	82
H(32C)	7778	4909	996	82
H(33A)	5608	1029	3765	50
H(33B)	5347	1193	2955	50
H(34A)	6954	183	3427	70
H(34B)	5868	-143	3174	70
H(35A)	6120	380	2050	68
H(35B)	6966	-267	2260	68
H(36A)	7702	820	1723	71
H(36B)	8122	734	2510	71
H(1S1)	7893	6696	1053	96
H(1S2)	6865	6906	634	96
H(1S3)	7012	7169	1438	96
H(2S1)	8297	8069	1120	72
H(2S2)	8149	7805	313	72
H(3S1)	7772	9196	66	81
H(3S2)	7847	9416	887	81
H(4S1)	6769	10322	299	94
H(4S2)	6141	9810	851	94
H(4S3)	6070	9594	32	94
H(6S1)	1719	4054	441	275
H(6S2)	638	3652	560	275
H(6S3)	999	4396	1035	275
H(7S1)	1023	5166	105	100
H(7S2)	722	4437	-383	100
H(8S1)	-257	5860	-694	98
H(8S2)	-641	5031	-1017	98
H(9S1)	-1862	5885	-1083	162
H(9S2)	-1743	6107	-267	162
H(9S3)	-2143	5238	-499	162

Table A.13. Torsion angles [°] for C₄₂H₆₉Cl_{10.25}FeN_{5.50}O_{1.50} (4.40).

C(5)-N(2)-C(1)-N(1)	-88.8(2)	C(8)-C(7)-C(12)-C(11)	-3.6(4)
C(4)-N(2)-C(1)-N(1)	57.1(3)	N(4)-C(7)-C(12)-C(11)	171.9(2)
C(5)-N(2)-C(1)-C(33)	153.4(2)	C(8)-C(7)-C(12)-C(16)	172.0(2)
C(4)-N(2)-C(1)-C(33)	-60.7(3)	N(4)-C(7)-C(12)-C(16)	-12.4(4)
C(5)-N(2)-C(1)-Fe(1)	24.7(3)	C(9)-C(8)-C(13)-C(15)	69.2(3)
C(4)-N(2)-C(1)-Fe(1)	170.51(17)	C(7)-C(8)-C(13)-C(15)	-112.2(3)
C(19)-N(1)-C(1)-N(2)	139.5(2)	C(9)-C(8)-C(13)-C(14)	-54.5(4)
C(2)-N(1)-C(1)-N(2)	-52.4(3)	C(7)-C(8)-C(13)-C(14)	124.0(3)
C(19)-N(1)-C(1)-C(33)	-100.8(3)	C(11)-C(12)-C(16)-C(18)	-31.0(4)
C(2)-N(1)-C(1)-C(33)	67.3(3)	C(7)-C(12)-C(16)-C(18)	153.4(3)
C(19)-N(1)-C(1)-Fe(1)	23.9(3)	C(11)-C(12)-C(16)-C(17)	92.9(3)
C(2)-N(1)-C(1)-Fe(1)	-167.99(19)	C(7)-C(12)-C(16)-C(17)	-82.7(3)
C(19)-N(1)-C(2)-C(3)	-142.5(3)	C(21)-N(3)-C(19)-N(1)	167.5(2)
C(1)-N(1)-C(2)-C(3)	50.3(3)	Fe(1)-N(3)-C(19)-N(1)	-5.7(3)
N(1)-C(2)-C(3)-C(4)	-49.3(3)	C(21)-N(3)-C(19)-C(20)	-13.8(4)
C(5)-N(2)-C(4)-C(3)	84.5(3)	Fe(1)-N(3)-C(19)-C(20)	172.9(2)
C(1)-N(2)-C(4)-C(3)	-60.0(3)	C(2)-N(1)-C(19)-N(3)	-179.9(2)
C(2)-C(3)-C(4)-N(2)	53.8(3)	C(1)-N(1)-C(19)-N(3)	-12.7(3)
C(7)-N(4)-C(5)-N(2)	171.4(2)	C(2)-N(1)-C(19)-C(20)	1.4(4)
Fe(1)-N(4)-C(5)-N(2)	-10.4(3)	C(1)-N(1)-C(19)-C(20)	168.6(2)
C(7)-N(4)-C(5)-C(6)	-12.2(4)	C(19)-N(3)-C(21)-C(26)	103.0(3)
Fe(1)-N(4)-C(5)-C(6)	165.9(2)	Fe(1)-N(3)-C(21)-C(26)	-84.7(3)
C(1)-N(2)-C(5)-N(4)	-9.2(3)	C(19)-N(3)-C(21)-C(22)	-81.0(3)
C(4)-N(2)-C(5)-N(4)	-153.4(2)	Fe(1)-N(3)-C(21)-C(22)	91.3(3)
C(1)-N(2)-C(5)-C(6)	174.2(2)	C(26)-C(21)-C(22)-C(23)	-2.3(4)
C(4)-N(2)-C(5)-C(6)	30.0(3)	N(3)-C(21)-C(22)-C(23)	-178.4(2)
C(5)-N(4)-C(7)-C(12)	116.2(3)	C(26)-C(21)-C(22)-C(27)	175.6(2)
Fe(1)-N(4)-C(7)-C(12)	-61.5(3)	N(3)-C(21)-C(22)-C(27)	-0.4(4)
C(5)-N(4)-C(7)-C(8)	-68.1(3)	C(21)-C(22)-C(23)-C(24)	1.2(4)
Fe(1)-N(4)-C(7)-C(8)	114.1(2)	C(27)-C(22)-C(23)-C(24)	-176.8(3)
C(12)-C(7)-C(8)-C(9)	3.2(4)	C(22)-C(23)-C(24)-C(25)	0.4(4)
N(4)-C(7)-C(8)-C(9)	-172.4(2)	C(23)-C(24)-C(25)-C(26)	-1.0(4)
C(12)-C(7)-C(8)-C(13)	-175.4(3)	C(24)-C(25)-C(26)-C(21)	-0.1(4)
N(4)-C(7)-C(8)-C(13)	9.1(4)	C(24)-C(25)-C(26)-C(30)	-176.7(2)
C(7)-C(8)-C(9)-C(10)	-0.3(4)	C(22)-C(21)-C(26)-C(25)	1.8(4)
C(13)-C(8)-C(9)-C(10)	178.3(3)	N(3)-C(21)-C(26)-C(25)	177.8(2)
C(8)-C(9)-C(10)-C(11)	-2.1(5)	C(22)-C(21)-C(26)-C(30)	178.2(2)
C(9)-C(10)-C(11)-C(12)	1.6(5)	N(3)-C(21)-C(26)-C(30)	-5.8(4)
C(10)-C(11)-C(12)-C(7)	1.2(4)	C(23)-C(22)-C(27)-C(28)	67.9(4)
C(10)-C(11)-C(12)-C(16)	-174.5(3)	C(21)-C(22)-C(27)-C(28)	-110.0(3)

C(23)-C(22)-C(27)-C(29)	-56.7(4)	Fe(1)-C(1)-C(33)-C(34)	62.8(3)
C(21)-C(22)-C(27)-C(29)	125.3(3)	C(1)-C(33)-C(34)-C(35)	-66.2(3)
C(25)-C(26)-C(30)-C(32)	-55.8(3)	C(33)-C(34)-C(35)-C(36)	62.2(4)
C(21)-C(26)-C(30)-C(32)	127.8(3)	C(34)-C(35)-C(36)-Fe(1)	-58.5(4)
C(25)-C(26)-C(30)-C(31)	67.3(3)	C(3S)-O(1S)-C(2S)-C(1S)	175.9(3)
C(21)-C(26)-C(30)-C(31)	-109.1(3)	C(2S)-O(1S)-C(3S)-C(4S)	179.3(3)
N(2)-C(1)-C(33)-C(34)	-61.9(3)	C(8S)-O(2S)-C(7S)-C(6S)	-166.3(17)
N(1)-C(1)-C(33)-C(34)	-179.0(2)	C(7S)-O(2S)-C(8S)-C(9S)	179.9(11)
